Efficient predictions of the vibratory response of mistuned bladed disks by reduced order modeling

Ronnie Bladh

EFFICIENT PREDICTIONS OF THE VIBRATORY RESPONSE OF MISTUNED BLADED DISKS BY REDUCED ORDER MODELING

by

Jan Ronnie Bladh

A dissertation submitted in partial fulfillment
of the requirements for the degree of
Doctor of Philosophy
(Mechanical Engineering)
in The University of Michigan
2001

Doctoral Committee:

Professor Christophe Pierre, Co-Chair
Assistant Research Scientist Matthew P. Castanier, Co-Chair
Professor Noel C. Perkins
Associate Professor Nickolas Vlahopoulos
Gísli S. Óttarsson, Ph.D., Mechanical Dynamics, Inc.

Dear Ewelina — a grand source of inspiration!
(Mackinac Island, June 1999)

To my father, whose untimely death prevents him from sharing this and countless other milestones of my life…

To my three First Ladies: my mother, wife, and daughter

ACKNOWLEDGEMENTS

I wish to express my most sincere gratitude to my advisors and co-chairs of my doctoral committee, Professor Christophe Pierre and Dr. Matthew P. Castanier, for their expert guidance during these years of hard work with seemingly equal shares of frustrations and rewards. I gratefully acknowledge their technical and strategic expertise, as well as their immense patience, leading to the successful completion of my doctorate.

I am also grateful to the remaining members of my doctoral committee, Professor Noel C. Perkins, Professor Nickolas Vlahopoulos, and Dr. Gísli S. Óttarsson, for their valuable comments and suggestions.

I am indebted to The Swedish Research Council for Engineering Sciences (TFR) for their generous financial support through their U.S. Ph.D. scholarship initiative. Special thanks are due to TFR research officer Dr. Per Karlsson for his dedicated work in supporting me and fellow scholars in this initiative.

TABLE OF CONTENTS

DEDICATION . . . . . **ii**

ACKNOWLEDGEMENTS . . . . . **iii**

LIST OF FIGURES . . . . . **viii**

LIST OF TABLES . . . . . **xviii**

LIST OF APPENDICES . . . . . **xix**

CHAPTER

I. Introduction 1

1.1 Dissertation Objectives 1
1.2 Background 3
1.3 Dissertation Outline 8

II. Cyclic Symmetry Analysis 11

2.1 Real Form Cyclic Analysis Using Isolated Substructures 11
2.2 Real Form Cyclic Analysis Using Integral Substructures 19
2.3 Complex Form Cyclic Analysis 20
2.4 Summary 22

III. Dynamic Response Predictions for a Mistuned Industrial Turbomachinery Rotor Using Reduced Order Modeling 23

3.1 Introduction 24
3.2 Reduced Order Modeling Technique 28
3.2.1 General Formulation of Reduced Order Model 28
3.2.2 Formulation Refinement for Unshrouded Designs . . . 31
3.2.3 Cantilever Blade Eigenvalue Adjustments 35
3.3 Rotor Description and Computational Models 36
3.4 Reduced Order Model Validation 37
3.4.1 Free Vibrations 37

3.4.2 Forced Response 42
3.5 Forced Response Statistics 47
3.6 Effects of Structural Interblade Coupling 51
3.7 Conclusions 59

IV. Reduced Order Modeling and Vibration Analysis of Mistuned Bladed Disk Assemblies with Shrouds 61

4.1 Introduction 62
4.2 Reduced Order Modeling Technique 64
4.2.1 General Formulation of Reduced Order Model 64
4.2.2 Formulation Refinement for Shrouded Designs 68
4.2.3 Mistuning of Shrouded Blades 70
4.2.4 Final Formulation for Shrouded Designs 74
4.3 Analysis of a Shrouded Test Case Rotor 75
4.3.1 Finite Element and Reduced Order Models 75
4.3.2 Free Vibration 78
4.3.3 Forced Response 82
4.4 Conclusions 83

V. Component-Mode-Based Reduced Order Modeling Techniques for Mistuned Bladed Disks, Part I: Theoretical Models 85

5.1 Introduction 86
5.2 Computational Issues and Assumptions 89
5.2.1 Cyclic Symmetry Description of the Disk Component 91
5.2.2 Engine Order Excitation Force 94
5.2.3 Mistuning Implementation 94
5.3 Fixed Interface Method (Craig-Bampton) 96
5.3.1 Blade Component 96
5.3.2 Cyclic Disk Component 98
5.3.3 CMS Model Assembly 100
5.4 Craig-Bampton with Partial Secondary Modal Analyses 103
5.4.1 Craig-Bampton with Modal Interface 103
5.4.2 Craig-Bampton with Modal Disk and Interface 105
5.5 Disk-Induced Blade Constraint Modes (REDUCE) 107
5.6 Non-CMS Mistuning Projection Method 110
5.7 Secondary Modal Analysis Reduction Technique (SMART) 114
5.8 Comparison of Methods 118
5.9 Conclusions 123

VI. Component-Mode-Based Reduced Order Modeling Techniques for Mistuned Bladed Disks, Part II: Application 125

6.1 Introduction 126
6.2 Description of Example Finite Element Models 128
6.2.1 Small Example Finite Element Model 130
6.2.2 Large Example Finite Element Model 131
6.3 Free Vibration 133
6.3.1 Tuned Assembly 133
6.3.2 Mistuned Assembly 136
6.4 Forced Response 144
6.5 Application of SMART to a Large-Size Model 148
6.6 Conclusions 154

VII. Effects of Multi-Stage Coupling and Disk Flexibility on Mistuned Bladed Disk Dynamics 155

7.1 Introduction 156
7.2 Description of Example Models 158
7.3 Features of Multi-Stage Response 160
7.3.1 Free Vibrations 161
7.3.2 Forced Response 167
7.4 Veering Response Sensitivity 171
7.4.1 Effects of Disk Flexibility 171
7.4.2 Effects of Interstage Coupling 177
7.5 Conclusions 186

VIII. Reduced Order Modeling Techniques for Dynamic Analysis of Mistuned Multi-Stage Turbomachinery Rotors 188

8.1 Introduction 189
8.2 Reduced Order Modeling Techniques 191
8.2.1 Single-Stage CMS Model 192
8.2.2 Engine Order Excitation Force 196
8.2.3 Multi-Stage Synthesis 197
8.2.4 Options for Secondary Condensation 199
8.2.5 Characteristic Constraint Modes (CCM) 200
8.2.6 Full Secondary Modal Analysis (SMART) 205
8.3 Test Case: Simple Two-Stage Rotor Model 207
8.3.1 Setup of CCM and SMART Reduced Order Models . . 207
8.3.2 Free Vibrations 213
8.3.3 Forced Response 219
8.4 Conclusions 224

IX. Current Topics in Bladed Disk Modeling 226

9.1 Numerical Instability of Classical Free-Interface Component Mode Synthesis Techniques 227
9.1.1 Test Model Description 228
9.1.2 Classical CMS Formulations in Brief 229
9.1.3 A Stabilized Free-Interface CMS Method 236
9.1.4 Modal Convergence and Numerical Stability Issues . . 237
9.2 "Optimal" Component Mode Basis for Dynamic Analyses of Mistuned Bladed Disks 241
9.2.1 A Hybrid-Interface CMS Approach 242
9.2.2 Modal Convergence Trends 243

X. Conclusions 247

10.1 Dissertation Contributions 248
10.2 Future Research 250

APPENDICES **252**

BIBLIOGRAPHY **256**

LIST OF FIGURES

Figure

1.1 Industrial jet engine. 1

2.1 Sector boundary index notations. 14

3.1 Finite element meshes for the industrial 29-blade compressor rotor: (a) the full model; (b) the fundamental sector. 24

3.2 Employed component modes: (a) normal modes of a cantilevered blade; (b) cyclic modes for a fundamental disk-blade sector, where the blade is massless. 28

3.3 Natural frequencies versus number of nodal diameters for the tuned rotor by finite element and reduced order modeling. Note the excellent agreement between finite element and adjusted ROM natural frequencies. 39

3.4 Comparison of tuned finite element and ROM four nodal diameter mode shapes (dominated by 1F motion). 41

3.5 Comparison of tuned finite element and ROM one nodal diameter mode shapes (dominated by 2F motion). This mode is located in the investigated veering. 41

3.6 Comparison of mistuned finite element and ROM mode shapes in the frequency region encompassing the 1F blade-dominated modes. The mode shape is spatially localized about blade number six. 42

3.7 Comparison of mistuned finite element and ROM mode shapes in the frequency region encompassing the investigated veering. Motion is dominated by the 2F blade mode and is localized about blade number six. . . 43

3.8 Comparison of tuned finite element and ROM forced responses, for blade tip excitation with C=4. 45

3.9 Comparison of mistuned finite element and ROM maximum blade forced responses, for blade tip excitation with C=4. 45

3.10 Comparison of tuned finite element and ROM forced responses, for blade tip excitation with C=1. 46

3.11 Comparison of mistuned finite element and ROM maximum blade forced responses, for blade tip excitation with C=1. 47

3.12 Histogram of the maximum blade response amplitudes for engine order one excitation. Obtained by Monte Carlo simulation of 1000 different mistuned systems with uniform distributions of zero mean and 3% standard deviation. 49

3.13 Comparison of Weibull and Monte Carlo determined responses for $5^{\mathbf{th}}$, $50^{\mathbf{th}}$, and $95^{\mathbf{th}}$ percentiles of maximum blade response amplitude magnification. The approximate percentiles from the Weibull distributions conform well with the Monte Carlo percentiles. 50

3.14 Comparison of Weibull estimates of the probability density function for several sets of 50 mistuning patterns each and the full set of 1000 mistuning patterns. The Weibull approximations based on the smaller sets conform well with the probability density function obtained with the full set. 51

3.15 Variation in maximum blade response amplitudes with standard deviation of mistuning. Note that a local maximum occurs for mistuning distributions with approximately 1% standard deviation. Mistuned maximum principal stresses are as much as 86% higher than the tuned maximum principal stress. 52

3.16 Definition of index notation. 54

3.17 Natural frequencies versus number of nodal diameters as a continuous variable. 56

3.18 Close-up view of intense veering region. 56

3.19 Finite difference approximation of curvature for the $4^{\mathbf{th}}$ and $5^{\mathbf{th}}$ mode sets. 57

3.20 Forced response statistical data for selected veerings. 58

4.1 Cantilever blade (a) and disk-induced (b) motions. 65

4.2 Proposed configuration for measuring natural frequencies of shrouded blades individually. 72

4.3 (a) Finite element mesh of a single disk-blade-shroud sector. (b) Finite element mesh of a single blade with shrouds. 76

4.4 Finite element mesh of full shrouded test case rotor. 76

4.5 Comparison of tuned eigenfrequencies from finite element model (FEM) and reduced order model (ROM) with and without eigenvalue adjustment iterations. 79

4.6 Comparison of the 80 lowest mistuned eigenfrequencies from finite element model (FEM) and reduced order model (ROM) with and without eigenvalue adjustment iterations. 81

4.7 Mistuned mode number 17 at 2861.7 Hz, as obtained by finite element model (FEM) and reduced order model (ROM) with and without eigenvalue adjustment iterations. This mode exhibits significant localization. 81

4.8 Tuned forced response for engine order 7 excitation, as obtained by finite element model (FEM) and reduced order model (ROM) with and without eigenvalue adjustment iterations. 83

4.9 Forced response for engine order 7 excitation, for both tuned and mistuned rotor, as obtained by finite element model (FEM) and reduced order model (ROM) with three eigenvalue adjustment iterations. The mistuned FEM has 56,376 degrees of freedom, while the ROM has only 240 degrees of freedom. 84

5.1 Substructuring approach and index notation. 90

5.2 Craig-Bampton component modes: (a) fixed-interface normal modes of vibration; (b) static constraint modes due to successive unit deflections of interface DOF. 95

5.3 REDUCE component modes: (a) fixed-interface (cantilevered) normal blade modes; (b) cyclic modes for the fundamental disk-blade sector with a massless blade. 108

5.4 Required number of floating point operations (flops) as a function of matrix size for generalized eigensolution, matrix multiplication, and matrix inversion. Note the slight “bumps” due to the iterative nature of the eigensolution. 119

5.5 Comparison of estimated cumulative numbers of floating point operations during statistical analyses for selected methods, including the model setup cost. 122

5.6 Comparison of estimated cumulative numbers of floating point operations during statistical analyses for selected methods, disregarding the model setup cost. 122

6.1 Finite element meshes for the "small" example blisk: (a) the full model; (b) the fundamental sector. 130

6.2 Finite element meshes for the "large" example blisk: (a) the full model; (b) the fundamental sector. 132

6.3 Natural frequencies versus nodal diameters for the small example finite element model. The circles show the natural frequency values, while the connecting lines are drawn to aid in visualization of the mode families and the frequency veerings. The character of each family of blade-dominated modes is indicated on the right (e.g., 1F = 1st flex mode). . . 134

6.4 Modal convergence trends in the region surrounding Veering #1 for the small example model. 135

6.5 Reduced order model representations of mistuned mode shape number 37 for the small example model. 137

6.6 Reduced order model representations of mistuned mode shape number 38 for the small example model. 138

6.7 Sensitivity of Modal Assurance Criterion (MAC) values (mistuned mode shape number 38). 139

6.8 Method efficiency with respect to mistuned natural frequencies for $\delta_f \leq 0.1\%$ for the small example model. 141

6.9 Method efficiency with respect to mistuned natural frequencies for $\delta_f \leq 1.0\%$ for the small example model. 141

6.10 Method efficiency with respect to mistuned mode shapes for $\delta_{mac} \leq 0.1\%$ for the small example model. 142

6.11 Method efficiency with respect to mistuned mode shapes for $\delta_{mac} \leq 1.0\%$ for the small example model. 142

6.12 Forced response frequency sweep through Veering #1 for engine order one (1E) excitation of the tuned small example model. 145

6.13 Forced response frequency sweep through Veering #1 for engine order one (1E) excitation of the mistuned small example model (tuned FEM solution included for reference). 146

6.14 Forced response frequency sweep through Veering #2 for engine order three (3E) excitation of the mistuned small example model (tuned FEM solution included for reference). 147

6.15 Maximum response amplitudes for all blades from forced response frequency sweep through Veering #1 for engine order one (1E) excitation of the mistuned small example model. 147

6.16 Natural frequencies versus nodal diameters for the large example model. The character of each family of blade-dominated modes is indicated on the right, where F=Flex, T=Torsion, and A=Axial (edgewise) bending. . 149

6.17 Reduced order model representations of mistuned mode shape number 64 for the large example model. 150

6.18 Reduced order model representations of mistuned mode shape number 135 for the large example model. 150

6.19 Forced response frequency sweep through Veering #1 for engine order two (2E) excitation of the tuned large example model. 152

6.20 Forced response frequency sweep through Veering #1 for engine order two (2E) excitation of the mistuned large example model (tuned FEM solution included for reference). 152

6.21 Forced response frequency sweep through Veering #2 for engine order three (3E) excitation of the mistuned large example model (tuned FEM solution included for reference). 153

7.1 Finite element meshes for the single- and two-stage example rotor models. 159

7.2 Employed blade mistuning patterns sampled from a uniform distribution of mean zero and standard deviation 0.5%. 159

7.3 Deformed finite element shapes for (a) a blade-dominated mode and (b) a disk-dominated mode, which are both globally localized onto stage 2 (lower stage). 161

7.4 Stage 1 strain energies relative to total multi-stage strain energies for "tuned" and blade mistuned multi-stage modes below 8000 Hz. 163

7.5 Deformed finite element shapes for (a) a multi-stage system mode and (b) a mode globally localized onto stage 1 (upper stage). 164

7.6 Natural frequencies versus number of nodal diameters for the tuned stage 1 model with fixed interstage boundaries, and for the "tuned" multi-stage model for modes localized to stage 1, as obtained with finite element models. 165

7.7 Natural frequencies versus number of nodal diameters for the tuned stage 2 model with fixed interstage boundaries, and for the "tuned" multi-stage model for modes localized to stage 2, as obtained with finite element models. 165

7.8 Tuned multi-stage mode shapes 54 and 83, as represented by the normalized deflection for one DOF at each blade tip. 166

7.9 Mistuned single- and multi-stage mode shapes 54 and 83, as represented by the normalized deflection for one DOF at each blade tip. 168

7.10 Stage 1 forced response from engine order 10 excitation (10E=-2E), using tuned and mistuned finite element single- and multi-stage models. . 169

7.11 Stage 2 forced response from engine order 15 excitation (15E=-1E), using tuned and mistuned finite element single- and multi-stage models. . 170

7.12 Detailed view over the stage 1 eigenfrequency veering region indicated in Fig. 7.6 (single-stage) using a pseudo-continuous interblade phase angle description for varying levels of disk flexibility (E = Young's modulus). 172

7.13 Upper and lower eigenfrequency curvatures in the stage 1 veering region indicated in Fig. 7.6 (single-stage) using a pseudo-continuous interblade phase angle description for varying levels of disk flexibility (E = Young's modulus). 173

7.14 Tuned stage 1 forced response from engine order 10 excitation (10E=-2E) using the single-stage finite element model for varying levels of disk flexibility (E = Young's modulus). 174

7.15 Mistuned stage 1 forced response from engine order 10 excitation (10E=-2E) using the single-stage finite element model for varying levels of disk flexibility (E = Young's modulus). 175

7.16 Stage 1 maximum tuned and mistuned forced responses from engine order 10 excitation (10E=-2E) as function of disk flexibility (E = Young's modulus) using the single-stage finite element model. 175

7.17 Mistuned response amplitude magnification from engine order 10 excitation (10E=-2E) for the stage 1 finite element model (single-stage) as function of disk flexibility (E = Young's modulus), plus the local eigenfrequency veering characteristics (uniformly scaled): maximum veering curvature, and distance between veering and applied excitation. 176

7.18 Natural frequencies versus number of nodal diameters for the tuned stage 1 rotor model using different interstage boundary conditions, plus identified harmonics of the "tuned" two-stage model. 178

7.19 Detailed view over the eigenfrequency veering region indicated in Fig. 7.18. 179

7.20 Stage 1 tuned finite element forced responses from engine order 10 excitation (10E=-2E) using different interstage boundary conditions, plus the "tuned" multi-stage finite element response. 181

7.21 Stage 1 mistuned finite element forced responses from engine order 10 excitation (10E=-2E) using different interstage boundary conditions, plus the blade mistuned multi-stage finite element response. 181

7.22 Detailed view over the eigenfrequency veering region indicated in the inserted plot of global free vibration characteristics (upper left). Included data is for the tuned stage 1 rotor model using different interstage boundary conditions, plus identified harmonics of the "tuned" two-stage model, with a four-fold increase of Young's modulus in the disk plus interstage rims. 182

7.23 Stage 1 tuned finite element forced responses from engine order 11 excitation (11E=-1E) using different interstage boundary conditions, plus the "tuned" multi-stage finite element response, with a four-fold increase of Young's modulus in the disk plus interstage rims. 183

7.24 Detailed view over the eigenfrequency veering region indicated in the inserted plot of global free vibration characteristics (upper left). Included data is for the tuned stage 1 rotor model using different interstage boundary conditions, plus identified harmonics of the "tuned" two-stage model, with a four-fold increase of Young's modulus in the disk alone. . 185

7.25 Stage 1 tuned finite element forced responses from engine order 11 excitation (11E=-1E) using different interstage boundary conditions, plus the "tuned" multi-stage finite element response, with a four-fold increase of Young's modulus in the disk alone. 185

8.1 Substructuring approach and index notation for the i^{th} rotor stage. . . . 191

8.2 Schematic representation of the reduced order modeling processes for the Characteristic Constraint Modes (CCM) and the full Secondary Modal Analysis Reduction Technique (SMART) approaches. 201

8.3 Finite element meshes for the single- and two-stage example rotor models (from Bladh *et al.* [1]). 208

8.4 Single- and multi-stage modal convergence: mean and max relative frequency error below 8000 Hz as a function of retained component normal modes in the primary CMS model. 209

8.5 Modal convergence of multi-stage CCM model: mean and max relative frequency error below 8000 Hz as a function of retained disk-blade interface and interstage characteristic constraint modes. 210

8.6 Natural frequencies versus number of nodal diameters for the tuned stage 1 model with fixed interstage boundaries, as obtained with finite element and reduced order models. 214

8.7 Natural frequencies versus number of nodal diameters for the tuned stage 2 model with fixed interstage boundaries, as obtained with finite element and reduced order models. 215

8.8 "Tuned" multi-stage mode shapes 54 and 83, as represented by normalized single blade tip DOF deflections for both stages. 216

8.9 Natural frequencies versus number of nodal diameters for the "tuned" multi-stage model for modes localized to stage 1, as obtained with finite element and reduced order models. The finite element single-stage natural frequencies are included for reference. 217

8.10 Natural frequencies versus number of nodal diameters for the "tuned" multi-stage model for modes localized to stage 2, as obtained with finite element and reduced order models. The finite element single-stage natural frequencies are included for reference. 217

8.11 Mistuned multi-stage mode shapes 54 and 83, as represented by normalized single blade tip DOF deflections for both stages. 219

8.12 Tuned stage 1 forced response from engine order 10 excitation (10E=-2E) using finite element and reduced order single- and multi-stage models. . 220

8.13 Mistuned stage 1 forced response from engine order 10 excitation (10E=-2E) using finite element and reduced order single- and multi-stage models. The tuned stage 1 finite element single- and multi-stage responses are included for reference. 221

8.14 Tuned stage 2 forced response from engine order 15 excitation (15E=-1E) using finite element and reduced order single- and multi-stage models. . 222

8.15 Mistuned stage 2 forced response from engine order 15 excitation (15E=-1E) using finite element and reduced order single- and multi-stage models. The tuned stage 2 finite element single- and multi-stage responses are included for reference. 223

9.1 Deformed finite element meshes for the four lowest modes of the fixed-tip two-component test model. 228

9.2 Deformed finite element meshes for the four lowest modes of the free-tip two-component test model. 229

9.3 Convergence of the four lowest natural frequencies of the fixed-tip model relative to finite element results for the considered CMS methods. . . . 238

9.4 Convergence of the four lowest natural frequencies of the free-tip model relative to finite element results for the considered CMS methods. . . . 238

9.5 Relationship between the condition of the residual flexibility matrix and Rubin natural frequency errors for the fixed-tip test model. 240

9.6 Finite element mesh for simple two-component disk-blade sector model. 244

9.7 Convergence of the five lowest natural frequencies of the simple two-component disk-blade sector model in Fig. 9.6 relative to finite element results for the considered CMS methods. 245

10.1 Example results from a mistuning sensitivity analysis based on comprehensive response statistics for the industrial compressor stage model depicted in Fig. 3.1. 249

LIST OF TABLES

Table

3.1 Blisk material properties. 36

3.2 Mistuning pattern for the case study rotor, based on natural frequency measurements on a prototype rotor. 38

5.1 Assumed model dimensions for flops count. 121

5.2 Essential steps during model construction and use in a forced response statistical study (M = Modal domain, M. P.=Mistuning Projection method, RED.=REDUCE). 121

6.1 Material properties (generic steel) for both models. 129

6.2 Basic model data for the small model. 131

6.3 Single mistuning pattern for the small model. 131

6.4 Basic model data for the large model. 132

6.5 Single mistuning pattern for the large model. 133

8.1 Finite element and reduced order model sizes (DOF). 213

10.1 Computational efficiency and accuracy trends of developed techniques, with reference to the mistuning sensitivity analysis results in Fig. 10.1. . 249

LIST OF APPENDICES

Appendix

A. The Kronecker Product 253

B. Circulant Matrices 254

CHAPTER I

Introduction

1.1 Dissertation Objectives

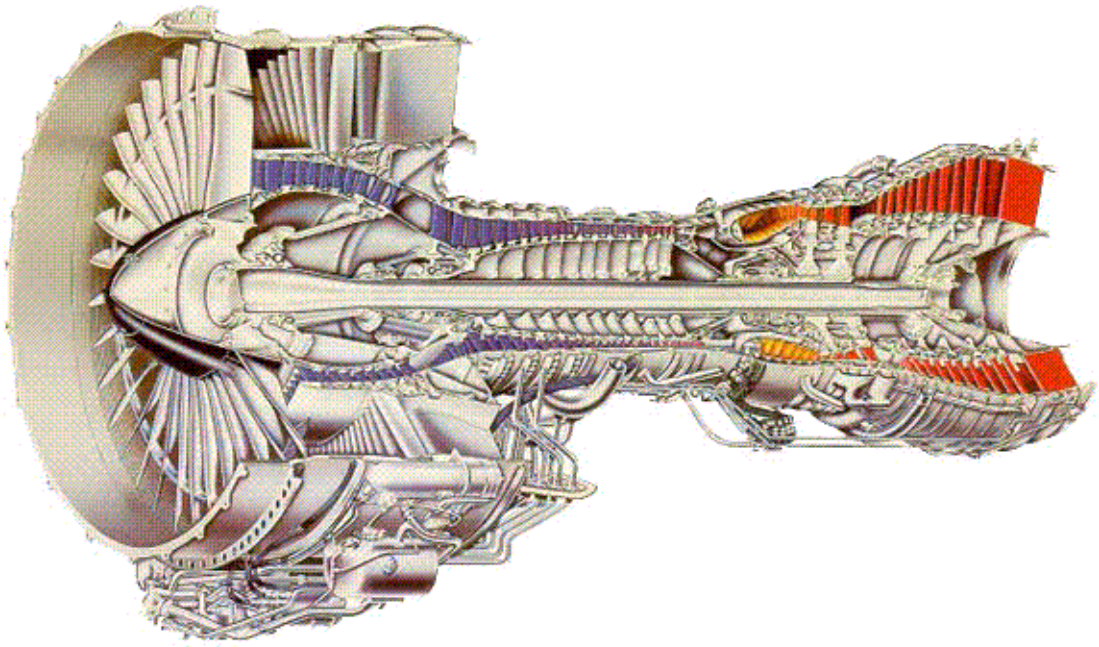

Figure 1.1: Industrial jet engine.

The research work reported in this dissertation aims to provide computational methodologies and to further the understanding of physical phenomena that will aid and improve the design of bladed disk assemblies from a structural dynamics standpoint. Bladed disk structures are found in a wide array of applications, including small impeller pumps and

automotive turbo systems; large gas, steam, and hydro turbines for power generation; and jet engines for military and commercial aircraft propulsion (Fig. 1.1).

Based on the nominal design, a bladed disk assembly is a rotationally periodic structure. If it is assumed that each disk-blade sector is identical, then the theory of cyclic symmetry may be used to analyze the dynamics of the entire structure based on one fundamental disk-blade sector (typically in finite element representation). In practice, however, there are always small differences among the structural properties of individual blades, which destroy the cyclic symmetry of the bladed disk assembly. These structural irregularities, commonly referred to as mistuning, may derive from manufacturing tolerances, deviations in material properties, or non-uniform operational wear. Mistuning is known to have a potentially dramatic effect on the vibratory behavior of the rotor, since it can lead to spatial localization of the vibration energy. Spatial localization implies that the vibration energy in a bladed disk becomes confined to one or a few blades rather than being uniformly distributed throughout the system. This phenomenon may be explained by viewing the vibration energy of the system as a circumferentially traveling wave. In a perfectly tuned system, the wave propagates through each identical disk-blade sector, yielding uniform vibration amplitudes that differ only in phase. In the mistuned case, however, the structural irregularities may cause the traveling wave to be partially reflected at each sector. This can lead to confinement of vibration energy to a small region of the assembly. As a result, certain blades may experience forced response amplitudes and stresses that are substantially larger than those predicted by an analysis of the nominal design. Hence, certain blades may exhibit much shorter lifespans than would be predicted by a fatigue life assessment based on the nominal assembly.

In order to address this concern, some efficient computational methods have been developed that can predict the effects of mistuning on the vibratory response of a turbo-

machinery rotor stage. Furthermore, these techniques enable analyses of large numbers of randomly mistuned bladed disks in order to estimate the mistuned forced response statistics for a rotor design. However, at the outset of this research effort, no methods possessed the combination of accuracy and computational efficiency required to allow reliable statistical assessments of mistuning sensitivity to be included as an integral part of the turbomachinery rotor design process.

Motivated by the turbomachinery community's need for practical design tools that incorporate mistuning effects, three distinct objectives are identified and addressed in this research effort:

- To develop highly efficient and accurate reduced order modeling techniques for the free and forced response of tuned and mistuned bladed disks, based on parent finite element representations of arbitrary complexity and detail in a consistent and systematic fashion.

- To broaden the scope of these reduced order modeling techniques by establishing linearized formulations for shrouded blade designs.

- To increase the understanding of the underlying physical mechanisms of the mistuning phenomenon, with particular emphasis on the role of disk flexibility and structural stage-to-stage coupling in determining a design's sensitivity to mistuning, leading to formulations for multi-stage synthesis and analysis.

1.2 Background

Investigations into the effects of imperfections on the vibrations of rotating disks can be traced back as far as to 1899, when Zenneck [2] presented a study on the dynamics of nearly perfectly axisymmetric disks. In the axisymmetric case, a disk features mode

pairs with identical natural frequencies and mode shapes that are positioned arbitrarily in the circumferential direction. Zenneck [2] showed both analytically and experimentally that structural imperfections cause the degenerate mode pairs to split into two distinct modes featuring spatially fixed mode shapes. Several decades later, the related mistuning phenomena found in turbomachinery rotors started to receive attention from researchers and engineers. In 1957, Tobias and Arnold [3] showed that in the case of nominally periodic, cyclic symmetric structures, mistuning causes mode pairs to split into two distinct modes. Almost in parallel, Anderson, who would later receive the Nobel Prize in Physics, documented the localization phenomenon in the field of solid state electronics in 1958 [4]. This would prove critical to yielding an understanding of the effects of mistuning on the dynamics of bladed disks.

Several researchers have since documented the effects of mistuning on blade vibrations by experiments, as well as by analyses of representative lumped parameter models using numerical, statistical, and perturbation methods (Wagner [5]; Dye and Henry [6]; Ewins [7, 8]; El-Bayoumy and Srinivasan [9]; Lu and Warner [10]; Griffin and Hoosac [11]; Abbas and Kamal [12]; Lin and Mignolet [13]). In particular, Wei and Pierre [14] examined first and second order perturbations of the general eigenvalue problem of periodic systems and concluded that structures with high modal densities (i.e., close eigenvalues) are more susceptible to mode localization than structures with widely spaced eigenvalues. However, although high modal density is a necessary condition for mode localization to occur, the existence of localized modes alone is not a sufficient condition for significant increases in resonant amplitudes in the forced response. In fact, Wei and Pierre [15] determined that significant resonant amplitude increases in the forced response also require moderately weak interblade coupling, while very weak or strong interblade coupling leads to mistuned response amplitudes that approach those of a tuned assembly. Hence, with the

additional insights provided by Óttarsson and Pierre [16], it has been concluded that bladed disk systems with low damping, high modal density, and moderately weak interblade coupling are most susceptible to resonant amplitude magnification due to localization of the vibration energy. In 1997, Srinivasan [17] published a particularly comprehensive survey of the literature on mistuning in bladed disks.

Although significant, the aforementioned efforts were primarily based on lumped parameter models of mistuned bladed disks. Unfortunately, in order to accurately represent an actual bladed disk design with a lumped parameter model, one must perform a difficult parameter identification which becomes infeasible as the number of model degrees of freedom (DOF) increases. Hence, to gain practical usefulness, there have been several efforts to generate reduced order models systematically from finite element models using component mode synthesis (CMS) methods (Irretier [18]; Zheng and Wang [19]; Castanier *et al*. [20]; Kruse and Pierre [21, 22]; Bladh *et al*. [23]). In CMS, the original structure is subdivided into smaller substructures, or components, for which normal modes are computed independently, and more inexpensively. The assembled system is then represented by a truncated set of component modes through necessary compatibility constraints in a systematic fashion. The result is highly-reduced order models based on parent finite element models of bladed disks of arbitrary complexity. Craig [24] and Seshu [25] have published excellent surveys on the development of CMS techniques. Other notable finite-element-based reduced order modeling methods include the receptance technique by Yang and Griffin [26], and an approach that incorporates classical modal analysis with mistuning projection by Yang and Griffin [27].

The technique of Castanier *et al*. [20] and Kruse and Pierre [21] is notable because it is specially-tailored to mistuned bladed disks. The key idea introduced by Castanier *et al*. [20] is that the motion of an individual blade is approximated by linear combinations of subsets

of cantilevered blade normal modes of vibration and disk-induced motion. The technique was thoroughly validated using a finite element model of an industrial rotor by Kruse and Pierre [22], and has been well received by industry. The significance of this technique is that it has enabled engineers to examine systematically the effects of random mistuning on forced response amplitudes.

This research focuses in part on the development of reduced order models of mistuned bladed disks based primarily on CMS techniques. Component mode synthesis in engineering practice was initiated by the work of Hurty [28]. Hurty employed three sets of component modes: (a) fixed interface normal modes; (b) static ("redundant") constraint modes; and (c) rigid-body modes. A few years later, Craig and Bampton [29] formulated a simplified CMS technique based on the work by Hurty. In this method, commonly referred to as Craig-Bampton (C-B), Hurty's set of rigid-body modes is left out. Instead, a complete set of "constraint modes" is supplemented to the fixed interface normal modes of the components. The constraint modes of a component are constructed by imposing successive unit deflections on each of the interface DOF, while all other interface DOF are held fixed. C-B has rightfully gained enormous popularity among structural analysts and has been applied to a wide array of engineering structures. However, applications of C-B to mistuned bladed disks are surprisingly scarce in the literature.

The principal drawback of C-B is the use of fixed interfaces while computing the component normal modes, since experimental data for a component is often obtained for free interface conditions. Goldman [30] was the first to formulate a CMS technique that employed free interface normal modes. MacNeal [31] then formulated a hybrid CMS technique that allowed for mixed interface representations. Furthermore, MacNeal's technique was the first to account for the residual flexibility from the unused component modes in order to improve accuracy. Rubin [32] went one step further and included residual inertial

and dissipative effects in addition to the residual flexibility introduced by MacNeal. Later, Craig and Chang [33] were able to construct an exceptionally compact residual flexibility CMS technique. In this technique, only the generalized coordinates pertaining to the free interface component normal modes appear in the assembled system of equations of motion. Thus, by eliminating the interface DOF entirely, they obtained a compact and highly efficient reduced order model. Irretier [18] applied this technique to a simple finite element model of a bladed disk. Irretier's work demonstrates the applicability of the Craig-Chang method for this class of structures, showing good accuracy for both tuned and mistuned models.

After this twelve-year burst of classical CMS technique development, the progress in the CMS field has been fairly modest. It appears from the literature that research has since focused primarily on replacing the traditional normal component modes (free, fixed, or hybrid interface), in order to alleviate the need to solve the component eigenvalue problems. This may be achieved with generated sets of admissible component displacement vectors, or Ritz vectors, provided they adequately span the deformation space of the component. This line of action was spearheaded by the work by Hale and Meirovitch [34] who formulated a generalized method of CMS using admissible functions. A number of related research efforts has followed using Wilson-Ritz vectors (Wilson *et al*. [35]; Wilson and Bayo [36]; Arnold *et al*. [37]; Abdallah and Huckelbridge [38]) and Block-Krylov Ritz vectors (Craig and Hale [39]). Other notable efforts in CMS development include, for instance, the intuitive coordinate transformation presented by Morgan *et al*. [40] to gain a physical interpretation of residual flexibility attachment modes, as well as the C-B method formulated with quasi-static rather than static constraint modes using a "centering frequency" approach demonstrated in Shyu *et al*. [41]. It should be pointed out, however, that the "centering frequency" approach leads to matrix ill-conditioning and eventually

fails due to matrix singularity as the component natural frequencies approach the "centering frequency", which is typically chosen close to a natural frequency of the system. This is not recognized in the work and, unfortunately, this is precisely the case for most turbomachinery rotor designs, since the blade is generally far more flexible than the disk. Hence, the natural frequencies of the blade component and the assembled system, and thus the "centering frequency", are often very close.

1.3 Dissertation Outline

This dissertation is directly compiled from a collection of six manuscripts that either have been or are in the process of being published in scientific journals. Two additional chapters (II and IX) are included that contain unpublished material on topics that are relevant to the main theme of this thesis. Note that repetition of some of the material is unavoidable, due to the chosen format and the coherent scope of the reported research. A brief outline of the chapters to follow in this dissertation is given next.

Chapter II outlines the theory of cyclic symmetry analysis, which is a central component of all reduced order modeling techniques considered in this work. Both real-valued and complex forms of cyclic symmetry analysis are considered. Important features of interest and value are highlighted.

Chapter III presents the theoretical foundation of the reduced order modeling technique originally developed by Castanier *et al*. [20] and extended by Kruse and Pierre [21]. The technique is validated using a finite element model of an advanced industrial compressor stage in the free and forced response, including predictions of response statistics utilizing Weibull distributions. Furthermore, a technique is presented for calculating pseudo-continuous interblade phase angle modes (i.e., non-integer harmonics) of cyclic assemblies, which allows one to calculate natural frequency veering data more precisely.

Chapter IV provides an extension of the technique of Castanier *et al*. [20] to mistuned bladed disk assemblies with shrouded blades. A technique is formulated for extracting blade stiffness deviations from experimental or numerically generated mistuning data. The reduced order modeling technique for shrouded blades includes the concept of projecting blade mistuning data onto cyclic modes of the blade-shroud-ring assembly — a central concept for techniques developed later in this dissertation.

Chapter V presents the theoretical bases for several state of the art reduced order modeling techniques for the dynamic analysis of mistuned bladed disk assemblies. The considered approaches use a cyclic component mode synthesis (CMS) formulation, cyclic finite element modal analysis with projection of mistuning data, and a sequential combination of the two. The techniques are compared in terms of computational efficiency, with emphasis on comprehensive analyses of response statistics.

Chapter VI presents thorough, comparative case studies using the techniques developed in Chapter V and the technique of Castanier *et al*. [20], via modal convergence trends, as well as mode shape and forced response conformity. The objective of this study is to determine which formulation offers the most efficient and accurate modeling of mistuned blade disk assemblies.

Chapter VII investigates the impact of disk flexibility and structural stage-to-stage coupling on the free and forced response of bladed disks in multi-stage rotor assemblies. Particular attention is devoted to the effects on eigenfrequency veering characteristics and veering response behavior.

Chapter VIII presents two related techniques for the reduced order modeling of mistuned multi-stage rotors in response to the findings in Chapter VII. The introduced techniques use cyclic CMS representations of single-stage models, which are coupled together through static constraint modes to form the multi-stage assembly. The multi-stage CMS

model is further reduced by secondary modal analyses on either constraint-mode partitions or the entire multi-stage CMS model. The techniques are validated against benchmark finite element solutions for a simple two-stage example model.

In **Chapter IX**, recent progress in the application of CMS-based techniques to bladed disk modeling is presented. Both numerical stability and modal convergence issues are investigated. Results are shown for simple test cases, and preliminary conclusions are summarized.

Finally, in **Chapter X**, the conclusions and contributions of this dissertation are summarized, and ideas for future work are outlined.

CHAPTER II

Cyclic Symmetry Analysis

Although cyclic symmetry is a well-known concept among structural analysts, it plays such an important role in the reduced order modeling techniques formulated later that a brief review is in place. A detailed description of modes of vibration for cyclic structures is contained in the important work by Thomas [42], although certain related mathematical aspects, such as the fundamentals of circulant matrices, appear to have been unrealized at the time.

2.1 Real Form Cyclic Analysis Using Isolated Substructures

This approach to cyclic symmetry analysis is employed in the commercial finite element method software package MSC/NASTRAN™. The review of the topic presented here is similar in spirit to that given by Joseph [43], although this presentation is intended to be more focused towards dynamic analysis.

From the theory of symmetrical components [44], it is found that one may relate some quantity $\mathbf{x_n}$ (i.e., displacements, forces, etc.) in physical coordinates for the n^{th} sector, to the corresponding quantity $\mathbf{u^k}$ in cyclic coordinates for a fundamental sector. This coordinate transformation is governed by the expression:

$$\mathbf{x_n} = \frac{1}{\sqrt{N}}\mathbf{u^0} + \sqrt{\frac{2}{N}}\sum_{k=1}^{K}\left[\mathbf{u^{k,c}}\cos{(n-1)k\alpha} + \mathbf{u^{k,s}}\sin{(n-1)k\alpha}\right] + \frac{(-1)^{n-1}}{\sqrt{N}}\mathbf{u^{\frac{N}{2}}}, \quad (2.1)$$

where k is the harmonic order; N is the total number of sectors; α is the fundamental interblade phase shift defined as $2\pi/N$; and K is defined as:

$$K = \begin{cases} \frac{N-1}{2} & \text{if } N \text{ is odd} \\ \frac{N-2}{2} & \text{if } N \text{ is even.} \end{cases} \tag{2.2}$$

Note that the last term in Eq. (2.1) only exists if the number of sectors, N, is even.

In this context, the quantities $\mathbf{x}$ and $\mathbf{u}$ represent nodal displacements in physical and cyclic coordinates, respectively. The corresponding backward transformation from physical to cyclic coordinates is then given by the following series of relations:

$$\begin{aligned} \mathbf{u^0} &= \frac{1}{\sqrt{N}} \sum_{n=1}^{N} \mathbf{x_n} \\ \mathbf{u^{k,c}} &= \sqrt{\frac{2}{N}} \sum_{n=1}^{N} \mathbf{x_n} \cos(n-1)k\alpha \\ \mathbf{u^{k,s}} &= \sqrt{\frac{2}{N}} \sum_{n=1}^{N} \mathbf{x_n} \sin(n-1)k\alpha \\ \mathbf{u^{\frac{N}{2}}} &= \frac{1}{\sqrt{N}} \sum_{n=1}^{N} (-1)^{n-1} \mathbf{x_n}. \end{aligned} \tag{2.3}$$

Defining the displacement vectors $\mathbf{x}$ and $\mathbf{u}$ as:

$$\mathbf{x} = \begin{Bmatrix} \mathbf{x_1} \\ \mathbf{x_2} \\ \mathbf{x_3} \\ \vdots \\ \mathbf{x_N} \end{Bmatrix} \qquad \mathbf{u} = \begin{Bmatrix} \mathbf{u^0} \\ \mathbf{u^{1,c}} \\ \mathbf{u^{1,s}} \\ \mathbf{u^{2,c}} \\ \vdots \\ \mathbf{u^{\frac{N}{2}}} \end{Bmatrix}, \tag{2.4}$$

Eq. (2.1) is more conveniently represented in matrix form as:

$$\mathbf{x} = (\mathbf{F} \otimes \mathbf{I})\, \mathbf{u}, \tag{2.5}$$

where $\mathbf{F}$ is the real-valued Fourier matrix defined in Eq. (B.3), and the symbol $\otimes$ denotes the Kronecker product defined in Appendix A. Note that the identity matrix, $\mathbf{I}$, has the

size of the number of elements in $\mathbf{u^k}$. Also, note that the backward transformation matrix $(\mathbf{F} \otimes \mathbf{I})^{-1}$ is simply $\mathbf{F^T} \otimes \mathbf{I}$.

While assuming harmonic motion, it is convenient to define the quantity $\mathbf{Y}$ as:

$$\mathbf{Y} = \mathbf{K} - \omega^2 \mathbf{M} \tag{2.6}$$

where $\mathbf{K}$ and $\mathbf{M}$ are, respectively, the stiffness and mass matrices of a fundamental sector, and ω is the frequency of motion. Note that these matrices include all elements related to both boundaries towards adjacent sectors, since the fundamental sector is still a completely isolated, uncoupled structure. One may perform permutations on the structural matrices involved to give the following matrix partitioning scheme:

$$\mathbf{Y} = \begin{bmatrix} \mathbf{Y_{aa}} & \mathbf{Y_{ai}} & \mathbf{Y_{ab}} \\ \mathbf{Y_{ai}^T} & \mathbf{Y_{ii}} & \mathbf{Y_{ib}} \\ \mathbf{Y_{ab}^T} & \mathbf{Y_{ib}^T} & \mathbf{Y_{bb}} \end{bmatrix} = \begin{bmatrix} \mathbf{K_{aa}} & \mathbf{K_{ai}} & \mathbf{K_{ab}} \\ \mathbf{K_{ai}^T} & \mathbf{K_{ii}} & \mathbf{K_{ib}} \\ \mathbf{K_{ab}^T} & \mathbf{K_{ib}^T} & \mathbf{K_{bb}} \end{bmatrix} - \omega^2 \begin{bmatrix} \mathbf{M_{aa}} & \mathbf{M_{ai}} & \mathbf{M_{ab}} \\ \mathbf{M_{ai}^T} & \mathbf{M_{ii}} & \mathbf{M_{ib}} \\ \mathbf{M_{ab}^T} & \mathbf{M_{ib}^T} & \mathbf{M_{bb}} \end{bmatrix}, \tag{2.7}$$

where subscripts a and b denote, respectively, degrees of freedom (DOF) on the independent and dependent boundaries, and i denotes internal DOF, as indicated in Fig. 2.1. Note that the structural matrices of the isolated sector are always symmetric. The displacement vector must be ordered accordingly:

$$\mathbf{u^k} = \begin{Bmatrix} \mathbf{u_a^k} \\ \mathbf{u_i^k} \\ \mathbf{u_b^k} \end{Bmatrix}. \tag{2.8}$$

The internal energy content E (strain and kinetic energy) of the entire system (all sectors) can now be expressed as:

$$E = \frac{1}{2} \mathbf{x^T} \left(\mathbf{I} \otimes \mathbf{Y} \right) \mathbf{x}, \tag{2.9}$$

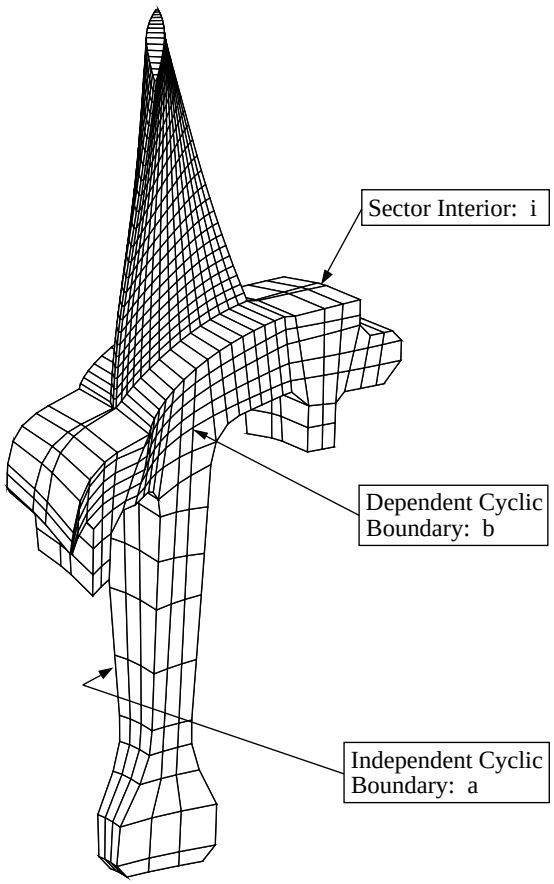

Figure 2.1: Sector boundary index notations.

where $\mathbf{I} \otimes \mathbf{Y}$ represents the compact form of the block-diagonal matrix:

$$\mathbf{I} \otimes \mathbf{Y} = \underset{n=1,\ldots,N}{\mathbf{Bdiag}}[\mathbf{Y}] = \begin{bmatrix} \mathbf{Y} & \mathbf{0} & \cdots & \mathbf{0} \\ \mathbf{0} & \mathbf{Y} & \cdots & \mathbf{0} \\ \vdots & \vdots & \ddots & \vdots \\ \mathbf{0} & \mathbf{0} & \cdots & \mathbf{Y} \end{bmatrix}. \tag{2.10}$$

By making the coordinate change to cyclic coordinates in accordance with Eq. (2.1), and applying Hamilton's principle, one obtains:

$$\int_{t_1}^{t_2} \delta E \, dt = \int_{t_1}^{t_2} \delta \mathbf{u}^{\mathbf{T}} \left(\mathbf{F}^{\mathbf{T}} \otimes \mathbf{I} \right) (\mathbf{I} \otimes \mathbf{Y}) (\mathbf{F} \otimes \mathbf{I}) \, \mathbf{u} \, dt = \int_{t_1}^{t_2} \delta \mathbf{u}^{\mathbf{T}} (\mathbf{I} \otimes \mathbf{Y}) \, \mathbf{u} \, dt = 0, \tag{2.11}$$

where it is noted that the similarity transformation $\left(\mathbf{F}^{\mathbf{T}} \otimes \mathbf{I} \right) (\mathbf{I} \otimes \mathbf{Y}) (\mathbf{F} \otimes \mathbf{I})$ simply yields

exactly the same block-diagonal matrix $\mathbf{I} \otimes \mathbf{Y}$. Realizing that Eq. (2.11) must hold true for any arbitrary set of virtual displacements $\delta\mathbf{u}$, Eqs. (2.4), (2.10), and (2.11) give a set of, for now unconstrained, eigenvalue problems in cyclic coordinates. For reasons that will soon be obvious, these eigenvalue problems are reduced to the size of either one or two sectors:

$$k = 0: \qquad \mathbf{Y}\mathbf{u}^{\mathbf{0}} = \mathbf{0}$$

$$1 \leq k \leq K: \qquad \begin{bmatrix} \mathbf{Y} & \mathbf{0} \\ \mathbf{0} & \mathbf{Y} \end{bmatrix} \begin{Bmatrix} \mathbf{u}^{\mathbf{k,c}} \\ \mathbf{u}^{\mathbf{k,s}} \end{Bmatrix} = \begin{Bmatrix} \mathbf{0} \\ \mathbf{0} \end{Bmatrix} \tag{2.12}$$

$$k = \tfrac{N}{2}: \qquad \mathbf{Y}\mathbf{u}^{\frac{\mathbf{N}}{\mathbf{2}}} = \mathbf{0} \quad \text{(if } N \text{ is even)}.$$

At this point, the above eigenvalue problems are in fact identical, since each displacement vector $\mathbf{u}^{\mathbf{k}}$ in the current form includes the nodes on both boundaries of the isolated sector substructure (e.g., boundaries a and b in Fig. 2.1). Considering the rotational symmetry of the assembly, it is obvious from displacement compatibility considerations that the nodal displacements on one of these two boundaries are dependent upon the nodal displacements of the other boundary in a non-arbitrary manner. Furthermore, this dependency is unique for each harmonic order. Hence, the missing piece is the boundary constraints, which, when introduced into Eq. (2.12), will give a unique eigenvalue problem to solve for each of the harmonics. Using the notation shown in Fig. 2.1, the required cyclic boundary constraints for actual and virtual displacement compatibility can be shown to be:

$$\begin{cases} \mathbf{u}_{\mathbf{b}}^{\mathbf{k,c}} = \mathbf{u}_{\mathbf{a}}^{\mathbf{k,c}} \cos k\alpha + \mathbf{u}_{\mathbf{a}}^{\mathbf{k,s}} \sin k\alpha \\ \mathbf{u}_{\mathbf{b}}^{\mathbf{k,s}} = -\mathbf{u}_{\mathbf{a}}^{\mathbf{k,c}} \sin k\alpha + \mathbf{u}_{\mathbf{a}}^{\mathbf{k,s}} \cos k\alpha \end{cases} \tag{2.13}$$

$$\begin{cases} \delta\mathbf{u}_{\mathbf{b}}^{\mathbf{k,c}} = \delta\mathbf{u}_{\mathbf{a}}^{\mathbf{k,c}} \cos k\alpha + \delta\mathbf{u}_{\mathbf{a}}^{\mathbf{k,s}} \sin k\alpha \\ \delta\mathbf{u}_{\mathbf{b}}^{\mathbf{k,s}} = -\delta\mathbf{u}_{\mathbf{a}}^{\mathbf{k,c}} \sin k\alpha + \delta\mathbf{u}_{\mathbf{a}}^{\mathbf{k,s}} \cos k\alpha. \end{cases}$$

Note that for $k = 0$ and, if it exists, $k = N/2$, the governing relations in Eq. (2.13) collapse to the following:

$$\begin{array}{llll} k = 0: & \mathbf{u}_{\mathbf{b}}^{\mathbf{0}} = \mathbf{u}_{\mathbf{a}}^{\mathbf{0}} & k = \frac{N}{2}: & \mathbf{u}_{\mathbf{b}}^{\frac{\mathbf{N}}{\mathbf{2}}} = -\mathbf{u}_{\mathbf{a}}^{\frac{\mathbf{N}}{\mathbf{2}}} \\ & \delta\mathbf{u}_{\mathbf{b}}^{\mathbf{0}} = \delta\mathbf{u}_{\mathbf{a}}^{\mathbf{0}} & & \delta\mathbf{u}_{\mathbf{b}}^{\frac{\mathbf{N}}{\mathbf{2}}} = -\delta\mathbf{u}_{\mathbf{a}}^{\frac{\mathbf{N}}{\mathbf{2}}}, \end{array} \tag{2.14}$$

which is consistent with the single-sector representations for these harmonics in Eq. (2.12).

By introducing Eqs. (2.8), (2.13), and (2.14) into Eq. (2.12), the following four sets of governing equations of motion are obtained after simplifications and collection of terms:

$$\begin{aligned} \delta\mathbf{u}_{\mathbf{a}}^{\mathbf{k,c}^{\mathbf{T}}}: \quad & \left[\mathbf{Y_{aa}} + \left(\mathbf{Y_{ab}} + \mathbf{Y_{ab}^{T}}\right)\cos k\alpha + \mathbf{Y_{bb}}\right]\mathbf{u}_{\mathbf{a}}^{\mathbf{k,c}} + \left[\mathbf{Y_{ai}} + \mathbf{Y_{ib}^{T}}\cos k\alpha\right]\mathbf{u}_{\mathbf{i}}^{\mathbf{k,c}} + \\ & + \left[\left(\mathbf{Y_{ab}} - \mathbf{Y_{ab}^{T}}\right)\sin k\alpha\right]\mathbf{u}_{\mathbf{a}}^{\mathbf{k,s}} - \left[\mathbf{Y_{ib}^{T}}\sin k\alpha\right]\mathbf{u}_{\mathbf{i}}^{\mathbf{k,s}} = 0 \\ \\ \delta\mathbf{u}_{\mathbf{i}}^{\mathbf{k,c}^{\mathbf{T}}}: \quad & \left[\mathbf{Y_{ai}^{T}} + \mathbf{Y_{ib}}\cos k\alpha\right]\mathbf{u}_{\mathbf{a}}^{\mathbf{k,c}} + \left[\mathbf{Y_{ii}}\right]\mathbf{u}_{\mathbf{i}}^{\mathbf{k,c}} + \left[\mathbf{Y_{ib}}\sin k\alpha\right]\mathbf{u}_{\mathbf{a}}^{\mathbf{k,s}} = 0 \\ \\ \delta\mathbf{u}_{\mathbf{a}}^{\mathbf{k,s}^{\mathbf{T}}}: \quad & \left[\left(\mathbf{Y_{ab}^{T}} - \mathbf{Y_{ab}}\right)\sin k\alpha\right]\mathbf{u}_{\mathbf{a}}^{\mathbf{k,c}} + \left[\mathbf{Y_{ib}^{T}}\sin k\alpha\right]\mathbf{u}_{\mathbf{i}}^{\mathbf{k,c}} + \\ & + \left[\mathbf{Y_{aa}} + \left(\mathbf{Y_{ab}} + \mathbf{Y_{ab}^{T}}\right)\cos k\alpha + \mathbf{Y_{bb}}\right]\mathbf{u}_{\mathbf{a}}^{\mathbf{k,s}} + \left[\mathbf{Y_{ai}} + \mathbf{Y_{ib}^{T}}\cos k\alpha\right]\mathbf{u}_{\mathbf{i}}^{\mathbf{k,s}} = 0 \\ \\ \delta\mathbf{u}_{\mathbf{i}}^{\mathbf{k,s}^{\mathbf{T}}}: \quad & -\left[\mathbf{Y_{ib}}\sin k\alpha\right]\mathbf{u}_{\mathbf{a}}^{\mathbf{k,c}} + \left[\mathbf{Y_{ai}^{T}} + \mathbf{Y_{ib}}\cos k\alpha\right]\mathbf{u}_{\mathbf{a}}^{\mathbf{k,s}} + \left[\mathbf{Y_{ii}}\right]\mathbf{u}_{\mathbf{i}}^{\mathbf{k,s}} = 0. \end{aligned} \tag{2.15}$$

Note that the eigenvalue problem for a "double" harmonic (i.e., for k such that $1 \leq k \leq K$) is examined here for generality. The above system of equations can be written in a more

convenient matrix form:

$$\tilde{\mathbf{Y}}^{\mathbf{k}}\tilde{\mathbf{u}}^{\mathbf{k}} = \begin{bmatrix} \mathbf{Y}_0^{\mathbf{k}} & \mathbf{Y}_1^{\mathbf{k}} \\ & \\ \mathbf{Y}_1^{\mathbf{k}^{\mathbf{T}}} & \mathbf{Y}_0^{\mathbf{k}} \end{bmatrix} \begin{Bmatrix} \mathbf{u}_{\mathbf{a}}^{\mathbf{k,c}} \\ \mathbf{u}_{\mathbf{i}}^{\mathbf{k,c}} \\ \dots \\ \mathbf{u}_{\mathbf{a}}^{\mathbf{k,s}} \\ \mathbf{u}_{\mathbf{i}}^{\mathbf{k,s}} \end{Bmatrix} = \begin{Bmatrix} \mathbf{0} \\ \mathbf{0} \\ \dots \\ \mathbf{0} \\ \mathbf{0} \end{Bmatrix}, \tag{2.16}$$

where

$$\mathbf{Y}_0^{\mathbf{k}} = \begin{bmatrix} \mathbf{Y_{aa}} + \left(\mathbf{Y_{ab}} + \mathbf{Y_{ab}^T}\right)\cos k\alpha + \mathbf{Y_{bb}} & \mathbf{Y_{ai}} + \mathbf{Y_{ib}^T}\cos k\alpha \\ \mathbf{Y_{ai}^T} + \mathbf{Y_{ib}}\cos k\alpha & \mathbf{Y_{ii}} \end{bmatrix}$$

$$\mathbf{Y}_1^{\mathbf{k}} = \begin{bmatrix} \left(\mathbf{Y_{ab}} - \mathbf{Y_{ab}^T}\right)\sin k\alpha & -\mathbf{Y_{ib}^T}\sin k\alpha \\ \mathbf{Y_{ib}}\sin k\alpha & \mathbf{0} \end{bmatrix}.$$

Note that $\tilde{\mathbf{Y}}^{\mathbf{k}}$ is symmetric, and that its two diagonal blocks are identical. The eigenvalue problem, $\mathbf{det}\left[\tilde{\mathbf{Y}}^{\mathbf{k}}\right] = 0$, belongs to a degenerate class of structural eigenvalue problems [45], and will yield pairs of real eigenvalues. Therefore, there will be an infinite number of eigenvectors satisfying the eigenvalue problem for each pair of eigenvalues, which, in general, will not be mutually orthogonal. However, since any linear combination of two eigenvectors associated with an eigenvalue pair is also a valid solution, the task of orthogonalizing the eigenvectors is quite trivial. For the same reason, the circumferential positioning of mode shapes pertaining to double harmonics is arbitrary. As a result, these mode shape pairs can also be represented by complex, counter-rotating waves.

Taking a closer look at the elements in the off-diagonal block of $\tilde{\mathbf{Y}}^{\mathbf{k}}$, it is observed that the off-diagonal block $\mathbf{Y}_1^{\mathbf{k}}$ consists of coupling masses and stiffnesses. In particular, it is only the direct coupling between the two cyclic boundaries (a and b), and the coupling between the dependent boundary (b) and the interior (i) that appear in the off-diagonal block. However, the direct cyclic boundary-to-boundary coupling, $\mathbf{Y_{ab}}$, is commonly

non-existent. Moreover, for $k = 0$ and, if it exists, for $k = N/2$, the off-diagonal block is zero. Thus, any diagonal block alone provides the complete eigenvalue problem in these two special cases, which is also indicated in Eq. (2.12).

As a point of interest, consider the pairs of orthogonalized cyclic eigenvectors associated with the double harmonics. The $2m$ vectors building the cyclic modal matrix associated with the k^{th} harmonic will appear as:

$$\mathbf{U^k} = \left[\begin{array}{c} \mathbf{U^{k,c}} \\ \mathbf{U^{k,s}} \end{array} \right] = \left[\begin{array}{cccc} \mathbf{u^{k,c}}\left(\omega_{1,1}\right) & \mathbf{u^{k,c}}\left(\omega_{1,2}\right) & \cdots & \mathbf{u^{k,c}}\left(\omega_{m,1}\right) & \mathbf{u^{k,c}}\left(\omega_{m,2}\right) \\ \mathbf{u^{k,s}}\left(\omega_{1,1}\right) & \mathbf{u^{k,s}}\left(\omega_{1,2}\right) & \cdots & \mathbf{u^{k,s}}\left(\omega_{m,1}\right) & \mathbf{u^{k,s}}\left(\omega_{m,2}\right) \end{array} \right]. \quad (2.17)$$

The interesting thing about these mode partitions is that it turns out that the sine mode components are related to the cosine mode components in a very simple fashion:

$$\left\{ \begin{array}{l} \mathbf{u^{k,s}}\left(\omega_{n,1}\right) = \pm \mathbf{u^{k,c}}\left(\omega_{n,2}\right) \\ \mathbf{u^{k,s}}\left(\omega_{n,2}\right) = \mp \mathbf{u^{k,c}}\left(\omega_{n,1}\right). \end{array} \right. \quad (2.18)$$

The order in which the signs appear in an actual cyclic eigen-analysis seems to be random, however. This suggests that this would be governed by some characteristic of the numerical solver in combination with the numerics of the eigenvalue problem at hand, rather than by any strict rules. Hence, to the author's knowledge, there is no way of telling *a priori* which pair of signs will appear in Eq. (2.18).

In addition, note that if there is no structural coupling between the interior and the dependent cyclic boundary, and if there is no cyclic boundary-to-boundary coupling, $\mathbf{Y_1^k}$ will be identically zero, which implies that the sign relations between the sine and cosine components of the modes become redundant. Incidentally, this circumstance comprises one of the major differences between the reduced order modeling technique for unshrouded blades in Castanier *et al*. [20] and its extension to shrouded blade designs in Bladh *et al*. [23]. The former, unshrouded formulation inherently assumes that there is no coupling between the blade (viewed as interior) and the dependent cyclic boundary of the

disk sector. It should be noted, however, that this may not hold true for all models, and this assumption can therefore introduce additional errors in certain cases.

2.2 Real Form Cyclic Analysis Using Integral Substructures

An alternative way of formulating the structural matrices is to view the substructure, or sector, as an integral part of the entire assembly. This implies that nodes formerly on boundary b are now viewed as nodes on boundary a of the adjacent sector. Moreover, the structural coupling between adjacent sectors is then already accounted for. This leads to block-circulant structural matrices, and consequently, a block-circulant eigenvalue problem for the entire structure. Since structural coupling will only be present between adjacent sectors, the following form is obtained:

$$\begin{aligned} \bar{\mathbf{Y}} &= \mathbf{Bcirc}\left[\bar{\mathbf{Y}}_0, \bar{\mathbf{Y}}_1, \mathbf{0}, \ldots, \mathbf{0}, \bar{\mathbf{Y}}_1^{\mathbf{T}}\right] \\ &= \begin{bmatrix} \bar{\mathbf{Y}}_0 & \bar{\mathbf{Y}}_1 & \mathbf{0} & \cdots & \mathbf{0} & \bar{\mathbf{Y}}_1^{\mathbf{T}} \\ \bar{\mathbf{Y}}_1^{\mathbf{T}} & \bar{\mathbf{Y}}_0 & \bar{\mathbf{Y}}_1 & \mathbf{0} & \cdots & \mathbf{0} \\ & \ddots & \ddots & \ddots & & \\ & & \ddots & \ddots & \ddots & \\ \mathbf{0} & \cdots & \mathbf{0} & \bar{\mathbf{Y}}_1^{\mathbf{T}} & \bar{\mathbf{Y}}_0 & \bar{\mathbf{Y}}_1 \\ \bar{\mathbf{Y}}_1 & \mathbf{0} & \cdots & \mathbf{0} & \bar{\mathbf{Y}}_1^{\mathbf{T}} & \bar{\mathbf{Y}}_0 \end{bmatrix}. \end{aligned} \tag{2.19}$$

Adopting the DOF partitioning scheme of the isolated substructure approach, these new blocks will have the following composition:

$$\bar{\mathbf{Y}}_0 = \begin{bmatrix} \mathbf{Y}_{\mathbf{aa}} + \mathbf{Y}_{\mathbf{bb}} & \mathbf{Y}_{\mathbf{ai}} \\ \mathbf{Y}_{\mathbf{ai}}^{\mathbf{T}} & \mathbf{Y}_{\mathbf{ii}} \end{bmatrix} \qquad \bar{\mathbf{Y}}_1 = \begin{bmatrix} \mathbf{Y}_{\mathbf{ab}} & \mathbf{0} \\ \mathbf{Y}_{\mathbf{ib}} & \mathbf{0} \end{bmatrix}, \tag{2.20}$$

where it is noted that the sector-to-sector coupling, $\bar{\mathbf{Y}}_1$, is non-symmetric. Furthermore, the dependent cyclic boundary nodes (b) are now excluded from both physical and cyclic

displacement vectors. Hence, in this case, the displacement vectors will have the representation:

$$\bar{\mathbf{x}}_{\mathbf{n}} = \left\{ \begin{array}{c} \bar{\mathbf{x}}_{\mathbf{n}}^{\mathbf{a}} \\ \bar{\mathbf{x}}_{\mathbf{n}}^{\mathbf{i}} \end{array} \right\} \qquad \bar{\mathbf{u}}^{\mathbf{k}} = \left\{ \begin{array}{c} \bar{\mathbf{u}}_{\mathbf{a}}^{\mathbf{k}} \\ \bar{\mathbf{u}}_{\mathbf{i}}^{\mathbf{k}} \end{array} \right\}. \tag{2.21}$$

By necessity, the real-valued relation between physical and cyclic coordinates given in Eq. (2.5) remains valid. Since $\bar{\mathbf{Y}}$ is block-circulant, the cyclic eigenvalue problem resulting from the transformation $\left(\mathbf{F}^{\mathbf{T}} \otimes \mathbf{I}\right) \bar{\mathbf{Y}} \left(\mathbf{F} \otimes \mathbf{I}\right)$ will be pseudo-block-diagonal (see Appendix B), where the block associated with the k^{th} double harmonic will have the following partitions:

$$\bar{\mathbf{Y}}^{\mathbf{k}} = \left[\begin{array}{cc} \bar{\mathbf{Y}}_{\mathbf{0}} + \left(\bar{\mathbf{Y}}_{\mathbf{1}} + \bar{\mathbf{Y}}_{\mathbf{1}}^{\mathbf{T}}\right) \cos k\alpha & \left(\bar{\mathbf{Y}}_{\mathbf{1}} - \mathbf{Y}_{\mathbf{1}}^{\mathbf{T}}\right) \sin k\alpha \\ \left(\bar{\mathbf{Y}}_{\mathbf{1}}^{\mathbf{T}} - \mathbf{Y}_{\mathbf{1}}\right) \sin k\alpha & \bar{\mathbf{Y}}_{\mathbf{0}} + \left(\bar{\mathbf{Y}}_{\mathbf{1}} + \bar{\mathbf{Y}}_{\mathbf{1}}^{\mathbf{T}}\right) \cos k\alpha \end{array} \right]. \tag{2.22}$$

By combining Eqs. (2.20) and (2.22), it is easy to show that exactly the same set of cyclic eigenvalue problems of the same general form as shown in Eq. (2.16) will be obtained, as required.

2.3 Complex Form Cyclic Analysis

Both of the aforementioned approaches for setting up the cyclic eigenvalue problem can use a complex transformation rather than the real-valued form shown. The expansion of the fundamental sector's displacements in cyclic coordinates to the corresponding displacements of the entire assembly is then performed by means of complex phase shifts. This is achieved simply by using the complex Fourier matrix, $\mathbf{E}$, in the transformations, instead of the real-valued "almost-equivalent" transformation matrix, $\mathbf{F}$. See Appendix B for definitions of Fourier matrices $\mathbf{E}$ and $\mathbf{F}$.

Although both isolated and integral substructure approaches to cyclic symmetry analysis may be cast in complex forms, only the latter is considered here for brevity. In the

case of an integral substructure, the matrix $\bar{\mathbf{Y}}$ is block-circulant as shown in Eq. (2.20). Since the columns of the Fourier matrix represent the eigenvectors of any circulant matrix, the transformation $(\mathbf{E}^* \otimes \mathbf{I})\, \bar{\mathbf{Y}}\, (\mathbf{E} \otimes \mathbf{I})$ will yield a true block-diagonal matrix, as opposed to the pseudo-block-diagonal structure achieved by $\mathbf{F}$. This implies that the eigenvalue problem for each harmonic order k is now the size of one sector, with no exceptions. On the other hand, the eigenvalue problems are now complex.

With reference to the notation in Eq. (2.22), the complex eigenvalue problems will take the following form:

$$\bar{\mathbf{Y}}^{\mathbf{n}}_{\mathbf{z}}\mathbf{z} = \left[\bar{\mathbf{Y}}_{\mathbf{0}} + \bar{\mathbf{Y}}_{\mathbf{1}} e^{j(n-1)\alpha} + \bar{\mathbf{Y}}^{\mathbf{T}}_{\mathbf{1}} e^{-j(n-1)\alpha}\right] \mathbf{z} = \mathbf{0}, \qquad n = 1, \ldots, N. \tag{2.23}$$

Note that the matrix $\bar{\mathbf{Y}}^{\mathbf{n}}_{\mathbf{z}}$ is *Hermitian*, evidenced by $\bar{\mathbf{Y}}^{\mathbf{n}}_{\mathbf{z}} = \bar{\mathbf{Y}}^{\mathbf{n}^*}_{\mathbf{z}}$. By virtue of a fundamental property of Hermitian matrices, the N eigenvalue problems $\mathbf{det}\left[\bar{\mathbf{Y}}^{\mathbf{n}}_{\mathbf{z}}\right] = 0$ will yield exclusively real eigenvalues, while the eigenvectors in general will be complex.

In terms of harmonics, the cyclic eigenvalues and eigenvectors associated with the k^{th} harmonic derive from the $(k+1)^{\text{th}}$ and $(N-k+1)^{\text{th}}$ eigenvalue problems, due to the periodicity of the complex phase shift. Again, note that $k = 0$ and, if it exists, $k = N/2$ (N even) are single harmonics. For the double harmonics, $1 \leq k \leq K$, the $(k+1)^{\text{th}}$ eigenvalue problem provides the first set of eigenvalues and eigenvectors, $\mathbf{z_k}$, and the $(N-k+1)^{\text{th}}$ eigenvalue problem will give a set of corresponding complex conjugates. Since all eigenvalues are real, this second set of eigenvalues will be identical to the first, while the second set of eigenvectors, $\mathbf{z}^*_{\mathbf{k}}$, will be the complex conjugates of $\mathbf{z_k}$. The correlation between the previous real eigenvectors and these complex ones is quite simple, as shown below:

$$\begin{cases} \bar{\mathbf{u}}^{\mathbf{k,c}}\left(\omega_{n,1}\right) = \Re\left[\mathbf{z_k}\right] \\ \bar{\mathbf{u}}^{\mathbf{k,s}}\left(\omega_{n,1}\right) = \mp\Im\left[\mathbf{z_k}\right] \end{cases} \qquad \begin{cases} \bar{\mathbf{u}}^{\mathbf{k,c}}\left(\omega_{n,2}\right) = \Im\left[\mathbf{z}^*_{\mathbf{k}}\right] \\ \bar{\mathbf{u}}^{\mathbf{k,s}}\left(\omega_{n,2}\right) = \mp\Re\left[\mathbf{z}^*_{\mathbf{k}}\right], \end{cases} \tag{2.24}$$

where $\Re$ and $\Im$ denote the real and imaginary parts, respectively.

2.4 Summary

To conclude, there are considerable savings in both computing time and data storage associated with the use of the cyclic symmetry concept. Assuming a finite element model with a sector size of n DOF, a real-valued cyclic symmetry approach leads, in the worst case, to one eigenvalue problem of size n and $(N-1)/2$ eigenvalue problems of size $2n$; a complex approach leads to N eigenvalue problems of size n; while the full analysis leads to a single, but very costly, eigenvalue problem of size Nn. It is reasonable to assume that the cost of a sparse eigenvalue solution is somewhere between $\mathcal{O}\left(p^2\right)$ and $\mathcal{O}\left(p^3\right)$, where p is the problem size. Thus, it is clear that cyclic symmetry techniques can provide great computational savings.

CHAPTER III

Dynamic Response Predictions for a Mistuned Industrial Turbomachinery Rotor Using Reduced Order Modeling

A reduced order model formulation based on component mode synthesis is presented for examining the forced response of tuned and mistuned unshrouded bladed disks. The technique uses modal data obtained from finite element models of arbitrary size to create computationally inexpensive models of mistuned bladed disks in a systematic manner. The resulting four to five orders of magnitude model size reduction enables analysts to examine the effects of variations in mistuning strengths and patterns, interblade coupling, and localized modes on forced response amplitudes. In order to demonstrate the capabilities of the technique, this paper explores the effects of random blade mistuning on the dynamics of an advanced industrial compressor rotor. Both free and forced responses of the rotor are considered, and the obtained results are compared with "benchmark" finite element solutions. The mistuned forced response amplitude is found to vary considerably with mistuning strength and the degree of structural coupling between the blades. Moreover, a brief statistical study is presented, in which Weibull distributions are shown to yield reliable estimates of forced response statistics. It is further demonstrated how the highly efficient reduced order modeling technique and Weibull estimates of the forced response statistics combine to facilitate thorough investigations of the important effects of structural

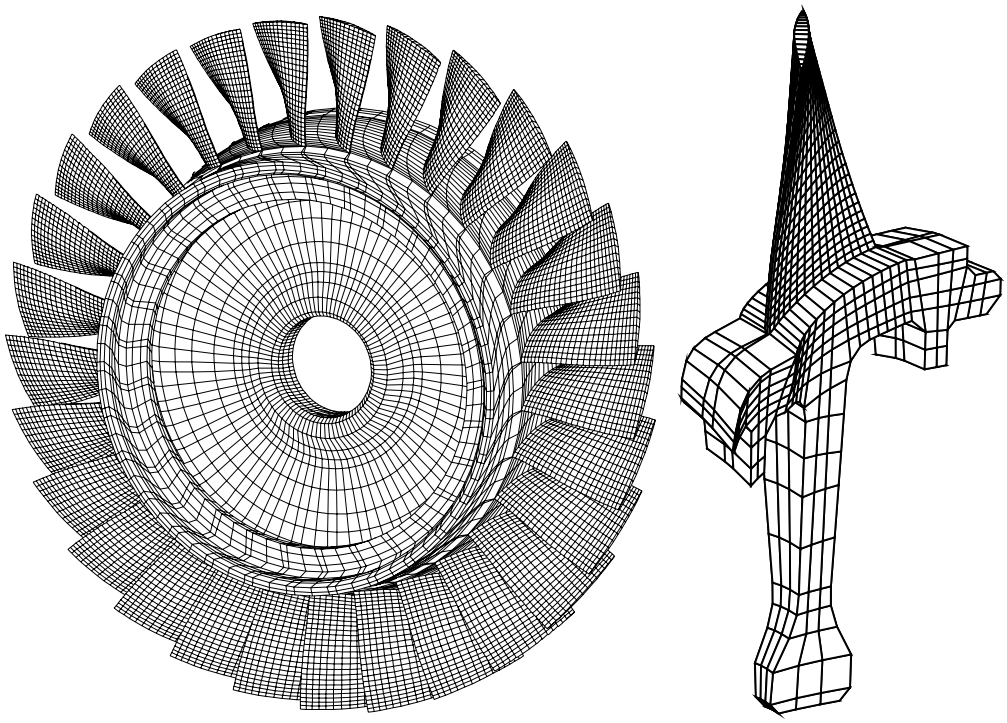

(a) (b)

Figure 3.1: Finite element meshes for the industrial 29-blade compressor rotor: (a) the full model; (b) the fundamental sector.

interblade coupling on mistuning sensitivity.

3.1 Introduction

In a dynamic analysis of a turbomachinery rotor, one traditionally assumes that the individual sectors that comprise the rotor are identical. The cyclic characteristic enables analysts to reduce the computational time considerably by modeling a single sector (e.g., Fig. 3.1b) rather than modeling the entire blade assembly (e.g., Fig. 3.1a). Prior experiences with turbomachinery rotors indicate that cyclic symmetry analyses are seldom adequate for predicting actual blade response [7, 46, 18]. In practice, there are small differences in the structural properties of individual blades, due to manufacturing and material tolerances or in-service degradation, which are referred to as blade mistuning. These vari-

ations destroy the cyclic symmetry of the system and may lead to qualitatively different dynamic behavior than that predicted for a perfectly tuned rotor. In particular, mistuning may confine vibration energy to a few blades or even a single blade. As a result, a single blade may experience deflections much larger than that predicted by a tuned analysis [14, 15]. Mistuning effects must thus be included in the analysis if accurate predictions of vibratory response amplitudes are to be made. In practice, blade mistuning is a random quantity, and statistical analyses that utilize computational Monte Carlo simulations are therefore critical in safely predicting the response amplitudes in the design process. However, a Monte Carlo simulation for a full finite element blade assembly, such as that shown in Fig. 3.1a, is enormously costly, and not even feasible for most industrial turbomachinery rotors. Some means of reduced order modeling is thus required to facilitate statistical analyses of mistuned bladed disk response.

The primary focus of this paper is to demonstrate that mistuned response statistics can be accurately and efficiently predicted via reduced order modeling. The technique employed in this paper was originally developed by Castanier *et al*. [20] and Kruse and Pierre [21], and it was recently extended by Bladh *et al*. [23]. This method produces reduced order models (ROMs) of turbomachinery rotors directly from their finite element models (FEMs) in a systematic fashion. The procedure involves a component mode analysis of the rotor, with a truncated number of modal amplitudes describing the response of the assembly. The principal advantage of the reduced order modeling technique is the considerable computational savings associated with solving for the dynamic response of an entire mistuned rotor with a reduced set of degrees of freedom. In this paper, this technique is employed to study the free and forced dynamic responses of an industrial turbomachinery rotor with blade mistuning. Comparisons are made with “benchmark” solutions obtained for the finite element model of the full assembly in Fig. 3.1a in order to

validate the ROM.

Once the validity of the ROM has been established, it is used to examine the effects of interblade coupling on mistuned forced response amplitudes. In unshrouded rotors, the two predominant forms of interblade coupling are aerodynamic coupling and structural coupling through the disk. However, aerodynamic coupling will not be considered in this study. Instead, the focus will be on the effects of structural interblade coupling, which governs the transmission of vibration energy between blades through the disk. It has previously been shown that interblade structural coupling plays a key role for mistuning sensitivity [16], such that there is an intermediate range of coupling stiffness at which the system is more susceptible to the effects of mistuning compared to both lower and higher values. So far, this has been shown only for relatively simple lumped parameter systems for which the interblade structural coupling is an easily accessed and controlled quantity. However, for more elaborate finite element models, identifying an effective measure of interblade coupling is much more complicated. In this work, it is suggested that the curvature of the eigenfrequency veerings when plotted versus the number of nodal diameters can be used to assess the interblade coupling strength [47, 21].

Furthermore, a simple method is presented for calculating eigenfrequencies for interblade phase angles that are between those corresponding to integer numbers of nodal diameters. By treating the interblade phase angle as a continuous variable rather than a discrete variable, the frequency veerings may be fully captured, and the curvature of the veerings may be quantified. This type of approach was used in [21] but here it is further shown how the eigenfrequency calculations may be performed using commercially available finite element software. This extended eigenvalue analysis may provide a tool for quantifying the interblade coupling, which would aid in determining the rotor's sensitivity to mistuning in terms of forced response.

There are two significant contributions of this work. *First*, the technique presented establishes a systematic approach for developing ROMs that are representative of industrial turbomachinery rotors, and for obtaining their forced response statistics in an accurate and inexpensive manner. ROM results are shown to correlate well with those of the finite element model of the industrial rotor, which is several orders of magnitude larger. The computational validation of the ROM technique is of particular importance to the industrial manufacturers of turbomachinery rotors. *Second*, both quantitative and qualitative findings in this case study indicate that important conclusions with regard to a design's sensitivity to mistuning may be drawn from the free vibration characteristics of the tuned system. Thus, it may be possible to avoid slow and costly statistical analyses during the design process. However, more rigorous work is still required in this area. Other contributions include the use of Weibull distributions to model forced response statistics, and the use of the interblade phase angle as a continuous variable.

This paper is organized as follows. The reduced order modeling technique and the formulation for the modal forcing vector in the ROM generalized coordinates are outlined in Section 3.2. Section 3.3 describes the studied rotor and discusses the finite element and reduced order models used in subsequent analyses. Selected FEM versus ROM validation results from free and forced response of tuned and mistuned rotors are examined in Section 3.4. Section 3.5 discusses the use of Weibull distributions as an approximation for the forced response statistics of randomly mistuned rotors. In Section 3.6, the validated ROM is used to examine the effects of structural interblade coupling on forced response amplitude increases due to mistuning. Finally, conclusions are given in Section 3.7.

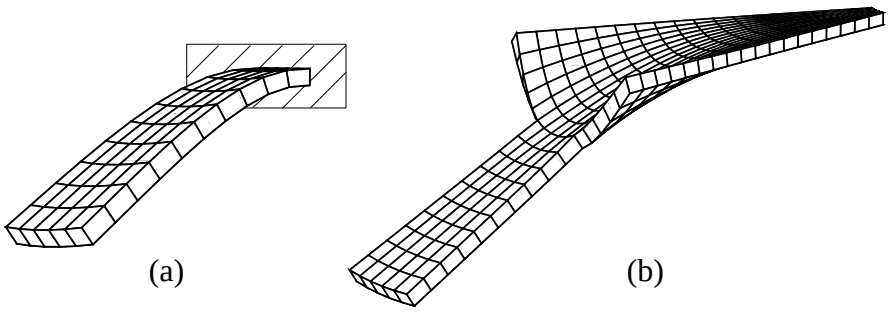

Figure 3.2: Employed component modes: (a) normal modes of a cantilevered blade; (b) cyclic modes for a fundamental disk-blade sector, where the blade is massless.

3.2 Reduced Order Modeling Technique

3.2.1 General Formulation of Reduced Order Model

It may be assumed that the disk (d) and blade (b) degrees of freedom are ordered in such a manner as to give the following block-diagonal form for the assembled stiffness matrix of the entire structure:

$$\mathbf{K} = \begin{bmatrix} \mathbf{K_d} & \mathbf{0} \\ \mathbf{0} & \mathbf{K_b} \end{bmatrix} = \begin{bmatrix} \mathbf{I} \otimes \tilde{\mathbf{K}}_\mathbf{d} & \mathbf{0} \\ \mathbf{0} & \mathbf{I} \otimes \tilde{\mathbf{K}}_\mathbf{b} \end{bmatrix}, \tag{3.1}$$

where $\mathbf{I}$ is an identity matrix, and the symbol $\otimes$ denotes the Kronecker product, which is defined in Appendix A. The structure of the mass matrix is identical to that of the stiffness matrix. The "tilde" notation is used to indicate that a quantity refers to a single blade or disk sector. Note that the location of the disk-blade interface can be chosen completely arbitrarily. In practice, though, this choice may affect the accuracy of the approximate solutions.

A key idea for the reduced order modeling technique of Castanier *et al*. [20] is to describe the motion of the bladed disk assembly using two particular sets of component modes. Figure 3.2 depicts the two fundamental component mode types for a greatly simplified finite element model of a bladed disk sector. The first mode set consists of the modes of a single blade that is clamped at the chosen disk-blade interface location

(Fig. 3.2a). For unshrouded blades, the modal matrix $\mathbf{U^b}$ for all N identical blades is block-diagonal and is assembled as $\mathbf{I} \otimes \tilde{\mathbf{u}}^{\mathbf{b}}$, where $\tilde{\mathbf{u}}^{\mathbf{b}}$ is the cantilever mode shapes of a single blade. The second set is comprised of disk-induced modes, which are the cyclic modes of the entire assembly where the attached blades are massless (Fig. 3.2b). In this case, the blade motion is a rigid-body motion plus elastic deformation due to the boundary motion. The blade portion of the disk-induced modes, i.e., the part belonging to the blade degrees of freedom, is denoted $\mathbf{U^d}$, and the disk portion $\mathbf{V^d}$.

By superposing these two sets of component modes, and using the node ordering configuration in Eq. (3.1), the resulting nodal displacements of the entire assembly can be expanded as

$$\mathbf{x} = \mathbf{V}\mathbf{a} + \bar{\mathbf{U}}^{\mathbf{b}}\mathbf{b} = \begin{bmatrix} \mathbf{V^d} \\ \\ \mathbf{U^d} \end{bmatrix} \mathbf{a} + \begin{bmatrix} \mathbf{0} \\ \\ \mathbf{U^b} \end{bmatrix} \mathbf{b}, \tag{3.2}$$

where $\mathbf{a}$ and $\mathbf{b}$ are modal coordinates for the disk modes and the cantilever blade modes, respectively. With the basic quantities defined, the total strain and kinetic energies of the entire structure may be expressed using Eqs. (3.1) and (3.2). Moreover, the external virtual work done by a time-harmonic engine order excitation force, $\mathbf{Q}$, may be formulated in component modal quantities as

$$\delta W^{ext} = \delta \mathbf{u}^{\mathbf{T}} \mathbf{Q} = \delta \mathbf{b}^{\mathbf{T}} \mathbf{U}^{\mathbf{b}^{\mathbf{T}}} \mathbf{Q} + \delta \mathbf{a}^{\mathbf{T}} \mathbf{U}^{\mathbf{d}^{\mathbf{T}}} \mathbf{Q}. \tag{3.3}$$

Applying Hamilton's principle yields the governing equations of motion for the reduced order model. They are conveniently written in matrix form as

$$\mathcal{M}\ddot{\mathbf{z}} + \mathcal{C}\dot{\mathbf{z}} + (1 + \gamma j)\,\mathcal{K}\mathbf{z} = \mathcal{Q}, \tag{3.4}$$

where

$$\mathbf{z} = \begin{Bmatrix} \mathbf{a} \\ \\ \mathbf{b} \end{Bmatrix} \qquad \mathcal{C} = \begin{bmatrix} \mathbf{0} & \mathbf{0} \\ \\ \mathbf{0} & \mathbf{C} \end{bmatrix} \qquad \mathcal{Q} = \begin{Bmatrix} \mathcal{Q}_{\mathbf{d}} \\ \\ \mathcal{Q}_{\mathbf{b}} \end{Bmatrix} = \begin{Bmatrix} \mathbf{U}^{\mathbf{d}^{\mathbf{T}}} \mathbf{Q} \\ \\ \mathbf{U}^{\mathbf{b}^{\mathbf{T}}} \mathbf{Q} \end{Bmatrix}$$

$$\mathcal{M} = \begin{bmatrix} \mathbf{I} + \mathbf{U^{d^T} M_b U^d} & \mathbf{U^{d^T} M_b U^b} \\ \mathbf{U^{b^T} M_b U^d} & \mathbf{I} \end{bmatrix} \qquad \mathcal{K} = \begin{bmatrix} \mathbf{\hat{K}_d} & \mathbf{U^{d^T} K_b U^b} \\ \mathbf{U^{b^T} K_b U^d} & \mathbf{\hat{K}_b + \Delta \hat{K}_b} \end{bmatrix}.$$

Note that structural damping with coefficient γ, as well as viscous modal damping of the cantilever blade modes, $\mathbf{C}$, have now been added to the reduced order model, in order to facilitate more realistic modeling of the structure's dynamic response. In addition, some measure of mistuning, $\Delta\hat{\mathbf{K}}_\mathbf{b}$, is added into the stiffness matrix $\mathcal{K}$. This measure of mistuning, although general at this point, implies three assumptions:

- The mistuned characteristics of a blade are restricted to its stiffness (lower-right quadrant of $\mathcal{K}$). While stiffness mistuning is sufficient for the purposes of this study, it may be more accurate to model mistuning in other structural parameters as well; for instance, by using the mixed least squares – maximum likelihood method of Mignolet and Lin [48].

- The effects of stiffness mistuning on the other three quadrants of $\mathcal{K}$ are assumed negligible. To a large extent, this is justified by considering the kind of rigid-body-like motion the blade undergoes in this set of component modes.

- The mistuned cantilever modes of a blade may be realized by a linear combination of the tuned modes (i.e., they span approximately the same space).

Note that the resulting structural matrices are all symmetric. In general, this symmetry is destroyed if aerodynamic coupling between blades is introduced into the system. However, aerodynamic coupling is not considered here. Next, a closer examination of the various partitions of the structural matrices reveals significant further simplifications.

3.2.2 Formulation Refinement for Unshrouded Designs

In the unshrouded case, the assembly of the disk-induced modes of the entire structure from the sector modes employs a mixed complex-to-real approach. This process is described in earlier works [20, 21] and will therefore not be repeated in detail here. The essential feature of the approach is that it implicitly utilizes the fact that no direct blade-to-blade structural coupling is present in the unshrouded case, which allows for a linear re-combination of the actual finite element modes. The final form for the cyclic disk-induced modes of the full unshrouded assembly is

$$\mathbf{U^d} = \left[\begin{array}{cccc} \mathbf{U_0^d} & \mathbf{U_1^d} & \cdots & \mathbf{U_P^d} \end{array} \right]. \tag{3.5}$$

The integer P is the highest possible harmonic given by $\mathbf{int}\,[N/2]$, where N is the total number of blades (sectors). The assembly modal vectors associated with the m^{th} cosine (c) and sine (s) mode pair of the h^{th} harmonic may be expanded as

$$\mathbf{U^d_{h,m}} = \left[\begin{array}{cc} \mathbf{f_h^c} \otimes \tilde{\mathbf{u}}^{\mathbf{d,c}}_{\mathbf{h,m}} - \mathbf{f_h^s} \otimes \tilde{\mathbf{u}}^{\mathbf{d,s}}_{\mathbf{h,m}} & \mathbf{f_h^s} \otimes \tilde{\mathbf{u}}^{\mathbf{d,c}}_{\mathbf{h,m}} + \mathbf{f_h^c} \otimes \tilde{\mathbf{u}}^{\mathbf{d,s}}_{\mathbf{h,m}} \end{array} \right], \tag{3.6}$$

where $\mathbf{f_h^{c/s}}$ is the appropriate column of the real Fourier matrix $\mathbf{F}$ defined in Appendix B, and $\tilde{\mathbf{u}}^{\mathbf{d,c/s}}_{\mathbf{h,m}}$ are the disk-induced mode shapes associated with the m^{th} repeated eigenvalue of the h^{th} harmonic for a fundamental sector. Note that there is only one mode per eigenvalue for the 0^{th} and, for N even, the P^{th} harmonic. Consequently, there is only one vector per mode in these two special cases.

Due to the cyclicity of $\mathbf{U^d}$, the projection product $\mathbf{U^{d^T} M_b U^d}$ in the upper-left quadrant of the ROM mass matrix $\mathcal{M}$ is pseudo-block-diagonal:

$$\mathbf{U^{d^T} M_b U^d} = \underset{h=0,\ldots,P}{\tilde{\mathbf{B}}\mathbf{diag}} \left[\tilde{\mathbf{u}}_{\mathbf{h}}^{\mathbf{d^T}} \tilde{\mathbf{M}}_{\mathbf{b}} \tilde{\mathbf{u}}_{\mathbf{h}}^{\mathbf{d}} \right], \tag{3.7}$$

since cyclic modes of different harmonics are mutually orthogonal with respect to the

mass and stiffness matrices (see Appendix B). $\tilde{\mathbf{B}}\mathbf{diag}\left[\bullet\right]$ denotes a pseudo-block-diagonal matrix, with the argument being the h^{th} "block", and the range of h is shown.

The projections $\mathbf{U^{d^T}M_bU^b}$ and $\mathbf{U^{d^T}K_bU^b}$ in the upper-right and lower-left quadrants of $\mathcal{M}$ and $\mathcal{K}$, respectively, can be expressed as:

$$\begin{aligned}\mathbf{U^{d^T}M_bU^b} &= \mathbf{U^{d^T}}\left(\mathbf{I}\otimes\tilde{\mathbf{M}}_\mathbf{b}\right)\left(\mathbf{I}\otimes\tilde{\mathbf{u}}^\mathbf{b}\right)=\mathbf{U^{d^T}}\left(\mathbf{I}\otimes\tilde{\mathbf{M}}_\mathbf{b}\tilde{\mathbf{u}}^\mathbf{b}\right)\\ \mathbf{U^{d^T}K_bU^b} &= \mathbf{U^{d^T}}\left(\mathbf{I}\otimes\tilde{\mathbf{K}}_\mathbf{b}\tilde{\mathbf{u}}^\mathbf{b}\right).\end{aligned} \tag{3.8}$$

No further simplifications apply to these partitions, and they are thus generally fully populated in the unshrouded case.

The external excitation force vector $\mathbf{Q}$ introduced in Eq. (3.3) defines the forcing on all the blade degrees of freedom of the assembly. The restriction to blade degrees of freedom is not an absolute requirement, but leads to a more compact formulation, and it should also be sufficient from a practical perspective. Moreover, an engine order excitation is assumed, which is harmonic in time and differs only in phase from blade to blade. The phase at the n^{th} blade, ϕ_n, is given by

$$\phi_n = \frac{2\pi C\left(n-1\right)}{N}, \qquad n=1,\ldots,N, \tag{3.9}$$

where C is the engine order of the excitation. The external force vector can then be expressed as

$$\mathbf{Q}=\left\{\begin{array}{c}\tilde{\mathbf{f}}e^{j\phi_1}\\ \tilde{\mathbf{f}}e^{j\phi_2}\\ \vdots\\ \tilde{\mathbf{f}}e^{j\phi_N}\end{array}\right\}=\sqrt{N}\mathbf{e_{C+1}}\otimes\tilde{\mathbf{f}}, \tag{3.10}$$

where $\mathbf{e_{C+1}}$ is the $(C+1)^{\text{th}}$ column of the complex Fourier matrix $\mathbf{E}$ defined in Appendix B, and $\tilde{\mathbf{f}}$ is the force vector on a single blade.

The expression for the modal force vector $\mathcal{Q}$ in Eq. (3.4) can be simplified to a much more convenient form in terms of the disk-induced and cantilevered blade mode shapes of a single sector, $\tilde{\mathbf{u}}_{\mathbf{h}}^{\mathbf{d}}$ and $\tilde{\mathbf{u}}^{\mathbf{b}}$, respectively. The principal advantage of expressing the modal forcing vector on a sector basis lies in the computer memory savings. In particular, the disk portion of the modal force vector will become greatly simplified when expressed in terms of sector-referred quantities:

$$\mathcal{Q}_{\mathbf{d}} = \mathbf{U}^{\mathbf{d}^{\mathbf{T}}}\mathbf{Q} = \mathbf{U}^{\mathbf{d}^{\mathbf{T}}}\left(\sqrt{N}\ \mathbf{e}_{\mathbf{C+1}} \otimes \tilde{\mathbf{f}}\right). \tag{3.11}$$

The expansion will yield a disk portion of the modal force vector that is zero everywhere, except for the C^{th} harmonic mode shapes as shown in the summary later in this section. Thus, the engine order excitation, C, determines which mode shapes of the assembly that are being excited. The remaining blade portion of the modal forcing vector can be expanded as

$$\mathcal{Q}_{\mathbf{b}} = \mathbf{U}^{\mathbf{b}^{\mathbf{T}}}\mathbf{Q} = \left(\mathbf{I} \otimes \tilde{\mathbf{u}}^{\mathbf{b}}\right)^{\mathbf{T}}\left(\sqrt{N}\mathbf{e}_{\mathbf{C+1}} \otimes \tilde{\mathbf{f}}\right) = \sqrt{N}\mathbf{e}_{\mathbf{C+1}} \otimes \tilde{\mathbf{u}}^{\mathbf{b}^{\mathbf{T}}}\tilde{\mathbf{f}}. \tag{3.12}$$

Furthermore, the modal viscous damping matrix for the cantilever blade modes, $\mathbf{C}$, will be diagonal:

$$\mathbf{C} = \left(\mathbf{I} \otimes \underset{k=1,\ldots,m_b}{\mathbf{diag}}\left[2\zeta^k\right]\right)\sqrt{\hat{\mathbf{K}}_{\mathbf{b}}} \tag{3.13}$$

where ζ^k is the modal damping coefficient of the k^{th} cantilever blade mode.

Perhaps the most fundamental feature of this technique is its suitability for mistuning of the individual blades. Each individual cantilever blade mode of all blades in the assembly is isolated in the diagonal matrix $\hat{\mathbf{K}}_{\mathbf{b}}$. Therefore, the formulation lends itself to a very convenient and simple input of individual mistuning of each cantilever blade mode of each blade as

$$\Delta\hat{\mathbf{K}}_{\mathbf{b}} = \mathbf{B}\underset{n=1,\ldots,N}{\mathbf{diag}}\left[\underset{k=1,\ldots,m_b}{\mathbf{diag}}\left[\delta_n^k\right]\right]\hat{\mathbf{K}}_{\mathbf{b}} \tag{3.14}$$

δ_n^k is the mistuning parameter associated with the k^{th} cantilever blade mode of the n^{th} blade and is defined as

$$\delta_n^k = \left(\frac{\bar{\omega}_n^k}{\omega^k}\right)^2 - 1, \tag{3.15}$$

where $\bar{\omega}_n^k$ represents the mistuned natural frequency of the k^{th} mode of blade n, and ω^k is the corresponding nominal, or tuned, natural frequency.

To summarize, the reduced order model structural matrices and forcing vector for unshrouded bladed disks, in the absence of aerodynamic coupling, are:

$$\mathcal{M} = \begin{bmatrix} \mathbf{I} + \tilde{\mathbf{B}}\mathbf{diag}_{h=0,\ldots,P}\left[\tilde{\mathbf{u}}_{\mathbf{h}}^{\mathbf{d}\mathbf{T}}\tilde{\mathbf{M}}_{\mathbf{b}}\tilde{\mathbf{u}}_{\mathbf{h}}^{\mathbf{d}}\right] & \mathbf{U}^{\mathbf{d}\mathbf{T}}\left(\mathbf{I}\otimes\tilde{\mathbf{M}}_{\mathbf{b}}\tilde{\mathbf{u}}^{\mathbf{b}}\right) \\ \left(\mathbf{I}\otimes\tilde{\mathbf{u}}^{\mathbf{b}\mathbf{T}}\tilde{\mathbf{M}}_{\mathbf{b}}\right)\mathbf{U}^{\mathbf{d}} & \mathbf{I} \end{bmatrix}$$

$$\mathcal{C} = \begin{bmatrix} \mathbf{0} & \mathbf{0} \\ \mathbf{0} & \left(\mathbf{I}\otimes\mathbf{diag}_{k=1,\ldots,m_b}\left[2\zeta^k\right]\right)\sqrt{\hat{\mathbf{K}}_{\mathbf{b}}} \end{bmatrix}$$

$$\mathcal{K} = \begin{bmatrix} \hat{\mathbf{K}}_{\mathbf{d}} & \mathbf{U}^{\mathbf{d}\mathbf{T}}\left(\mathbf{I}\otimes\tilde{\mathbf{K}}_{\mathbf{b}}\tilde{\mathbf{u}}^{\mathbf{b}}\right) \\ \left(\mathbf{I}\otimes\tilde{\mathbf{u}}^{\mathbf{b}\mathbf{T}}\tilde{\mathbf{K}}_{\mathbf{b}}\right)\mathbf{U}^{\mathbf{d}} & \mathbf{Bdiag}_{n=1,\ldots,N}\left[\mathbf{diag}_{k=1,\ldots,m_b}\left[1+\delta_n^k\right]\hat{\mathbf{K}}_{\mathbf{b}}\right] \end{bmatrix}$$

$$\mathcal{Q} = \left\{ \begin{array}{ccc} \mathcal{Q}_{\mathbf{d}}^{\mathbf{T}} & \vdots & \mathcal{Q}_{\mathbf{b}}^{\mathbf{T}} \end{array} \right\}^T = \left\{ \begin{array}{ccccccccc} \mathbf{0} & \cdots & \mathbf{0} & \mathcal{Q}_{\mathbf{d}}^{\mathbf{C}\mathbf{T}} & \mathbf{0} & \cdots & \mathbf{0} & \vdots & \mathcal{Q}_{\mathbf{b}}^{\mathbf{T}} \end{array} \right\}^T$$

$$\mathcal{Q}_{\mathbf{d}}^{\mathbf{C}} = \left\{ \begin{array}{c} \sqrt{N}\left\{\mathbf{f}_{\mathbf{C},\mathbf{c}}^{\mathbf{T}}\mathbf{e}_{\mathbf{C}+\mathbf{1}}\otimes\tilde{\mathbf{u}}_{\mathbf{C},\mathbf{1}}^{\mathbf{d},\mathbf{c}\mathbf{T}}\tilde{\mathbf{f}} - \mathbf{f}_{\mathbf{C},\mathbf{s}}^{\mathbf{T}}\mathbf{e}_{\mathbf{C}+\mathbf{1}}\otimes\tilde{\mathbf{u}}_{\mathbf{C},\mathbf{1}}^{\mathbf{d},\mathbf{s}\mathbf{T}}\tilde{\mathbf{f}}\right\} \\ \sqrt{N}\left\{\mathbf{f}_{\mathbf{C},\mathbf{s}}^{\mathbf{T}}\mathbf{e}_{\mathbf{C}+\mathbf{1}}\otimes\tilde{\mathbf{u}}_{\mathbf{C},\mathbf{1}}^{\mathbf{d},\mathbf{c}\mathbf{T}}\tilde{\mathbf{f}} + \mathbf{f}_{\mathbf{C},\mathbf{c}}^{\mathbf{T}}\mathbf{e}_{\mathbf{C}+\mathbf{1}}\otimes\tilde{\mathbf{u}}_{\mathbf{C},\mathbf{1}}^{\mathbf{d},\mathbf{s}\mathbf{T}}\tilde{\mathbf{f}}\right\} \\ \vdots \\ \sqrt{N}\left\{\mathbf{f}_{\mathbf{C},\mathbf{c}}^{\mathbf{T}}\mathbf{e}_{\mathbf{C}+\mathbf{1}}\otimes\tilde{\mathbf{u}}_{\mathbf{C},\mathbf{m_d}}^{\mathbf{d},\mathbf{c}\mathbf{T}}\tilde{\mathbf{f}} - \mathbf{f}_{\mathbf{C},\mathbf{s}}^{\mathbf{T}}\mathbf{e}_{\mathbf{C}+\mathbf{1}}\otimes\tilde{\mathbf{u}}_{\mathbf{C},\mathbf{m_d}}^{\mathbf{d},\mathbf{s}\mathbf{T}}\tilde{\mathbf{f}}\right\} \\ \sqrt{N}\left\{\mathbf{f}_{\mathbf{C},\mathbf{s}}^{\mathbf{T}}\mathbf{e}_{\mathbf{C}+\mathbf{1}}\otimes\tilde{\mathbf{u}}_{\mathbf{C},\mathbf{m_d}}^{\mathbf{d},\mathbf{c}\mathbf{T}}\tilde{\mathbf{f}} + \mathbf{f}_{\mathbf{C},\mathbf{c}}^{\mathbf{T}}\mathbf{e}_{\mathbf{C}+\mathbf{1}}\otimes\tilde{\mathbf{u}}_{\mathbf{C},\mathbf{m_d}}^{\mathbf{d},\mathbf{s}\mathbf{T}}\tilde{\mathbf{f}}\right\} \end{array} \right\}$$

$$\mathcal{Q}_{\mathbf{b}} = \sqrt{N}\mathbf{e}_{\mathbf{C}+\mathbf{1}}\otimes\tilde{\mathbf{u}}^{\mathbf{b}\mathbf{T}}\tilde{\mathbf{f}},$$

As a concluding remark, the reduced order model for unshrouded bladed disks requires the following input from finite element analyses:

$\hat{\mathbf{K}}_\mathbf{d}$,$\tilde{\mathbf{u}}^\mathbf{d}$**:** The modal stiffnesses and corresponding cyclic mode shapes from a cyclic symmetry eigenmode analysis for a bladed disk sector, where the density of the blade's elements are set to zero.

$\hat{\mathbf{K}}_\mathbf{b}$,$\tilde{\mathbf{u}}^\mathbf{b}$**:** The modal stiffnesses and corresponding normal mode shapes from a normal eigenmode analysis for a single blade, clamped at the chosen disk-blade interface.

$\tilde{\mathbf{M}}_\mathbf{b}$,$\tilde{\mathbf{K}}_\mathbf{b}$**:** The full finite element mass and stiffness matrices for a completely unconstrained blade.

3.2.3 Cantilever Blade Eigenvalue Adjustments

In this method, the disk motion is described by the disk portion from the second mode set alone (Fig. 3.2b). Hence, no separate set of constraint modes for the disk is employed. This causes the disk to be too stiff at the interface, which degrades the performance (modal convergence) of the method. However, it has been found that artificial softening of the cantilevered blade modes [20] yields significant accuracy improvements for both free and forced response. This is achieved by adjusting the eigenvalues (modal stiffnesses) of the cantilevered blade modes in an iterative fashion. The used iteration scheme is the simplest possible where the cantilevered blade eigenvalues are scaled linearly based on the ratio of the tuned ROM and exact (in the finite element sense) system eigenvalues for blade-dominated modes. For the i^{th} eigenvalue adjustment iteration, the scaled cantilevered blade eigenvalues are computed as

$$\left(\omega_b^k\right)^2\Big|_i = \frac{\left(\omega_{fe}^{P,k}\right)^2}{\left(\omega_r^{P,k}\right)^2\Big|_{i-1}} \left(\omega_b^k\right)^2\Big|_{i-1}, \qquad k = 1, \ldots, m_b. \tag{3.16}$$

$\omega_{fe}^{P,k}$ is the exact eigenvalue of the tuned assembly mode characterized by the k^{th} cantilevered blade mode family at the highest possible harmonic, P, $\omega_r^{P,k}$ is the corresponding eigenvalue from the tuned ROM, and m_b is the number of retained cantilever blade modes.

Material Property	Notation	Value	Unit
Modulus of Elasticity	E_o	203.4	GPa
Modulus of Rigidity	G	77.9	GPa
Mass Density	ρ	7909	kg/m^3
Poisson's Ratio	ν	0.305	–
Structural Damping	γ	0.006	–

Table 3.1: Blisk material properties.

Although heuristic, this technique has proved to be very efficient. In one case study, it was seen to converge to residual errors among the blade-dominated mode eigenvalues that were less than 0.001% after as few as two iterations [23].

3.3 Rotor Description and Computational Models

The industrial rotor illustrated in Fig. 3.1 is the second stage of a four-drum compressor rotor used in an advanced gas turbine application. There are 29 blades in the rotor. The design is referred to as a blisk, since the blades and disk are machined from a single, continuous piece of material. The material properties are listed in Table 3.1.

The tuned finite element model is represented by the single sector model in Fig. 3.1b, using MSC/NASTRAN™ cyclic symmetry routines. The sector model is clamped at the ribs located at the outer edges of the disk, which is a rough approximation of boundary conditions due to neighboring stages. The sector finite element model is constructed with standard linear brick elements (eight-noded solids). The disk portion of the model contains 528 elements, and the blade portion has 375 elements. There are 4374 degrees of freedom per sector in the finite element model. In contrast, the ROM used for technique validation consists of five disk-induced modes and ten cantilever blade modes, for a total

of 15 degrees of freedom per sector.

The mistuned finite element model consists of the entire blade assembly, as shown in Fig. 3.1a. The same element type and mesh pattern is used in the single-sector cyclic symmetry model and the full mistuned model. There are thus 126,846 degrees of freedom in the mistuned finite element model, as compared to 435 degrees of freedom in the mistuned ROM. Mistuning is introduced into the assembly by allowing each blade to have a different Young's modulus:

$$E_n = E_o\,(1+\delta_n)\,, \qquad n = 1, \ldots, N, \tag{3.17}$$

where E_o is Young's modulus for a tuned blade, and δ_n is a dimensionless mistuning parameter associated with the n^{th} blade. A specific mistuning distribution, or pattern, for the industrial rotor that was used to obtain the FEM versus ROM validating results is listed in Table 3.2. These mistuning parameters are based on experimental natural frequency measurements on a prototype rotor.

3.4 Reduced Order Model Validation

3.4.1 Free Vibrations

It is convenient to describe the mode shapes of a tuned rotor in terms of nodal diameters (nodal lines across the diameter of the disk) and nodal circles (nodal lines in the circumferential direction). To the number of nodal diameters for a mode shape corresponds a phase shift between adjacent blades, also denoted interblade phase angle, which is given by

$$\phi_h = \frac{2\pi h}{N}, \qquad h = 0, \ldots, P, \tag{3.18}$$

where h is the number of nodal diameters, and N is the number of blades in the assembly. These modes are accordingly referred to as constant interblade phase angle modes.

Blade	Mistuning δ_i	Blade	Mistuning δ_i	Blade	Mistuning δ_i
1	0.05704	11	-0.03631	21	0.02919
2	0.01207	12	-0.03570	22	-0.00328
3	0.04670	13	-0.03631	23	0.00086
4	-0.01502	14	-0.03631	24	-0.03654
5	0.05969	15	0.00242	25	-0.03631
6	-0.03324	16	0.04934	26	-0.01665
7	-0.00078	17	0.04479	27	0.00783
8	-0.01688	18	0.03030	28	-0.01169
9	0.00242	19	0.00242	29	-0.01332
10	-0.02747	20	0.01734		

Table 3.2: Mistuning pattern for the case study rotor, based on natural frequency measurements on a prototype rotor.

The characteristics of the free vibration modes are conveniently summarized by a plot of natural frequencies versus the number of nodal diameters, as shown in Fig. 3.3. This plot reveals two interesting features of the tuned rotor's modal structure. First, as the number of nodal diameters increases, the disk stiffens rapidly, and the slanted lines in Fig. 3.3 thus correspond to disk-dominated modes. In the absence of blade tip or mid-span shrouding, the blade-dominated modes do not stiffen significantly as the number of nodal diameters increases. Hence, lines that are approximately horizontal represent families of blade-dominated modes. For instance, the family of modes around 2150 Hz features motion that is dominated by the first flexural bending mode (1F) of a cantilevered blade, while motion in the second family of modes around 7400 Hz is dominated by the first torsional mode (1T). Neither of these families of modes exhibit nodal circles. Motion in the third family of modes (9100 Hz) is dominated by the second flexural bending mode (2F) and

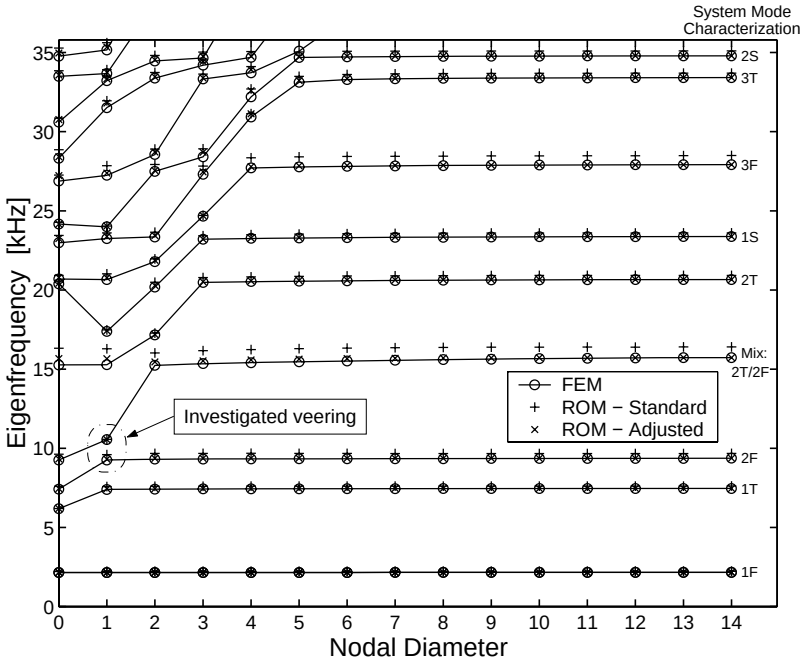

Figure 3.3: Natural frequencies versus number of nodal diameters for the tuned rotor by finite element and reduced order modeling. Note the excellent agreement between finite element and adjusted ROM natural frequencies.

features one nodal circle, and so on. Note that Fig. 3.3 lists these physical descriptions of the blade-dominated mode families (S denotes plate-type "stripe" modes characterized by flexural motion along the chord of the blade). A second notable feature in Fig. 3.3 is the numerous eigenfrequency veerings, in which blade- and disk-dominated mode families veer away from each other. Physically, eigenfrequency veerings indicate the degree of coupling between families of disk and blade modes. The strength of a veering may be measured by the distance between the natural frequencies and the local curvature in the veering region [47]. The impact of the eigenfrequency veerings on the forced response of mistuned rotors will be highlighted further in later sections.

The average error for the standard (unadjusted) ROM among the natural frequencies in the frequency range shown in Fig. 3.3 is 2.2%, where the maximum error of 6.9% is found at the 5^{th} zero nodal diameter mode. The corresponding errors after cantilever blade

eigenvalue adjustments are 0.3% and 2.6%, respectively. The demonstrated accuracy of the reduced order modeling technique in terms of tuned natural frequencies also extends to mode shapes. This is evidenced in Figs. 3.4 and 3.5, which depict example four nodal diameter and one diameter mode shapes, respectively, obtained from finite element and reduced order models. The four nodal diameter mode is characterized by 1F motion, while the one nodal diameter mode is dominated by 2F motion. The mode shapes are represented by a scalar denoted "relative blade Euclidean displacement norm". The norm, $\bar{u}_n^r$, for each blade n, is defined as

$$\bar{u}_n^r = \frac{\sqrt{\sum_{j=1}^{N_b} u_{j,n}^2}}{\sqrt{\sum_{n=1}^{N} \left[\sum_{j=1}^{N_b} u_{j,n}^2\right]}}, \qquad n = 1, \ldots, N, \tag{3.19}$$

where $u_{j,n}$ is the displacement of the j^{th} degree of freedom of the n^{th} blade, N_b is the number of degrees of freedom in one blade, and N is the number of blades in the assembly. For these tuned mode shapes, the signs of the blade deflections were identified to enable a more familiar sinusoidal representation, since the motion extends uniformly throughout the blade assembly. Note that the one nodal diameter mode is located in the center of the investigated eigenfrequency veering (see Fig. 3.3).

The nodal diameter description inherently implies that the mode shapes of the rotor are spatially periodic, which is true for tuned rotors. However, small blade mistuning may alter mode shapes and cause confinement of vibration energy to only a few blades — the so-called phenomenon of localization. The observation that the first-order mode shape perturbation due to mistuning is inversely proportional to the difference in the tuned system's natural frequencies, leads to the well-known property that mode localization is most acute in frequency regions of high modal density [47]. From Fig. 3.3 it can be deduced that all families of blade-dominated modes in the depicted range exhibit high modal density and are therefore susceptible to mode localization upon the introduction of mistuning. Exam-

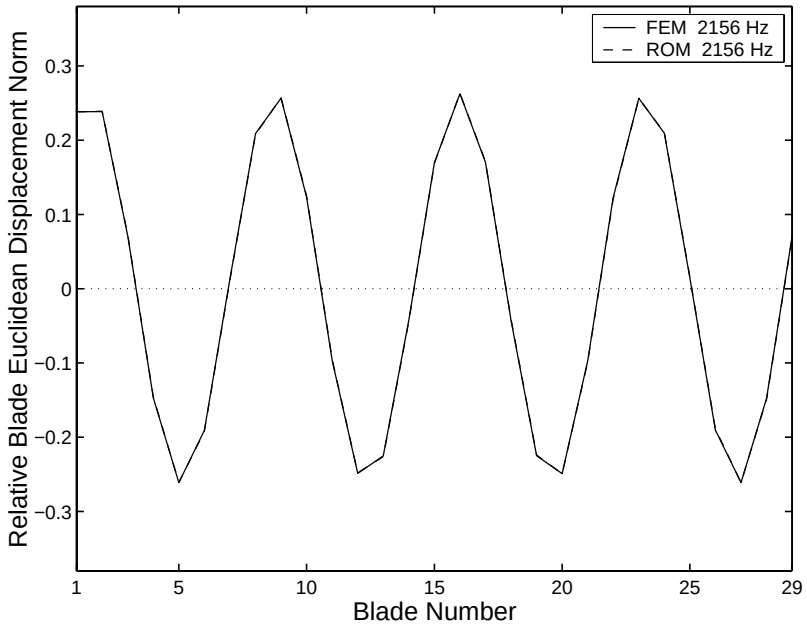

Figure 3.4: Comparison of tuned finite element and ROM four nodal diameter mode shapes (dominated by 1F motion).

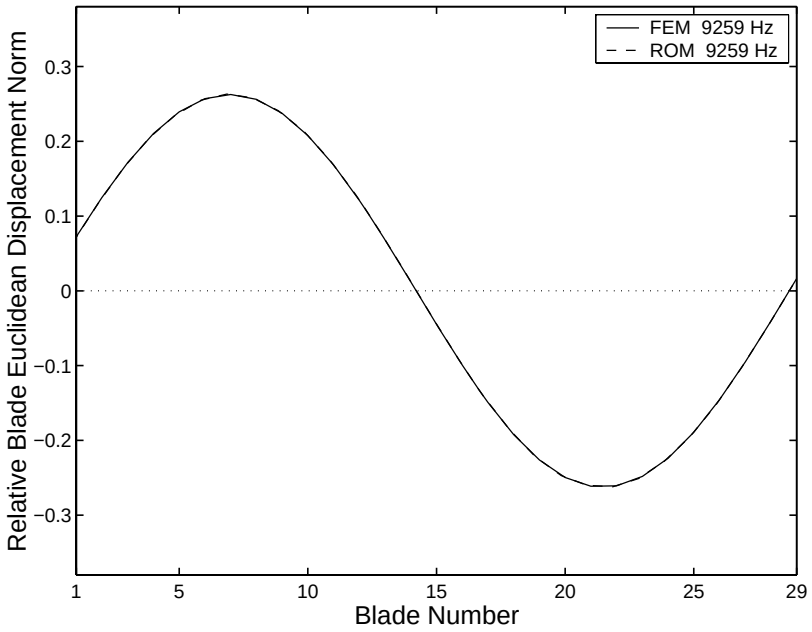

Figure 3.5: Comparison of tuned finite element and ROM one nodal diameter mode shapes (dominated by 2F motion). This mode is located in the investigated veering.

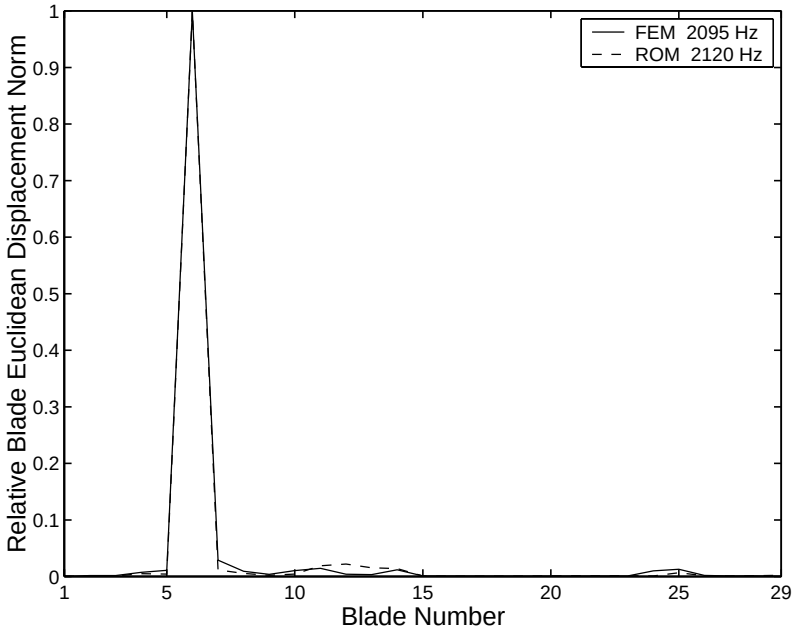

Figure 3.6: Comparison of mistuned finite element and ROM mode shapes in the frequency region encompassing the 1F blade-dominated modes. The mode shape is spatially localized about blade number six.

ination of the selected mode shapes from the mistuned rotor model depicted in Figs. 3.6 and 3.7 indicates significant mode localization as expected. The ROM mode shapes display the same severe localization, and they correlate well with the finite element mode shapes.

3.4.2 Forced Response

The external loading is assumed to consist of a single load located at the tip and mid-chord of each blade, and normal to the surface of the blade. This is of course a simplified case of any actual loading, where the blades are subject to distributed pressure loads. More realistic pressure loads can very easily be applied to the ROM by specifying the equivalent nodal loading on all blade degrees of freedom. Structural damping, γ, which had been experimentally determined to be 0.006, is used in both the finite element and ROM forced response calculations. A scalar representation of blade deflection amplitude similar to

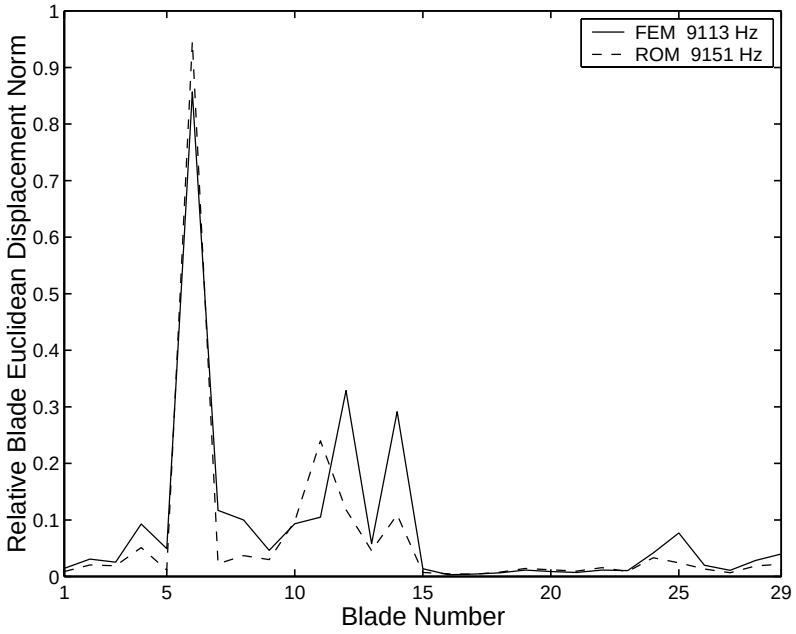

Figure 3.7: Comparison of mistuned finite element and ROM mode shapes in the frequency region encompassing the investigated veering. Motion is dominated by the 2F blade mode and is localized about blade number six.

Eq. (3.19) is utilized to represent the forced response of the assembly:

$$\bar{u}_n = \sqrt{\sum_{j=1}^{N_b} u_{j,n}^2}, \qquad n = 1, \ldots, N. \tag{3.20}$$

In the tuned system response, all blades have identical displacement norms. However, this is not true for a mistuned rotor, where the various blades may have vastly different response amplitudes. In the mistuned case, the maximum blade displacement norm throughout the assembly is selected at each driving frequency, defining the maximum response amplitude.

Figure 3.8 depicts the frequency response of the tuned assembly using both finite element and reduced order models in the frequency region encompassing the 1F family of blade-dominated modes. An engine order four excitation is applied ($C = 4$). Figure 3.8 shows that the resonant response amplitude of the tuned system using the ROM formulation is less than 2% higher than the corresponding finite element result. Figure 3.9 depicts a comparison of mistuned finite element and ROM maximum blade responses. The highly

complex response pattern is very well captured by the ROM. Only small discrepancies in resonant frequencies and response amplitudes are observed. The response sampling for the mistuned finite element model is relatively coarse, due to the tremendous computational expense associated with solving a full blade assembly. Each sampled response (one data point) for the mistuned finite element model requires approximately 27 cpu minutes on a 360 MHz UNIX workstation. In contrast, each ROM response sample requires less than 2.7 cpu seconds on the same workstation. Note in Fig. 3.9 that the maximum mistuned response amplitude is only 17% higher than the tuned resonant amplitude. Recall, from the works of Wei and Pierre [15] and Óttarsson and Pierre [16] that significant amplitude increases occur when there is moderately weak interblade coupling. From Fig. 3.3 it is seen that this particular frequency region exhibits no eigenfrequency veerings. This implies minimal disk-blade modal interaction and very weak interblade coupling. Hence, the mode shapes are dominated by cantilever blade motion, where the individual blades are isolated from each other by the disk and cannot effectively communicate energy to one another. The mistuned system thus responds very much like a collection of uncoupled blades, yielding a relatively modest response amplitude increase due to mistuning.

An excitation close to an eigenfrequency veering is considered next, since it is crucial that interblade coupling effects be well captured by the ROM. Figure 3.10 illustrates the tuned finite element and ROM responses to an engine order one excitation. The resonance in Fig. 3.10 corresponds to the 2F mode of a cantilever blade. It is located in the heart of the investigated eigenfrequency veering, between the third family of blade-dominated modes and the first family of disk-dominated modes, as can be seen in Fig. 3.3. As with the 1F mode family, the correlation between tuned finite element and ROM responses in Fig. 3.10 is excellent. Figure 3.11 depicts a comparison of mistuned finite element and ROM maximum blade response amplitudes for engine order one excitation. It is again seen

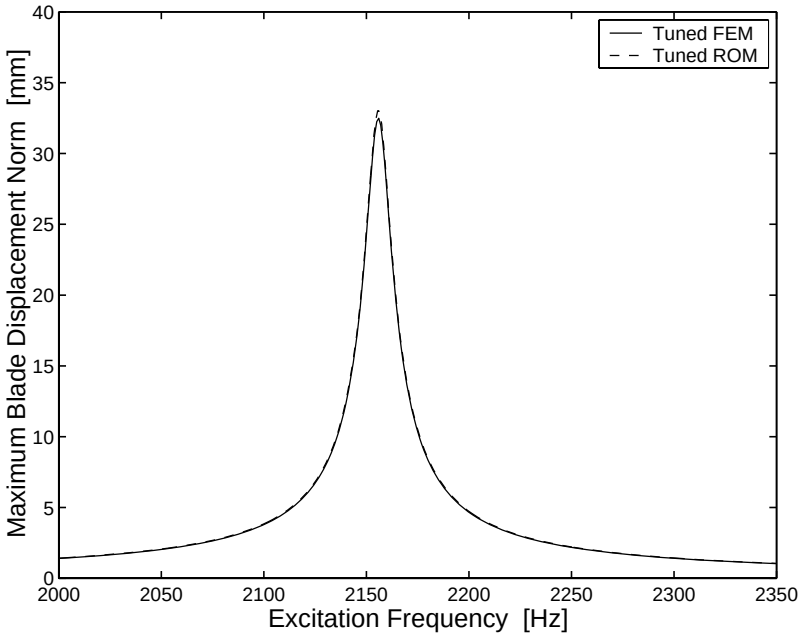

Figure 3.8: Comparison of tuned finite element and ROM forced responses, for blade tip excitation with C=4.

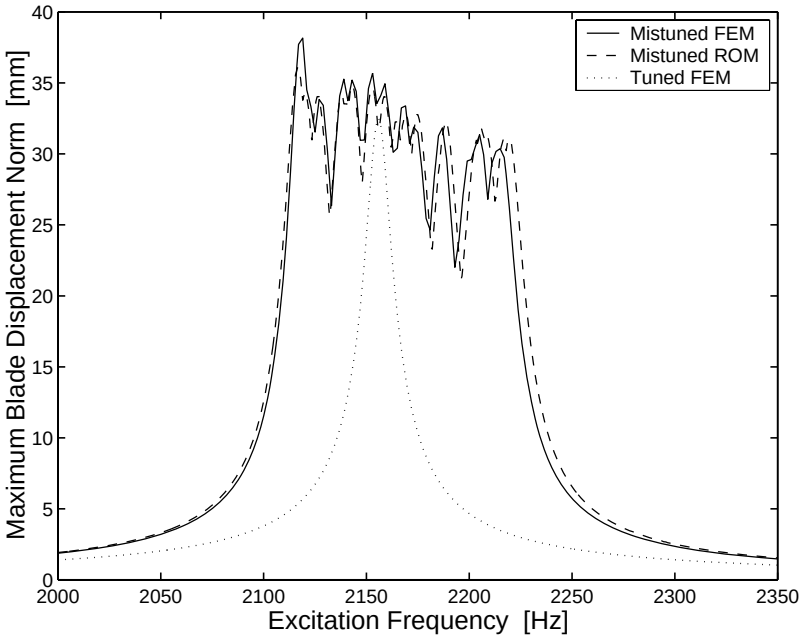

Figure 3.9: Comparison of mistuned finite element and ROM maximum blade forced responses, for blade tip excitation with C=4.

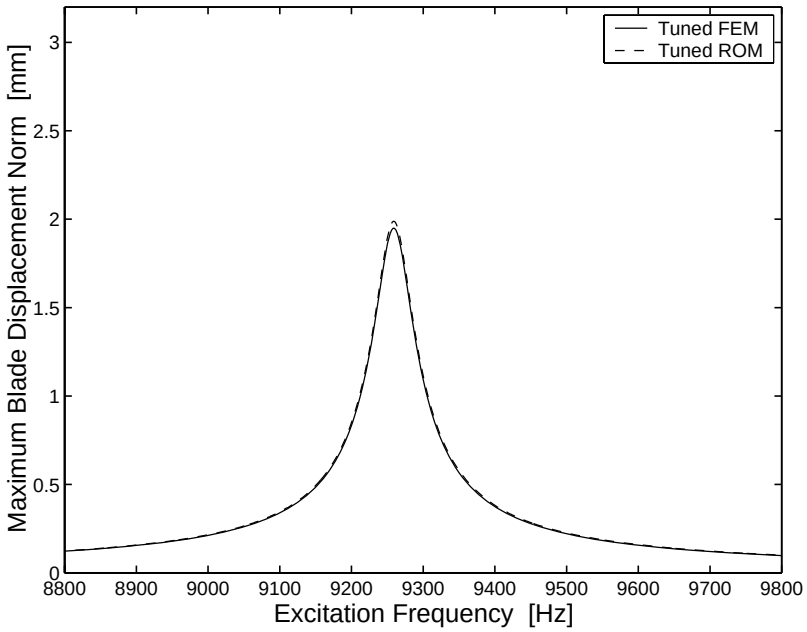

Figure 3.10: Comparison of tuned finite element and ROM forced responses, for blade tip excitation with C=1.

that the ROM yields a good representation of the mistuned response pattern. However, the ROM response amplitudes do not compare as well as in the previous case. Note that the maximum mistuned response exceeds the tuned response by 57%. Per earlier discussion, this is due to the increased disk-blade modal interaction found in veering regions, enabling vibration energy transfer and confinement.

Once the displacement field has been solved with the efficient ROM, displacements can be imported back into the finite element model for post-processing of stresses and strains. For the engine order one excitation, the maximum principal stresses in the blade at tuned resonance are 507 and 527 MPa ($+4\%$) as obtained with the finite element model and the ROM, respectively. The corresponding maximum principal stresses in the mistuned case are 777 and 751 MPa (-3%). Hence, the maximum principal stresses obtained with the ROM are in this case within $\pm 5\%$ of the principal stresses determined with the finite element model. Furthermore, note that the maximum principal stress for the mistuned

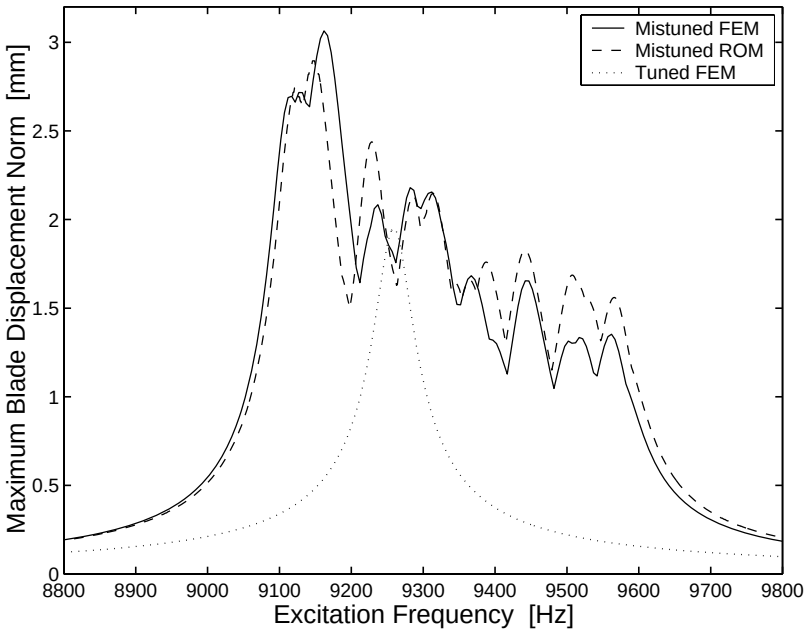

Figure 3.11: Comparison of mistuned finite element and ROM maximum blade forced responses, for blade tip excitation with C=1.

finite element model is as much 53% higher than that for the tuned model. This 53% increase in principal stress corresponds to the 57% increase in resonant response amplitude observed in Fig. 3.11.

3.5 Forced Response Statistics

As the above free and forced response results illustrate, reduced order models of bladed disks correlate well with much larger finite element models. The technique successfully captures and predicts mistuning effects on response amplitudes for industrial rotors. More importantly, however, reduced order modeling enables engineers to determine the statistical characteristics of blade forced response amplitudes for randomly mistuned rotors. Random mistuning must be compensated for by increasing the overall fatigue strength of the blades in order to meet some statistically determined stress level. Alternatively, if feasible, the designer could choose an intentional mistuning pattern in an attempt to minimize

the increase in mistuned vibratory stresses. Recent work by Castanier and Pierre [49] indicates mode-wise robustness of such an approach. Note that in both instances, reduced order modeling can aid the designer in capturing mistuning effects.

Figure 3.12 illustrates a Monte Carlo simulation of the statistics of the maximum blade response amplitude for engine order one excitation over the frequency range of 8750 to 10,750 Hz, which encompasses the 2F family of blade modes. The simulation consists of frequency sweeps for 1000 different mistuning patterns, obtained from a uniform distribution with zero mean and 3% standard deviation. In Fig. 3.12, the 95^{th} percentile of the maximum blade response amplitude (i.e., the amplitude such that, statistically, 95% of all mistuned rotors exhibit smaller maximum amplitudes) is seen to correspond to a 54% increase over the tuned system's resonant response amplitude. The corresponding maximum principal stress for one 95^{th} percentile mistuning pattern is 830 MPa. Recall that the tuned maximum principal stress is 527 MPa. The stress level for the 95^{th} percentile of the maximum blade response amplitude is thus as much as 58% higher than the tuned stress level. If the current rotor design is based on tuned stress magnitudes, fatigue properties of the blades should be increased to compensate for the effect of random mistuning.

A simulation using 1000 mistuning patterns is computationally expensive, even with the ROM. In addition, if compliance of 95% of the rotors is not acceptable, and, for instance, 99.9^{th} percentile compliance is required, 1000 realizations will not suffice. Determining the 99.9^{th} percentile forced response amplitudes with Monte Carlo simulations requires analyses of an estimated 50,000 mistuned rotors, which is a formidable task. Therefore, a new statistical analysis method is proposed, whereby the probability distributions of forced response amplitudes are approximated with statistical models.

Weibull distributions are frequently used to describe probabilistic engineering observations due to the versatility of the shape of the probability density function. Furthermore,

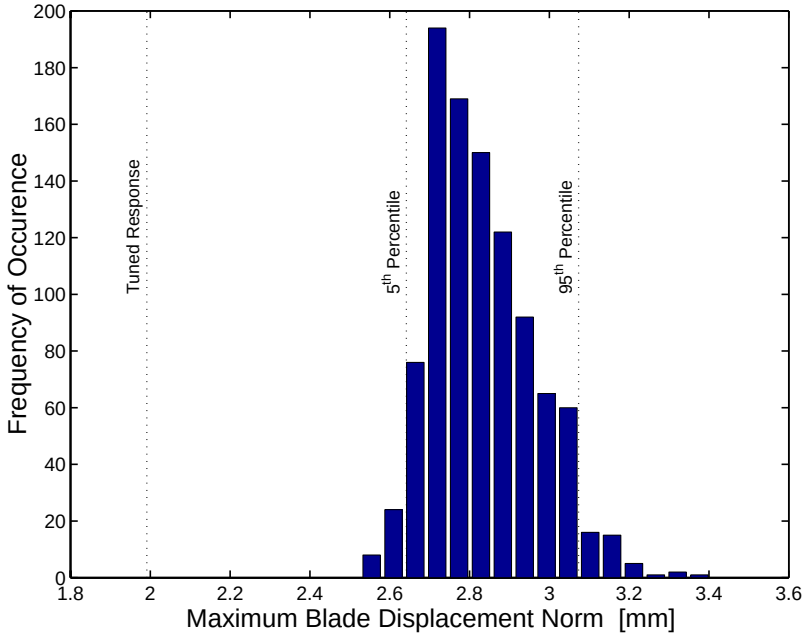

Figure 3.12: Histogram of the maximum blade response amplitudes for engine order one excitation. Obtained by Monte Carlo simulation of 1000 different mistuned systems with uniform distributions of zero mean and 3% standard deviation.

using the theory of the statistics of extreme values, the amplitude of the largest-responding blade on a rotor will have a Weibull distribution [50]. The probability density function of a three-parameter Weibull distribution is given by Gumbel [51] as

$$f(x) = \frac{\beta}{\delta}\left(\frac{\lambda - x}{\delta}\right)^{\beta-1} e^{-\left(\frac{\lambda-x}{\delta}\right)^{\beta}}, \tag{3.21}$$

where δ, β, and λ are scale, shape, and location parameters, respectively, and x is the random variable under investigation (i.e., the maximum blade amplitude magnification). In this study, the location parameter, λ, is approximated by the theoretical maximum response magnification factor, which was determined by Whitehead [52, 53] to be

$$\lambda = \frac{1}{2}\left(1 + \sqrt{N}\right). \tag{3.22}$$

Using this approximation for λ, the remaining two parameters, δ and β, may be estimated by least squares linear regression [49].

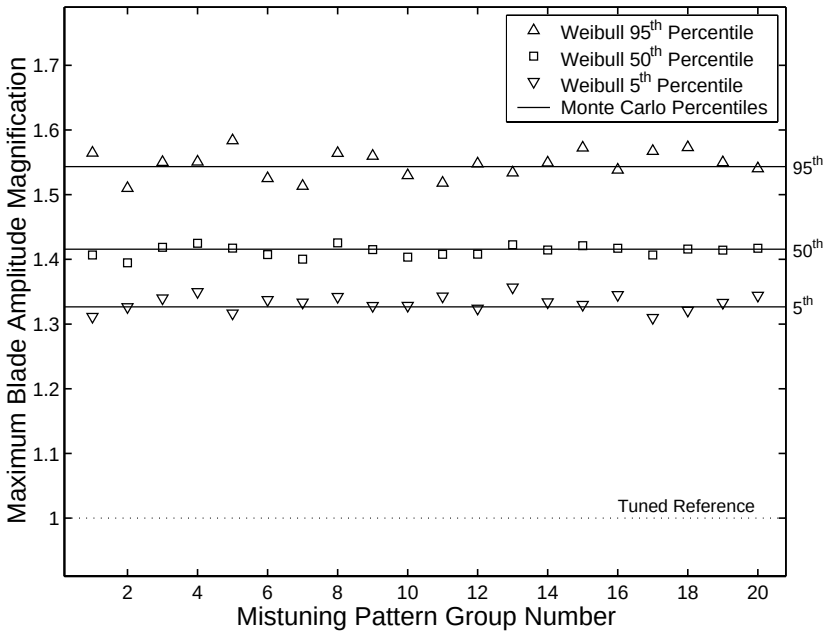

Figure 3.13: Comparison of Weibull and Monte Carlo determined responses for $5^{\mathbf{th}}$, $50^{\mathbf{th}}$, and $95^{\mathbf{th}}$ percentiles of maximum blade response amplitude magnification. The approximate percentiles from the Weibull distributions conform well with the Monte Carlo percentiles.

To determine the correlation between Weibull estimates of response amplitudes and "true" response amplitudes, the maximum blade response statistics from the Monte Carlo simulation were compared to numerous Weibull approximations of the response amplitudes that utilize only 50 mistuned rotors. This comparison is presented in Fig. 3.13 for the 5^{th}, 50^{th}, and 95^{th} percentiles of the maximum blade response amplitude. Note how closely the three-parameter Weibull distribution approximate the "true" distribution. In addition, the quality of the Weibull estimates of the probability density function based on several subsets containing 50 mistuning patterns each is displayed in Fig. 3.14. Clearly, the probability density is well captured using a significantly smaller number of patterns than the full set of 1000 patterns.

Using Weibull distributions to calculate approximate maximum forced response statistics in the described manner, the effect of mistuning strength was investigated for the

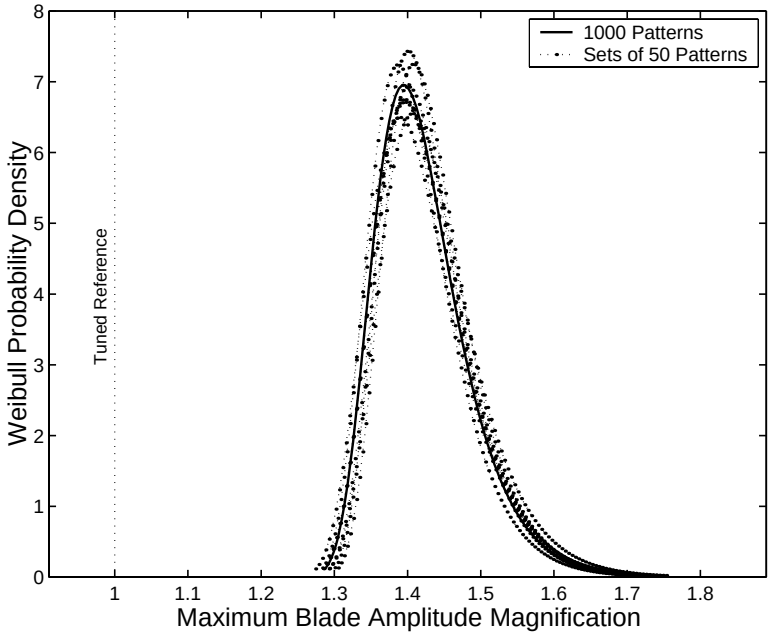

Figure 3.14: Comparison of Weibull estimates of the probability density function for several sets of 50 mistuning patterns each and the full set of 1000 mistuning patterns. The Weibull approximations based on the smaller sets conform well with the probability density function obtained with the full set.

5^{th}, 50^{th}, and 95^{th} percentile responses in the frequency veering considered here (see Fig. 3.3). As shown in Fig. 3.15, there is a local maximum in the maximum blade response amplitudes for mistuning distributions with approximately 1% standard deviation. The maximum principal stress for one mistuning pattern corresponding to the 95^{th} percentile response amplitude at 0.8% mistuning standard deviation is $\sigma_1 = 978$ MPa. This principal stress represents an 86% increase over the tuned principal stress reported earlier.

3.6 Effects of Structural Interblade Coupling

As mentioned earlier, the two factors that determine response increases for a given level of mistuning are mode localization and interblade coupling. Using a single-degree of freedom per sector bladed disk model, Wei and Pierre [15] and Óttarsson and Pierre [16] determined that moderately weak interblade coupling is required for significant increases

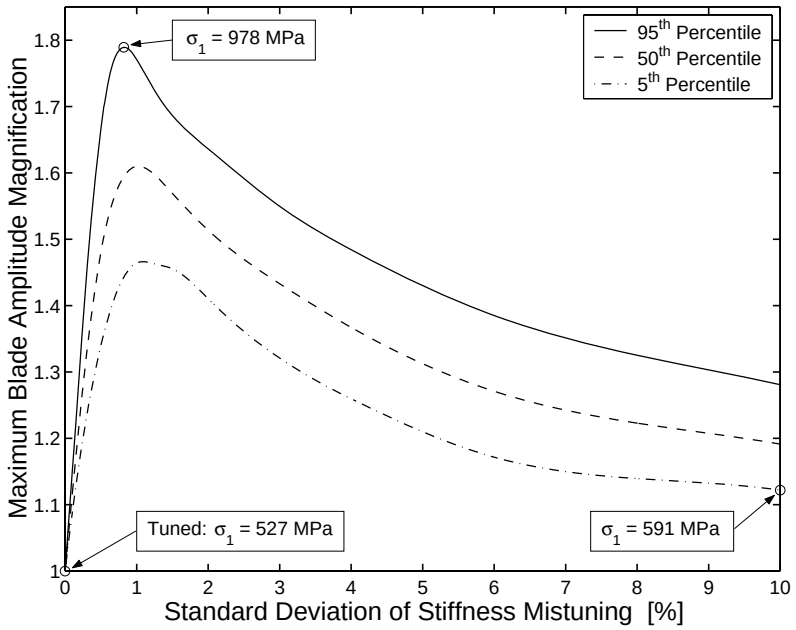

Figure 3.15: Variation in maximum blade response amplitudes with standard deviation of mistuning. Note that a local maximum occurs for mistuning distributions with approximately 1% standard deviation. Mistuned maximum principal stresses are as much as 86% higher than the tuned maximum principal stress.

in forced response amplitudes. If there is no interblade coupling, then each blade acts as an individual mistuned oscillator, and the mistuned response does not deviate significantly from the tuned response. As coupling increases, an avenue is created for the blades to communicate vibrational energy, which raises the possibility of confining energy to a few blades. The mistuned response may then deviate significantly from the tuned response, until further increases in coupling prohibit the confinement of energy, yielding tuned-like response for large coupling values.

In a structural model of an unshrouded bladed disk, the only means of communication from one blade to the next is through the disk. Therefore, it is reasonable to assume that the interblade coupling is indicated by the amount of interaction between disk- and blade-dominated modes. Such modal interaction appears as veering regions in a natural frequency versus nodal diameter plot, where the lines that connect natural frequencies

veer away from each other [47]. This relationship between the veerings and the interblade coupling was investigated for simple finite element models of bladed disks in Kruse and Pierre [21] and Bladh *et al*. [54]. From curve veering theory [47], it is known that the strength of the disk-blade interaction, and thus the interblade coupling, is a function of the veering curvature. If the interaction between disk-dominated and blade-dominated motion is negligible, then the disk-dominated and the blade-dominated frequency curves will appear to "pass through" each other, or cross. Thus, the veering is extremely sharp, with high curvature. In contrast, a lower-curvature veering indicates a higher level of modal interaction, and thus, stronger interblade coupling. This does not imply that the maximum sensitivity to mistuning is always found in the veering region, since the interblade coupling here might fall above the critical range. In this case, a critical amount of interblade coupling may exist at a harmonic that is not adjacent to the veering, since the effective interblade coupling decays with increasing "distance" from the veering region.

For the tuned system, cyclic symmetry arguments lead to a defined number of natural modes at discrete interblade phase angles, representing integer harmonics. That is, the modes shapes associated with natural frequencies form standing waves that undergo, over the assembly, integer multiples of 2π phase shift. However, from these discrete points representing the true modes of the system, it is impossible to obtain reliable estimates for the veering curvatures and mode distances, since the center point of the veerings will likely be missed in most cases. To overcome this problem, one may compute modes based on arbitrary, intermediate interblade phase angles (non-integer harmonics) to obtain approximations of curvatures and mode distances in the veering regions. Note that this leads to displacement discontinuity at the interface between the N^{th} and the first cyclic sector, and these modes can therefore not occur in reality. They can, however, be viewed as traveling wave modes [55].

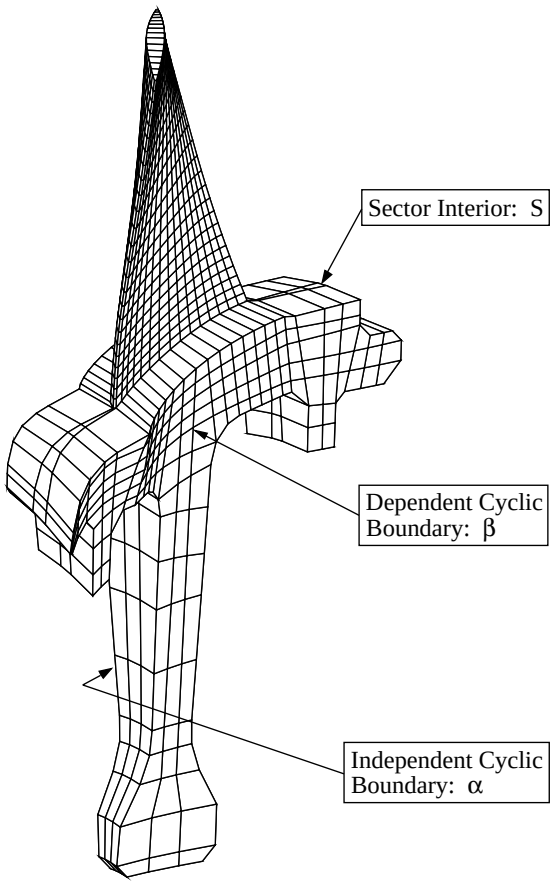

Figure 3.16: Definition of index notation.

Following the indices defined in Fig. 3.16, the eigenvalue problem for a cyclic structure may be formulated in real-valued matrix form as

$$\left[\begin{bmatrix} \tilde{\mathbf{K}}_{\mathbf{0}}^{\mathbf{h}} & \tilde{\mathbf{K}}_{\mathbf{1}}^{\mathbf{h}} \\ \tilde{\mathbf{K}}_{\mathbf{1}}^{\mathbf{h}^{\mathbf{T}}} & \tilde{\mathbf{K}}_{\mathbf{0}}^{\mathbf{h}} \end{bmatrix} - \omega^2 \begin{bmatrix} \tilde{\mathbf{M}}_{\mathbf{0}}^{\mathbf{h}} & \tilde{\mathbf{M}}_{\mathbf{1}}^{\mathbf{h}} \\ \tilde{\mathbf{M}}_{\mathbf{1}}^{\mathbf{h}^{\mathbf{T}}} & \tilde{\mathbf{M}}_{\mathbf{0}}^{\mathbf{h}} \end{bmatrix}\right] \begin{Bmatrix} \tilde{\mathbf{u}}_{\mathbf{h}}^{\mathbf{c}} \\ \tilde{\mathbf{u}}_{\mathbf{h}}^{\mathbf{s}} \end{Bmatrix} = \begin{Bmatrix} \mathbf{0} \\ \mathbf{0} \end{Bmatrix}, \tag{3.23}$$

where

$$\tilde{\mathbf{K}}_{\mathbf{0}}^{\mathbf{h}} = \begin{bmatrix} \mathbf{K}_{\alpha\alpha} + \left(\mathbf{K}_{\beta\alpha} + \mathbf{K}_{\beta\alpha}^{\mathbf{T}}\right)\cos\phi_h + \mathbf{K}_{\beta\beta} & \mathbf{K}_{\mathbf{S}\alpha} + \mathbf{K}_{\beta\mathbf{S}}^{\mathbf{T}}\cos\phi_h \\ \mathbf{K}_{\mathbf{S}\alpha}^{\mathbf{T}} + \mathbf{K}_{\beta\mathbf{S}}\cos\phi_h & \mathbf{K}_{\mathbf{SS}} \end{bmatrix}$$

$$\tilde{\mathbf{K}}_{\mathbf{1}}^{\mathbf{h}} = \begin{bmatrix} \left(\mathbf{K}_{\beta\alpha} - \mathbf{K}_{\beta\alpha}^{\mathbf{T}}\right)\sin\phi_h & -\mathbf{K}_{\beta\mathbf{S}}^{\mathbf{T}}\sin\phi_h \\ \mathbf{K}_{\beta\mathbf{S}}\sin\phi_h & \mathbf{0} \end{bmatrix},$$

and the mass matrix is partitioned in exactly the same fashion. The trigonometric argument, ϕ_h, is the interblade phase angle defined in Eq. (3.18), from which one observes that the interblade phase angle is a function of the ratio h/N. Thus, a continuous interblade phase angle mode description may be obtained either by letting h be a "continuous" variable (i.e., using small, non-integer steps), or, equivalently, by specifying integer values of h and N that yield the same ratio. The latter option offers a possibility to use commercial finite element software featuring cyclic symmetry to compute these intermediate interblade phase angle modes, as long as the finite element code does not check for geometric consistency. The continuous solid lines in Fig. 3.17 were obtained using MSC/NASTRAN™ for an assembly of 580 blades (compared to the actual number, 29) to get 20 data points per integer harmonic. Moreover, Fig. 3.18 provides a detail view of the highly complex region of modal interaction at lower harmonics (i.e., the lower left portion of Fig. 3.17). From Fig. 3.18 it is particularly clear that much of the complex interaction between blade- and disk-dominated modes will be missed by viewing integer harmonics alone.

Using a continuous interblade phase angle representation with sufficiently small step size, one may invoke, for instance, a finite difference scheme to compute the curvature of the eigenfrequency "function", $F_k(\phi_h)$, in the neighborhood of the veerings as

$$\kappa(\phi_h) = \frac{\frac{d^2 F_k(\phi_h)}{d\phi_h^2}}{\left[1 + \left(\frac{dF_k(\phi_h)}{d\phi_h}\right)^2\right]^{\frac{3}{2}}}, \tag{3.24}$$

for each mode set k (ordered by ascending frequencies as shown in Fig. 3.18). As an example, consider the veering region at the 2^{nd} harmonic for the 4^{th} and 5^{th} mode sets seen in Fig. 3.18. Using a fourth order finite difference scheme, approximations of the first and second derivatives with respect to the interblade phase angle were obtained to compute the veering curvatures depicted in Fig. 3.19. This plot quantifies the relatively sharp veering occurring close to the 2^{nd} harmonic, where mode sets 4 and 5 veer away from

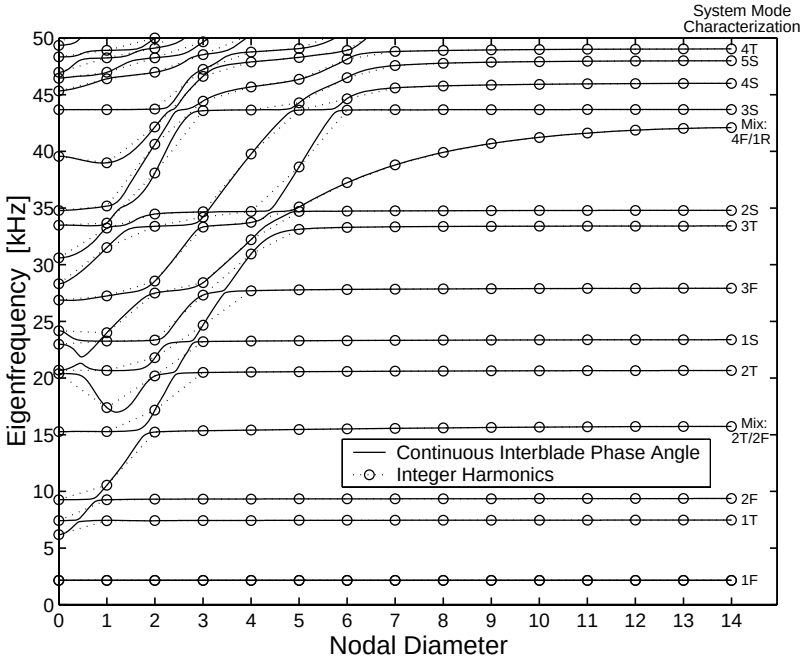

Figure 3.17: Natural frequencies versus number of nodal diameters as a continuous variable.

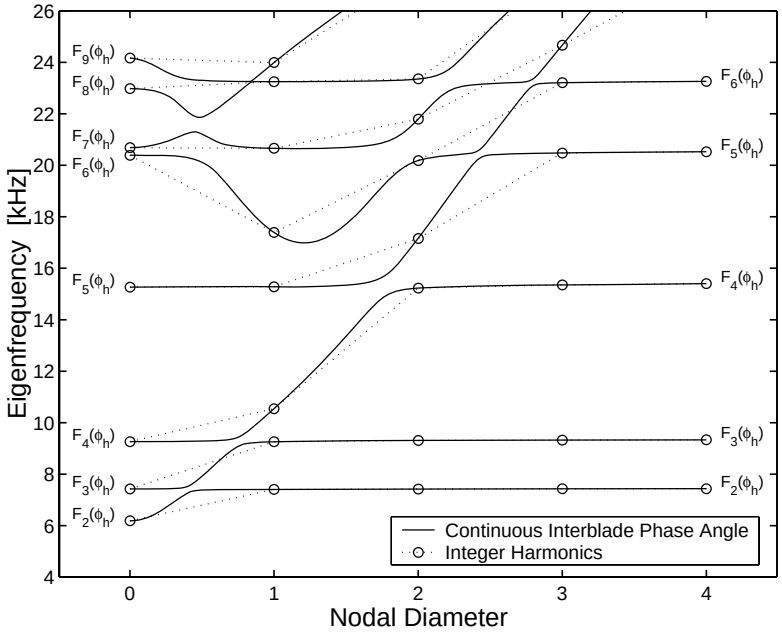

Figure 3.18: Close-up view of intense veering region.

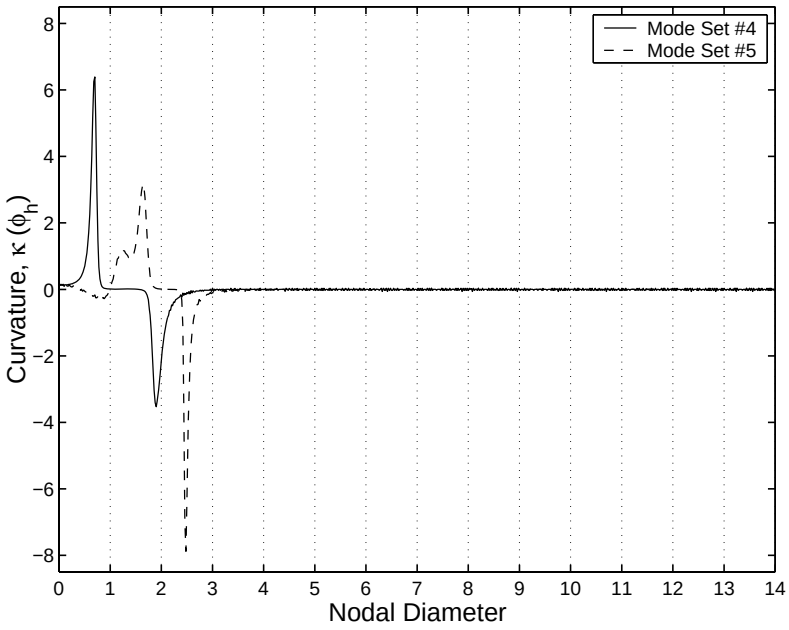

Figure 3.19: Finite difference approximation of curvature for the $4^{\mathbf{th}}$ and $5^{\mathbf{th}}$ mode sets.

each other with curvatures of comparable magnitudes but of opposite signs. Also visible are the obtained curvatures of the 1^{st} harmonic veering (between mode sets 3 and 4), and of the veering located between the 2^{nd} and 3^{rd} harmonic (between mode sets 5 and 6).

Comprehensive statistical analyses similar to the one presented in Fig. 3.15 were carried out for several veerings among the low-order mode families. The analyses use Weibull fits based on 50 random mistuning patterns, and the selected results are shown in Fig. 3.20. Figure 3.20 shows the locations and maximum curvatures (κ) of the analyzed veerings. Note that the maximum veering curvatures are averaged between the lower and upper mode sets. In addition, Fig. 3.20 shows the engine order of the excitation (C), the maximum 99.9^{th} percentile response amplitude magnification factor relative to the tuned response (A), and the standard deviation of the mistuning distribution yielding maximum amplification (σ) at selected locations.

Several interesting observations can be made in Fig. 3.20. As shown, the response

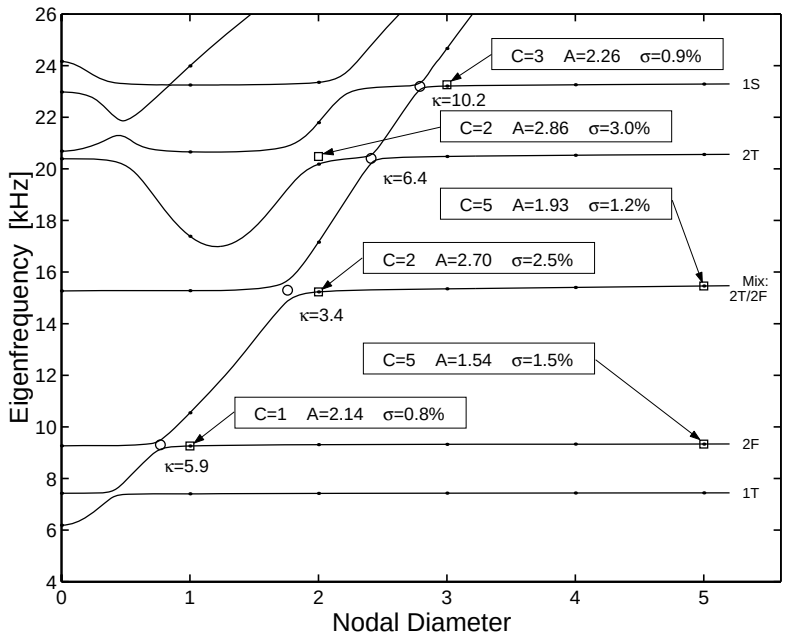

Figure 3.20: Forced response statistical data for selected veerings.

increases due to mistuning can be very large — close to 200% above tuned levels in some cases. Based on the large magnification factors found for excitations near the veerings, it may be deduced that the veering curvatures are such that the corresponding interblade coupling values are near critical levels relatively close to the analyzed veerings. The depicted results also indicate that the amplitude magnification decays significantly with the distance from the veering. This important observation is consistent with the decay of interblade coupling with increasing distance from the veering. Moreover, comparing the 2F and 2T veerings, it is observed that these two veerings have comparable curvatures. However, both maximum amplifications and the mistuning strength for which maximum occurs are vastly different. In fact, based on the displayed results, the blade-dominated mode families with torsion (T) content appear to be significantly more sensitive to mistuning than purely flexural mode families (F and S). This may be explained by significant differences in disk-blade interface motion and how far this motion extends in the disk. Another interesting

observation is that the maximum amplifications are found at a much higher level of mistuning strength for both families exhibiting torsion content. Hence, these results indicate that the blade mode type may also be a factor influencing the sensitivity to mistuning.

One focus of future work is to be able to relate mistuning sensitivity to veering curvature, distance between eigenfrequencies, and distance of eigenfrequencies from the veering. If such a relationship can be thoroughly understood, this extended eigenvalue analysis may provide an inexpensive design tool for early assessments of mistuning sensitivity.

3.7 Conclusions

In this paper, the ROM free response formulation presented by Castanier *et al*. [20] was successfully extended to the forced response case. The ROM forcing vector was expressed in terms of single sector quantities, which minimizes computer memory and computational costs. In order to validate the extended ROM formulation, the technique was employed to investigate mistuned free and forced response characteristics for an industrial turbomachinery rotor. In all investigations, very good correlation was observed between finite element and ROM responses. The computationally inexpensive ROM was further used to determine statistically the variation in response amplitudes due to mistuning.

This investigation verified the existence of localized modes in industrial turbomachinery rotors. Localized modes were found to exist in areas of high modal density, such as blade-dominated modes. Moreover, the existence of localized modes raises the possibility of significant amplitude increases in the forced response of the rotor. In particular, it was shown that mistuned responses can exceed tuned response levels by nearly 200%, if appropriate levels of mistuning and interblade coupling are present.

The relationship between blade mistuning for a particular rotor and the associated mistuned forced response is not simple. Previous works have shown that there exists a critical,

intermediate level of interblade coupling that leads to maximum mistuned forced response amplitudes [16]. In this study, the analysis of the curvature of eigenfrequency veerings was considered as a means of determining the interblade coupling strength for a bladed disk. A simple method was presented for calculating eigenfrequencies for interblade phase angles corresponding to non-integer harmonics. This calculation may be performed using commercial finite element software. Since this analysis allows one to quantify the veering curvature, it might also allow one to quantify the interblade coupling strength. A brief forced response statistical study utilizing this technique, indicated that there are four principal factors governing mistuned forced response: (a) modal density; (b) interblade coupling; (c) mistuning strength; (d) characteristic blade motion. Future work will aim to quantitatively relate these factors to mistuned forced response amplifications.

CHAPTER IV

Reduced Order Modeling and Vibration Analysis of Mistuned Bladed Disk Assemblies with Shrouds

This paper presents important improvements and extensions to a computationally efficient reduced order modeling technique for the vibration analysis of mistuned bladed disks. In particular, this work shows how the existing modeling technique is readily extended to turbomachinery rotors with shrouded blades. The modeling technique employs a component mode synthesis approach to systematically generate a Reduced Order Model (ROM) using component modes calculated from a Finite Element Model (FEM) of the rotor. Based on the total number of degrees of freedom, the ROM is typically two or three orders of magnitude smaller than the FEM. This makes it feasible to predict the forced response statistics of mistuned bladed disks using Monte Carlo simulations. In this work, particular attention is devoted to the introduction of mistuning into the ROM of a shrouded assembly. Mistuning is modeled by projecting the mistuned natural frequencies of a single, cantilever blade with free shrouds onto the harmonic modes of the shrouded blade assembly. Thus, the necessary mistuning information may be measured by testing individual blades.

4.1 Introduction

Based on the nominal design, a bladed disk assembly is a rotationally periodic structure. If it is assumed that each sector is identical, then the theory of cyclic symmetry may be used to analyze the dynamics of the entire structure based on, say, a finite element model of one sector (Joseph [43]; Elchuri *et al*. [56]; Hitchings and Singh [57]). In practice, however, there are small differences among the structural properties of individual blades – due to manufacturing tolerances, material deviations, and non-uniform operational wear. These small, random discrepancies, commonly referred to as mistuning, are unavoidable. Furthermore, mistuning destroys the cyclic symmetry of the bladed disk assembly, and it can drastically affect the vibratory behavior of the structure. In particular, certain mode shapes may become spatially localized. As a result, a blade may experience forced response amplitudes and stresses that are substantially larger than those predicted by a tuned analysis.

The effects of mistuning on blade vibrations have been documented by experiments, as well as by analyses of representative lumped parameter models using numerical, statistical, and perturbation methods (Wagner [5]; Dye and Henry [6]; Ewins [7, 8]; El-Bayoumy and Srinivasan [9]; Griffin and Hoosac [11]; Wei and Pierre [14, 15]; Lin and Mignolet [13]). See Srinivasan [17] for a survey of the literature. More recently, there have been efforts to use component mode synthesis (Irretier [18]; Zheng and Wang [19]; Castanier *et al*. [20]) and receptance techniques (Yang and Griffin [26]) combined with finite element models in order to obtain more accurate models of mistuned bladed disks.

The studies by Castanier *et al*. [20] and Yang and Griffin [26] are notable because specially-tailored techniques were employed to obtain, in a systematic fashion, highly reduced order models from parent finite element models of bladed disks. In particular,

significant order reduction was achieved by reducing the number of degrees of freedom (DOF) needed to connect the disk and blade components. Yang and Griffin treated the disk-blade interface as having only rigid body motion, which reduced the necessary DOF to six for each blade. However, this approximation did cause some loss in accuracy in frequency regions that feature disk-blade interaction. In Castanier *et al*. [20], a novel component mode technique was developed to eliminate the so-called constraint modes.

The technique of Castanier *et al*. [20] has been applied to the analysis of the forced response of mistuned bladed disks (Kruse and Pierre [21]) and it has been validated using a finite element model of an industrial rotor (Kruse and Pierre [22]). However, these investigations concentrated on unshrouded bladed disk assemblies. In this paper, the reduced order modeling technique is extended to turbomachinery rotors with shrouded blades. The tuned blade-shroud ring is modeled as a single, cyclic component structure. Thus, the limiting cases of full stick or full slip at the shroud interfaces may be treated. Mistuning is added by projecting the mistuned natural frequencies of a single blade onto the cyclic modes of the blade-shroud ring. For an example finite element model, using the case of full stick at the shroud connections, excellent correlation between finite element and ROM predictions of the free and forced response is demonstrated.

This paper is organized as follows. The reduced order modeling technique is presented in Section 4.2, including updates to the ROM matrices, and specific formulations pertinent to shrouded assemblies are derived. A fairly detailed derivation of the proposed method to model mistuned shrouded assemblies is also included. In Section 4.3, the technique is applied to the vibration analysis of a shrouded test case rotor. The results are validated by comparisons with finite element results. Concluding remarks are given in Section 4.4.

4.2 Reduced Order Modeling Technique

4.2.1 General Formulation of Reduced Order Model

It may be assumed that the disk (d) and blade (b) degrees of freedom are ordered in such a manner as to give the following partitioning of the assembled mass and stiffness matrices of the entire structure:

$$\mathbf{M} = \begin{bmatrix} \mathbf{M_d} & \mathbf{0} \\ \mathbf{0} & \mathbf{M_b} \end{bmatrix} \qquad \mathbf{K} = \begin{bmatrix} \mathbf{K_d} & \mathbf{0} \\ \mathbf{0} & \mathbf{K_b} \end{bmatrix} \tag{4.1}$$

The location of the disk-to-blade interface can be chosen completely arbitrarily. In practice, though, this choice may affect the accuracy of the approximate solutions.

Each sector is here treated as an isolated substructure and since all sectors are assumed identical, the non-zero matrix blocks will be block-diagonal:

$$\begin{aligned} \mathbf{M_d} &= \mathbf{I} \otimes \tilde{\mathbf{M}}_\mathbf{d} \qquad & \mathbf{M_b} &= \mathbf{I} \otimes \tilde{\mathbf{M}}_\mathbf{b} \\ \mathbf{K_d} &= \mathbf{I} \otimes \tilde{\mathbf{K}}_\mathbf{d} \qquad & \mathbf{K_b} &= \mathbf{I} \otimes \tilde{\mathbf{K}}_\mathbf{b} \end{aligned} \tag{4.2}$$

where $\mathbf{I}$ is an identity matrix, and the symbol $\otimes$ denotes the Kronecker product, which is defined in Appendix A. The "tilde" notation will be used throughout the following to indicate that a quantity refers to a single blade or disk sector. Note that this implies that all degrees of freedom associated with the boundaries between adjacent sectors will appear twice.

A key idea for this reduced order modeling technique (Castanier *et al*. [20]) is to describe the motion of the bladed disk assembly using two particular sets of component modes. Figure 4.1 depicts the two fundamental component mode types for a greatly simplified finite element model of a bladed disk sector. The first set is comprised of disk-induced modes, which are the cyclic modes of the entire assembly where the attached blades are massless. In this case, the blade motion is a rigid-body motion plus elastic deformation due to the boundary motion. The blade portion of the disk-induced modes, i.e.,

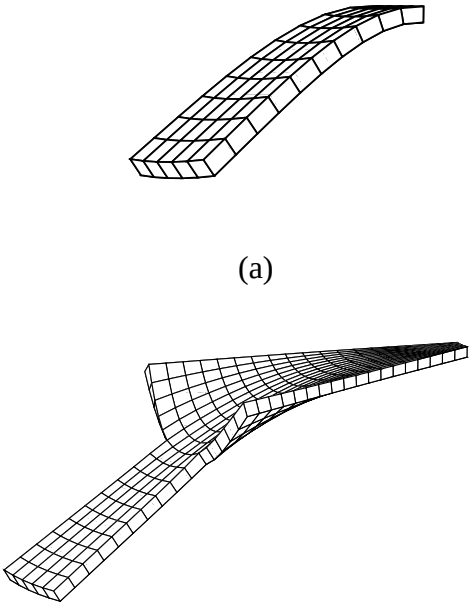

(a)

(b)

Figure 4.1: Cantilever blade (a) and disk-induced (b) motions.

the part belonging to the blade degrees of freedom, will be denoted $\mathbf{U^d}$, and the disk portion $\mathbf{V^d}$. The second mode set consists of the modes of a cantilever blade alone, which is clamped at the chosen disk-blade interface location. Note that for unshrouded blades, the modal matrix $\mathbf{U^b}$ for all N identical blades is block-diagonal and is assembled as $\mathbf{I} \otimes \tilde{\mathbf{u}}^{\mathbf{b}}$, where $\tilde{\mathbf{u}}^{\mathbf{b}}$ is the cantilever mode shapes of a single blade. For shrouded blades, however, this set of modes is also cyclic in nature, due to the presence of direct blade-to-blade structural coupling, and thus, the cyclic assembly modes will yield a full matrix $\mathbf{U^b}$.

Through superposition of these two sets of component modes, and using the node ordering configuration in Eq. (4.1), the resulting nodal displacements of the entire assembly can be expanded as:

$$\mathbf{x} = \begin{bmatrix} \mathbf{V^d} \\ \\ \mathbf{U^d} \end{bmatrix} \mathbf{a} + \begin{bmatrix} \mathbf{0} \\ \\ \mathbf{U^b} \end{bmatrix} \mathbf{b} \tag{4.3}$$

where $\mathbf{a}$ and $\mathbf{b}$ are modal coordinates for the disk-induced and the cantilever blade modes,

respectively. With above definitions, the strain and kinetic energies of the system, as well as the external virtual work done by a time-harmonic engine order excitation force, $\mathbf{Q}$, may be formulated in component modal-referred quantities.

Applying Hamilton's principle yields the governing equations of motion for the reduced order model. They are conveniently written in matrix form as:

$$\mathcal{M}\ddot{\mathbf{z}} + \mathcal{C}\dot{\mathbf{z}} + (1 + Gj)\,\mathcal{K}\mathbf{z} = \mathcal{Q} \tag{4.4}$$

where:

$$\mathbf{z} = \begin{Bmatrix} \mathbf{a} \\ \mathbf{b} \end{Bmatrix} \qquad \mathcal{C} = \begin{bmatrix} \mathbf{0} & \mathbf{0} \\ \mathbf{0} & \mathbf{C} \end{bmatrix} \qquad \mathcal{Q} = \begin{Bmatrix} \mathcal{Q}_{\mathbf{d}} \\ \mathcal{Q}_{\mathbf{b}} \end{Bmatrix} = \begin{Bmatrix} \mathbf{U^{d}}^{\mathbf{T}}\mathbf{Q} \\ \mathbf{U^{b}}^{\mathbf{T}}\mathbf{Q} \end{Bmatrix}$$

$$\mathcal{M} = \begin{bmatrix} \mathbf{I_d} + \mathbf{U^{d}}^{\mathbf{T}}\mathbf{M_b}\mathbf{U^{d}} & \mathbf{U^{d}}^{\mathbf{T}}\mathbf{M_b}\mathbf{U^{b}} \\ \mathbf{U^{b}}^{\mathbf{T}}\mathbf{M_b}\mathbf{U^{d}} & \mathbf{I_b} \end{bmatrix} \qquad \mathcal{K} = \begin{bmatrix} \hat{\mathbf{K}}_{\mathbf{d}} & \mathbf{U^{d}}^{\mathbf{T}}\mathbf{K_b}\mathbf{U^{b}} \\ \mathbf{U^{b}}^{\mathbf{T}}\mathbf{K_b}\mathbf{U^{d}} & \hat{\mathbf{K}}_{\mathbf{b}} + \Delta\hat{\mathbf{K}}_{\mathbf{b}} \end{bmatrix}$$

$\hat{\mathbf{K}}_{\mathbf{d}}$ and $\hat{\mathbf{K}}_{\mathbf{b}}$ are *diagonal* matrices, and the elements on the diagonals are modal stiffnesses (eigenvalues) obtained from the disk-induced and cantilever blade finite element analyses, respectively. $\mathbf{I_d}$ and $\mathbf{I_b}$ are the corresponding modal mass matrices, which in view of the employed method of eigenvector normalization will be identity matrices. Recall that the blade is massless in the disk-induced analysis. Thus, the effect of blade mass on the disk is included as the second term in the upper-left quadrant of the mass matrix, but no such term is needed in the stiffness matrix.

Structural damping with damping coefficient G, as well as viscous modal damping of the cantilever blade modes, $\mathbf{C}$, have now been added to the reduced order model, in order to facilitate more realistic modeling of the structure's dynamic response. In addition, some general measure of mistuning, $\Delta\hat{\mathbf{K}}_{\mathbf{b}}$, is added into the stiffness matrix $\mathcal{K}$. This measure of mistuning, although general at this point, implies three assumptions:

- The mistuned characteristics of a blade are restricted to its stiffness (lower-right quadrant of $\mathcal{K}$). While stiffness mistuning is sufficient for the purposes of this study, it may be more accurate to model mistuning in other structural parameters as well; for instance, by using the mixed least squares – maximum likelihood method of Mignolet and Lin [48].

- The effects of stiffness mistuning on the other three quadrants of $\mathcal{K}$ are assumed negligible. This is to a large extent justified by considering the kind of rigid-body-like motion the blade undergoes in this set of component modes.

- The mistuned cantilever modes of a blade may be realized by a linear combination of the tuned modes (i.e., they span approximately the same space).

Note that the resulting structural matrices are all symmetric. In general, this symmetry is destroyed if aerodynamic coupling between blades is introduced into the system. However, aerodynamic coupling will not be considered in this work.

At this point, the reduced order model formulation is completely general in that it is applicable to both unshrouded and shrouded assemblies. However, a closer examination of the various partitions of the structural matrices reveals significant differences between the two designs, leading to slightly different degrees of further simplifications. Further refinement of the formulation for unshrouded assemblies is detailed for the free response by Castanier *et al*. [20], and extended for the forced response by Kruse and Pierre [21], and will therefore not be repeated here. A presentation of formulation details for the reduced order model of a shrouded assembly, including a novel method for modeling shrouded blade mistuning, will follow.

4.2.2 Formulation Refinement for Shrouded Designs

A modal matrix containing cyclic modes can be represented as:

$$\mathbf{U^r} = (\mathbf{F} \otimes \mathbf{I})\, \tilde{\mathbf{U}}^{\mathbf{r}}, \tag{4.5}$$

where $\mathbf{F}$ is defined in Eq. (B.3), and $\tilde{\mathbf{U}}^{\mathbf{r}}$, which contains the mode shapes of a fundamental sector in cyclic coordinates, has a pseudo-block-diagonal structure (see Appendix B):

$$\tilde{\mathbf{U}}^{\mathbf{r}} = \underset{k=0,\ldots,P}{\tilde{\mathbf{B}}\mathbf{diag}}[\tilde{\mathbf{u}}^{\mathbf{r}}_{\mathbf{k}}]\,, \tag{4.6}$$

where $\tilde{\mathbf{B}}\mathbf{diag}\,[\bullet]$ denotes a pseudo-block-diagonal matrix, with the argument being the k^{th} "block", and the range of k is shown. The mode type designation $\mathbf{r}$ could be either the disk-induced modes, $\mathbf{d}$, or the cantilever blade modes, $\mathbf{b}$, since the structure of both these modal matrices is cyclic. Combining Eqs. (4.5) and (4.6), one may write the internal structure of a cyclic modal matrix $\mathbf{U^r}$ as:

$$\begin{aligned} \mathbf{U^r} \;=\; \Big[\; & \mathbf{f_0} \otimes \tilde{\mathbf{u}}^{\mathbf{r}}_{\mathbf{0}} \quad \mathbf{f_{1,c}} \otimes \tilde{\mathbf{u}}^{\mathbf{r}}_{\mathbf{1,c}} + \mathbf{f_{1,s}} \otimes \tilde{\mathbf{u}}^{\mathbf{r}}_{\mathbf{1,s}} \quad \cdots \\ & \cdots \quad \mathbf{f_{k,c}} \otimes \tilde{\mathbf{u}}^{\mathbf{r}}_{\mathbf{k,c}} + \mathbf{f_{k,s}} \otimes \tilde{\mathbf{u}}^{\mathbf{r}}_{\mathbf{k,s}} \quad \cdots \quad \mathbf{f_{N/2}} \otimes \tilde{\mathbf{u}}^{\mathbf{r}}_{\mathbf{N/2}} \;\Big]\,. \end{aligned} \tag{4.7}$$

Because of the cyclicity of both $\mathbf{U^d}$ and $\mathbf{U^b}$ and the block-diagonal structure of $\mathbf{M}$ and $\mathbf{K}$, all three projection products in $\mathcal{M}$ and $\mathcal{K}$ will become pseudo-block-diagonal:

$$\begin{aligned} \mathbf{U^{d^T} M_b U^d} &= \underset{k=0,\ldots,P}{\tilde{\mathbf{B}}\mathbf{diag}}\Big[\tilde{\mathbf{u}}^{\mathbf{d^T}}_{\mathbf{k}} \tilde{\mathbf{M}}_{\mathbf{b}} \tilde{\mathbf{u}}^{\mathbf{d}}_{\mathbf{k}}\Big] \\ \mathbf{U^{d^T} M_b U^b} &= \underset{k=0,\ldots,P}{\tilde{\mathbf{B}}\mathbf{diag}}\Big[\tilde{\mathbf{u}}^{\mathbf{d^T}}_{\mathbf{k}} \tilde{\mathbf{M}}_{\mathbf{b}} \tilde{\mathbf{u}}^{\mathbf{b}}_{\mathbf{k}}\Big] \\ \mathbf{U^{d^T} K_b U^b} &= \underset{k=0,\ldots,P}{\tilde{\mathbf{B}}\mathbf{diag}}\Big[\tilde{\mathbf{u}}^{\mathbf{d^T}}_{\mathbf{k}} \tilde{\mathbf{K}}_{\mathbf{b}} \tilde{\mathbf{u}}^{\mathbf{b}}_{\mathbf{k}}\Big]\,. \end{aligned} \tag{4.8}$$

The external excitation force vector shown in Eq. (4.4), $\mathbf{Q}$, defines the forcing on all the blade degrees of freedom of the assembly. The restriction to blade degrees of freedom is not an absolute requirement, but leads to a more compact formulation, and it should also

be sufficient from a practical perspective. Moreover, we assume an engine order excitation which is harmonic in time and differs only in phase from blade to blade. The phase at blade i, ϕ_i, is given by:

$$\phi_i = \frac{2\pi C(i-1)}{N}, \qquad i = 1, \ldots, N, \tag{4.9}$$

where C is the engine order of the excitation. The external force vector can then be expressed as:

$$\mathbf{Q} = \left\{ \begin{array}{c} \tilde{\mathbf{f}} e^{j\phi_1} \\ \tilde{\mathbf{f}} e^{j\phi_2} \\ \vdots \\ \tilde{\mathbf{f}} e^{j\phi_N} \end{array} \right\}, \tag{4.10}$$

where $\tilde{\mathbf{f}}$ is the force vector on a single blade.

The expression for the modal force vector $\mathcal{Q}$ given in Eq. (4.4) can be simplified to a much more convenient form in terms of the disk-induced and cantilevered blade mode shapes of a single sector, $\tilde{\mathbf{u}}^{\mathbf{d}}_{\mathbf{k}}$ and $\tilde{\mathbf{u}}^{\mathbf{b}}_{\mathbf{k}}$, respectively. Using Eq. (4.10), and the modal matrix as written in Eq. (4.7), the corresponding modal force partition becomes:

$$\mathcal{Q}_{\mathbf{r}} = \mathbf{U}^{\mathbf{r}^{\mathbf{T}}}\mathbf{Q} = \sqrt{N} \left\{ \begin{array}{c} \left(\mathbf{f_0} \otimes \tilde{\mathbf{u}}^{\mathbf{r}}_{\mathbf{0}}\right)^{\mathbf{T}} \left(\mathbf{e_C} \otimes \tilde{\mathbf{f}}\right) \\ \left(\mathbf{f_{1,c}} \otimes \tilde{\mathbf{u}}^{\mathbf{r}}_{\mathbf{1,c}} + \mathbf{f_{1,s}} \otimes \tilde{\mathbf{u}}^{\mathbf{r}}_{\mathbf{1,s}}\right)^{\mathbf{T}} \left(\mathbf{e_C} \otimes \tilde{\mathbf{f}}\right) \\ \vdots \\ \left(\mathbf{f_{k,c}} \otimes \tilde{\mathbf{u}}^{\mathbf{r}}_{\mathbf{k,c}} + \mathbf{f_{k,s}} \otimes \tilde{\mathbf{u}}^{\mathbf{r}}_{\mathbf{k,s}}\right)^{\mathbf{T}} \left(\mathbf{e_C} \otimes \tilde{\mathbf{f}}\right) \\ \vdots \\ \left(\mathbf{f_{N/2}} \otimes \tilde{\mathbf{u}}^{\mathbf{r}}_{\mathbf{N/2}}\right)^{\mathbf{T}} \left(\mathbf{e_C} \otimes \tilde{\mathbf{f}}\right) \end{array} \right\}, \tag{4.11}$$

where $\mathbf{e_C}$ is the $(C+1)^{\text{th}}$ column of the complex Fourier matrix, $\mathbf{E}$, defined in Eq. (B.2). This expression can now be greatly simplified, first by using the general algebraic properties of the Kronecker product stated in Eqs. (A.2) and (A.4), and then by making use of the orthogonal properties of the transformation column vectors involved. The expansion

of Eq. (4.11) will yield modal force partitions that are zero everywhere, except for the C^{th} harmonic disk-induced and cantilever blade modes. Thus, the engine order excitation, C, determines which modes of the assembly that are being excited. The resulting modal force vector is given in Section 4.2.4.

The modal viscous damping matrix for the shrouded cantilever blade modes, $\mathbf{C}$, will be a diagonal matrix expressed as:

$$\mathbf{C} = \underset{k=0,\ldots,P}{\tilde{\mathbf{B}}\mathbf{diag}}\left[\mathbf{diag}\left[2\zeta_n^k\right]_{n=1,\ldots,m_b/2m_b}\right]\sqrt{\hat{\mathbf{K}}_\mathbf{b}}, \tag{4.12}$$

where $\mathbf{diag}\,[\bullet]$ denotes a diagonal matrix (block), with the argument being the n^{th} diagonal element, and the range of n is shown. Also, ζ_n^k is the modal damping coefficient of the n^{th} cantilever blade mode of the k^{th} harmonic. Note that for shrouded blades, $\hat{\mathbf{K}}_\mathbf{b}$ is comprised of diagonal blocks associated with the various cyclic harmonics of the assembly of shrouded blades.

4.2.3 Mistuning of Shrouded Blades

Perhaps the most fundamental feature of this technique is its suitability for stiffness mistuning of the individual blades, since the modal stiffness of each individual cantilever blade mode is isolated in the diagonal matrix $\hat{\mathbf{K}}_\mathbf{b}$. Therefore, in the unshrouded case, the formulation lends itself to a very convenient and simple input of individual mistuning of each cantilever blade modal stiffness for each blade as:

$$\Delta\hat{\mathbf{K}}_\mathbf{b} = \underset{n=1,\ldots,N}{\mathbf{Bdiag}}\left[\mathbf{diag}\left[\delta_n^k\right]_{k=1,\ldots,m_b}\right]\hat{\mathbf{K}}_\mathbf{b}, \tag{4.13}$$

where $\mathbf{Bdiag}\,[\bullet]$ denotes a block-diagonal (versus pseudo-block-diagonal) matrix. The mistuning parameter associated with the k^{th} cantilever blade mode of the n^{th} blade, δ_n^k, is defined as:

$$\delta_n^k = \left(\frac{\bar{\omega}_n^k}{\omega^k}\right)^2 - 1, \tag{4.14}$$

where $\bar{\omega}_n^k$ represents the mistuned natural frequency of the k^{th} mode of blade n, and ω^k is the corresponding nominal, or tuned, natural frequency.

However, the manner in which the mistuning is put into the ROM stiffness matrix for unshrouded blades is not particularly well suited for shrouded assemblies, in that $\hat{\mathbf{K}}_{\mathbf{b}}$ is now represented in *cyclic*, or *harmonic*, modal coordinates. This implies that in order to obtain any relevant measures of mistuning, one would need to know the effects of individual blade mistuning on the whole shrouded blade assembly. In theory, it would be possible to obtain this information through frequency tests of the full blade-shroud assembly, but this approach is not practical.

In view of this, an alternative approach is to project mistuning measurements for a single blade onto the cyclic modes of the blade assembly. In this case, the test data would consist of the deviations in natural frequencies of each individual mode of each blade. This data could then be used to generate estimates of the mistuned stiffness matrices for all blades, which would then be included in the ROM formulation. In addition, this would be possible to achieve without very complicated and specialized testing procedures.

First, one must establish the manner in which the individual shrouded blade natural frequencies are measured. Here, it is assumed that the shrouded blades are tested while being clamped at the root, but are otherwise completely unconstrained, as indicated in Fig. 4.2. Thus, the tests give measurements of the natural frequencies of a cantilever blade with free shrouds, $\bar{\omega}_n^k$. Using the mistuning parameter δ_n^k defined in Eq. (4.14), a diagonal matrix containing the measured mistuned natural frequencies may be defined as:

$$\underset{n=1,\ldots,N}{\mathbf{Bdiag}}\left[\underset{k=1,\ldots,p}{\mathbf{diag}}\left[1+\delta_n^k\right]\right]\hat{\mathbf{K}}_{\mathbf{b}}^{\mathbf{nom}} = \left(\mathbf{I}\otimes\bar{\mathbf{u}}^{\mathbf{b}}\right)^{\mathbf{T}}\mathbf{K}_{\mathbf{b}}^{\mathbf{mt}}\left(\mathbf{I}\otimes\bar{\mathbf{u}}^{\mathbf{b}}\right), \tag{4.15}$$

where $\bar{\mathbf{u}}^{\mathbf{b}}$ is the nominal modal matrix, or the nominal mode shapes, for one cantilever blade; $\mathbf{K}_{\mathbf{b}}^{\mathbf{mt}}$ is a mistuned, block-diagonal stiffness matrix, where each block corresponds

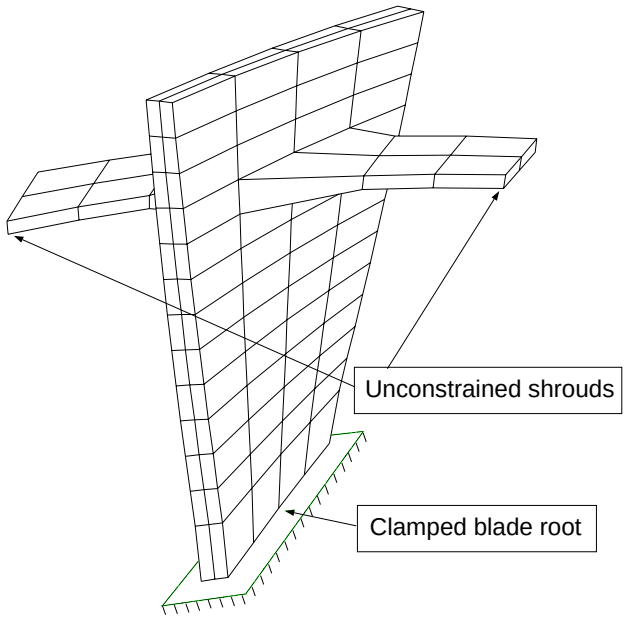

Figure 4.2: Proposed configuration for measuring natural frequencies of shrouded blades individually.

to the stiffness matrix of one of the N mistuned blades; and $\hat{\mathbf{K}}_{\mathbf{b}}^{\mathbf{nom}}$ is a diagonal matrix of squared nominal natural frequencies for a tuned cantilever blade. The nominal natural frequencies may be taken either as some average values from tests, or directly from the finite element analysis needed to obtain the tuned cantilever blade mode shapes $\bar{\mathbf{u}}^{\mathbf{b}}$. Note that there is already an approximation made at this point, namely that the eigenvectors $\bar{\mathbf{u}}^{\mathbf{b}}$ of the mistuned blades are the same as the tuned ones (see discussion in Section 4.2.1).

Returning to Eq. (4.15), the mistuned frequencies are grouped in blocks associated with each individual blade, where these blocks are diagonal in themselves. Moreover, the mistuned stiffness matrix will have the following block-diagonal configuration:

$$\mathbf{K}_{\mathbf{b}}^{\mathbf{mt}} = \underset{n=1,..,N}{\mathbf{Bdiag}} \left[\bar{\mathbf{K}}_{\mathbf{b,n}}^{\mathbf{mt}} \right] \tag{4.16}$$

Finally, the matrix of nominal modal stiffnesses will also be of a block-diagonal form, but where all the blocks are identical and diagonal. By denoting such a diagonal block $\hat{\bar{\mathbf{K}}}_{\mathbf{b}}^{\mathbf{nom}}$,

the matrix of nominal modal stiffnesses can be expressed as:

$$\hat{\mathbf{K}}_{\mathbf{b}}^{\mathbf{nom}} = \underset{n=1,\ldots,N}{\mathbf{Bdiag}}\left[\hat{\tilde{\mathbf{K}}}_{\mathbf{b}}^{\mathbf{nom}}\right] = \mathbf{I} \otimes \hat{\tilde{\mathbf{K}}}_{\mathbf{b}}^{\mathbf{nom}} \tag{4.17}$$

Since $\hat{\tilde{\mathbf{K}}}_{\mathbf{b}}^{\mathbf{nom}}$ represents the nominal modal stiffnesses for one blade, Eq. (4.17) can be rewritten as:

$$\hat{\mathbf{K}}_{\mathbf{b}}^{\mathbf{nom}} = \mathbf{I} \otimes \bar{\mathbf{u}}^{\mathbf{b}^{\mathbf{T}}} \tilde{\mathbf{K}}_{\mathbf{b}} \bar{\mathbf{u}}^{\mathbf{b}} = \left(\mathbf{I} \otimes \bar{\mathbf{u}}^{\mathbf{b}}\right)^{\mathbf{T}} \left(\mathbf{I} \otimes \tilde{\mathbf{K}}_{\mathbf{b}}\right) \left(\mathbf{I} \otimes \bar{\mathbf{u}}^{\mathbf{b}}\right) \tag{4.18}$$

From Eqs. (4.15) and (4.18), one obtains:

$$\mathbf{K}_{\mathbf{b}}^{\mathbf{mt}} = \left(\mathbf{I} \otimes \bar{\mathbf{u}}^{\mathbf{b}}\right)^{\mathbf{T}^{-1}} \underset{n=1,\ldots,N}{\mathbf{Bdiag}}\left[\underset{k=1,\ldots,p}{\mathbf{diag}}\left[1+\delta_n^k\right]\right] \left(\mathbf{I} \otimes \bar{\mathbf{u}}^{\mathbf{b}^{\mathbf{T}}} \tilde{\mathbf{K}}_{\mathbf{b}}\right), \tag{4.19}$$

by virtue of the Kronecker product property given in Eq. (A.2).

Now, making use of the eigenvector normalization assumption, it is realized that:

$$\begin{aligned} \mathbf{I} &= \underset{n=1,\ldots,N}{\mathbf{Bdiag}}\left[\bar{\mathbf{u}}^{\mathbf{b}^{\mathbf{T}}} \tilde{\mathbf{M}}_{\mathbf{b}} \bar{\mathbf{u}}^{\mathbf{b}}\right] = \left(\mathbf{I} \otimes \bar{\mathbf{u}}^{\mathbf{b}}\right)^{\mathbf{T}} \left(\mathbf{I} \otimes \tilde{\mathbf{M}}_{\mathbf{b}}\right) \left(\mathbf{I} \otimes \bar{\mathbf{u}}^{\mathbf{b}}\right) \\ \Rightarrow \quad & \left(\mathbf{I} \otimes \bar{\mathbf{u}}^{\mathbf{b}}\right)^{\mathbf{T}^{-1}} = \mathbf{I} \otimes \tilde{\mathbf{M}}_{\mathbf{b}} \bar{\mathbf{u}}^{\mathbf{b}} \end{aligned} \tag{4.20}$$

By substituting Eq. (4.20) into Eq. (4.19), and by using the fact that $\tilde{\mathbf{M}}_{\mathbf{b}}$ is symmetric, one may express the mistuned blade stiffness matrix as:

$$\mathbf{K}_{\mathbf{b}}^{\mathbf{mt}} = \mathbf{I} \otimes \tilde{\mathbf{K}}_{\mathbf{b}} + \left(\mathbf{I} \otimes \tilde{\mathbf{M}}_{\mathbf{b}} \bar{\mathbf{u}}^{\mathbf{b}}\right) \underset{n=1,\ldots,N}{\mathbf{Bdiag}}\left[\underset{k=1,\ldots,p}{\mathbf{diag}}\left[\delta_n^k\right]\right] \left(\mathbf{I} \otimes \bar{\mathbf{u}}^{\mathbf{b}^{\mathbf{T}}} \tilde{\mathbf{K}}_{\mathbf{b}}\right). \tag{4.21}$$

For convenience, the quantity $\Delta\mathbf{K}_{\mathbf{b}}$ is introduced to denote the stiffness deviation matrix as:

$$\Delta\mathbf{K}_{\mathbf{b}} = \left(\mathbf{I} \otimes \tilde{\mathbf{M}}_{\mathbf{b}} \bar{\mathbf{u}}^{\mathbf{b}}\right) \underset{n=1,\ldots,N}{\mathbf{Bdiag}}\left[\underset{k=1,\ldots,p}{\mathbf{diag}}\left[\delta_n^k\right]\right] \left(\mathbf{I} \otimes \bar{\mathbf{u}}^{\mathbf{b}^{\mathbf{T}}} \tilde{\mathbf{K}}_{\mathbf{b}}\right), \tag{4.22}$$

such that:

$$\mathbf{K}_{\mathbf{b}}^{\mathbf{mt}} = \mathbf{I} \otimes \tilde{\mathbf{K}}_{\mathbf{b}} + \Delta\mathbf{K}_{\mathbf{b}} = \mathbf{K}_{\mathbf{b}} + \Delta\mathbf{K}_{\mathbf{b}}. \tag{4.23}$$

The expression for the stiffness deviation matrix, $\Delta\mathbf{K}_{\mathbf{b}}$, can be simplified to:

$$\Delta\mathbf{K}_{\mathbf{b}} = \underset{n=1,\ldots,N}{\mathbf{Bdiag}}\left[\tilde{\mathbf{M}}_{\mathbf{b}} \bar{\mathbf{u}}^{\mathbf{b}} \underset{k=1,\ldots,p}{\mathbf{diag}}\left[\delta_n^k\right] \bar{\mathbf{u}}^{\mathbf{b}^{\mathbf{T}}} \tilde{\mathbf{K}}_{\mathbf{b}}\right]. \tag{4.24}$$

Finally, the complete blade stiffness matrix for the tuned case, $\mathbf{K_b}$, is now simply replaced by $\mathbf{K_b^{mt}}$ in the reduced order model formulation. Thus, replacing $\mathbf{K_b}$ by $\mathbf{K_b^{mt}}$ in Eq. (4.1), and ignoring any contributions of mistuning from the projection onto the disk-induced modes, as per discussion in Section 4.2.1, yield the ROM stiffness matrix for a general mistuned shrouded bladed disk assembly:

$$\mathcal{K} = \begin{bmatrix} \hat{\mathbf{K}}_\mathbf{d} & \tilde{\mathbf{B}}\mathbf{diag}_{k=0,\ldots,P}\left[\tilde{\mathbf{u}}_\mathbf{k}^{\mathbf{d}^T}\tilde{\mathbf{K}}_\mathbf{b}\tilde{\mathbf{u}}_\mathbf{k}^\mathbf{b}\right] \\ \tilde{\mathbf{B}}\mathbf{diag}_{k=0,\ldots,P}\left[\tilde{\mathbf{u}}_\mathbf{k}^{\mathbf{b}^T}\tilde{\mathbf{K}}_\mathbf{b}\tilde{\mathbf{u}}_\mathbf{k}^\mathbf{d}\right] & \hat{\mathbf{K}}_\mathbf{b} + \mathbf{U}^{\mathbf{b}^T}\Delta\mathbf{K_b}\mathbf{U}^\mathbf{b} \end{bmatrix} \tag{4.25}$$

$$\Delta\mathbf{K_b} = \mathbf{B}\mathbf{diag}_{n=1,\ldots,N}\left[\tilde{\mathbf{M}}_\mathbf{b}\bar{\mathbf{u}}^\mathbf{b}\mathbf{diag}_{k=1,\ldots,p}\left[\delta_n^k\right]\bar{\mathbf{u}}^{\mathbf{b}^T}\tilde{\mathbf{K}}_\mathbf{b}\right].$$

Thus, the stiffness mistuning $\Delta\mathbf{K_b}$, which may be obtained from measuring natural frequencies of individual blades with clamped roots and unconstrained shrouds, is now projected onto the cyclic modes of the shrouded blade assembly, $\mathbf{U^b}$. Note that the mistuning projection term $\mathbf{U}^{\mathbf{b}^T}\Delta\mathbf{K_b}\mathbf{U}^\mathbf{b}$ does not yield any particular matrix structure, since there are no special relations, such as orthogonality, between the modes of the cantilever blade with unconstrained shrouds, and the cyclic modes of the shrouded blade assembly. Thus, in general, the lower-right quadrant of the ROM stiffness matrix becomes fully populated when mistuning is introduced for shrouded bladed disk assemblies.

4.2.4 Final Formulation for Shrouded Designs

To conclude this section, the reduced order model structural matrices (in the absence of aerodynamic coupling) and modal force for shrouded bladed disks are stated in their final forms:

$$\mathcal{M} = \begin{bmatrix} \mathbf{I_d} + \tilde{\mathbf{B}}\mathbf{diag}_{k=0,\ldots,P}\left[\tilde{\mathbf{u}}_\mathbf{k}^{\mathbf{d}^T}\tilde{\mathbf{M}}_\mathbf{b}\tilde{\mathbf{u}}_\mathbf{k}^\mathbf{d}\right] & \tilde{\mathbf{B}}\mathbf{diag}_{k=0,\ldots,P}\left[\tilde{\mathbf{u}}_\mathbf{k}^{\mathbf{d}^T}\tilde{\mathbf{M}}_\mathbf{b}\tilde{\mathbf{u}}_\mathbf{k}^\mathbf{b}\right] \\ \tilde{\mathbf{B}}\mathbf{diag}_{k=0,\ldots,P}\left[\tilde{\mathbf{u}}_\mathbf{k}^{\mathbf{b}^T}\tilde{\mathbf{M}}_\mathbf{b}\tilde{\mathbf{u}}_\mathbf{k}^\mathbf{d}\right] & \mathbf{I_b} \end{bmatrix}$$

$$\mathcal{C} = \begin{bmatrix} \mathbf{0} & \mathbf{0} \\ \mathbf{0} & \underset{k=1,\ldots,m_b N}{\mathbf{diag}}\left[2\zeta^k\right]\sqrt{\hat{\mathbf{K}}_\mathbf{b}} \end{bmatrix}$$

$$\mathcal{K} = \begin{bmatrix} \hat{\mathbf{K}}_\mathbf{d} & \tilde{\mathbf{B}}\underset{k=0,\ldots,P}{\mathbf{diag}}\left[\tilde{\mathbf{u}}_\mathbf{k}^{\mathbf{d}^\mathbf{T}}\tilde{\mathbf{K}}_\mathbf{b}\tilde{\mathbf{u}}_\mathbf{k}^\mathbf{b}\right] \\ \tilde{\mathbf{B}}\underset{k=0,\ldots,P}{\mathbf{diag}}\left[\tilde{\mathbf{u}}_\mathbf{k}^{\mathbf{b}^\mathbf{T}}\tilde{\mathbf{K}}_\mathbf{b}\tilde{\mathbf{u}}_\mathbf{k}^\mathbf{d}\right] & \hat{\mathbf{K}}_\mathbf{b} + \mathbf{U}^{\mathbf{b}^\mathbf{T}}\Delta\mathbf{K}_\mathbf{b}\mathbf{U}^\mathbf{b} \end{bmatrix}$$

$$\Delta\mathbf{K}_\mathbf{b} = \mathbf{B}\underset{n=1,\ldots,N}{\mathbf{diag}}\left[\tilde{\mathbf{M}}_\mathbf{b}\bar{\mathbf{u}}^\mathbf{b}\underset{k=1,\ldots,p}{\mathbf{diag}}\left[\delta_n^k\right]\bar{\mathbf{u}}^{\mathbf{b}^\mathbf{T}}\tilde{\mathbf{K}}_\mathbf{b}\right]$$

$$\mathcal{Q} = \left\{ \begin{array}{c|c} \mathcal{Q}_\mathbf{d}^\mathbf{T} & \mathcal{Q}_\mathbf{b}^\mathbf{T} \end{array} \right\}^T$$

$$\mathcal{Q}_{[\mathbf{d/b}]} = \left\{ \begin{array}{c} \mathbf{0} \\ \vdots \\ \mathbf{0} \\ \sqrt{N}\left\{\mathbf{f}_{\mathbf{C},\mathbf{c}}^\mathbf{T}\mathbf{e}_\mathbf{C} \otimes \tilde{\mathbf{u}}_{\mathbf{C},\mathbf{c}}^{[\mathbf{d/b}]^\mathbf{T}}\tilde{\mathbf{f}} + \mathbf{f}_{\mathbf{C},\mathbf{s}}^\mathbf{T}\mathbf{e}_\mathbf{C} \otimes \tilde{\mathbf{u}}_{\mathbf{C},\mathbf{s}}^{[\mathbf{d/b}]^\mathbf{T}}\tilde{\mathbf{f}}\right\} \\ \mathbf{0} \\ \vdots \\ \mathbf{0} \end{array} \right\}.$$

4.3 Analysis of a Shrouded Test Case Rotor

4.3.1 Finite Element and Reduced Order Models

The finite element model of the test case rotor that is analyzed in this study is shown in Figs. 4.3 and 4.4. The rotor features 24 blades. Each blade has a base pitch of 30° (measured from the axial direction), and a uniform twist of an additional 30° over its length. The base radius is 212 mm, and the blade length is 68 mm. The rotor is fixed at the interfaces towards adjacent rotating blade stages. This is believed to provide a reasonable description of the dynamics of the bladed disk assembly. Moreover, the studied test case rotor features shrouds, which are arbitrarily positioned at $10/13$ of the blade length.

The construction of the reduced order model of a shrouded assembly requires the fol-

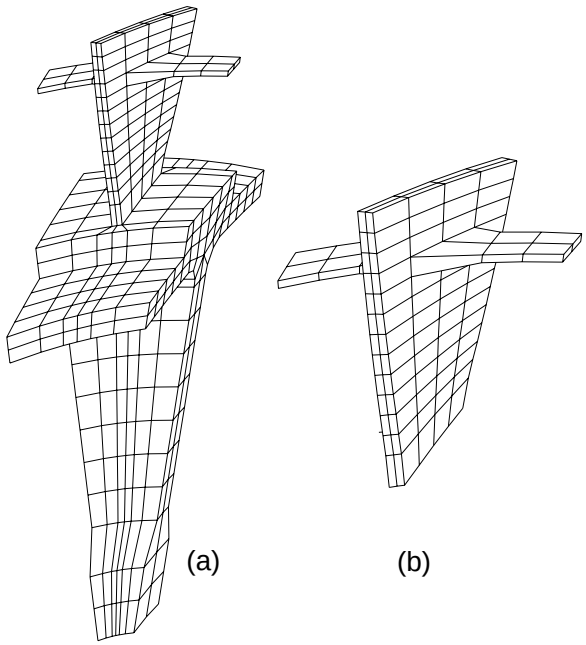

Figure 4.3: (a) Finite element mesh of a single disk-blade-shroud sector. (b) Finite element mesh of a single blade with shrouds.

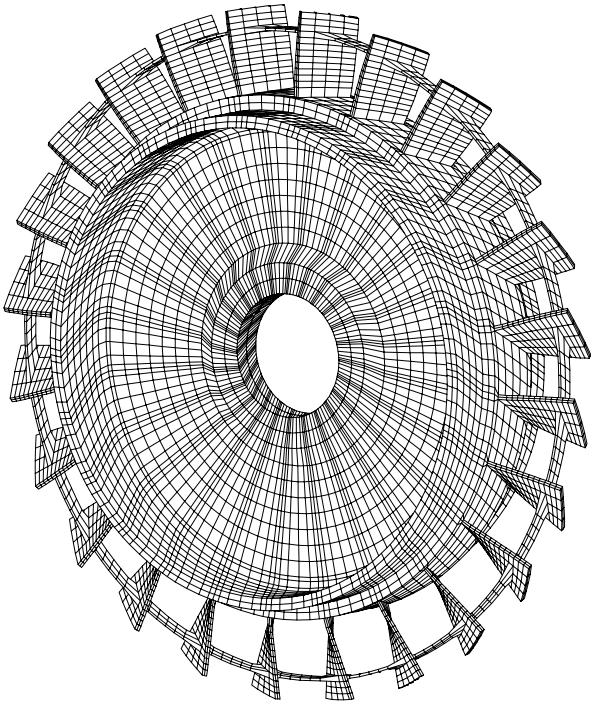

Figure 4.4: Finite element mesh of full shrouded test case rotor.

lowing two finite element models:

- A complete sector subject to cyclic constraints at disk-to-disk and shroud-to-shroud interfaces. This model consists of 488 eight-noded brick elements and 2,646 degrees of freedom *before* model reduction due to applied constraints. The finite element mesh of this model is shown in Fig. 4.3a.

- A single cantilever blade. This model consists of 116 linear solid elements, and 738 degrees of freedom before model reduction. The finite element mesh of this model is shown in Fig. 4.3b.

From these fundamental finite element models, the reduced order model (ROM) is derived using the component mode synthesis technique described in Section 4.2. This analysis is based on a reduced order model that is created from five cantilever blade modes $(m_b = 5)$ and five disk-induced modes $(m_d = 5)$ per harmonic, leading to a total of 240 degrees of freedom.

In addition, five cantilever blade modes with unconstrained shrouds were used to generate the stiffness deviation matrix, $\Delta\mathbf{K_b}$ $(p = 5)$. This, however, does not influence the size of the resulting reduced order model. It should be pointed out that, if the cantilever blade mode shapes from the cyclic symmetry analysis conform relatively closely with the cantilever blade mode shapes with unconstrained shrouds, very little improvement in accuracy is gained by including more than m_b modes for the stiffness deviation generation. In this case, the principal effects of the stiffness deviations are already captured by the m_b modes. However, using fewer than m_b modes yields poor accuracy and thus, in general, the condition $p \geq m_b$ should always be satisfied in order to obtain a reduced order model with reasonable accuracy.

Finally, a finite element model of the full mistuned rotor was created to allow com-

parisons of mistuned mode shapes and forced responses for a single, random mistuning pattern. The mistuning pattern was sampled from a uniform distribution of mean zero and standard deviation 5%. Individual mode mistuning is not employed in this analysis. Therefore, the mistuning is readily introduced to the full finite element model by appropriately varying Young's modulus in the blade elements as:

$$E_n = (1 + \delta_n)\, E_o, \qquad n = 1, \ldots, N. \tag{4.26}$$

The material properties for the finite element model were taken to be those of steel. The full finite element model consists of $11,712$ linear solid elements and $56,376$ degrees of freedom, and its finite element mesh is shown in Fig. 4.4.

It should be noted that the shroud-to-shroud connection is modeled as being continuous (full stick). Since no effort has been made to include friction at the shroud mating surfaces, the present modeling technique can be used for the limiting cases of full stick or full slip conditions. The incorporation of shroud interface models (Srinivasan *et al*. [58]; Menq *et al*. [59]; Valero and Bendiksen [60]) into this type of reduced order model will be the subject of future work.

4.3.2 Free Vibration

Figure 4.5 displays the tuned natural frequencies versus the number of nodal diameters for the test case rotor in the lower frequency range, as obtained from finite element analysis and ROM analysis. MSC/NASTRAN™ was used to calculate the natural frequencies and mode shapes of the finite element models, and to extract the blade mass and stiffness matrices ($\tilde{\mathbf{M}}_\mathbf{b}$ and $\tilde{\mathbf{K}}_\mathbf{b}$).

Clearly, as the number of nodal diameters increases, the disk becomes much more stiff. Thus, the slanted lines to the left in Fig. 4.5 correspond to disk-dominated modes. The lines which are approximately horizontal represent families of blade-dominated modes.

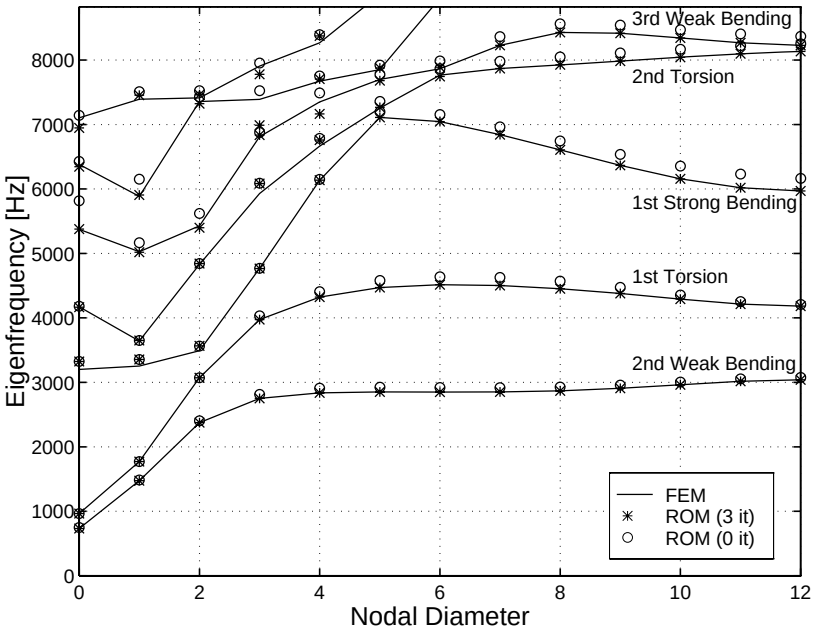

Figure 4.5: Comparison of tuned eigenfrequencies from finite element model (FEM) and reduced order model (ROM) with and without eigenvalue adjustment iterations.

The characteristic types of blade motion for the blade-dominated mode families are indicated in the plot. One can observe that, depending on the mode family, a slight stiffening or a slight softening occurs as the number of nodal diameters increase for the blade-dominated modes. This is somewhat different from the unshrouded case, where the frequencies associated with a certain family of blade-dominated modes are nearly constant over a certain range of nodal diameters.

Figure 4.5 also depicts the increase in ROM accuracy via eigenvalue adjustment. By directly adjusting the eigenvalues, or modal stiffnesses, associated with the blade modes (i.e., the diagonal elements of $\hat{\mathbf{K}}_b$), the ROM's representation of the blade-dominated modes is enhanced.

The adjustment procedure is a simple iterative process, where the cantilever blade

eigenvalues are re-scaled based on the ratio between the tuned finite element eigenvalues from a cyclic symmetry analysis of a complete sector and the corresponding ROM eigenvalues. Once a sufficiently small residual is achieved, one may move on and introduce mistuning. As seen in Fig. 4.5, after three iterations of eigenvalue adjustments, the blade-mode frequencies for the ROM are nearly identical to those of the FEM. Naturally, the adjustments of the cantilever blade mode eigenvalues have a much smaller effect on the disk-dominated modes.

Figure 4.6 illustrates the correlation between finite element and ROM natural frequencies for the mistuned rotor. Since the nodal diameter description of the modes fails for certain mistuned modes due to localization, the natural frequencies are instead plotted versus the mode number in the mistuned case. Again, the results obtained from the reduced order model after eigenvalue adjustments compare very well with the finite element results.

Figure 4.7 illustrates the correlation between finite element and ROM mistuned mode shapes. The Euclidean norm displacement measure, $\bar{u}_i$, for each blade i, is defined as:

$$\bar{u}_i = \left[\frac{\sum_{j=1}^{N_n} \left(u_{ij,r}^2 + u_{ij,\theta}^2 + u_{ij,z}^2 \right)}{\sum_{i=1}^{N_b} \sum_{j=1}^{N_n} \left(u_{ij,r}^2 + u_{ij,\theta}^2 + u_{ij,z}^2 \right)} \right]^{\frac{1}{2}}, \tag{4.27}$$

where $u_{ij,x}$ is the displacement component in the x-direction; N_n is the number of nodes in one blade; and N_b is the total number of blades. The Euclidean norm is a scalar value, which may be interpreted as a measure of relative blade energy content.

Specifically, Fig. 4.7 shows the 17th mistuned mode at 2862 Hz, in which the vibration energy is largely confined to blades 17 and 19. The dramatic mode localization exhibited by this mode is due to the high modal density in this particular frequency region (Pierre [47]). In fact, it is virtually impossible to find any traces of the corresponding smooth harmonic tuned shape from which it derives.

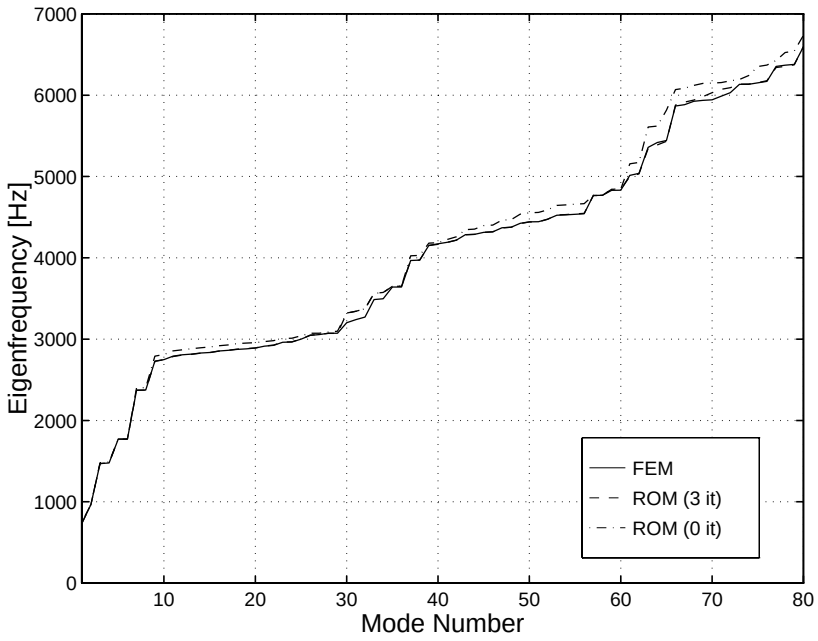

Figure 4.6: Comparison of the 80 lowest mistuned eigenfrequencies from finite element model (FEM) and reduced order model (ROM) with and without eigenvalue adjustment iterations.

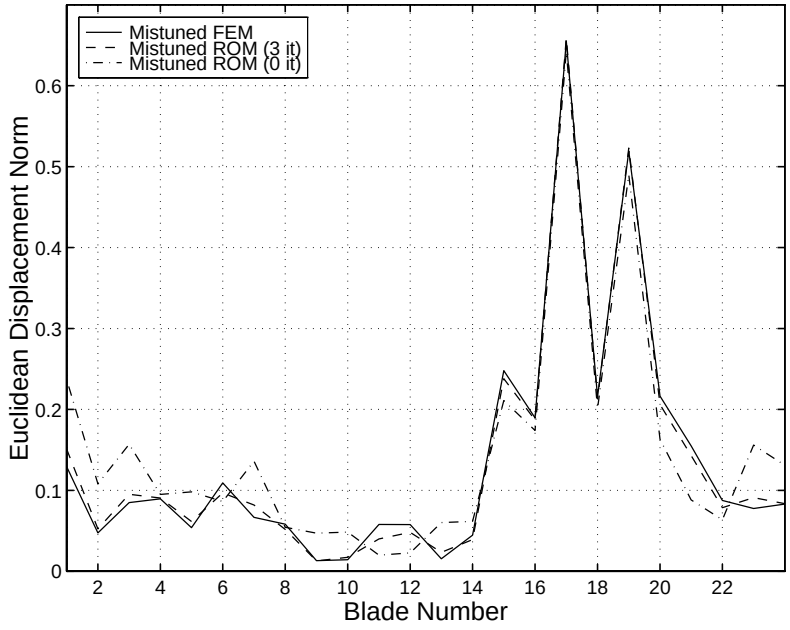

Figure 4.7: Mistuned mode number 17 at 2861.7 Hz, as obtained by finite element model (FEM) and reduced order model (ROM) with and without eigenvalue adjustment iterations. This mode exhibits significant localization.

Note the excellent agreement between the FEM and the ROM mode shapes, especially after eigenvalue adjustment. Several important factors are extremely well captured, such as peak amplitude, position of localization, and rate of spatial decay away from the localized area.

4.3.3 Forced Response

Next, we consider the forced response of the blisk. The external excitation force consists of a unit nodal load applied on the tip of the blade's leading edge in the axial direction. This applied force was chosen arbitrarily, and it serves only to verify the accuracy of the reduced order model. Furthermore, the structure is excited according to engine order 7 excitation, which has a blade-to-blade forcing phase shift of 105°.

The tuned rotor's response to this external forcing is shown in Fig. 4.8. After only two iterations of eigenvalue adjustments, the FEM and ROM predictions of the tuned rotor's response are nearly identical. The difference between the resonant frequencies of the FEM and the ROM is reduced from 2.3% to 0.0007% after these two iterations. Also, the error in peak response amplitude decreases from -3.9% to 0.9%. This amplitude error did not improve during subsequent iterations.

Figure 4.9 shows the response of the mistuned rotor for the same source of excitation. The mistuning and localization effects lead to a substantial increase in peak response amplitude and, in addition, a very significant widening of the resonant frequency bandwidth, compared to the corresponding response of a tuned rotor. In absolute normed displacement values, the maximum resonance amplitude predicted by the ROM is less than 0.2% lower than that predicted by the FEM (0.649 versus 0.650), which is an acceptable discrepancy, considering the huge difference in model sizes.

A notable effect of the order reduction is that the reduced order model here predicts

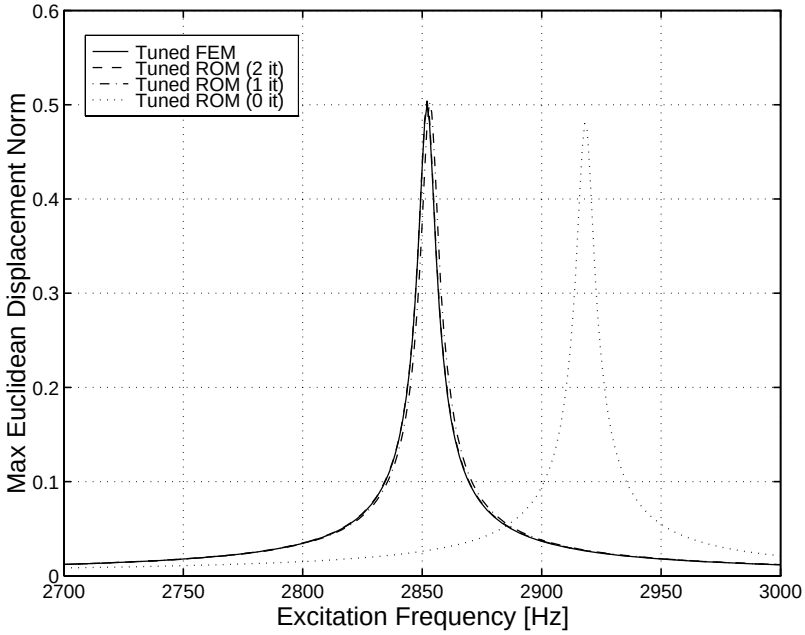

Figure 4.8: Tuned forced response for engine order 7 excitation, as obtained by finite element model (FEM) and reduced order model (ROM) with and without eigenvalue adjustment iterations.

a somewhat wider band of resonant frequencies, compared to the finite element analysis, due to residual errors in the ROM mistuned eigenfrequencies. The ROM mistuned eigenfrequency of the 12th mode is 0.16% lower than the corresponding FEM frequency, while the approximation of the 17th mode eigenfrequency is 0.04% higher. The conformity of the response characteristics predicted by the reduced order model is otherwise reasonably accurate.

4.4 Conclusions

This paper demonstrates how the vibratory behavior of a mistuned bladed disk of a general design may be analyzed by a systematic and computationally efficient reduced order modeling technique, based on a component mode approach. In particular, this work showed how the technique could be extended to designs with shrouded blades, and how a

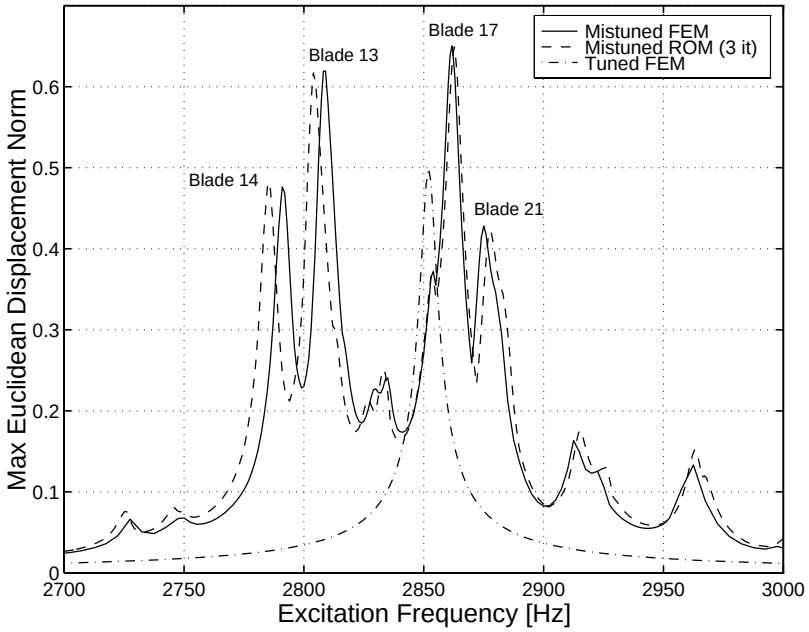

Figure 4.9: Forced response for engine order 7 excitation, for both tuned and mistuned rotor, as obtained by finite element model (FEM) and reduced order model (ROM) with three eigenvalue adjustment iterations. The mistuned FEM has 56,376 degrees of freedom, while the ROM has only 240 degrees of freedom.

convenient measure of individual blade mistuning may be incorporated into the analysis with relative ease. Stiffness mistuning was included by projecting the mistuned natural frequencies of individual blades (with clamped roots and free shrouds) onto the cyclic modes of the shrouded blade assembly.

The reduced order modeling technique and the proposed method of mistuning for shrouded blade assemblies were validated using a finite element model (FEM) of a test case rotor. The total number of degrees of freedom for this FEM was 56,376, compared to only 240 for the reduced order model (ROM). The free and forced response results obtained for the ROM were in excellent agreement with those of the much larger FEM. Of special importance was the agreement of the forced response amplitudes for a rotor with mistuned blades. These results show that this reduced order modeling technique may provide a valuable tool for predicting the statistics of forced response for mistuned bladed disks.

CHAPTER V

Component-Mode-Based Reduced Order Modeling Techniques for Mistuned Bladed Disks, Part I: Theoretical Models

Component mode synthesis (CMS) techniques are widely used for dynamic analyses of complex structures. Significant computational savings can be achieved by using CMS, since a modal analysis is performed on each component structure (substructure). Mistuned bladed disks are a class of structures for which CMS is well suited. In the context of blade mistuning, it is convenient to view the blades as individual components, while the entire disk may be treated as a single component. Individual blade mistuning may then be incorporated into the CMS model in a straightforward manner. In this paper, the Craig-Bampton (C-B) method of CMS is formulated specifically for mistuned bladed disks, using a cyclic disk description. The primary focus, however, is the implementation of novel formulations based on the robust C-B approach. After generating the mass and stiffness matrices using the C-B method, a secondary modal analysis is performed in three different ways: (a) on the partitions of the matrices that pertain to the constraint modes; (b) on the partitions of the matrices that pertain to the disk normal modes *plus* the constraint modes; and (c) on the entire C-B CMS model. All three approaches yield further model order reduction, and they may also eliminate matrix ill-conditioning. Furthermore, these extensions to the

classic C-B technique are applicable to any complex structure. In addition, a straightforward non-CMS method is developed in which the blade mistuning is projected onto the tuned system modes. Though similar approaches have been reported previously, here it is generalized to a form that is more useful in practical applications. The theoretical models are discussed and compared from both computational and practical perspectives. It is concluded that using a secondary modal analysis reduction technique (SMART) based on a C-B model has tremendous potential for highly efficient, accurate modeling of the vibration of mistuned bladed disks.

5.1 Introduction

The adverse effects of structural irregularities, or mistuning, among the blades of turbomachinery rotors is a persisting concern in the gas turbine community. Mistuning is caused by manufacturing tolerances, deviations in material properties, or non-uniform operational wear; therefore, mistuning is unavoidable. Furthermore, even small mistuning can have a dramatic effect on the vibratory behavior of a rotor, because it can lead to spatial localization of the vibration energy. As a result, certain blades may experience forced response amplitudes and stresses that are substantially larger than those predicted by an analysis of the nominal (tuned) design. Unfortunately, these random uncertainties in blade properties, and the immense computational effort involved in obtaining statistically reliable design data, combine to make this aspect of rotor design cumbersome.

Since the 1960s, several researchers have documented the effects of mistuning on blade vibrations by analyses of representative lumped parameter models, using numerical, statistical, and perturbation methods (Wagner [5]; Dye and Henry [6]; Ewins [7, 8]; El-Bayoumy and Srinivasan [9]; Griffin and Hoosac [11]; Wei and Pierre [14, 15]; Lin and Mignolet [13]). See Srinivasan [17] for a comprehensive survey of the literature. Un-

fortunately, in order to accurately represent an actual bladed disk design with a lumped parameter model, one must perform a difficult parameter identification which becomes infeasible as the number of model degrees of freedom (DOF) increases. Hence, to gain practical usefulness, there is a pressing need to employ accurate finite element models of rotor designs in mistuning studies.

To address this issue, there have been several efforts to generate reduced order models systematically from finite element models using component mode synthesis (CMS) methods (Irretier [18]; Kruse and Pierre [21, 22]; Castanier *et al*. [20]; Bladh *et al*. [23]), receptance techniques (Yang and Griffin [26]), and classical modal analysis with mistuning projection (Yang and Griffin [27]). In CMS, the original structure is subdivided into smaller substructures, or components, for which normal modes are computed independently. The global structure is then represented by a truncated set of component modes that are assembled in a systematic fashion through compatibility constraints. This process yields highly-reduced-order models for bladed disks that are based on finite element models of arbitrary complexity.

The focus of this study is on the development of reduced order models of mistuned bladed disks, based primarily on CMS techniques. In this first part of the two-part paper, component-mode-based reduced order modeling techniques are derived and presented. In particular, the Craig-Bampton (C-B) CMS method [29] is re-formulated specifically for the analysis of mistuned bladed disks. This tailored formulation uses a cyclic symmetry description of the disk. Moreover, two novel extensions of the C-B method are formulated. First, a recent advance of the C-B method used in power flow analysis [61] is considered. This approach employs a secondary modal analysis on the constraint-mode partitions of the C-B mass and stiffness matrices. A truncated set of characteristic interface modes is then selected, resulting in significant model reduction. Second, a related extension of the

C-B technique is introduced. In this case, a secondary modal analysis is performed on the disk-normal-mode *plus* constraint-mode partitions with subsequent selection of a truncated set of modes. This yields model reduction comparable to Tan *et al*.'s approach, but is perhaps more straightforward in terms of the secondary mode selection. The obtained reduced order model is similar in appearance to that of Castanier *et al*. [20], having only (modified) disk modes and the normal blade modes as resulting generalized coordinates. The new approaches are by no means restricted to mistuned bladed disks only, but may be applied to any C-B synthesized system for additional model reduction. Furthermore, these novel extensions to the classic C-B technique may eliminate matrix ill-conditioning due to the mix of modal and physical coordinates present in the original C-B formulation.

In addition, a straightforward non-CMS technique is formulated. This method consists of a modal analysis of the nominal (tuned) system, with a subsequent projection of the blade mistuning data onto the nominal system modes of vibration. This mistuning projection approach is a generalization of the mistuning formulation for shrouded blade assemblies developed in Bladh *et al*. [23]. Also, Yang and Griffin [27] presented an analogous technique for the case in which each blade is mistuned by a small deviation in its Young's modulus.

Finally, the general idea of a secondary modal analysis reduction technique (SMART) is introduced. In the SMART approach, a secondary modal analysis is performed on a model already reduced by CMS. This two-step reduction decreases dramatically the order of the original model. Also, in contrast to the non-CMS mistuning projection method, the SMART mistuning is introduced in the modal domain rather than the physical domain. This reduces significantly the associated computational effort, and it allows a straightforward implementation of individual blade natural frequency mistuning.

This paper is organized as follows. General assumptions and model issues are sum-

marized in Section 5.2. The modeling theory begins in Section 5.3 with a derivation of the Craig-Bampton technique tailored to a mistuned rotor with a cyclic symmetry description of the disk. Section 5.4 outlines the two related extensions of the Craig-Bampton technique employing partial secondary modal analyses. In Section 5.5, the method of Castanier *et al*. [20], which uses a prescribed interface motion approach, is reviewed. In Section 5.6, the mistuning projection method is outlined. In Section 5.7, the secondary modal analysis reduction technique is formulated for mistuned rotors using the C-B method for the intermediate model. In Section 5.8, a comparison is presented of the number of floating point operations required for the various methods. The conclusions are summarized in Section 5.9.

5.2 Computational Issues and Assumptions

An N-bladed disk assembly can be divided into one disk component (d) and N individual blades (b). It is assumed that the disk features cyclic symmetry, meaning that it is composed of N identical sectors. A disk sector and a blade component are depicted in Fig. 5.1, which also outlines the index notation used throughout this paper for the components and the interfaces with neighboring components.

Initially, it is assumed that each disk sector or blade is an identical (tuned) and physically isolated substructure. At this point, the stiffness matrix of all disk sectors and blades, $\mathcal{K}$, has a block-diagonal structure:

$$\mathcal{K} = \begin{bmatrix} \mathcal{K}^{\mathbf{d}} & \mathbf{0} \\ \mathbf{0} & \mathcal{K}^{\mathbf{b}} \end{bmatrix} = \begin{bmatrix} \mathbf{I} \otimes \mathbf{K}^{\mathbf{d}} & \mathbf{0} \\ \mathbf{0} & \mathbf{I} \otimes \mathbf{K}^{\mathbf{b}} \end{bmatrix}, \tag{5.1}$$

where $\mathbf{I}$ is an identity matrix of dimension N, the symbol $\otimes$ denotes the Kronecker product (see Appendix A), and $\mathbf{K}^{\mathbf{d}}$ (disk) and $\mathbf{K}^{\mathbf{b}}$ (blade) are the stiffness matrices of the two fundamental, stand-alone substructures. Using the notation of Fig. 5.1, the displacement

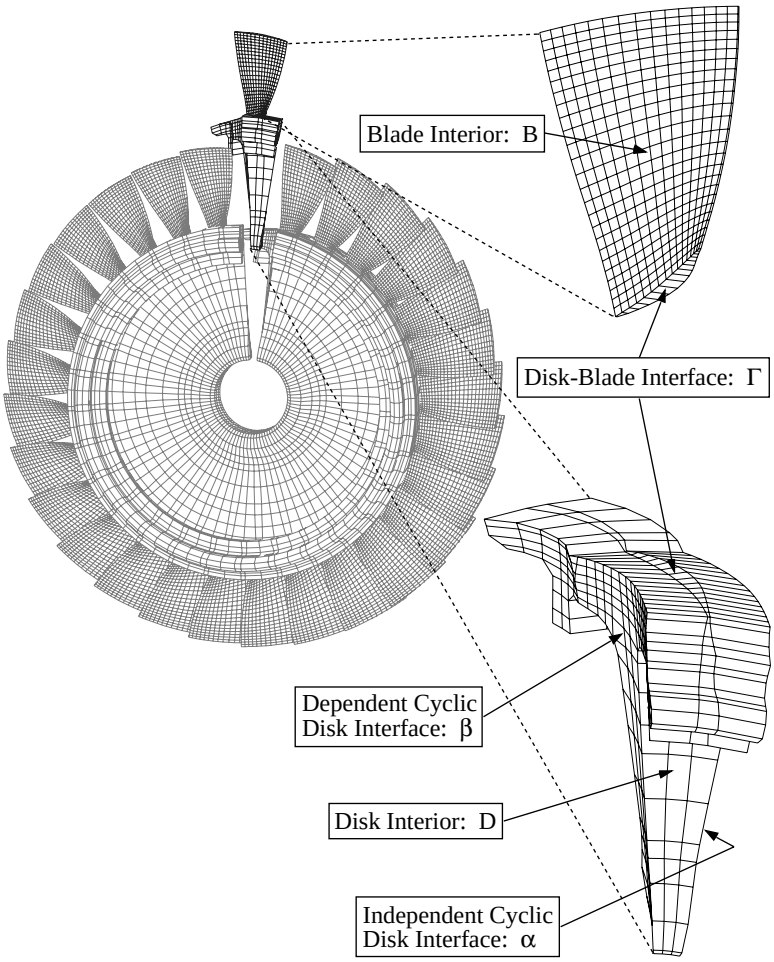

Figure 5.1: Substructuring approach and index notation.

vectors and the corresponding stiffness matrices may be partitioned in detail as

$$\mathbf{x^d} = \begin{Bmatrix} \mathbf{x^d_D} \\ \mathbf{x^d_\Gamma} \\ \mathbf{x^d_\alpha} \\ \mathbf{x^d_\beta} \end{Bmatrix} \quad \mathbf{K^d} = \begin{bmatrix} \mathbf{K^d_{DD}} & \mathbf{K^d_{D\Gamma}} & \mathbf{K^d_{D\alpha}} & \mathbf{K^d_{D\beta}} \\ \mathbf{K^{d^T}_{D\Gamma}} & \mathbf{K^d_{\Gamma\Gamma}} & \mathbf{K^d_{\Gamma\alpha}} & \mathbf{K^d_{\Gamma\beta}} \\ \mathbf{K^{d^T}_{D\alpha}} & \mathbf{K^{d^T}_{\Gamma\alpha}} & \mathbf{K^d_{\alpha\alpha}} & \mathbf{K^d_{\alpha\beta}} \\ \mathbf{K^{d^T}_{D\beta}} & \mathbf{K^{d^T}_{\Gamma\beta}} & \mathbf{K^{d^T}_{\alpha\beta}} & \mathbf{K^d_{\beta\beta}} \end{bmatrix} \tag{5.2}$$

$$\mathbf{x^b} = \begin{Bmatrix} \mathbf{x^b_B} \\ \mathbf{x^b_\Gamma} \end{Bmatrix} \quad \mathbf{K^b} = \begin{bmatrix} \mathbf{K^b_{BB}} & \mathbf{K^b_{B\Gamma}} \\ \mathbf{K^{b^T}_{B\Gamma}} & \mathbf{K^b_{\Gamma\Gamma}} \end{bmatrix}. \tag{5.3}$$

The mass matrices are partitioned in exactly the same fashion.

5.2.1 Cyclic Symmetry Description of the Disk Component

The treatment of the disk component is greatly simplified by using a cyclic symmetry analysis. There are two principal benefits from treating the disk as a cyclic assembly rather than an assembly of N arbitrary components. First, the DOF at each interface between adjacent disk sectors are eliminated by cyclic constraints, which yields a smaller CMS model. Second, the disk component mode shapes bear a greater resemblance to the system modes, which improves modal convergence.

The cyclic symmetry analysis employed here is identical to the implementation in the commercial finite element software package MSC/NASTRAN™. This approach is a real-valued formulation, and it was outlined by Joseph [43]. From the theory of symmetrical components (Fortescue [44]) some quantity $\mathbf{x}$ (displacements, forces, etc.) in physical coordinates for all N disk sectors may be expressed as a linear combination of the corresponding quantity $\tilde{\mathbf{u}}$ in cyclic coordinates for the fundamental disk sector as

$$\mathbf{x} = \begin{Bmatrix} \mathbf{x_1} \\ \mathbf{x_2} \\ \mathbf{x_3} \\ \vdots \\ \mathbf{x_N} \end{Bmatrix} = (\mathbf{F} \otimes \mathbf{I}) \begin{Bmatrix} \tilde{\mathbf{u}}^{\mathbf{0}} \\ \tilde{\mathbf{u}}^{\mathbf{1,c}} \\ \tilde{\mathbf{u}}^{\mathbf{1,s}} \\ \tilde{\mathbf{u}}^{\mathbf{2,c}} \\ \vdots \\ \tilde{\mathbf{u}}^{\mathbf{P}} \end{Bmatrix} = \hat{\mathbf{F}}\tilde{\mathbf{u}}, \tag{5.4}$$

where $\mathbf{F}$ is the real-valued Fourier matrix defined in Appendix B. Moreover, the dimension of $\mathbf{I}$ is equal to the number of elements in $\tilde{\mathbf{u}}^{\mathbf{h}}$, h represents the harmonic order, and P is the highest possible harmonic for an N-bladed disk, which is defined as $P = \mathbf{int}\,[N/2]$. The "tilde" notation is used throughout this paper to indicate when a quantity is represented in cyclic coordinates. The cyclic coordinate representation is essentially a Fourier series expansion of the disk motion. However, it is *not* an approximation, as the series contains

the complete set of admissible circumferential shapes of the cyclic assembly.

The cyclic coordinate transformation of Eq. (5.4) yields a set of trigonometric relations that describe the motion of the disk sector's dependent cyclic boundary (β) relative to the independent cyclic boundary (α) as follows:

$$\begin{cases} \tilde{\mathbf{u}}_{\beta}^{\mathbf{h,c}} = \tilde{\mathbf{u}}_{\alpha}^{\mathbf{h,c}} \cos\phi_h + \tilde{\mathbf{u}}_{\alpha}^{\mathbf{h,s}} \sin\phi_h \\ \tilde{\mathbf{u}}_{\beta}^{\mathbf{h,s}} = -\tilde{\mathbf{u}}_{\alpha}^{\mathbf{h,c}} \sin\phi_h + \tilde{\mathbf{u}}_{\alpha}^{\mathbf{h,s}} \cos\phi_h \end{cases} \qquad h = 0, \ldots, P, \tag{5.5}$$

where $\phi_h = 2\pi h/N$ is the interblade phase angle for the h^{th} harmonic. Note that the two equations in Eq. (5.5) collapse to one for harmonics 0 and, if it exists, $N/2$. These are "single" harmonics and require only a single sector description, as in Eq. (5.2). All other harmonics are "double" and require a two-sector description:

$$\mathbf{K}_{\mathbf{2x}}^{\mathbf{d}} = \begin{bmatrix} \mathbf{K^d} & \mathbf{0} \\ \mathbf{0} & \mathbf{K^d} \end{bmatrix}. \tag{5.6}$$

For generality, a "double" harmonic is considered below. By enforcing Eq. (5.5) on the double disk sector's stiffness matrix in Eq. (5.6), the dependent β DOF are eliminated. Moreover, for the disk's subsequent CMS implementation, it is necessary to partition with respect to interior (D and α) DOF—which are collectively denoted Sector (S) DOF—and disk-blade interface (Γ) DOF. With this in mind, the cyclic disk stiffness matrix and displacement vector of harmonic h ($h \neq 0, h \neq N/2$) may be written as

$$\tilde{\mathbf{K}}_{\mathbf{d}}^{\mathbf{h}} = \begin{bmatrix} \tilde{\mathbf{K}}_{\mathbf{d,SS}}^{\mathbf{h}} & \tilde{\mathbf{K}}_{\mathbf{d,S\Gamma}}^{\mathbf{h}} \\ \\ \tilde{\mathbf{K}}_{\mathbf{d,S\Gamma}}^{\mathbf{h^T}} & \tilde{\mathbf{K}}_{\mathbf{d,\Gamma\Gamma}}^{\mathbf{h}} \end{bmatrix} \qquad \tilde{\mathbf{u}}_{\mathbf{d}}^{\mathbf{h}} = \begin{Bmatrix} \tilde{\mathbf{u}}_{\mathbf{S}}^{\mathbf{h,c}} \\ \tilde{\mathbf{u}}_{\mathbf{S}}^{\mathbf{h,s}} \\ \ldots \\ \tilde{\mathbf{u}}_{\mathbf{\Gamma}}^{\mathbf{h,c}} \\ \tilde{\mathbf{u}}_{\mathbf{\Gamma}}^{\mathbf{h,s}} \end{Bmatrix}. \tag{5.7}$$

The interior (SS) partition is sub-partitioned as

$$\tilde{\mathbf{K}}^{\mathbf{h}}_{\mathbf{d,SS}} = \begin{bmatrix} \tilde{\mathbf{K}}^{\mathbf{h,0}}_{\mathbf{d,SS}} & \tilde{\mathbf{K}}^{\mathbf{h,1}}_{\mathbf{d,SS}} \\ \\ \tilde{\mathbf{K}}^{\mathbf{h,1^T}}_{\mathbf{d,SS}} & \tilde{\mathbf{K}}^{\mathbf{h,0}}_{\mathbf{d,SS}} \end{bmatrix}, \tag{5.8}$$

where

$$\tilde{\mathbf{K}}^{\mathbf{h,0}}_{\mathbf{d,SS}} = \begin{bmatrix} \mathbf{K}^{\mathbf{d}}_{\alpha\alpha} + \left(\mathbf{K}^{\mathbf{d}}_{\alpha\beta} + \mathbf{K}^{\mathbf{d^T}}_{\alpha\beta}\right)\cos\phi_h + \mathbf{K}^{\mathbf{d}}_{\beta\beta} & \mathbf{K}^{\mathbf{d^T}}_{\mathbf{D}\alpha} + \mathbf{K}^{\mathbf{d^T}}_{\mathbf{D}\beta}\cos\phi_h \\ \mathbf{K}^{\mathbf{d}}_{\mathbf{D}\alpha} + \mathbf{K}^{\mathbf{d}}_{\mathbf{D}\beta}\cos\phi_h & \mathbf{K}^{\mathbf{d}}_{\mathbf{DD}} \end{bmatrix} \tag{5.9}$$

$$\tilde{\mathbf{K}}^{\mathbf{h,1}}_{\mathbf{d,SS}} = \begin{bmatrix} \left(\mathbf{K}^{\mathbf{d}}_{\alpha\beta} - \mathbf{K}^{\mathbf{d^T}}_{\alpha\beta}\right)\sin\phi_h & -\mathbf{K}^{\mathbf{d^T}}_{\mathbf{D}\beta}\sin\phi_h \\ \mathbf{K}^{\mathbf{d}}_{\mathbf{D}\beta}\sin\phi_h & \mathbf{0} \end{bmatrix}. \tag{5.10}$$

The remaining partitions (SΓ and $\Gamma\Gamma$) take on the following forms:

$$\tilde{\mathbf{K}}^{\mathbf{h}}_{\mathbf{d,S\Gamma}} = \begin{bmatrix} \mathbf{K}^{\mathbf{d^T}}_{\mathbf{\Gamma}\alpha} + \mathbf{K}^{\mathbf{d^T}}_{\mathbf{\Gamma}\beta}\cos\phi_h & -\mathbf{K}^{\mathbf{d^T}}_{\mathbf{\Gamma}\beta}\sin\phi_h \\ \mathbf{K}^{\mathbf{d}}_{\mathbf{D\Gamma}} & \mathbf{0} \\ \mathbf{K}^{\mathbf{d^T}}_{\mathbf{\Gamma}\beta}\sin\phi_h & \mathbf{K}^{\mathbf{d^T}}_{\mathbf{\Gamma}\alpha} + \mathbf{K}^{\mathbf{d^T}}_{\mathbf{\Gamma}\beta}\cos\phi_h \\ \mathbf{0} & \mathbf{K}^{\mathbf{d}}_{\mathbf{D\Gamma}} \end{bmatrix} \tag{5.11}$$

$$\tilde{\mathbf{K}}^{\mathbf{h}}_{\mathbf{d,\Gamma\Gamma}} = \begin{bmatrix} \mathbf{K}^{\mathbf{d}}_{\mathbf{\Gamma\Gamma}} & \mathbf{0} \\ \\ \mathbf{0} & \mathbf{K}^{\mathbf{d}}_{\mathbf{\Gamma\Gamma}} \end{bmatrix}. \tag{5.12}$$

Note that for $h = 0$ and, if it exists, for $h = N/2$, the "sine blocks" are zero. By rearranging the DOF order in this case, two identical blocks form on the diagonal of $\tilde{\mathbf{K}}^{\mathbf{h}}_{\mathbf{d}}$, while the off-diagonal block is zero. Thus, as indicated earlier, one such block on the diagonal alone provides the complete disk description in these two special cases. The corresponding cyclic disk partitions for "single" harmonics are given by:

$$\tilde{\mathbf{K}}^{\mathbf{h}}_{\mathbf{d,SS}} = \begin{bmatrix} \mathbf{K}^{\mathbf{d}}_{\alpha\alpha} + \left(\mathbf{K}^{\mathbf{d}}_{\alpha\beta} + \mathbf{K}^{\mathbf{d^T}}_{\alpha\beta}\right)\cos\phi_h + \mathbf{K}^{\mathbf{d}}_{\beta\beta} & \mathbf{K}^{\mathbf{d^T}}_{\mathbf{D}\alpha} + \mathbf{K}^{\mathbf{d^T}}_{\mathbf{D}\beta}\cos\phi_h \\ \mathbf{K}^{\mathbf{d}}_{\mathbf{D}\alpha} + \mathbf{K}^{\mathbf{d}}_{\mathbf{D}\beta}\cos\phi_h & \mathbf{K}^{\mathbf{d}}_{\mathbf{DD}} \end{bmatrix} \tag{5.13}$$

$$\tilde{\mathbf{K}}^{\mathbf{h}}_{\mathbf{d},\mathbf{S\Gamma}} = \begin{bmatrix} \mathbf{K}^{\mathbf{d^T}}_{\mathbf{\Gamma}\alpha} + \mathbf{K}^{\mathbf{d^T}}_{\mathbf{\Gamma}\beta}\cos\phi_h \\ \mathbf{K}^{\mathbf{d}}_{\mathbf{D\Gamma}} \end{bmatrix} \qquad \tilde{\mathbf{K}}^{\mathbf{k}}_{\mathbf{d},\mathbf{\Gamma\Gamma}} = \mathbf{K}^{\mathbf{d}}_{\mathbf{\Gamma\Gamma}}. \tag{5.14}$$

Again, the manipulations of the mass matrix are completely analogous.

5.2.2 Engine Order Excitation Force

In this section, an external excitation force vector, $\mathbf{Q}$, is constructed for all the blade DOF of the assembly. The restriction to blade DOF is not an absolute requirement, but it leads to a more compact formulation, and it should be sufficient from a practical perspective. An engine order excitation is assumed, which is harmonic in time and differs only in phase from blade to blade. The phase at the n^{th} blade, φ_n, is given by:

$$\varphi_n = \frac{2\pi C(n-1)}{N}, \tag{5.15}$$

where C is the engine order of the excitation. The external force vector can then be expressed as:

$$\mathbf{Q} = \begin{Bmatrix} \mathbf{Q_B} \\ \mathbf{Q_\Gamma} \end{Bmatrix} = \begin{Bmatrix} \sqrt{N}\mathbf{e_{C+1}} \otimes \mathbf{f_B} \\ \sqrt{N}\mathbf{e_{C+1}} \otimes \mathbf{f_\Gamma} \end{Bmatrix}, \tag{5.16}$$

where $\mathbf{e_{C+1}}$ is the $(C+1)^{\text{th}}$ column of the complex Fourier matrix defined in Appendix B. The column vectors $\mathbf{f_B}$ and $\mathbf{f_\Gamma}$ contain the forces on, respectively, the interior and interface DOF of a fundamental blade.

5.2.3 Mistuning Implementation

In this work, the blade mistuning is modeled by offsets in modal stiffnesses Λ — or, equivalently, offsets in natural frequencies ω — of the blades while fixed at the base (cantilevered). The mistuned modal stiffness of the k^{th} cantilevered blade mode for the n^{th} blade may be expressed as

$$\bar{\Lambda}^k_{b,n} = \left(\bar{\omega}^k_{b,n}\right)^2 = \left(1+\delta^k_n\right)\Lambda^k_b, \tag{5.17}$$

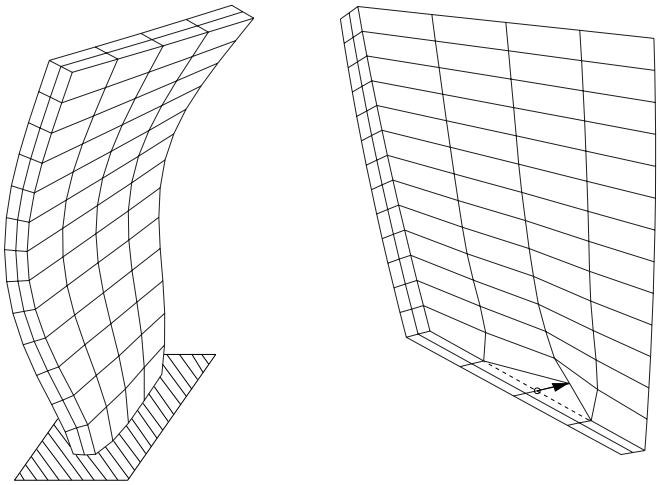

(a) (b)

Figure 5.2: Craig-Bampton component modes: (a) fixed-interface normal modes of vibration; (b) static constraint modes due to successive unit deflections of interface DOF.

where Λ_b^k is the modal stiffness of the k^{th} tuned cantilevered blade mode, and δ_n^k is the corresponding mistuning parameter for the n^{th} blade. Note that this implies that the mistuned modes of a blade may be realized by a linear combination of the tuned modes (i.e., it is assumed that they span the same space). Also, note that it is assumed throughout this paper that mode shapes are normalized to yield unit modal masses.

Due to simple implementation and validation, most of the published studies on mistuned bladed disks have considered variations in Young's modulus as the only source of blade mistuning. This implies a uniform re-scaling of the blade stiffness matrix, which translates into a uniform re-scaling of the modal stiffnesses as well. The mistuning parameter δ_n^k in Eq. (5.17) is then replaced by δ_n, which represents the offset of Young's modulus from its nominal value for the n^{th} blade.

5.3 Fixed Interface Method (Craig-Bampton)

The Craig-Bampton (C-B) method [29, 62, 24] employs two sets of modes to represent the motion of each component:

- $\mathbf{\Phi}$, a truncated set of normal elastic modes of vibration with the DOF at component interfaces held fixed (see Fig. 5.2a)
- $\mathbf{\Psi}$, a complete set of static elastic constraint modes induced by successive unit deflections of each interface DOF while all other interface DOF are held fixed (see Fig. 5.2b)

The modes in $\mathbf{\Phi}$ are linearly independent by definition, and the manner in which the interface DOF are successively displaced ensures linear independence among the constraint modes in $\mathbf{\Psi}$, as well as linear independence between the two mode sets. Furthermore, if all modes are retained, the number of modes in $\mathbf{\Phi}$ will equal the total number of interior DOF in the component. By construction, the number of modes in $\mathbf{\Psi}$ always equals the number of interface DOF. Hence, in the limit, linear independence and completeness combine to yield the exact solution for the C-B method relative to the parent finite element model (i.e., it spans the complete deformation space of the finite element model).

The following subsections outline the assembly of the C-B model as applied to mistuned bladed disks with a cyclic disk description, as well as two reduced order model formulations that derive from the former.

5.3.1 Blade Component

For now, all N blades are assumed to be identical (tuned). Furthermore, from a component perspective, the blades are not directly coupled, since only unshrouded blades are considered in this study. Hence, for computing the component quantities, it is sufficient to

look at a single blade and then expand to N blades.

First, the normal modes for the cantilevered blade are obtained from the conventional eigenvalue problem:

$$\left[\mathbf{K}^{\mathbf{b}}_{\mathbf{BB}} - \omega^2 \mathbf{M}^{\mathbf{b}}_{\mathbf{BB}}\right] \phi_{\mathbf{b}} = \mathbf{0}. \tag{5.18}$$

The mode shapes $\phi_{\mathbf{b}}$ of interest are collected into a matrix $\mathbf{\Phi_b}$, and the corresponding eigenvalues form the elements in a diagonal matrix $\mathbf{\Lambda_b}$. Second, the constraint modes, $\mathbf{\Psi_b}$, are computed from the static problem

$$\begin{bmatrix} \mathbf{K}^{\mathbf{b}}_{\mathbf{BB}} & \mathbf{K}^{\mathbf{b}}_{\mathbf{B\Gamma}} \\ \mathbf{K}^{\mathbf{b^T}}_{\mathbf{B\Gamma}} & \mathbf{K}^{\mathbf{b}}_{\mathbf{\Gamma\Gamma}} \end{bmatrix} \begin{bmatrix} \mathbf{\Psi_b} \\ \mathbf{I} \end{bmatrix} = \begin{bmatrix} \mathbf{0} \\ \mathbf{R_\Gamma} \end{bmatrix}, \tag{5.19}$$

where $\mathbf{R_\Gamma}$ contains the reaction forces due to the imposed unit displacements, $\mathbf{I}$. Solving the first block of equations in Eq. (5.19) yields:

$$\mathbf{\Psi_b} = -\mathbf{K}^{\mathbf{b^{-1}}}_{\mathbf{BB}} \mathbf{K}^{\mathbf{b}}_{\mathbf{B\Gamma}}. \tag{5.20}$$

Note that the matrix inverse need not be computed, since the columns of $\mathbf{\Psi_b}$ are the solution vectors $\mathbf{x}$ of $\mathbf{K}^{\mathbf{b}}_{\mathbf{BB}}\mathbf{x} = -\mathbf{K}^{\mathbf{b}}_{\mathbf{B\Gamma}}$.

The physical blade displacements can now be expressed in terms of the two sets of component modes, which form the traditional Craig-Bampton modal matrix, $\mathbf{U}^{\mathbf{b}}_{\mathbf{cb}}$, as

$$\mathbf{x^b} = \begin{Bmatrix} \mathbf{x}^{\mathbf{b}}_{\mathbf{B}} \\ \mathbf{x}^{\mathbf{b}}_{\mathbf{\Gamma}} \end{Bmatrix} = \begin{bmatrix} \mathbf{\Phi_b} & \mathbf{\Psi_b} \\ \mathbf{0} & \mathbf{I} \end{bmatrix} \begin{Bmatrix} \mathbf{p}^{\mathbf{b}}_{\mathbf{b}} \\ \mathbf{p}^{\mathbf{b}}_{\mathbf{c}} \end{Bmatrix} = \mathbf{U}^{\mathbf{b}}_{\mathbf{cb}} \mathbf{p^b}. \tag{5.21}$$

The transformation from physical blade coordinates $\mathbf{x^b}$ to C-B blade modal coordinates $\mathbf{p^b}$ via $\mathbf{U}^{\mathbf{b}}_{\mathbf{cb}}$ yields the reduced C-B mass and stiffness matrices for the blade component:

$$\begin{aligned} \mu^{\mathbf{b}} &= \mathbf{U}^{\mathbf{b^T}}_{\mathbf{cb}} \mathbf{M^b} \mathbf{U}^{\mathbf{b}}_{\mathbf{cb}} = \begin{bmatrix} \mathbf{I} & \mu_{\mathbf{bc}} \\ \mu^{\mathbf{T}}_{\mathbf{bc}} & \mu_{\mathbf{cc,b}} \end{bmatrix} \\ \kappa^{\mathbf{b}} &= \mathbf{U}^{\mathbf{b^T}}_{\mathbf{cb}} \mathbf{K^b} \mathbf{U}^{\mathbf{b}}_{\mathbf{cb}} = \begin{bmatrix} \mathbf{\Lambda_b} & \mathbf{0} \\ \mathbf{0} & \kappa_{\mathbf{cc,b}} \end{bmatrix}, \end{aligned} \tag{5.22}$$

where

$$\begin{aligned}
\mu_{\mathbf{bc}} &= \mathbf{\Phi_b^T}\left[\mathbf{M_{BB}^b\Psi_b + M_{B\Gamma}^b}\right] \\
\mu_{\mathbf{cc,b}} &= \mathbf{\Psi_b^T}\left[\mathbf{M_{BB}^b\Psi_b + M_{B\Gamma}^b}\right] + \mathbf{M_{B\Gamma}^{b^T}\Psi_b + M_{\Gamma\Gamma}^b} \\
\kappa_{\mathbf{cc,b}} &= \mathbf{K_{\Gamma\Gamma}^b + K_{B\Gamma}^{b^T}\Psi_b}.
\end{aligned}$$

In the absence of direct blade-to-blade structural coupling, Eq. (5.22) is expanded for all N blades as

$$\bar{\mu}^{\mathbf{b}} = \begin{bmatrix} \mathbf{I} & \mathbf{I}\otimes\mu_{\mathbf{bc}} \\ \mathbf{I}\otimes\mu_{\mathbf{bc}}^{\mathbf{T}} & \mathbf{I}\otimes\mu_{\mathbf{cc,b}} \end{bmatrix} \qquad \bar{\kappa}^{\mathbf{b}} = \begin{bmatrix} \mathbf{I}\otimes\mathbf{\Lambda_b} & \mathbf{0} \\ \mathbf{0} & \mathbf{I}\otimes\kappa_{\mathbf{cc,b}} \end{bmatrix}. \tag{5.23}$$

5.3.2 Cyclic Disk Component

The construction of the required quantities for the disk component is more computationally intensive than for the blade component, although the steps are the same. For the setup of the cyclic structural matrices involved, the reader is referred to Section 5.2.1, Eqs. (5.7)–(5.14).

To begin, the cyclic normal modes for the disk component are obtained for each harmonic h from the cyclic eigenvalue problem:

$$\left[\tilde{\mathbf{K}}_{\mathbf{d,SS}}^{\mathbf{h}} - \omega^2\tilde{\mathbf{M}}_{\mathbf{d,SS}}^{\mathbf{h}}\right]\tilde{\phi}_{\mathbf{d}}^{\mathbf{h}} = \mathbf{0}, \qquad h = 0,\ldots,P. \tag{5.24}$$

Moreover, the cyclic constraint modes, $\tilde{\mathbf{\Psi}}_{\mathbf{d}}^{\mathbf{h}}$, are computed for each harmonic h from the cyclic static problem

$$\begin{bmatrix} \tilde{\mathbf{K}}_{\mathbf{d,SS}}^{\mathbf{h}} & \tilde{\mathbf{K}}_{\mathbf{d,S\Gamma}}^{\mathbf{h}} \\ \tilde{\mathbf{K}}_{\mathbf{d,S\Gamma}}^{\mathbf{h^T}} & \tilde{\mathbf{K}}_{\mathbf{d,\Gamma\Gamma}}^{\mathbf{h}} \end{bmatrix}\begin{bmatrix} \tilde{\mathbf{\Psi}}_{\mathbf{d}}^{\mathbf{h}} \\ \mathbf{I} \end{bmatrix} = \begin{bmatrix} \mathbf{0} \\ \mathbf{R}_{\mathbf{\Gamma}}^{\mathbf{h}} \end{bmatrix}. \tag{5.25}$$

Again, solving the first block of equations in Eq. (5.25) for the cyclic disk constraint modes yields

$$\tilde{\mathbf{\Psi}}_{\mathbf{d}}^{\mathbf{h}} = -\tilde{\mathbf{K}}_{\mathbf{d,SS}}^{\mathbf{h^{-1}}}\tilde{\mathbf{K}}_{\mathbf{d,S\Gamma}}^{\mathbf{h}}. \tag{5.26}$$

While keeping normal and constraint modes separated, the retained cyclic normal modes and the cyclic constraint modes of the disk are merged into a cyclic Craig-Bampton modal matrix, $\tilde{\mathbf{U}}^{\mathbf{d}}_{\mathbf{cb}}$, as

$$\tilde{\mathbf{U}}^{\mathbf{d}}_{\mathbf{cb}} = \begin{bmatrix} \tilde{\mathbf{B}}\mathbf{diag}_{h=0,\ldots,P}\left[\tilde{\mathbf{\Phi}}^{\mathbf{h}}_{\mathbf{d}}\right] & \tilde{\mathbf{B}}\mathbf{diag}_{h=0,\ldots,P}\left[\tilde{\mathbf{\Psi}}^{\mathbf{h}}_{\mathbf{d}}\right] \\ \mathbf{0} & \mathbf{I} \end{bmatrix}, \tag{5.27}$$

where $\tilde{\mathbf{B}}\mathbf{diag}\left[\bullet\right]$ denotes a pseudo-block-diagonal matrix (see Appendix B), with the argument being the h^{th} "block", and the range of h is shown. In this context, the h^{th} "block" pertains to the h^{th} harmonic. Similarly, the eigenvalues corresponding to the retained cyclic normal modes form the elements in a pseudo-block-diagonal generalized stiffness matrix $\tilde{\mathbf{\Lambda}}_{\mathbf{d}}$, where each block is diagonal in itself.

Using Eq. (5.27), the physical disk displacements can now be expressed in terms of the two sets of cyclic component modes by virtue of Eq. (5.4):

$$\bar{\mathbf{x}}^{\mathbf{d}} = \begin{Bmatrix} \bar{\mathbf{x}}^{\mathbf{d}}_{\mathbf{D}} \\ \bar{\mathbf{x}}^{\mathbf{d}}_{\mathbf{\Gamma}} \end{Bmatrix} = \mathbf{U}^{\mathbf{d}}_{\mathbf{cb}} \begin{Bmatrix} \tilde{\mathbf{p}}^{\mathbf{d}}_{\mathbf{d}} \\ \tilde{\mathbf{p}}^{\mathbf{d}}_{\mathbf{c}} \end{Bmatrix} = \mathbf{U}^{\mathbf{d}}_{\mathbf{cb}} \tilde{\mathbf{p}}^{\mathbf{d}}. \tag{5.28}$$

where

$$\mathbf{U}^{\mathbf{d}}_{\mathbf{cb}} = \begin{bmatrix} \hat{\mathbf{F}}\tilde{\mathbf{B}}\mathbf{diag}_{h=0,\ldots,P}\left[\tilde{\mathbf{\Phi}}^{\mathbf{h}}_{\mathbf{d}}\right] & \hat{\mathbf{F}}\tilde{\mathbf{B}}\mathbf{diag}_{h=0,\ldots,P}\left[\tilde{\mathbf{\Psi}}^{\mathbf{h}}_{\mathbf{d}}\right] \\ \mathbf{0} & \hat{\mathbf{F}} \end{bmatrix}. \tag{5.29}$$

The transformation from physical disk coordinates $\bar{\mathbf{x}}^{\mathbf{d}}$ to C-B cyclic disk coordinates $\tilde{\mathbf{p}}^{\mathbf{d}}$ via $\mathbf{U}^{\mathbf{d}}_{\mathbf{cb}}$ yields the reduced C-B mass and stiffness matrices for the disk component:

$$\tilde{\mu}^{\mathbf{d}} = \begin{bmatrix} \mathbf{I} & \tilde{\mu}_{\mathbf{dc}} \\ \tilde{\mu}^{\mathbf{T}}_{\mathbf{dc}} & \tilde{\mu}_{\mathbf{cc,d}} \end{bmatrix} \qquad \tilde{\kappa}^{\mathbf{d}} = \begin{bmatrix} \tilde{\mathbf{\Lambda}}_{\mathbf{d}} & \mathbf{0} \\ \mathbf{0} & \tilde{\kappa}_{\mathbf{cc,d}} \end{bmatrix}, \tag{5.30}$$

where

$$\begin{aligned} \tilde{\mu}_{\mathbf{dc}} &= \tilde{\mathbf{B}}\mathbf{diag}_{h=0,\ldots,P}\left[\tilde{\mathbf{\Phi}}^{\mathbf{h}^{\mathbf{T}}}_{\mathbf{d}}\left[\tilde{\mathbf{M}}^{\mathbf{h}}_{\mathbf{d,ss}}\tilde{\mathbf{\Psi}}^{\mathbf{h}}_{\mathbf{d}} + \tilde{\mathbf{M}}^{\mathbf{h}}_{\mathbf{d,s\Gamma}}\right]\right] \\ \tilde{\mu}_{\mathbf{cc,d}} &= \tilde{\mathbf{B}}\mathbf{diag}_{h=0,\ldots,P}\left[\tilde{\mathbf{\Psi}}^{\mathbf{h}^{\mathbf{T}}}_{\mathbf{d}}\left[\tilde{\mathbf{M}}^{\mathbf{h}}_{\mathbf{d,ss}}\tilde{\mathbf{\Psi}}^{\mathbf{h}}_{\mathbf{d}} + \tilde{\mathbf{M}}^{\mathbf{h}}_{\mathbf{d,s\Gamma}}\right] + \tilde{\mathbf{M}}^{\mathbf{h}^{\mathbf{T}}}_{\mathbf{d,s\Gamma}}\tilde{\mathbf{\Psi}}^{\mathbf{h}}_{\mathbf{d}} + \tilde{\mathbf{M}}^{\mathbf{h}}_{\mathbf{d,\Gamma\Gamma}}\right] \\ \tilde{\kappa}_{\mathbf{cc,d}} &= \tilde{\mathbf{B}}\mathbf{diag}_{h=0,\ldots,P}\left[\mathbf{K}^{\mathbf{h}}_{\mathbf{d,\Gamma\Gamma}} + \mathbf{K}^{\mathbf{h}^{\mathbf{T}}}_{\mathbf{d,s\Gamma}}\mathbf{\Psi}^{\mathbf{h}}_{\mathbf{d}}\right]. \end{aligned}$$

Note that there is no coupling between the harmonics due to the orthogonality of the cyclic modes.

5.3.3 CMS Model Assembly

In the Craig-Bampton method, the CMS model assembly is achieved by satisfying displacement compatibility over the component interfaces, i.e., $\bar{\mathbf{x}}_{\mathbf{\Gamma}}^{\mathbf{b}} = \bar{\mathbf{x}}_{\mathbf{\Gamma}}^{\mathbf{d}}$. The physical interface displacements for the blades and the disk are found in Eqs. (5.21) and (5.28), respectively, and result in the following necessary condition:

$$\bar{\mathbf{x}}_{\mathbf{\Gamma}}^{\mathbf{b}} = \left\{ \begin{array}{c} \mathbf{x}_{\mathbf{\Gamma},1}^{\mathbf{b}} \\ \mathbf{x}_{\mathbf{\Gamma},2}^{\mathbf{b}} \\ \vdots \\ \mathbf{x}_{\mathbf{\Gamma},N}^{\mathbf{b}} \end{array} \right\} = \left\{ \begin{array}{c} \mathbf{p}_{\mathbf{c},1}^{\mathbf{b}} \\ \mathbf{p}_{\mathbf{c},2}^{\mathbf{b}} \\ \vdots \\ \mathbf{p}_{\mathbf{c},N}^{\mathbf{b}} \end{array} \right\} = \bar{\mathbf{p}}_{\mathbf{c}}^{\mathbf{b}} = \hat{\mathbf{F}} \tilde{\mathbf{p}}_{\mathbf{c}}^{\mathbf{d}} = \bar{\mathbf{x}}_{\mathbf{\Gamma}}^{\mathbf{d}}. \tag{5.31}$$

Hence, keeping $\tilde{\mathbf{p}}_{\mathbf{c}}^{\mathbf{d}}$ as active DOF, the substructure coupling is represented by the constraint transformation

$$\left\{ \begin{array}{c} \tilde{\mathbf{p}}_{\mathbf{d}}^{\mathbf{d}} \\ \tilde{\mathbf{p}}_{\mathbf{c}}^{\mathbf{d}} \\ \bar{\mathbf{p}}_{\mathbf{b}}^{\mathbf{b}} \\ \bar{\mathbf{p}}_{\mathbf{c}}^{\mathbf{b}} \end{array} \right\} = \left[\begin{array}{ccc} \mathbf{I} & \mathbf{0} & \mathbf{0} \\ \mathbf{0} & \mathbf{I} & \mathbf{0} \\ \mathbf{0} & \mathbf{0} & \mathbf{I} \\ \mathbf{0} & \hat{\mathbf{F}} & \mathbf{0} \end{array} \right] \left\{ \begin{array}{c} \tilde{\mathbf{p}}_{\mathbf{d}} \\ \tilde{\mathbf{p}}_{\mathbf{c}} \\ \bar{\mathbf{p}}_{\mathbf{b}} \end{array} \right\} = \mathbf{T}_{\mathbf{cb}} \mathbf{p}_{\mathbf{cb}}. \tag{5.32}$$

After this final transformation, the synthesized system mass and stiffness matrices for the C-B method take on the following forms:

$$\mathbf{M}^{\mathbf{cb}} = \mathbf{T}_{\mathbf{cb}}^{\mathbf{T}} \left[\begin{array}{cc} \tilde{\mu}^{\mathbf{d}} & \mathbf{0} \\ \mathbf{0} & \bar{\mu}^{\mathbf{b}} \end{array} \right] \mathbf{T}_{\mathbf{cb}} = \left[\begin{array}{ccc} \mathbf{I} & \tilde{\mu}_{\mathbf{dc}} & \mathbf{0} \\ \tilde{\mu}_{\mathbf{dc}}^{\mathbf{T}} & \tilde{\mu}_{\mathbf{cc,d}} + \mathbf{I} \otimes \mu_{\mathbf{cc,b}} & \hat{\mathbf{F}}^{\mathbf{T}} \left(\mathbf{I} \otimes \mu_{\mathbf{bc}}^{\mathbf{T}} \right) \\ \mathbf{0} & \left(\mathbf{I} \otimes \mu_{\mathbf{bc}} \right) \hat{\mathbf{F}} & \mathbf{I} \end{array} \right] \tag{5.33}$$

$$\mathbf{K^{cb}} \;=\; \ldots = \begin{bmatrix} \tilde{\mathbf{\Lambda}}_\mathbf{d} & \mathbf{0} & \mathbf{0} \\ \mathbf{0} & \tilde{\kappa}_{\mathbf{cc,d}} + \mathbf{I} \otimes \kappa_{\mathbf{cc,b}} & \mathbf{0} \\ \mathbf{0} & \mathbf{0} & \mathbf{I} \otimes \mathbf{\Lambda_b} \end{bmatrix},$$

where it is recognized that similarity transformations of expanded matrices follow $\hat{\mathbf{F}}^\mathbf{T} \left(\mathbf{I} \otimes \mathbf{A}\right) \hat{\mathbf{F}} = \mathbf{I} \otimes \mathbf{A}$.

Note that the derived model is still for the tuned assembly. However, since the C-B modal coordinates pertaining to the normal blade modes are for a cantilevered blade, the introduction of modal stiffness mistuning is exquisitely simple. The cantilevered blade modal stiffnesses on the diagonal of $\mathbf{I} \otimes \mathbf{\Lambda_b}$ (extreme lower-right partition in Eq. (5.34)) may be perturbed directly and individually to give the following $\mathbf{K_{bb}^{cb}}$ partition:

$$\mathbf{K_{bb}^{cb}} = \underset{n=1,\ldots,N}{\mathbf{Bdiag}} \left[\underset{k=1,\ldots,m_b}{\mathbf{diag}} \left[1 + \delta_n^k\right] \mathbf{\Lambda_b} \right], \tag{5.34}$$

where m_b is the number of retained cantilevered blade modes. Introducing mistuning in this way implies that any mistuning effects on the constraint modes are neglected. This is not a severe approximation, but as shown in the second part of this study, it does affect the performance of the method. However, except in the simplistic case of varying Young's modulus, quantifying mistuning for the constraint modes is a rather ambiguous task.

Finally, the C-B modal force is constructed. Projecting the component modal matrices of Eqs. (5.21) and (5.29) onto the physical blade force vector described in Eq. (5.16), while enforcing the constraints of Eq. (5.32), the modal force is obtained as

$$\mathbf{F^{cb}} = \begin{Bmatrix} \mathbf{0} \\ \mathbf{F_c^{cb}} \\ \mathbf{F_b^{cb}} \end{Bmatrix}, \tag{5.35}$$

where

$$\mathbf{F_c^{cb}} = \begin{Bmatrix} \mathbf{0} \\ \vdots \\ \mathbf{0} \\ \sqrt{N}\mathbf{f_{C,c}^T e_{C+1}} \otimes \left\{ \mathbf{\Psi_b^T f_B} + \mathbf{f_\Gamma} \right\} \\ \sqrt{N}\mathbf{f_{C,s}^T e_{C+1}} \otimes \left\{ \mathbf{\Psi_b^T f_B} + \mathbf{f_\Gamma} \right\} \\ \mathbf{0} \\ \vdots \\ \mathbf{0} \end{Bmatrix}$$

$$\mathbf{F_b^{cb}} = \sqrt{N}\mathbf{e_{C+1}} \otimes \mathbf{\Phi_b^T f_B}.$$

Note how orthogonality between columns of $\mathbf{E}$ and $\mathbf{F}$ of different interblade phase angles simplifies the modal force partition pertaining to the constraint modes.

Using Eqs. (5.32), (5.33), (5.34), and (5.35), the complete C-B model of a mistuned bladed disk (in the absence of aerodynamic coupling) can now be set up as

$$\mathbf{M^{cb}}\ddot{\mathbf{p}}_\mathbf{cb} + \mathbf{C^{cb}}\dot{\mathbf{p}}_\mathbf{cb} + (1 + Gj)\,\mathbf{K^{cb}}\mathbf{p_{cb}} = \mathbf{F^{cb}}, \tag{5.36}$$

where j denotes the imaginary unit, $\sqrt{-1}$. To facilitate more realistic modeling of the structure's dynamic response, Eq. (5.36) includes structural damping with coefficient G, as well as viscous modal damping of the cantilevered blade modes, which is implemented as

$$\mathbf{C^{cb}} = \begin{bmatrix} \mathbf{0} & \mathbf{0} & \mathbf{0} \\ \mathbf{0} & \mathbf{0} & \mathbf{0} \\ \mathbf{0} & \mathbf{0} & \mathbf{I} \otimes \underset{k=1,\ldots,m_b}{\mathbf{diag}} \left[2\zeta^k \right] \sqrt{\mathbf{\Lambda_b}} \end{bmatrix}, \tag{5.37}$$

where ζ^k is the viscous damping coefficient associated with the k^{th} cantilevered blade mode.

5.4 Craig-Bampton with Partial Secondary Modal Analyses

5.4.1 Craig-Bampton with Modal Interface

This approach was recently developed by Tan *et al*. [61] for power flow analysis. The fundamental step is a secondary modal analysis of the constraint-mode partition of the traditional C-B model. In this case, the constraint-mode partition is represented in cyclic coordinates. Therefore, the characteristic modes of the disk-blade interface, $\tilde{\psi}^{\mathbf{h}}_{\mathbf{cc}}$, are obtained successively for each harmonic h. Using the quantities defined in the previous section, this is achieved by solving

$$\left[\tilde{\mathbf{K}}^{\mathbf{cb,h}}_{\mathbf{cc,d}} + \tilde{\mathbf{K}}^{\mathbf{cb,h}}_{\mathbf{cc,b}} - \omega^2 \left[\tilde{\mathbf{M}}^{\mathbf{cb,h}}_{\mathbf{cc,d}} + \tilde{\mathbf{M}}^{\mathbf{cb,h}}_{\mathbf{cc,b}}\right]\right] \tilde{\psi}^{\mathbf{h}}_{\mathbf{cc}} = \mathbf{0}, \qquad h = 0, \ldots, P, \tag{5.38}$$

where

$$\begin{aligned}
\tilde{\mathbf{K}}^{\mathbf{cb,h}}_{\mathbf{cc,d}} &= \mathbf{K}^{\mathbf{h}}_{\mathbf{d},\Gamma\Gamma} + \mathbf{K}^{\mathbf{h^T}}_{\mathbf{d},\mathbf{S}\Gamma}\boldsymbol{\Psi}^{\mathbf{h}}_{\mathbf{d}} \\
\tilde{\mathbf{M}}^{\mathbf{cb,h}}_{\mathbf{cc,d}} &= \tilde{\boldsymbol{\Psi}}^{\mathbf{h^T}}_{\mathbf{d}} \left[\tilde{\mathbf{M}}^{\mathbf{h}}_{\mathbf{d},\mathbf{SS}}\tilde{\boldsymbol{\Psi}}^{\mathbf{h}}_{\mathbf{d}} + \tilde{\mathbf{M}}^{\mathbf{h}}_{\mathbf{d},\mathbf{S}\Gamma}\right] + \tilde{\mathbf{M}}^{\mathbf{h^T}}_{\mathbf{d},\mathbf{S}\Gamma}\tilde{\boldsymbol{\Psi}}^{\mathbf{h}}_{\mathbf{d}} + \tilde{\mathbf{M}}^{\mathbf{h}}_{\mathbf{d},\Gamma\Gamma} \\
\tilde{\mathbf{K}}^{\mathbf{cb,h}}_{\mathbf{cc,b}} &= \begin{cases} \kappa_{\mathbf{cc,b}} & h = 0, h = \frac{N}{2} \text{ (if it exists)} \\ \begin{bmatrix} \kappa_{\mathbf{cc,b}} & \mathbf{0} \\ \mathbf{0} & \kappa_{\mathbf{cc,b}} \end{bmatrix} & h \neq 0, h \neq \frac{N}{2}, \end{cases}
\end{aligned}$$

and correspondingly for $\tilde{\mathbf{M}}^{\mathbf{cb,h}}_{\mathbf{cc,b}}$.

To study the response of a limited set of blade mode families, only a relatively small number of interface modes in $\tilde{\psi}^{\mathbf{h}}_{\mathbf{cc}}$ is usually required for adequate accuracy. Typically, it is sufficient to keep interface modes that represent interface motion due to blade torsion and flexural motion. This mode selection may be done manually, either by inspection of visualized shapes, or by the order of the interface generalized stiffnesses (usually, lower generalized stiffness implies more "fundamental" interface motion). As a third, and perhaps more appealing option, the modes may be selected in a more automated fashion

via the commonly used Modal Assurance Criterion (MAC), introduced by Allemang and Brown [63]. This implies selecting the modes based on how well they conform with the corresponding harmonic portions, $\tilde{\mathbf{p}}^{\mathbf{h}}_{\mathbf{c}}$, of the global C-B eigenvectors of interest, using some user-defined tolerance, δ_{mac}. Hence, an interface mode, $\tilde{\psi}^{\mathbf{h}}_{\mathbf{cc,i}}$, is selected and collected into the cyclic modal matrix $\tilde{\mathbf{\Psi}}^{\mathbf{s}}_{\mathbf{cc}}$ only if it passes the criterion

$$1 - \frac{\left(\tilde{\psi}^{\mathbf{h^T}}_{\mathbf{cc,i}} \tilde{\mathbf{p}}^{\mathbf{h}}_{\mathbf{c,j}}\right)^2}{\left(\tilde{\psi}^{\mathbf{h^T}}_{\mathbf{cc,i}} \tilde{\psi}^{\mathbf{h}}_{\mathbf{cc,i}}\right)\left(\tilde{\mathbf{p}}^{\mathbf{h^T}}_{\mathbf{c,j}} \tilde{\mathbf{p}}^{\mathbf{h}}_{\mathbf{c,j}}\right)} \leq \delta_{mac}, \tag{5.39}$$

for any $\tilde{\mathbf{p}}^{\mathbf{h}}_{\mathbf{c,j}}$ of interest. The eigenvalues corresponding to selected modes are collected into a cyclic (ordered by harmonics) diagonal generalized stiffness matrix $\tilde{\mathbf{\Lambda}}_{\mathbf{c}}$. The columns of $\tilde{\mathbf{\Psi}}^{\mathbf{s}}_{\mathbf{cc}}$ represent a new, reduced basis for the disk-blade interface motion. This gives a secondary modal expansion of the $\tilde{\mathbf{p}}_{\mathbf{c}}$ portion of C-B generalized coordinates, $\tilde{\mathbf{p}}_{\mathbf{c}} = \tilde{\mathbf{\Psi}}^{\mathbf{s}}_{\mathbf{cc}} \tilde{\mathbf{q}}_{\mathbf{c}}$, to yield the resulting equations of motion:

$$\mathbf{M^{mi}} \ddot{\mathbf{p}}_{\mathbf{mi}} + \mathbf{C^{mi}} \dot{\mathbf{p}}_{\mathbf{mi}} + (1 + Gj)\, \mathbf{K^{mi}} \mathbf{p}_{\mathbf{mi}} = \mathbf{F^{mi}}, \tag{5.40}$$

where

$$\mathbf{M^{mi}} = \begin{bmatrix} \mathbf{I} & \tilde{\mu}_{\mathbf{dc}} \tilde{\mathbf{\Psi}}^{\mathbf{s}}_{\mathbf{cc}} & \mathbf{0} \\ \tilde{\mathbf{\Psi}}^{\mathbf{s^T}}_{\mathbf{cc}} \tilde{\mu}^{\mathbf{T}}_{\mathbf{dc}} & \mathbf{I} & \tilde{\mathbf{\Psi}}^{\mathbf{s^T}}_{\mathbf{cc}} \hat{\mathbf{F}}^{\mathbf{T}} \left(\mathbf{I} \otimes \mu^{\mathbf{T}}_{\mathbf{bc}}\right) \\ \mathbf{0} & (\mathbf{I} \otimes \mu_{\mathbf{bc}})\, \hat{\mathbf{F}} \tilde{\mathbf{\Psi}}^{\mathbf{s}}_{\mathbf{cc}} & \mathbf{I} \end{bmatrix}$$

$$\mathbf{C^{mi}} = \begin{bmatrix} \mathbf{0} & \mathbf{0} & \mathbf{0} \\ \mathbf{0} & \mathbf{0} & \mathbf{0} \\ \mathbf{0} & \mathbf{0} & \mathbf{I} \otimes \underset{k=1,\ldots,m_b}{\mathbf{diag}} \left[2\zeta^k\right] \sqrt{\mathbf{\Lambda_b}} \end{bmatrix}$$

$$\mathbf{K^{mi}} = \begin{bmatrix} \tilde{\mathbf{\Lambda}}_{\mathbf{d}} & \mathbf{0} & \mathbf{0} \\ \mathbf{0} & \tilde{\mathbf{\Lambda}}_{\mathbf{c}} & \mathbf{0} \\ \mathbf{0} & \mathbf{0} & \underset{n=1,\ldots,N}{\mathbf{Bdiag}} \left[\underset{k=1,\ldots,m_b}{\mathbf{diag}} \left[1 + \delta^k_n\right] \mathbf{\Lambda_b} \right] \end{bmatrix}$$

$$\mathbf{F^{mi}} = \left\{ \begin{array}{l} \mathbf{0} \\ \tilde{\mathbf{\Psi}}_{\mathbf{cc}}^{\mathbf{s^T}} \mathbf{F}_{\mathbf{c}}^{\mathbf{cb}} \\ \mathbf{F}_{\mathbf{b}}^{\mathbf{cb}} \end{array} \right\} \qquad \mathbf{p_{mi}} = \left\{ \begin{array}{l} \tilde{\mathbf{p}}_{\mathbf{d}} \\ \tilde{\mathbf{q}}_{\mathbf{c}} \\ \bar{\mathbf{p}}_{\mathbf{b}} \end{array} \right\}.$$

Note from Eq. (5.35) that only interface modes of the C^{th} harmonic get involved in the secondary modal force projection.

It is clear that by using a truncated set of interface modes, the size of the classical C-B model may be significantly reduced. In addition, the conditioning of the synthesized mass and stiffness matrices is improved, since all quantities are now in the modal domain. Matrix ill-conditioning may occur in the classical C-B setup, since it contains both modal- and physical-coordinate matrix partitions, which elements may differ by several orders of magnitude.

5.4.2 Craig-Bampton with Modal Disk and Interface

This approach is similar in spirit to the method of Tan *et al*. [61]. Here, a secondary modal analysis is performed on the disk-normal-mode *plus* constraint-mode partitions of the traditional C-B model. Both partitions are represented in cyclic coordinates, and the characteristic modes of the disk plus disk-blade interface, $\tilde{\psi}_{\mathbf{dc}}^{\mathbf{h}}$, are therefore obtained successively for each harmonic h. Again, using the quantities defined in Sections 5.3 and 5.4.1, this is achieved by solving

$$\left[\tilde{\mathbf{K}}_{\mathbf{dc}}^{\mathbf{h}} - \omega^2 \tilde{\mathbf{M}}_{\mathbf{dc}}^{\mathbf{h}}\right] \tilde{\psi}_{\mathbf{dc}}^{\mathbf{h}} = \mathbf{0}, \qquad h = 0, \ldots, P, \tag{5.41}$$

where

$$\begin{aligned} \tilde{\mathbf{K}}_{\mathbf{dc}}^{\mathbf{h}} &= \begin{bmatrix} \tilde{\mathbf{\Lambda}}_{\mathbf{d}}^{\mathbf{h}} & \mathbf{0} \\ \mathbf{0} & \tilde{\mathbf{K}}_{\mathbf{cc,d}}^{\mathbf{cb,h}} + \tilde{\mathbf{K}}_{\mathbf{cc,b}}^{\mathbf{cb,h}} \end{bmatrix} \\ \tilde{\mathbf{M}}_{\mathbf{dc}}^{\mathbf{h}} &= \begin{bmatrix} \mathbf{I} & \tilde{\mathbf{M}}_{\mathbf{dc}}^{\mathbf{cb,h}} \\ \tilde{\mathbf{M}}_{\mathbf{dc}}^{\mathbf{cb,h^T}} & \tilde{\mathbf{M}}_{\mathbf{cc,d}}^{\mathbf{cb,h}} + \tilde{\mathbf{M}}_{\mathbf{cc,b}}^{\mathbf{cb,h}} \end{bmatrix} \end{aligned}$$

$$\tilde{\mathbf{M}}^{\mathbf{cb,h}}_{\mathbf{dc}} \;=\; \tilde{\mathbf{\Phi}}^{\mathbf{h^T}}_{\mathbf{d}} \left[\tilde{\mathbf{M}}^{\mathbf{h}}_{\mathbf{d,SS}} \tilde{\mathbf{\Psi}}^{\mathbf{h}}_{\mathbf{d}} + \tilde{\mathbf{M}}^{\mathbf{h}}_{\mathbf{d,S\Gamma}} \right].$$

As in the previous section, a severely truncated subset of modes in $\tilde{\psi}^{\mathbf{h}}_{\mathbf{dc}}$ is selected, either manually by inspection of visualized shapes or by the order of the obtained generalized stiffnesses, or automatically by using MAC comparisons. In the latter case, a mode $\tilde{\psi}^{\mathbf{h}}_{\mathbf{dc,i}}$ is selected and collected into the cyclic modal matrix $\tilde{\mathbf{\Psi}}^{\mathbf{s}}_{\mathbf{mdi}}$ only if it satisfies a relation analogous to Eq. (5.39) for any $\tilde{\mathbf{p}}^{\mathbf{h}}_{\mathbf{dc,j}}$ of interest. The modal matrices involved here are partitioned into disk-normal-mode and constraint-mode portions as

$$\tilde{\psi}^{\mathbf{h}}_{\mathbf{dc}} = \begin{bmatrix} \tilde{\psi}^{\mathbf{h}}_{\mathbf{dc,d}} \\ \\ \tilde{\psi}^{\mathbf{h}}_{\mathbf{dc,c}} \end{bmatrix}; \qquad \tilde{\mathbf{p}}^{\mathbf{h}}_{\mathbf{dc}} = \begin{bmatrix} \tilde{\mathbf{p}}^{\mathbf{h}}_{\mathbf{d}} \\ \\ \tilde{\mathbf{p}}^{\mathbf{h}}_{\mathbf{c}} \end{bmatrix}; \qquad \tilde{\mathbf{\Psi}}^{\mathbf{s}}_{\mathbf{mdi}} = \begin{bmatrix} \tilde{\mathbf{\Psi}}^{\mathbf{s}}_{\mathbf{mdi,d}} \\ \\ \tilde{\mathbf{\Psi}}^{\mathbf{s}}_{\mathbf{mdi,c}} \end{bmatrix}. \tag{5.42}$$

The eigenvalues corresponding to selected modes are collected into a cyclic diagonal generalized stiffness matrix $\tilde{\mathbf{\Lambda}}_{\mathbf{mdi}}$. The columns of $\tilde{\mathbf{\Psi}}^{\mathbf{s}}_{\mathbf{mdi}}$ represent a new, reduced basis for the disk plus disk-blade interface motion. This gives a secondary modal expansion of the $\tilde{\mathbf{p}}_{\mathbf{d}}$ and $\tilde{\mathbf{p}}_{\mathbf{c}}$ portions of the C-B generalized coordinates as

$$\tilde{\mathbf{p}}_{\mathbf{dc}} = \begin{Bmatrix} \tilde{\mathbf{p}}_{\mathbf{d}} \\ \\ \tilde{\mathbf{p}}_{\mathbf{c}} \end{Bmatrix} = \begin{bmatrix} \tilde{\mathbf{\Psi}}^{\mathbf{s}}_{\mathbf{mdi,d}} \\ \\ \tilde{\mathbf{\Psi}}^{\mathbf{s}}_{\mathbf{mdi,c}} \end{bmatrix} \tilde{\mathbf{q}}_{\mathbf{dc}}. \tag{5.43}$$

Introducing this secondary modal expansion into the classical C-B setup yields the resulting equations of motion:

$$\mathbf{M}^{\mathbf{mdi}} \ddot{\mathbf{p}}_{\mathbf{mdi}} + \mathbf{C}^{\mathbf{mdi}} \dot{\mathbf{p}}_{\mathbf{mdi}} + (1 + Gj)\, \mathbf{K}^{\mathbf{mdi}} \mathbf{p}_{\mathbf{mdi}} = \mathbf{F}^{\mathbf{mdi}}, \tag{5.44}$$

where

$$\mathbf{M}^{\mathbf{mdi}} \;=\; \begin{bmatrix} \mathbf{I} & \tilde{\mathbf{\Psi}}^{\mathbf{s^T}}_{\mathbf{mdi,c}} \hat{\mathbf{F}}^{\mathbf{T}} \left(\mathbf{I} \otimes \mu^{\mathbf{T}}_{\mathbf{bc}} \right) \\ \left(\mathbf{I} \otimes \mu_{\mathbf{bc}} \right) \hat{\mathbf{F}}\, \tilde{\mathbf{\Psi}}^{\mathbf{s}}_{\mathbf{mdi,c}} & \mathbf{I} \end{bmatrix}$$

$$\mathbf{C}^{\mathbf{mdi}} \;=\; \begin{bmatrix} \mathbf{0} & \mathbf{0} \\ \mathbf{0} & \mathbf{I} \otimes \underset{k=1,\ldots,m_b}{\mathbf{diag}} \left[2\zeta^k \right] \sqrt{\mathbf{\Lambda_b}} \end{bmatrix}$$

$$\mathbf{K^{mdi}} = \begin{bmatrix} \tilde{\mathbf{\Lambda}}_{\mathbf{mdi}} & \mathbf{0} \\ \mathbf{0} & \underset{n=1,\ldots,N}{\mathbf{Bdiag}} \left[\underset{k=1,\ldots,m_b}{\mathbf{diag}} \left[1 + \delta_n^k \right] \mathbf{\Lambda_b} \right] \end{bmatrix}$$

$$\mathbf{F^{mdi}} = \begin{Bmatrix} \tilde{\mathbf{\Psi}}^{\mathbf{s^T}}_{\mathbf{mdi,c}} \mathbf{F^{cb}_c} \\ \mathbf{F^{cb}_b} \end{Bmatrix} \qquad \mathbf{p_{mdi}} = \begin{Bmatrix} \tilde{\mathbf{q}}_{\mathbf{dc}} \\ \bar{\mathbf{p}}_{\mathbf{b}} \end{Bmatrix}.$$

Note that in this case too, only the selected modes of the C^{th} harmonic contribute to the secondary modal force projection.

This approach yields a reduction of the classical C-B model comparable to Tan *et al*.'s method. Besides the more compact final formulation, another advantage of this last approach is that it may allow a more intuitive secondary mode selection. Note that the matrix conditioning improvement discussed in Section 5.4.1 also applies to this approach.

5.5 Disk-Induced Blade Constraint Modes (REDUCE)

The method presented in this section is referred to by the name of the associated computer code, REDUCE. It was thoroughly outlined for free vibrations by Castanier *et al*. [20]. It was extended to the forced response by Kruse and Pierre [21], and subsequently revised and further extended to cover shrouded assemblies by Bladh *et al*. [23]. In terms of generality and versatility, REDUCE represents the current state of the art for modeling the structural dynamics of mistuned bladed disk assemblies. Moreover, REDUCE is actively used by several gas turbine engine companies. However, as will be shown in this study, alternative methods may be formulated that yield superior performance.

The REDUCE method employs two sets of modes:

- A truncated set of cantilevered blade modes — blade component modes with the disk-blade interface DOF held fixed (see Fig. 5.3a). The mode shapes and associated eigenvalues are collected into a modal matrix $\mathbf{u^b}$ and a diagonal generalized stiffness

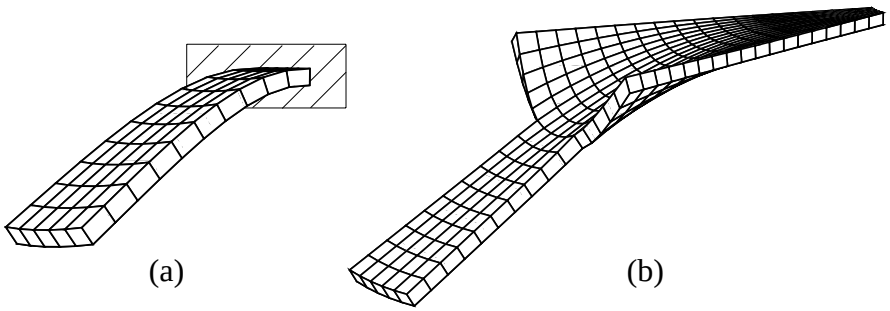

Figure 5.3: REDUCE component modes: (a) fixed-interface (cantilevered) normal blade modes; (b) cyclic modes for the fundamental disk-blade sector with a massless blade.

matrix $\hat{\mathbf{K}}_\mathbf{b}$, respectively. The corresponding generalized coordinates are denoted $\mathbf{b}$. Note that $\hat{\mathbf{K}}_\mathbf{b}$ is equivalent to $\mathbf{I} \otimes \mathbf{\Lambda}_\mathbf{b}$ of the C-B method.

- A truncated set of cyclic modes for the fundamental disk-blade sector with a massless blade (see Fig. 5.3b). The blade portions of the cyclic mode shapes are collected into modal matrices $\tilde{\mathbf{u}}_\mathbf{h}^\mathbf{d}$ for each harmonic h. These shapes may be described as disk-induced blade constraint modes. The modal matrices $\tilde{\mathbf{u}}_\mathbf{h}^\mathbf{d}$ and the associated eigenvalues are assembled into $\tilde{\mathbf{U}}^\mathbf{d}$ and a diagonal generalized stiffness matrix $\hat{\mathbf{K}}_\mathbf{d}$, respectively. The corresponding generalized coordinates are denoted $\mathbf{a}$.

By definition, each set of modes, $\mathbf{u}^\mathbf{b}$ and $\tilde{\mathbf{U}}^\mathbf{d}$, are linearly independent. Moreover, since $\mathbf{u}^\mathbf{b}$ does not contain any disk motion, it is clear that the two mode sets are linearly independent with respect to each other as well. Furthermore, in the limit, the number of modes in $\mathbf{u}^\mathbf{b}$ will equal the total number of interior (B) DOF in the blade, and the number of modes in $\tilde{\mathbf{U}}^\mathbf{d}$ will equal the number of independent disk interior (D+α) plus interface (Γ) DOF. Hence, just as for the C-B method, linear independence and DOF completeness in the limit combine to yield the exact solution for the REDUCE method relative to the parent finite element model. Finally, note that this is not a true CMS method, since the assembled disk-blade sector is needed to obtain the disk-induced blade constraint modes.

The resulting equations of motion are restated here for convenience:

$$\mathcal{M}\ddot{\mathbf{z}} + \mathcal{C}\dot{\mathbf{z}} + (1 + Gj)\,\mathcal{K}\mathbf{z} = \mathcal{Q}, \tag{5.45}$$

where

$$\mathbf{z} = \left\{ \begin{array}{c} \mathbf{a} \\ \mathbf{b} \end{array} \right\} \qquad \mathcal{C} = \left[\begin{array}{cc} \mathbf{0} & \mathbf{0} \\ \mathbf{0} & \left(\mathbf{I} \otimes \underset{k=1,\ldots,m_b}{\mathbf{diag}} \left[2\zeta^k \right] \right) \sqrt{\hat{\mathbf{K}}_\mathbf{b}} \end{array} \right]$$

$$\mathcal{M} = \left[\begin{array}{cc} \mathbf{I} + \tilde{\mathbf{B}} \underset{h=0,\ldots,P}{\mathbf{diag}} \left[\tilde{\mathbf{u}}_\mathbf{h}^{\mathbf{d^T}} \mathbf{M}^\mathbf{b} \tilde{\mathbf{u}}_\mathbf{h}^\mathbf{d} \right] & \tilde{\mathbf{U}}^{\mathbf{d^T}} \left(\mathbf{I} \otimes \mathbf{M}^\mathbf{b} \mathbf{u}^\mathbf{b} \right) \\ \left(\mathbf{I} \otimes \mathbf{u}^{\mathbf{b^T}} \mathbf{M}^\mathbf{b} \right) \tilde{\mathbf{U}}^\mathbf{d} & \mathbf{I} \end{array} \right]$$

$$\mathcal{K} = \left[\begin{array}{cc} \hat{\mathbf{K}}_\mathbf{d} & \tilde{\mathbf{U}}^{\mathbf{d^T}} \left(\mathbf{I} \otimes \mathbf{K}^\mathbf{b} \mathbf{u}^\mathbf{b} \right) \\ \left(\mathbf{I} \otimes \mathbf{u}^{\mathbf{b^T}} \mathbf{K}^\mathbf{b} \right) \tilde{\mathbf{U}}^\mathbf{d} & \mathbf{B} \underset{n=1,\ldots,N}{\mathbf{diag}} \left[\underset{k=1,\ldots,m_b}{\mathbf{diag}} \left[1 + \delta_n^k \right] \right] \hat{\mathbf{K}}_\mathbf{b} \end{array} \right]$$

$$\mathcal{Q} = \left\{ \begin{array}{ccc} \mathcal{Q}_\mathbf{d}^\mathbf{T} & \vdots & \mathcal{Q}_\mathbf{b}^\mathbf{T} \end{array} \right\}^T = \left\{ \begin{array}{ccccccccc} \mathbf{0} & \cdots & \mathbf{0} & \mathcal{Q}_\mathbf{d}^{\mathbf{C^T}} & \mathbf{0} & \cdots & \mathbf{0} & \vdots & \mathcal{Q}_\mathbf{b}^\mathbf{T} \end{array} \right\}^T$$

$$\mathcal{Q}_\mathbf{d}^\mathbf{C} = \left\{ \begin{array}{c} \sqrt{N} \left\{ \mathbf{f}_{\mathbf{C},\mathbf{c}}^\mathbf{T} \mathbf{e}_{\mathbf{C}+1} \otimes \tilde{\mathbf{u}}_{\mathbf{C},1}^{\mathbf{d},\mathbf{c}^\mathbf{T}} \mathbf{f}_\mathbf{b} - \mathbf{f}_{\mathbf{C},\mathbf{s}}^\mathbf{T} \mathbf{e}_{\mathbf{C}+1} \otimes \tilde{\mathbf{u}}_{\mathbf{C},1}^{\mathbf{d},\mathbf{s}^\mathbf{T}} \mathbf{f}_\mathbf{b} \right\} \\ \sqrt{N} \left\{ \mathbf{f}_{\mathbf{C},\mathbf{s}}^\mathbf{T} \mathbf{e}_{\mathbf{C}+1} \otimes \tilde{\mathbf{u}}_{\mathbf{C},1}^{\mathbf{d},\mathbf{c}^\mathbf{T}} \mathbf{f}_\mathbf{b} + \mathbf{f}_{\mathbf{C},\mathbf{c}}^\mathbf{T} \mathbf{e}_{\mathbf{C}+1} \otimes \tilde{\mathbf{u}}_{\mathbf{C},1}^{\mathbf{d},\mathbf{s}^\mathbf{T}} \mathbf{f}_\mathbf{b} \right\} \\ \vdots \\ \sqrt{N} \left\{ \mathbf{f}_{\mathbf{C},\mathbf{c}}^\mathbf{T} \mathbf{e}_{\mathbf{C}+1} \otimes \tilde{\mathbf{u}}_{\mathbf{C},\mathbf{m_d}}^{\mathbf{d},\mathbf{c}^\mathbf{T}} \mathbf{f}_\mathbf{b} - \mathbf{f}_{\mathbf{C},\mathbf{s}}^\mathbf{T} \mathbf{e}_{\mathbf{C}+1} \otimes \tilde{\mathbf{u}}_{\mathbf{C},\mathbf{m_d}}^{\mathbf{d},\mathbf{s}^\mathbf{T}} \mathbf{f}_\mathbf{b} \right\} \\ \sqrt{N} \left\{ \mathbf{f}_{\mathbf{C},\mathbf{s}}^\mathbf{T} \mathbf{e}_{\mathbf{C}+1} \otimes \tilde{\mathbf{u}}_{\mathbf{C},\mathbf{m_d}}^{\mathbf{d},\mathbf{c}^\mathbf{T}} \mathbf{f}_\mathbf{b} + \mathbf{f}_{\mathbf{C},\mathbf{c}}^\mathbf{T} \mathbf{e}_{\mathbf{C}+1} \otimes \tilde{\mathbf{u}}_{\mathbf{C},\mathbf{m_d}}^{\mathbf{d},\mathbf{s}^\mathbf{T}} \mathbf{f}_\mathbf{b} \right\} \end{array} \right\}$$

$$\mathcal{Q}_\mathbf{b} = \sqrt{N} \mathbf{e}_{\mathbf{C}+1} \otimes \mathbf{u}^{\mathbf{b^T}} \mathbf{f}_\mathbf{b},$$

and $\mathbf{f_b}$ is the force vector on the fundamental blade (i.e., a composite of $\mathbf{f_B}$ and $\mathbf{f_\Gamma}$ from Section 5.2.2). In this formulation, quantities in physical coordinates (structural matrices, mode shapes) pertain to the blade part only.

Since the disk motion is described by the disk portion from the second mode set alone (Fig. 5.3b), no separate set of constraint modes for the disk is employed. This causes the

disk to be too stiff at the interface, which degrades the performance (modal convergence) of the method. However, it has been found that artificial softening of the cantilevered blade modes yields significant accuracy improvements for both free and forced response. This is achieved by adjusting the eigenvalues of the cantilevered blade modes in an iterative fashion, based on the finite element eigenvalues for blade-dominated assembly modes. Though it is heuristic, this technique has proved very efficient (Bladh *et al*. [23]).

5.6 Non-CMS Mistuning Projection Method

This method is based on the assumption that the mistuned modes of a bladed disk assembly may be realized by a linear combination of its tuned modes. This assumption is justified by two observations: (a) the local motion of a blade in a mistuned assembly is, to a large extent, merely an amplification of its tuned motion; and (b) any admissible disk shape, no matter how spatially localized, may be realized by a linear combination of its harmonic shapes in cyclic coordinates if all harmonics 0 through P are included in the model.

By separating disk and blade parts by partitioning as shown in Eq. (5.1), the stiffness matrix of the mistuned bladed disk may be represented as

$$\bar{\mathcal{K}} = \begin{bmatrix} \mathbf{I} \otimes \mathbf{K^d} & \mathbf{0} \\ \mathbf{0} & \mathbf{I} \otimes \mathbf{K^b} + \underset{n=1,\ldots,N}{\mathbf{Bdiag}} \left[\mathbf{\Delta K_n^b} \right] \end{bmatrix}, \tag{5.46}$$

where $\mathbf{\Delta K_n^b}$ is a matrix containing the stiffness deviations from the nominal stiffness matrix for the n^{th} blade. Recall that only blade stiffness mistuning is considered here; thus, all other partitions remain unaffected.

First, a set of nominal, cyclic eigenvalues and eigenvectors are computed for each harmonic h from

$$\left[\tilde{\mathcal{K}}^{\mathbf{h}} - \omega^2 \tilde{\mathcal{M}}^{\mathbf{h}} \right] \tilde{\mathbf{u}}^{\mathbf{h}} = \mathbf{0}, \qquad h = 0, \ldots, P, \tag{5.47}$$

where

$$\tilde{\mathcal{K}}^{\mathbf{h}} = \begin{bmatrix} \tilde{\mathbf{K}}^{\mathbf{h}}_{\mathbf{d},\mathbf{SS}} & \tilde{\mathbf{K}}^{\mathbf{h}}_{\mathbf{d},\mathbf{S\Gamma}} & \mathbf{0} \\ \tilde{\mathbf{K}}^{\mathbf{h}^{\mathbf{T}}}_{\mathbf{d},\mathbf{S\Gamma}} & \tilde{\mathbf{K}}^{\mathbf{h}}_{\mathbf{d},\mathbf{\Gamma\Gamma}} + \tilde{\mathbf{K}}^{\mathbf{h}}_{\mathbf{b},\mathbf{\Gamma\Gamma}} & \tilde{\mathbf{K}}^{\mathbf{h}^{\mathbf{T}}}_{\mathbf{b},\mathbf{B\Gamma}} \\ \mathbf{0} & \tilde{\mathbf{K}}^{\mathbf{h}}_{\mathbf{b},\mathbf{B\Gamma}} & \tilde{\mathbf{K}}^{\mathbf{h}}_{\mathbf{b},\mathbf{BB}} \end{bmatrix}.$$

The cyclic disk quantities are defined in Section 5.2.1. Referring to Eq. (5.3), the cyclic blade quantities have the common form

$$\tilde{\mathbf{K}}^{\mathbf{h}}_{\mathbf{b},\mathbf{xy}} = \begin{cases} \mathbf{K}^{\mathbf{b}}_{\mathbf{xy}} & h = 0, h = \frac{N}{2} \text{ (if it exists)} \\ \begin{bmatrix} \mathbf{K}^{\mathbf{b}}_{\mathbf{xy}} & \mathbf{0} \\ \mathbf{0} & \mathbf{K}^{\mathbf{b}}_{\mathbf{xy}} \end{bmatrix} & h \neq 0, h \neq \frac{N}{2}, \end{cases} \tag{5.48}$$

where "xy" represents BB, BΓ, or $\Gamma\Gamma$. The structure of $\tilde{\mathcal{M}}^{\mathbf{h}}$ is identical to that of $\tilde{\mathcal{K}}^{\mathbf{h}}$.

A fundamental step in this method is to use a small subset of the obtained cyclic modes in order to form a reduced order model by classical modal analysis. The disk-blade interface plus interior blade portions of the selected mode shapes are collected into a cyclic modal matrix $\tilde{\mathbf{U}}_{\mathbf{s}}$, while the associated eigenvalues are collected into a cyclic generalized stiffness matrix $\tilde{\mathbf{\Lambda}}_{\mathbf{s}}$. In the typical case, the analyst concentrates on a particular family of blade modes and/or eigenfrequency veerings that are deemed critical due to engine operating conditions. As shown by Yang and Griffin [27], mistuned bladed disks are particularly well adapted to system mode selections in relatively narrow frequency bands. Hence, the mode selection is typically based on a frequency range encompassing the blade mode family (or families) of interest. Thus, in most cases, the number of modes needed, m_s, is on the order of the number of blades, $\mathcal{O}(N)$. This is also the size of the resulting reduced order model.

In the tuned case, classical modal analysis simply results in a small, fully decoupled system, where the modal mass matrix is an identity matrix, and the modal stiffness matrix is a diagonal matrix with the selected eigenvalues as elements. The mistuned case,

however, requires some additional work. By representing the mistuned blades by stiffness matrix deviations as indicated in Eq. (5.46), the mistuning is entered into the reduced order model by projecting the stiffness deviations onto the selected tuned modes of the assembly. Note, however, that the stiffness deviations are in physical coordinates while the nominal modes are cyclic. Hence, the mistuning projection takes the form:

$$\boldsymbol{\Delta}\tilde{\mathbf{K}}^{\mathbf{b}} = \tilde{\mathbf{U}}_{\mathbf{s}}^{\mathbf{T}}\hat{\mathbf{F}}^{\mathbf{T}}\mathbf{B}\underset{n=1,\ldots,N}{\mathbf{diag}}\left[\boldsymbol{\Delta}\mathbf{K}_{\mathbf{n}}^{\mathbf{b}}\right]\hat{\mathbf{F}}\tilde{\mathbf{U}}_{\mathbf{s}}. \tag{5.49}$$

The reduced order model may then be formulated as

$$\ddot{\mathbf{q}} + \tilde{\mathbf{C}}^{\mathbf{mp}}\dot{\mathbf{q}} + (1+Gj)\left[\tilde{\boldsymbol{\Lambda}}_{\mathbf{s}} + \boldsymbol{\Delta}\tilde{\mathbf{K}}^{\mathbf{b}}\right]\mathbf{q} = \tilde{\mathbf{F}}^{\mathbf{mp}}, \tag{5.50}$$

where

$$\tilde{\mathbf{C}}^{\mathbf{mp}} = \underset{k=1,\ldots,m_s}{\mathbf{diag}}\left[2\zeta^k\right]\sqrt{\tilde{\boldsymbol{\Lambda}}_{\mathbf{s}}}$$

$$\tilde{\mathbf{F}}^{\mathbf{mp}} = \left\{\begin{array}{c} \mathbf{0} \\ \vdots \\ \mathbf{0} \\ \sqrt{N}\mathbf{f}_{\mathbf{C},\mathbf{c}}^{\mathbf{T}}\mathbf{e}_{\mathbf{C+1}} \otimes \tilde{\mathbf{u}}_{\mathbf{s},\mathbf{b}}^{\mathbf{C}^{\mathbf{T}}}\mathbf{f}_{\mathbf{b}} \\ \sqrt{N}\mathbf{f}_{\mathbf{C},\mathbf{s}}^{\mathbf{T}}\mathbf{e}_{\mathbf{C+1}} \otimes \tilde{\mathbf{u}}_{\mathbf{s},\mathbf{b}}^{\mathbf{C}^{\mathbf{T}}}\mathbf{f}_{\mathbf{b}} \\ \mathbf{0} \\ \vdots \\ \mathbf{0} \end{array}\right\},$$

$\mathbf{f}_{\mathbf{b}}$ is the fundamental blade force vector (same as in Section 5.5), and $\tilde{\mathbf{u}}_{\mathbf{s},\mathbf{b}}^{\mathbf{C}}$ contains the blade portions of the selected mode shapes of the C^{th} harmonic. Note that the stiffness deviation projection matrix, $\boldsymbol{\Delta}\tilde{\mathbf{K}}^{\mathbf{b}}$, does not possess any particular matrix structure other than symmetry. Thus, in general, the reduced order model stiffness matrix becomes fully

populated when mistuning is introduced. Also, note that the viscous modal damping introduced here refers to the nominal assembly modes, not the cantilevered blade modes as in previous methods. As seen in Eq. (5.50), once the blade stiffness deviations have been established, this method is conceptually very straightforward. However, the process for obtaining the blade stiffness deviations requires some further consideration.

In the simplistic case of offsets in blade Young's modulus, this method allows for simple input of mistuning in the following manner:

$$\mathbf{\Delta K_n^b} = \delta_n \mathbf{K^b}, \qquad n = 1, \ldots, N. \tag{5.51}$$

However, for input of mistuning individually for each mode of each cantilevered blade, as in the previous methods, the task becomes more cumbersome. In this case, an approach analogous to the mistuning of shrouded assemblies in the REDUCE method has to be adopted. This approach is outlined in Bladh *et al*. [23], but here it is reviewed briefly and adapted to current notation. To begin, a diagonal matrix containing the mistuned modal stiffnesses (measured or generated) of the n^{th} blade may be written as:

$$\underset{k=1,\ldots,m_b}{\mathbf{diag}} \left[1 + \delta_n^k\right] \mathbf{\Lambda_b} = \mathbf{u^{b^T}} \left[\mathbf{K^b} + \mathbf{\Delta K_n^b}\right] \mathbf{u^b}, \tag{5.52}$$

where $\mathbf{u^b}$ contains the nominal mode shapes for a cantilevered blade, and $\mathbf{\Lambda_b}$ is a diagonal matrix containing the corresponding modal stiffnesses for a tuned cantilevered blade. Note that there is already an approximation made at this point, namely that the mode shapes of a mistuned blade are the same as those of a tuned blade. Rearranging Eq. (5.52) and identifying $\mathbf{\Lambda_b} = \mathbf{u^{b^T} K^b u^b}$, yields the following expression for the stiffness deviation:

$$\mathbf{\Delta K_n^b} = \mathbf{u^{b^{T^{-1}}}} \underset{k=1,\ldots,m_b}{\mathbf{diag}} \left[\delta_n^k\right] \mathbf{\Lambda_b u^{b^{-1}}}. \tag{5.53}$$

Now, making use of the eigenvector normalization assumption, it is realized that:

$$\mathbf{I} = \mathbf{u^{b^T} M^b u^b} \quad \Rightarrow \quad \mathbf{u^{b^{T^{-1}}}} \approx \mathbf{M^b u^b} \tag{5.54}$$

$$\mathbf{\Lambda_b} = \mathbf{u^{b^T} K^b u^b} \quad \Rightarrow \quad \mathbf{\Lambda_b u^{b^{-1}}} \approx \mathbf{u^{b^T} K^b}.$$

It is assumed here that $\mathbf{u^{b^{-1}}}$ exists, i.e., that it is complete (square). This is seldom the case in practice, as it would be impractically large, and thus, as indicated, Eq. (5.55) is an approximation. The non-existent inverse does not pose a problem, however, since it need not be computed. Moreover, the implied approximation is of the same order as the modal analysis itself, and it does not cause a noticeable decrease in accuracy.

By substituting Eq. (5.55) into Eq. (5.53), the stiffness deviation matrix may be expressed in its final form as

$$\mathbf{\Delta K_n^b} = \mathbf{M^b u^b} \underset{k=1,\ldots,m_b}{\mathbf{diag}} \left[\delta_n^k\right] \mathbf{u^{b^T} K^b}. \tag{5.55}$$

In this manner, stiffness deviations of individual blades can be incorporated into the reduced order model by projection onto the selected cyclic modes of the assembly.

5.7 Secondary Modal Analysis Reduction Technique (SMART)

The key idea for this new technique is to whittle the size of the reduced order model to an absolute minimum, without incurring severe truncation errors or sacrificing versatility. This is achieved by performing a full-scale secondary modal analysis on an intermediate model that has already been reduced through modal analysis in some fashion (e.g., by the C-B method). The secondary modal analysis is based on those modes of the intermediate model that fall within a frequency range encompassing the blade mode family (or families) of interest during subsequent mistuned free and/or forced response analyses. In this respect, the approach is very similar to the mistuning projection method of the previous section. However, a distinct advantage of the SMART model is the fact that the required projection of mistuning data is carried out in the low-order modal domain, while the mistuning projection method must deal with the projections in the physical domain. This

SMART idea may be applied to any intermediate model that is constructed from a CMS (or other) method. In this work, the intermediate models are constructed with the C-B method, due to its robustness and excellent accuracy. Furthermore, the C-B method is a natural choice in view of the mistuning implementation employed in this study, since it gives direct access to the blade modal stiffnesses.

As in the mistuning projection method, the first step is to obtain the tuned modes from which to form the new selected basis. This is done for each harmonic h using the tuned C-B model entirely in cyclic coordinates, which results in the following set of eigenvalue problems:

$$\left[\tilde{\mathbf{K}}^{\mathbf{h}}_{\mathbf{cb}} - \omega^2 \tilde{\mathbf{M}}^{\mathbf{h}}_{\mathbf{cb}}\right] \tilde{\mathbf{u}}^{\mathbf{h}}_{\mathbf{cb}} = \mathbf{0}, \qquad h = 0, \ldots, P, \tag{5.56}$$

where

$$\tilde{\mathbf{K}}^{\mathbf{h}}_{\mathbf{cb}} = \begin{bmatrix} \tilde{\mathbf{\Lambda}}^{\mathbf{h}}_{\mathbf{d}} & \mathbf{0} & \mathbf{0} \\ \mathbf{0} & \tilde{\mathbf{K}}^{\mathbf{cb,h}}_{\mathbf{cc,d}} + \tilde{\mathbf{K}}^{\mathbf{cb,h}}_{\mathbf{cc,b}} & \mathbf{0} \\ \mathbf{0} & \mathbf{0} & \tilde{\mathbf{\Lambda}}^{\mathbf{h}}_{\mathbf{b}} \end{bmatrix}$$

$$\tilde{\mathbf{M}}^{\mathbf{h}}_{\mathbf{cb}} = \begin{bmatrix} \mathbf{I} & \tilde{\mathbf{M}}^{\mathbf{cb,h}}_{\mathbf{dc}} & \mathbf{0} \\ \tilde{\mathbf{M}}^{\mathbf{cb,h^T}}_{\mathbf{dc}} & \tilde{\mathbf{M}}^{\mathbf{cb,h}}_{\mathbf{cc,d}} + \tilde{\mathbf{M}}^{\mathbf{cb,h}}_{\mathbf{cc,b}} & \tilde{\mathbf{M}}^{\mathbf{cb,h^T}}_{\mathbf{bc}} \\ \mathbf{0} & \tilde{\mathbf{M}}^{\mathbf{cb,h}}_{\mathbf{bc}} & \mathbf{I} \end{bmatrix}.$$

The disk partitions as well as the blade cc-partitions are defined in Section 5.3. For the remaining cyclic blade partitions in the C-B model, the definitions in Section 5.3.1 give

$$\tilde{\mathbf{M}}^{\mathbf{cb,h}}_{\mathbf{bc}} = \begin{cases} \mu_{\mathbf{bc}} & h = 0, h = \frac{N}{2} \text{ (if it exists)} \\ \begin{bmatrix} \mu_{\mathbf{bc}} & \mathbf{0} \\ \mathbf{0} & \mu_{\mathbf{bc}} \end{bmatrix} & h \neq 0, h \neq \frac{N}{2}, \end{cases} \tag{5.57}$$

$$\tilde{\mathbf{\Lambda}}_{\mathbf{b}}^{\mathbf{h}} = \begin{cases} \mathbf{\Lambda_b} & h = 0, h = \frac{N}{2} \text{ (if it exists)} \\ \begin{bmatrix} \mathbf{\Lambda_b} & \mathbf{0} \\ \mathbf{0} & \mathbf{\Lambda_b} \end{bmatrix} & h \neq 0, h \neq \frac{N}{2}. \end{cases} \tag{5.58}$$

Similar to the mistuning projection method, the next step is to select a small subset of the obtained C-B cyclic modes. This subset is then used to form a further reduced order model by classical modal analysis, which is the secondary modal analysis indicated by the name of the method. The constraint-mode portions of the selected mode shapes, $\tilde{\mathbf{u}}_{\mathbf{cb}}^{\mathbf{h,c}}$, are collected into a cyclic modal matrix $\tilde{\mathbf{U}}_{\mathbf{cb}}^{\mathbf{s,c}}$, while the normal-blade-mode portions, $\tilde{\mathbf{u}}_{\mathbf{cb}}^{\mathbf{h,b}}$, are collected into $\tilde{\mathbf{U}}_{\mathbf{cb}}^{\mathbf{s,b}}$. The associated eigenvalues are collected into a cyclic generalized stiffness matrix $\tilde{\mathbf{\Lambda}}_{\mathbf{cb}}^{\mathbf{s}}$. Both the mode selection process and the resulting reduced tuned system follow the discussion in Section 5.5 for the mistuning projection method. The difference, however, is that the selected eigenvalues are exact (with respect to the parent finite element model) in the mistuning projection method, while they are only as accurate as the intermediate model in the SMART case.

As shown in Eq. (5.34), mistuning is represented in the C-B model by perturbing the diagonal elements of the normal-blade-mode (bb) partition, which represent the individual modal stiffnesses for each cantilevered blade mode of each blade in the assembly. Hence, using the selected tuned, cyclic modes as the basis for the secondary modal expansion, mistuning enters into the SMART model by projecting these modal stiffness perturbations onto the selected tuned modes of the assembly. Note that the perturbations are in normal coordinates while the nominal modes are cyclic. Hence, the mistuning projection takes the form:

$$\mathbf{\Delta}\tilde{\mathbf{K}}_{\mathbf{cb}}^{\mathbf{s}} = \tilde{\mathbf{U}}_{\mathbf{cb}}^{\mathbf{s,b^T}} \hat{\mathbf{F}}^{\mathbf{T}} \mathbf{B} \underset{n=1,\ldots,N}{\mathbf{diag}} \left[\underset{k=1,\ldots,m_b}{\mathbf{diag}} \left[\delta_n^k \right] \mathbf{\Lambda_b} \right] \hat{\mathbf{F}} \tilde{\mathbf{U}}_{\mathbf{cb}}^{\mathbf{s,b}}. \tag{5.59}$$

Note that only the mode shape portions pertaining to the blade normal modes are involved in the projection, which normally are of modest size. Equation (5.59) represents the key

to this method's versatility and suitability for statistical studies: versatility by enabling input of a practical measure of mistuning obtained for cantilevered blades; and suitability for statistical studies due to its computational efficiency, since this mistuning projection is made in the low-order modal domain. In the next section, it is shown how the latter makes the task of obtaining comprehensive forced response statistics nearly effortless compared to other methods of comparable accuracy.

With the mistuning projection in place, the SMART C-B model may be formulated as

$$\ddot{\mathbf{q}} + \tilde{\mathbf{C}}^{\mathbf{s}}_{\mathbf{cb}}\dot{\mathbf{q}} + (1+Gj)\left[\tilde{\mathbf{\Lambda}}^{\mathbf{s}}_{\mathbf{cb}} + \mathbf{\Delta}\tilde{\mathbf{K}}^{\mathbf{s}}_{\mathbf{cb}}\right]\mathbf{q} = \tilde{\mathbf{F}}^{\mathbf{s}}_{\mathbf{cb}}, \tag{5.60}$$

where

$$\begin{aligned}
\tilde{\mathbf{C}}^{\mathbf{s}}_{\mathbf{cb}} &= \tilde{\mathbf{U}}^{\mathbf{s,b^T}}_{\mathbf{cb}}\left[\mathbf{I}\otimes\underset{k=1,\ldots,m_b}{\mathbf{diag}}\left[2\zeta^k\right]\sqrt{\mathbf{\Lambda_b}}\right]\tilde{\mathbf{U}}^{\mathbf{s,b}}_{\mathbf{cb}} \\
\tilde{\mathbf{F}}^{\mathbf{s}}_{\mathbf{cb}} &= \left\{\begin{array}{c} \mathbf{0} \\ \vdots \\ \mathbf{0} \\ \tilde{\mathbf{u}}^{\mathbf{C,c^T}}_{\mathbf{cb}}\tilde{\mathbf{F}}^{\mathbf{C,c}}_{\mathbf{cb}} + \tilde{\mathbf{u}}^{\mathbf{C,b^T}}_{\mathbf{cb}}\tilde{\mathbf{F}}^{\mathbf{C,b}}_{\mathbf{cb}} \\ \mathbf{0} \\ \vdots \\ \mathbf{0} \end{array}\right\} \\
\tilde{\mathbf{F}}^{\mathbf{C,c}}_{\mathbf{cb}} &= \left\{\begin{array}{l} \sqrt{N}\mathbf{f}^{\mathbf{T}}_{\mathbf{C,c}}\mathbf{e}_{\mathbf{C+1}}\otimes\left\{\mathbf{\Psi}^{\mathbf{T}}_{\mathbf{b}}\mathbf{f}_{\mathbf{B}} + \mathbf{f}_{\mathbf{\Gamma}}\right\} \\ \sqrt{N}\mathbf{f}^{\mathbf{T}}_{\mathbf{C,s}}\mathbf{e}_{\mathbf{C+1}}\otimes\left\{\mathbf{\Psi}^{\mathbf{T}}_{\mathbf{b}}\mathbf{f}_{\mathbf{B}} + \mathbf{f}_{\mathbf{\Gamma}}\right\} \end{array}\right\} \\
\tilde{\mathbf{F}}^{\mathbf{C,b}}_{\mathbf{cb}} &= \left\{\begin{array}{l} \sqrt{N}\mathbf{f}^{\mathbf{T}}_{\mathbf{C,c}}\mathbf{e}_{\mathbf{C+1}}\otimes\mathbf{\Phi}^{\mathbf{T}}_{\mathbf{b}}\mathbf{f}_{\mathbf{B}} \\ \sqrt{N}\mathbf{f}^{\mathbf{T}}_{\mathbf{C,s}}\mathbf{e}_{\mathbf{C+1}}\otimes\mathbf{\Phi}^{\mathbf{T}}_{\mathbf{b}}\mathbf{f}_{\mathbf{B}} \end{array}\right\}.
\end{aligned}$$

Note that this generally leads to a fully populated, symmetric stiffness matrix, similar to that of the mistuning projection method.

5.8 Comparison of Methods

In this section, the number of floating point operations (flops) required to set up and use a reduced order model is estimated for some of the previously introduced techniques. Four methods have been selected for this comparison — Craig-Bampton, REDUCE, mistuning projection, and SMART Craig-Bampton. From the outset it is realized that including REDUCE in this comparison is not quite fair, as REDUCE does not possess nearly the same accuracy as the other methods. However, since REDUCE has gained popularity with several industrial users, it is included as a benchmark for comparison.

The standard algorithms for matrix inversion (for solving $\mathbf{Ax} = \mathbf{b}$) and multiplication of square matrices are $\mathcal{O}(n^3)$ processes, where n is the order of the matrix (Strang [64]). Moreover, for this comparison it is essential to have an estimate of the computational effort involved in solving an eigenvalue problem, since it is a central component in all methods. However, this is not possible to obtain explicitly, because it is an iterative process for $n > 2$. Since some estimate of the eigensolver cost is necessary, a brief numerical investigation was conducted using MATLAB™, which has a built-in flops counter. Two matrices, $\mathbf{A}$ and $\mathbf{B}$, were constructed with increasing size n as follows (upper triangle only):

$$A_{ij} = \begin{cases} \frac{i^4}{j^2} & i = j \\ -\frac{i^2}{j} & i \neq j \end{cases} \qquad B_{ij} = \begin{cases} \frac{(i+j)^2}{i^2} & i = j \\ -\frac{(i+j)}{i} & i \neq j \end{cases} \qquad \begin{matrix} j = 1, \ldots, n \\ i = 1, \ldots, j. \end{matrix} \tag{5.61}$$

The generated matrices, which are fully populated, real-valued, symmetric, positive definite, and diagonally dominant, were used to get estimates of the required number of flops for the three basic matrix operations required here: generalized real, symmetric eigensolutions, $\mathbf{Au} = \mathbf{\Lambda Bu}$; multiplication of two square matrices, $\mathbf{A} \cdot \mathbf{B}$; and matrix inversion, $\mathbf{A^{-1}}$. The results are shown in Fig. 5.4.

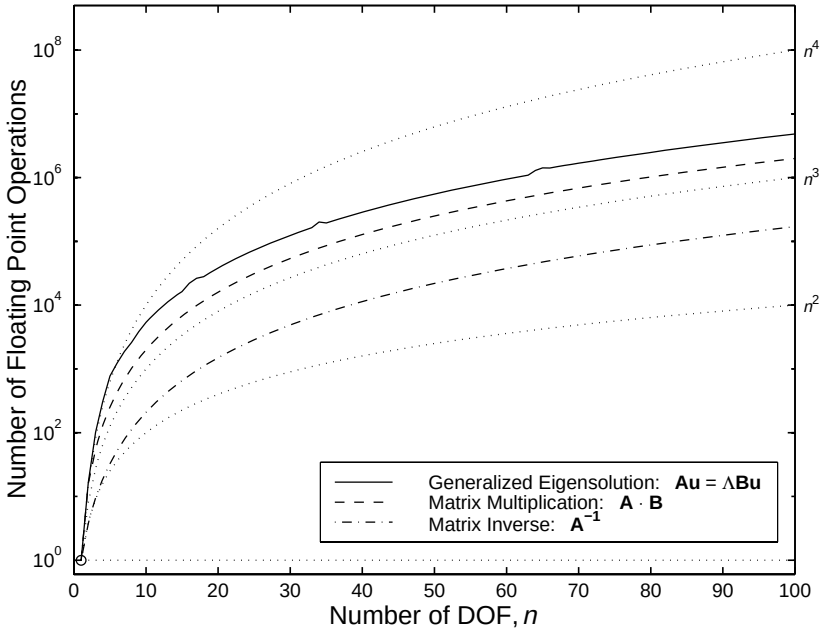

Figure 5.4: Required number of floating point operations (flops) as a function of matrix size for generalized eigensolution, matrix multiplication, and matrix inversion. Note the slight "bumps" due to the iterative nature of the eigensolution.

The results in Fig. 5.4 confirm the n^3-proportionality of matrix inversion and multiplication. The eigensolution closely follows the n^3-curve, too. Hence, it is assumed that n^3-proportionality may be used for all three matrix operations to get fair comparisons. Note that the iterative nature of the eigenvalue problem shows up in Fig. 5.4 as a few slight "bumps".

To compare the methods pseudo-quantitatively, estimates of the required flops during statistical studies were obtained. The term "pseudo" is used because the flops count only considers the three basic types of operations mentioned above, not the various administrative tasks, variable initialization, passing of variables, etc. Furthermore, the flops count does not take efficient coding into consideration, such as using sparse matrix routines. Hence, the results presented here should not be taken as the true "costs" required by actual analyses. However, they should provide a fair basis for a rough comparison of the

methods.

The “initial conditions” for each method are the required finite element structural matrices for the components. Table 5.1 outlines the model dimensions used in this comparison, which represent fairly typical dimensions for a finite element model of an industrial bladed disk. Table 5.2 outlines the essential steps considered for each method. The upper portion of Table 5.2 represents the model setup. The lower portion contains the required steps for the mistuned forced response, which must be repeated for each new mistuning pattern. The results are shown in Figs. 5.5 (model setup cost included) and 5.6 (model setup cost excluded).

As Fig. 5.5 indicates, the mistuning projection method and REDUCE carry a similar setup cost, due largely to the set of cyclic eigenvalue problems involving the fundamental sector they have in common. Recall, the blades are massless in the REDUCE method, but the problem size is unaffected by this fact. Note how insignificant is the effort required to go from a C-B model to a SMART model. Of course, the set of cyclic eigenvalue problems using the C-B model does result in an increased setup cost for the SMART model, but that cost is trivial on this scale.

A mistuned forced response statistics simulation was carried out for Figs. 5.5 and 5.6 by calculating the mistuned response at 1000 sampled excitation frequencies for 100 mistuning patterns. From Fig. 5.5, it is clear that the C-B model suffers from carrying all the interface DOF in the reduced order model. It is equally clear that the mistuning projection in the physical domain severely degrades the performance of the mistuning projection method. Note that even in the simplistic case of mistuning via Young’s modulus offsets there is a significant number of operations required to project the mistuning. In contrast, studying a sequence of mistuning patterns is relatively effortless with the SMART model.

Figure 5.6 shows the flops after the setup costs, to highlight the “long-term” perfor-

Number of…	**Variable**	**Value**
Blades	N	50
Blade Interior (B) DOF	n_b	2000
Disk Independent (D+α) DOF	n_d	1000
Disk-Blade Interface (Γ) DOF	n_c	100
Blade Modes	m_b	3
Disk Modes (per harmonic)	m_d	3

Table 5.1: Assumed model dimensions for flops count.

Calculation	**C-B**	**SMART**	**M. P.**	**RED.**
Sector Normal Modes		M	X	X
Blade Normal Modes	X	X		X
Blade Constraint Modes	X	X		
Disk Normal Modes	X	X		
Disk Constraint Modes	X	X		
Model Assembly	X	X		X
Modal Force	X	X	X	X
Mistuning Projection		M	X	
Response Amplitudes	M	M	M	M

Table 5.2: Essential steps during model construction and use in a forced response statistical study (M = Modal domain, M. P.=Mistuning Projection method, RED.=REDUCE).

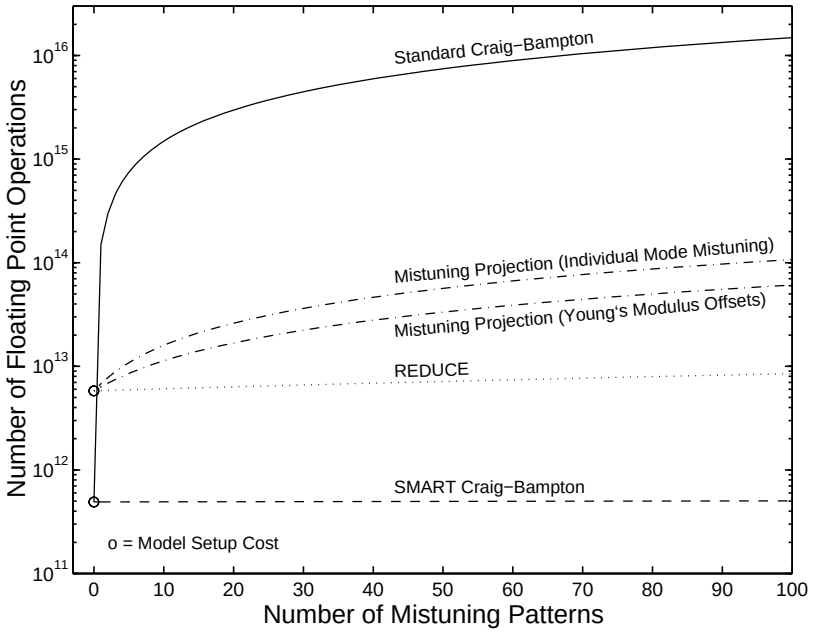

Figure 5.5: Comparison of estimated cumulative numbers of floating point operations during statistical analyses for selected methods, including the model setup cost.

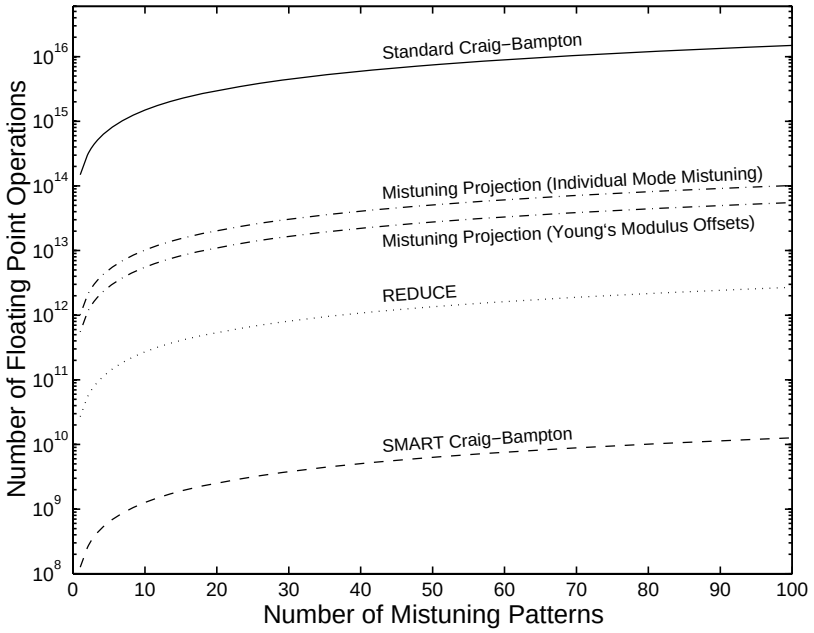

Figure 5.6: Comparison of estimated cumulative numbers of floating point operations during statistical analyses for selected methods, disregarding the model setup cost.

mance of each method. REDUCE demonstrates good speed, and requires approximately one and four orders of magnitude fewer flops per mistuning pattern than mistuning projection and C-B, respectively. However, it must again be emphasized that REDUCE lacks the high accuracy of those two methods. As shown, SMART cuts the flops even further: it is close to four orders of magnitude less computationally intensive per mistuning pattern than mistuning projection. Thus, it is deduced that SMART is clearly the most appealing method for performing vibration analyses of mistuned bladed disks.

5.9 Conclusions

Component mode synthesis (CMS) is an efficient technique for dynamic analyses of complex structures. However, the applications of CMS to mistuned bladed disk assemblies are remarkably scarce. In this first part of the two-part paper, it was shown how the Craig-Bampton (C-B) method of CMS can be applied to mistuned bladed disks in a systematic manner.

The primary contribution of this paper is the introduction of four new approaches for efficient and realistic modeling of mistuned bladed disks. Two of the new methods are modifications of the classical Craig-Bampton method by partial secondary modal analyses:

1. Modal interface formulation.

2. Modal interface *plus* disk formulation.

These two methods result in comparable, significant order reduction beyond that provided by the initial C-B formulation. The remaining two methods utilize the assumption of a common deformation space for tuned and mistuned mode families:

3. Mistuning Projection Method:

   Classical modal analysis of the tuned finite element model, followed by a projection

of individual blade mistuning onto the retained system modes.

4. Secondary Modal Analysis Reduction Technique (SMART):

   Formulation of a cyclic Craig-Bampton model, followed by classical modal analysis of the full C-B model. The mistuning is input in the C-B modal space and then projected to the SMART model via the blade portions of the retained secondary modes.

This results in minimized reduced order models, while requiring projection of blade mistuning data onto a selection of tuned modes.

A subset of the developed methods were compared by means of a theoretical count of floating point operations required for model setup and use in statistical forced response predictions. It was demonstrated that the most straightforward technique — the mistuning projection method — suffers a high computational cost due to carrying out the mistuning projections in the physical domain. In contrast, the SMART mistuning projections are performed in the low-order modal domain. Furthermore, it was shown that SMART analyses are exceptionally fast. Therefore, it is clear that the SMART approach is well-suited for performing comprehensive studies of mistuned forced response statistics.

CHAPTER VI

Component-Mode-Based Reduced Order Modeling Techniques for Mistuned Bladed Disks, Part II: Application

In this paper, the component-mode-based methods formulated in the companion paper (Part I: Theoretical Models) are applied to the dynamic analysis of two example finite element models of bladed disks. Free and forced responses for both tuned and mistuned rotors are considered. Comprehensive comparisons are made among the techniques using full system finite element solutions as a benchmark. The accurate capture of eigenfrequency veering regions is of critical importance for obtaining high-fidelity predictions of the rotor's sensitivity to mistuning. Therefore, particular attention is devoted to this subject. It is shown that the Craig-Bampton component mode synthesis (CMS) technique is robust and yields highly reliable results. However, this is achieved at considerable computational cost due to the retained component interface degrees of freedom (DOF). It is demonstrated that this problem is alleviated by a secondary modal analysis reduction technique (SMART). In addition, a non-CMS mistuning projection method is considered. Although this method is elegant and accurate, it is seen that it lacks the versatility and efficiency of the CMS-based SMART. Overall, this work shows that significant improvements on the accuracy and efficiency of current reduced order modeling methods are possible.

6.1 Introduction

The blades of a bladed disk are intended to be identical, but in fact there are always small, random differences among the blades, called mistuning. Mistuning can result in blade forced response amplitudes and stresses that are much larger than those predicted for a perfectly tuned rotor. (See Srinivasan [17] for a comprehensive survey of the literature.) Thus, mistuning has a critical impact on blade fatigue life in turbine engines, and it is of great importance to be able to predict the mistuned forced response in an accurate and efficient manner. Several recent studies have presented reduced order modeling techniques that are capable of generating low order models of bladed disks from parent finite element models (Irretier [18]; Zheng and Wang [19]; Kruse and Pierre [21, 22]; Castanier *et al*. [20]; Yang and Griffin [26, 27]; Bladh *et al*. [23]).

In the companion paper (Part I: Theoretical Models), some new reduced order modeling techniques were introduced that are well-suited for the efficient and accurate vibration analysis of mistuned bladed disks. These techniques are summarized as follows:

- **Craig-Bampton (C-B) Method:** The C-B method (Craig and Bampton [29]) of Component Mode Synthesis (CMS), formulated specifically for bladed disks, is employed. A cyclic symmetry description is used for the disk component. Each blade is treated as a separate component.

- **C-B method with secondary modal analysis on matrix partitions:** The C-B method is used to generate a primary reduced order model, and then a secondary eigen-analysis is performed on partitions of the C-B mass and stiffness matrices. A truncated set of these eigenvectors is used to transform the matrices to secondary modal coordinates in order to further reduce the model size. In particular, there are two choices of matrix partitions that are convenient for this secondary reduction:

  - constraint-mode degrees of freedom (DOF)
  - constraint-mode plus disk-mode DOF

- **Mistuning projection method:** A classical modal analysis is performed on the full finite element model, and then the individual blade mistuning is projected onto the cyclic system modes.

- **Secondary Modal Analysis Reduction Technique (SMART):** A primary reduced order model is generated using CMS (e.g., the C-B method), and then a secondary modal analysis is performed on the full CMS matrices. Only the system modes of interest are retained. Blade mistuning is introduced in the CMS matrices (blade component DOF) and then projected from the primary modal coordinates to the secondary modal coordinates.

In addition, the method of Castanier *et al*. [20] was revisited, which is here denoted REDUCE. Since the code is being actively used in industry, REDUCE represents the current state of the art.

In this paper, the above techniques are applied to simple, yet representative finite element models of bladed disks. First, tuned free vibrations are considered, and the methods are compared by studying their modal convergence trends. The eigenfrequency veerings that occur when plotting natural frequencies versus number of nodal diameters have been shown to play a crucial role in determining a bladed disk's sensitivity to mistuning (Kruse and Pierre [21]; Bladh *et al*. [54]). Therefore, the modal convergence study focuses on how well the derived methods capture the eigenfrequencies in a particular veering region.

Next, it is demonstrated how well the methods represent mistuned, localized modes of vibration. A modal convergence study is presented with respect to the capture of both mistuned natural frequencies and mistuned mode shapes using the well-known Modal As-

surance Criterion, or MAC (Allemang and Brown [63]). This study is relevant, since the introduction of mistuning data differs among the methods and results in an approximation for some of them. Hence, a good tuned representation does not necessarily translate to a good mistuned representation.

Predictions of forced response amplitudes are then considered, for both tuned and mistuned configurations. This is the primary application of these methods. The efficiency and accuracy of the methods are examined via forced response frequency sweeps. The SMART approach is also applied to a large-size model, using a C-B model as the intermediate CMS basis. The excellent accuracy and tremendous computational savings that result from using this approach are demonstrated.

This paper is organized as follows. The finite element models used in this study are presented in Section 6.2. The validation of the developed methods begins with free vibration results in Section 6.3, where particular emphasis is placed on the capture of tuned natural frequency veerings and the mistuned mode shapes. Forced response results are examined in Section 6.4. In Section 6.5, the SMART approach is validated for a large-size model to further demonstrate the potential of this method. Finally, concluding remarks are given in Section 6.6.

6.2 Description of Example Finite Element Models

Two different finite element models of mistuned bladed disks are used for the validation of the developed methods:

- A simple, “small” model (see Fig. 6.1) that allows for extensive studies of modal convergence.
- A more realistic, “large” model (see Fig. 6.2) that is used to demonstrate the potential of the SMART approach.

The finite elements are all eight-noded brick (linear solid) elements. It should be noted that both meshes are relatively coarse compared to that of a typical industrial finite element model, and they may not represent precisely the behavior of actual bladed disks with the depicted geometries. However, this is not a concern for this study, since all of the methods are applied to the same parent finite element models.

The material properties for both models are those of steel (see Table 6.1). However, the models differ in the structural damping coefficient, G, used during the forced response. Note that viscous damping is not considered in this study.

For the mistuned results, a single mistuning pattern is used for each model. The mistuning patterns were sampled from a uniform distribution of mean zero, and one mistuning value, δ_n, is assigned to each blade. The mistuning is introduced to the full finite element model by varying Young's modulus in the blade elements:

$$E_n = (1 + \delta_n)\, E_o, \qquad n = 1, \ldots, N, \tag{6.1}$$

where n is the blade number and N is the total number of blades. Note that the methods developed in this study are not restricted to mistuning by variations in Young's modulus. However, individual mode mistuning is not considered in this paper.

Property	**Notation**	**Value**	**Unit**
Nominal Young's Modulus	E_o	$2.00 \cdot 10^5$	MPa
Poisson's Ratio	ν	0.25	—
Mass Density	ϱ	$7.86 \cdot 10^3$	kg/m^3

Table 6.1: Material properties (generic steel) for both models.

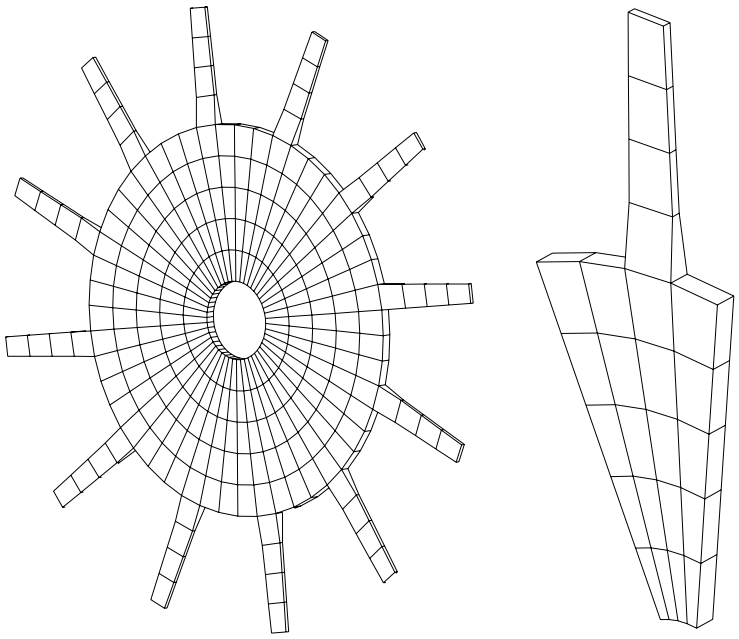

(a) (b)

Figure 6.1: Finite element meshes for the “small” example blisk: (a) the full model; (b) the fundamental sector.

6.2.1 Small Example Finite Element Model

The smaller of the two finite element models that are analyzed in this study is shown in Fig. 6.1. Due to its relatively low number of DOF, this model is used extensively in this study. This model features 12 blades, each with length 60 mm and base width 7.5 degrees ($\sim$13 mm). The blades are slightly tapered along the radial direction, from 5 mm thickness at the base to 2 mm thickness at the tip. The disk is 5 mm thick. It has an outer radius of 100 mm, and an inner radius of 20 mm. The disk is clamped at the inner radius.

For the Craig-Bampton method, the fundamental sector in Fig. 6.1b is further substructured into a disk sector component (for a cyclic symmetry analysis) and a blade component. Model data for the components are listed in Table 6.2. For the forced response, the structural damping coefficient is taken to be $G = 0.01$.

The single mistuning pattern used for this model is taken from a uniform distribution

Component	**Elements**	**Nodes**	**DOF**
Cantilevered Blade	4	20	48
Disk Sector	20	60	108
Disk-Blade interface	—	4	12
Fundamental Sector	24	76	168
Full Assembly	288	768	2016

Table 6.2: Basic model data for the small model.

Blade	δ_n	**Blade**	δ_n	**Blade**	δ_n
1	-0.0276	5	0.0161	9	-0.0107
2	0.0050	6	-0.0112	10	-0.0090
3	0.0449	7	0.0132	11	0.0161
4	-0.0171	8	0.0207	12	0.0351

Table 6.3: Single mistuning pattern for the small model.

of mean zero and standard deviation 3.0%. The mistuning parameters, δ_n, used for each blade are listed in Table 6.3.

6.2.2 Large Example Finite Element Model

The finite element model of the "large" test case rotor is depicted in Fig. 6.2. This model is used in Section 6.5 as a more realistic case. This rotor has 24 blades. Each blade has a base pitch of 30 degrees (measured from the axial direction), and a uniform twist of an additional 30 degrees over its length. The base radius is 212 mm, and the blade length is 68 mm. The rotor is fixed at the interfaces towards adjacent stages. This is believed to provide a reasonable description of the dynamics of a bladed disk assembly.

As was done with the smaller model, the fundamental sector is substructured into a

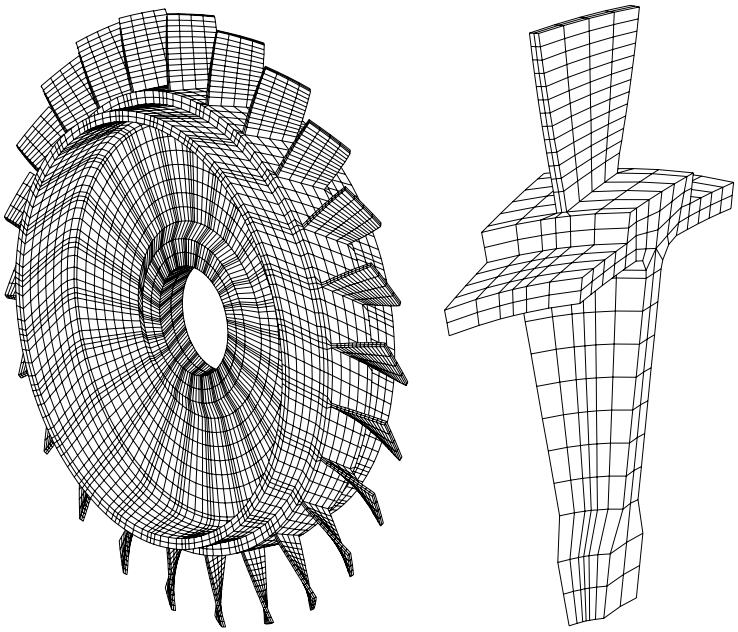

(a) (b)

Figure 6.2: Finite element meshes for the “large” example blisk: (a) the full model; (b) the fundamental sector.

Component	**Elements**	**Nodes**	**DOF**
Cantilevered Blade	104	210	585
Disk Sector	372	651	1521
Disk-Blade interface	—	15	45
Fundamental sector	476	846	2151
Full assembly	11,424	18,072	51,624

Table 6.4: Basic model data for the large model.

disk sector and a blade component. The model data are found in Table 6.4. This model is assigned a structural damping coefficient of $G = 0.0025$.

The single mistuning pattern is taken from a uniform distribution of mean zero and standard deviation 5.0%. The corresponding mistuning parameters, δ_n, are listed in Table 6.5.

Blade	δ_n	**Blade**	δ_n	**Blade**	δ_n
1	-0.00515	9	0.02930	17	-0.00415
2	-0.01875	10	0.02720	18	0.00430
3	-0.01820	11	0.02770	19	0.01840
4	-0.00390	12	-0.04925	20	-0.05475
5	-0.05005	13	-0.08075	21	0.02395
6	-0.00850	14	-0.04905	22	0.03810
7	0.01415	15	0.05935	23	0.04110
8	0.07620	16	-0.06925	24	0.03930

Table 6.5: Single mistuning pattern for the large model.

6.3 Free Vibration

6.3.1 Tuned Assembly

In Fig. 6.3, an assessment is made of the small model's tuned characteristics by plotting the natural frequencies of the tuned system versus the number of nodal diameters. The nearly horizontal connecting lines correspond to assembly modes that are dominated by blade motion, while the slanted connecting lines correspond to disk-dominated modes. The rapid increase of the eigenfrequencies of the disk-dominated modes is due to stiffening of the disk as the circumferential wavelength decreases with increasing number of nodal diameters.

Two significant eigenfrequency veering regions are highlighted in Fig. 6.3: one located at one nodal diameter, around 3300 Hz (Veering #1); and a second located at three nodal diameters, around 6500 Hz (Veering #2). Earlier studies (Kruse and Pierre [21]; Bladh *et al*. [54]) have shown that the characteristics of eigenfrequency veerings are crucial in determining a design's sensitivity to mistuning. Furthermore, it has been found

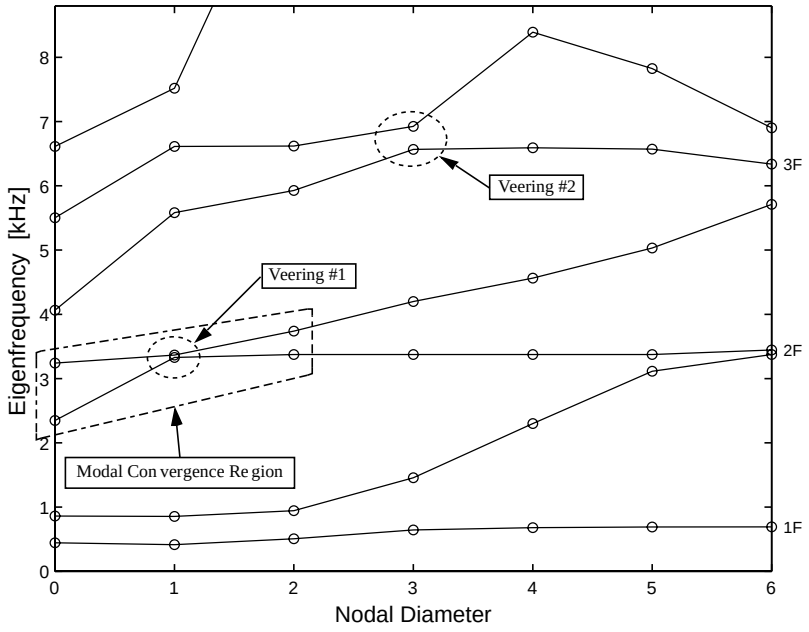

Figure 6.3: Natural frequencies versus nodal diameters for the small example finite element model. The circles show the natural frequency values, while the connecting lines are drawn to aid in visualization of the mode families and the frequency veerings. The character of each family of blade-dominated modes is indicated on the right (e.g., 1F = 1st flex mode).

that maximum mistuned forced response amplitudes are likely to occur in veering regions (that is, when the frequency and engine order of excitation correspond to the frequency and nodal diameters of a veering). Therefore, the ability to capture veering regions is an important consideration when assessing the performance of a modeling method.

As pointed out in Part I, all methods considered in this study are complete, in the limit, for the tuned case: they yield the finite element solution when all the component modes are included in the model. Hence, for the tuned case, one may compare the performance of the methods by examining their rates of modal convergence. In combination with the veering discussion above, the methods are evaluated by comparing modal convergence trends based on the eigenfrequency errors in the “Modal Convergence Region” of Fig. 6.3.

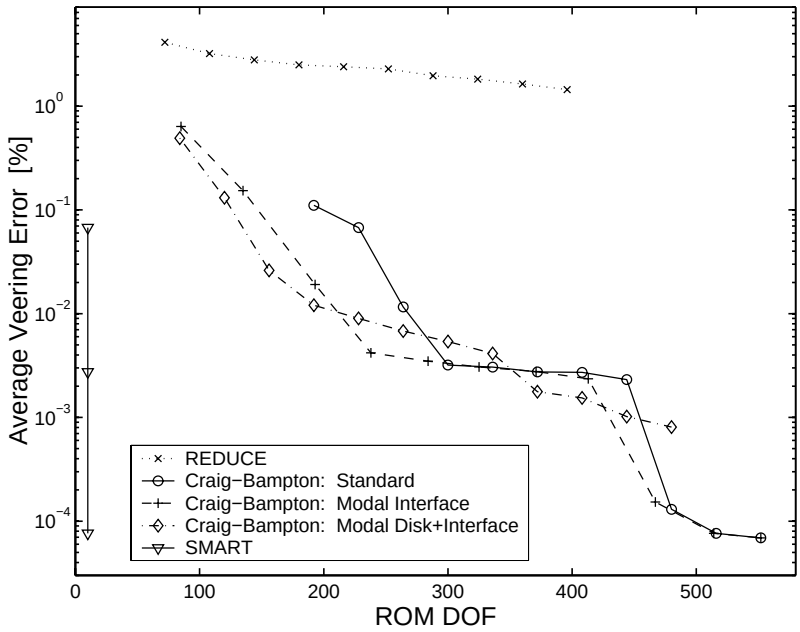

Figure 6.4: Modal convergence trends in the region surrounding Veering #1 for the small example model.

The modal convergence for each method (except for mistuning projection, which is irrelevant for the tuned case) is presented in Fig. 6.4. This figure shows the average percent error among the six distinct eigenfrequencies in the Modal Convergence Region versus the number of retained modes in the reduced order model (ROM). Note that there are actually ten modes in this region: four double modes, and two single modes. However, to avoid counting the double-mode errors twice, this region is evaluated at only the six distinct eigenfrequencies. The results in Fig. 6.4 clearly illustrate the remarkable difference in both accuracy and modal convergence rate between the standard C-B model and REDUCE. However, it must be emphasized that the superiority of the C-B model is achieved at a considerable expense in terms of minimum model size relative to REDUCE. As shown, C-B does not capture this veering at all with fewer than around 200 DOF, while REDUCE yields a fair veering representation with much fewer than 100 DOF.

Moreover, it is here demonstrated that the C-B representation may be improved upon

by the partial secondary modal analyses on either the constraint-mode partition (modal interface), or the disk-normal-mode plus constraint-mode partitions (modal disk+interface). There are two principal beneficial effects of this: (1) a fair approximation of the veering eigenfrequencies is obtained with a much smaller model than the smallest possible standard C-B model; (2) the characteristic modes representation yields the same accuracy level with fewer DOF compared to the standard C-B model. However, the improvement gained by the partial secondary modal analyses is nevertheless deemed insufficient in terms of justifying the additional effort. Thus, these two methods are not considered in results presented later in this paper.

The vertical line in Fig. 6.4 represents the SMART approach with a C-B model as intermediate CMS basis. The implication of the vertical line is that the tuned SMART model is always as accurate as the intermediate CMS model from which it derives, while its size stays constant at the number of modes selected by the analyst. Hence, it may be viewed as collapsing the C-B model onto an arbitrarily smaller, n-dimensional subspace. Alternatively, a graphical interpretation using Fig. 6.4 would be to collapse a C-B model of certain accuracy horizontally to the left onto a point on an arbitrarily positioned vertical line. In Fig. 6.4, where only six modes are considered, the SMART model has only the minimum six DOF. Note that using SMART for tuned free vibration analyses makes no sense; it is included here only to aid in demonstrating the approach.

6.3.2 Mistuned Assembly

The small model is now mistuned by offsets in blade Young's modulus, in accordance with Eq. (6.1) and Table 6.3. First, the selected methods' representations of two mistuned mode shapes are considered. The finite element mode shapes and the approximations obtained through the various methods are depicted in Figs. 6.5 and 6.6. The obtained

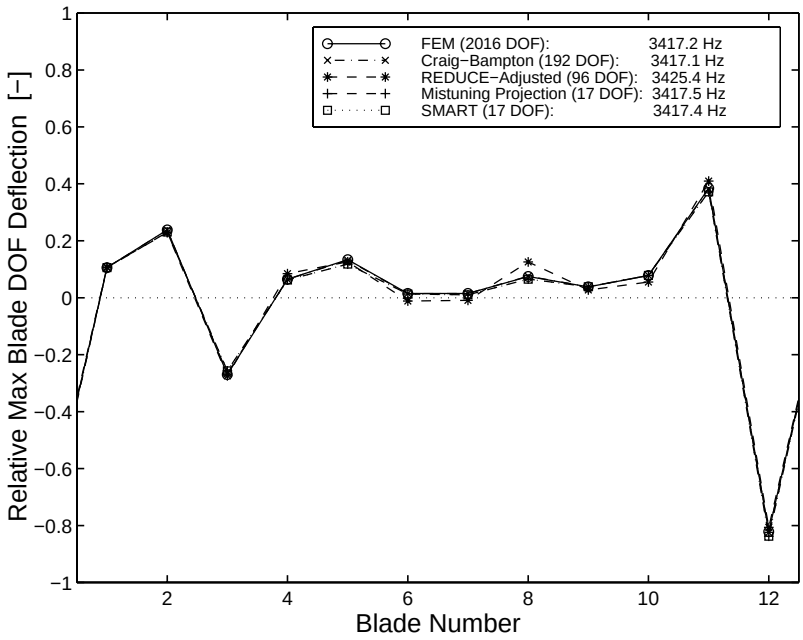

Figure 6.5: Reduced order model representations of mistuned mode shape number 37 for the small example model.

mode shape representations come from first finding the maximum physical displacement of any DOF in any blade. The physical displacements of the DOF where the maximum was found are then plotted for each blade, normalized by the Euclidean norm of the N displacements as

$$A^n = \frac{z_m^n}{\sqrt{\sum_{n=1}^{N} z_m^{n^2}}}, \qquad n = 1, \ldots, N, \tag{6.2}$$

where z_m^n is the displacement in physical coordinates for the n^{th} blade's m^{th} DOF (the DOF at which the maximum was found).

The two modes depicted in Figs. 6.5 and 6.6 belong to the second family of blade-dominated system modes (2F, see Fig. 6.3) located around 3300 Hz. The two mode shapes can be characterized as intermediately localized, which means that several blades participate in the motion, but there is still a clear dominance by one or two blades. This type of intermediate localization has been shown to cause the most severe increases in resonant forced response amplitudes (Óttarsson and Pierre [16]; Bladh *et al*. [54]).

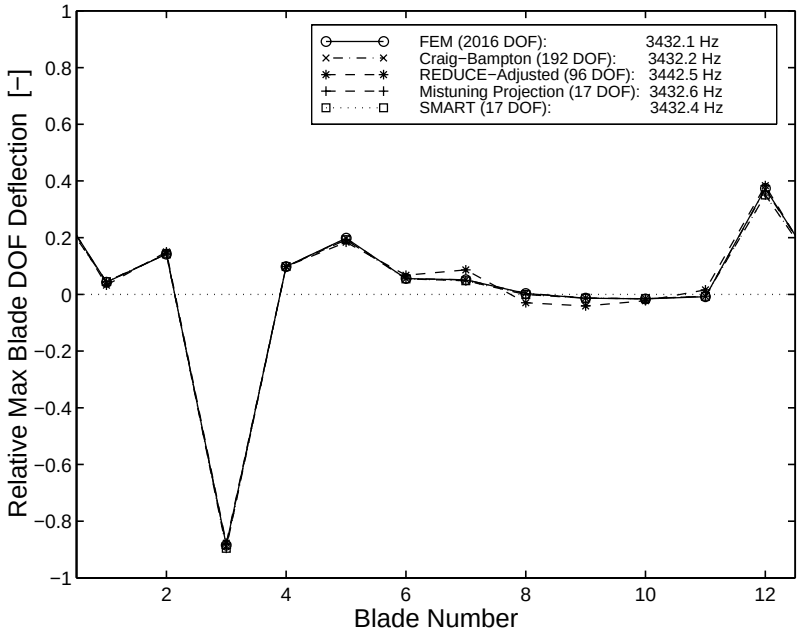

Figure 6.6: Reduced order model representations of mistuned mode shape number 38 for the small example model.

The SMART model used here is based on an intermediate C-B model that incorporates the first seven normal disk modes and the first six normal blade modes (plus the complete set of constraint modes). Furthermore, the 17 tuned modes that fall inside the frequency range 3000–3500 Hz are selected for both the mistuning projection method and the SMART approach. This means that the two models include all harmonics of the tuned modes associated with the second family of blade-dominated modes. This completeness in terms of harmonic content is a basic requirement for these methods.

Except for REDUCE, note the excellent agreement among eigenfrequencies in Figs. 6.5 and 6.6. The relative error is less than 0.02% for both modes. REDUCE, however, cannot quite match these excellent results with errors around 0.3%. These results translate nicely to the mode shapes as well, where the approximated shapes are virtually indistinguishable from those obtained by full finite element analysis. Although REDUCE's mode shape representations are not as accurate, the method does an excellent job in capturing the relative

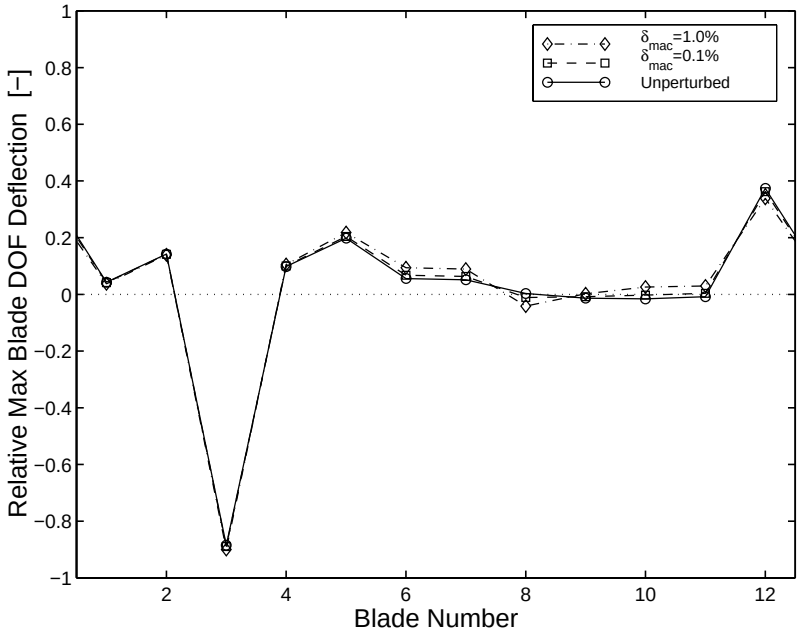

Figure 6.7: Sensitivity of Modal Assurance Criterion (MAC) values (mistuned mode shape number 38).

peaks as well as their locations.

Next, an aspect of method efficiency is investigated. All the obtained approximations of natural frequencies and mode shapes are compared to the finite element results, in order to establish how many system modes each method captures versus the number of possible modes, m_r (i.e., the total number of DOF in the ROM). A system mode is regarded as "captured" if the error is below a pre-defined tolerance — δ_f for natural frequencies, or δ_{mac} for mode shapes. The obtained natural frequencies, f_i^r, are compared with the finite element frequencies, f_j^{fe}, through straightforward fractions

$$\frac{f_i^r}{f_j^{fe}} - 1 \leq \delta_f, \qquad i = 1, \ldots, m_r; \quad j = 1, \ldots, m_{fe}, \tag{6.3}$$

where m_{fe} is the total number of DOF in the full finite element model. If the above inequality is satisfied for any f_j^{fe}, then the natural frequency f_i^r is regarded as captured. In a similar fashion, the approximated mode shapes, $\psi_{\mathbf{i}}^{\mathbf{r}}$, are compared to the exact ones via

MAC conformity:

$$1 - \frac{\left(\psi_{\mathbf{i}}^{\mathbf{r}^{\mathbf{T}}} \psi_{\mathbf{j}}^{\mathbf{fe}}\right)^2}{\left(\psi_{\mathbf{i}}^{\mathbf{r}^{\mathbf{T}}} \psi_{\mathbf{i}}^{\mathbf{r}}\right)\left(\psi_{\mathbf{j}}^{\mathbf{fe}^{\mathbf{T}}} \psi_{\mathbf{j}}^{\mathbf{fe}}\right)} \leq \delta_{mac}, \qquad i = 1, \ldots, m_r; \quad j = 1, \ldots, m_{fe}, \tag{6.4}$$

where $\psi_{\mathbf{j}}^{\mathbf{fe}}$ is the finite element mode shape of the j^{th} mode. It is clear that when an exact match between two mode shapes is obtained, the MAC ratio becomes one; it is between zero and one in all other cases. However, it is not clear just how good a match a MAC value of, for instance, 0.99 represents. To assess this, the 38^{th} mistuned mode shape in Fig. 6.6 was perturbed by applying randomly generated scale factors to each blade's relative amplitude. The MAC conformity with respect to the unperturbed shape was then computed. The resulting perturbed mode shapes are shown in Fig. 6.7 for MAC values of 0.99 and 0.999. Note that a 1.0% deviation from a perfect match might be considered a very good representation of the mode shape.

The two different tolerance levels (1.0% and 0.1%) were employed in order to get an indication of how large the errors were among the unacceptable modes. The separate results for natural frequencies and mode shapes are shown in Figs. 6.8–6.11. As indicated, the straight line, $y = x$, represents what could be called the "ROM Jackpot", which means that one system mode of desired accuracy is captured for each DOF in the ROM.

The C-B formulation suffers considerably from having a full, physical set of interface DOF in the ROM. These DOF, the constraint modes, are of course necessary in order to form the flexible motion of the otherwise fully constrained interfaces. However, they also result in many purely computational modes, which have little or no physical meaning, leading to the relatively poor efficiency displayed by the C-B method. Moreover, by relaxing the tolerance level to 1.0%, the results show that C-B gives only fair (0.1–1.0%) representations of several modes.

Note that the REDUCE model quickly yields "recognizable" mode shapes. Moreover,

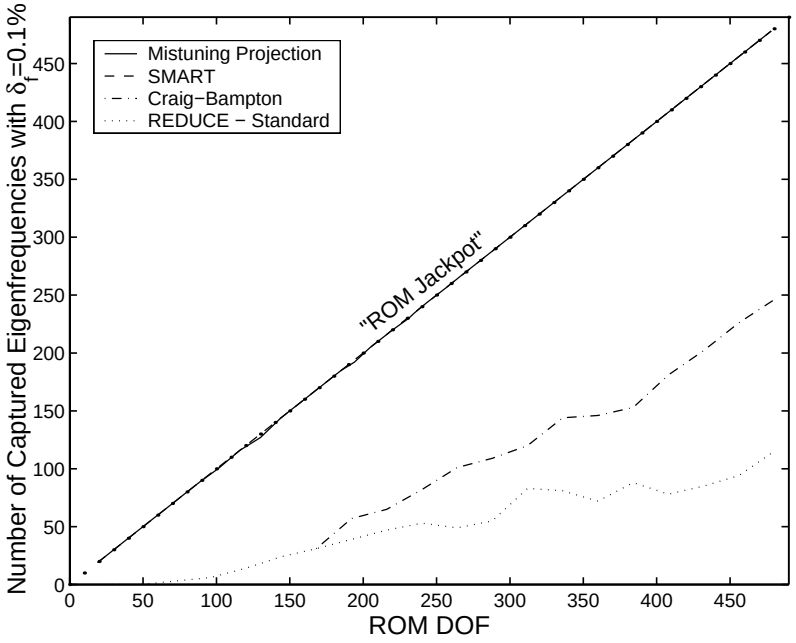

Figure 6.8: Method efficiency with respect to mistuned natural frequencies for $\delta_f \leq 0.1\%$ for the small example model.

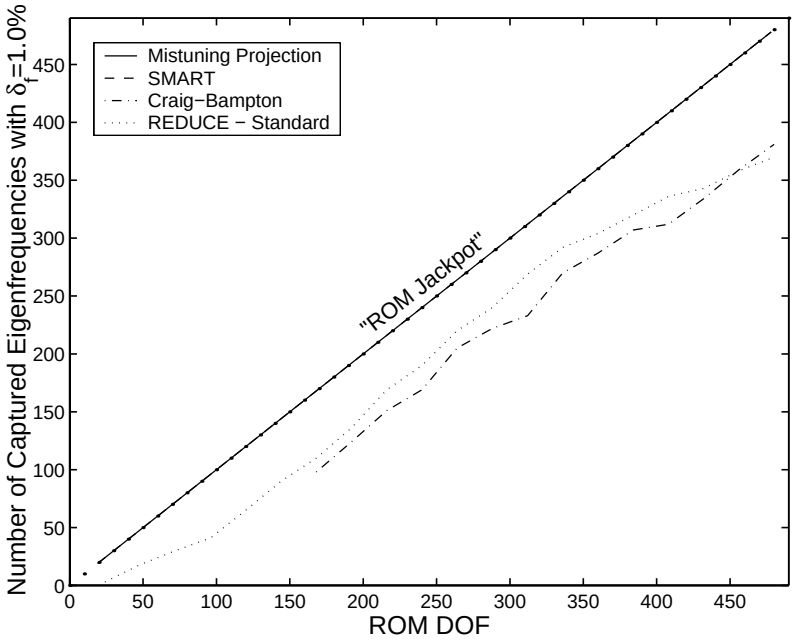

Figure 6.9: Method efficiency with respect to mistuned natural frequencies for $\delta_f \leq 1.0\%$ for the small example model.

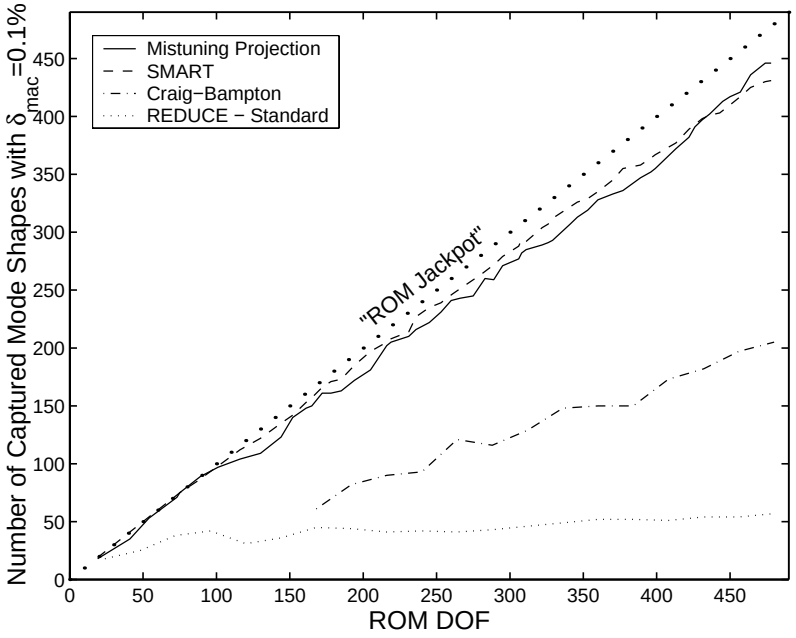

Figure 6.10: Method efficiency with respect to mistuned mode shapes for $\delta_{mac} \leq 0.1\%$ for the small example model.

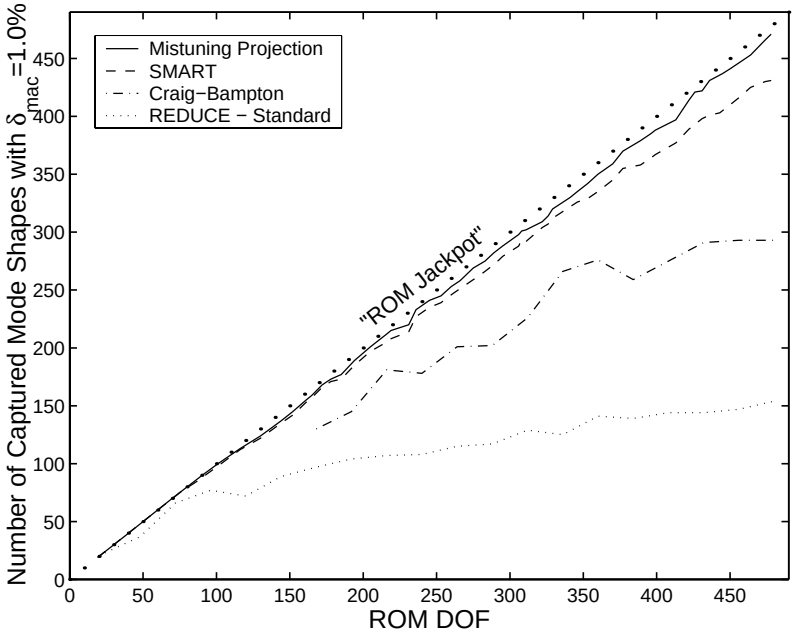

Figure 6.11: Method efficiency with respect to mistuned mode shapes for $\delta_{mac} \leq 1.0\%$ for the small example model.

observing the dramatic difference between Figs. 6.8 and 6.9, it is clear that most of the natural frequencies fall between the two tolerance levels. However, these results show that very few modes are predicted with high accuracy, which is evidenced by the very poor progress as the number of retained modes increases for the smaller tolerance (Fig. 6.8). This is consistent with the tuned results in Fig. 6.4.

In contrast, both the mistuning projection method and the SMART approach come very close to the ideal "jackpot" state for the lower order modes. The capture of mistuned natural frequencies (Figs. 6.8 and 6.9) is outstanding. Both methods also display excellent efficiency in terms of mode shapes (Figs. 6.10 and 6.11), although they appear to be less impressive in this respect. However, the mode match requirements imposed by the MAC tolerances are very strict (see Fig. 6.7).

There is a notable deterioration in mode shape representation of the SMART model as the mode numbers increase. Note that the missed mode shapes in Fig. 6.10 are not accepted even with the relaxed tolerance in Fig. 6.11. This may be explained, in part, by the approximation implied by neglecting mistuning effects among the constraint modes in the intermediate C-B model. First, for higher modes there is more and more local waviness in the structure. Second, since the constraint modes are obtained by successive unit interface DOF deflections, they are also very local in nature. Thus, it is hypothesized that the neglected mistuning among the constraint modes has more impact as the order of the mode increases. This is not a problem for the mistuning projection method, where the entire physical blade stiffness matrices are re-scaled properly. (The mistuning projection method does degrade somewhat for higher order modes, but to a much lesser extent.) Furthermore, note that for this method (as opposed to the SMART model) several of the misrepresented mode shapes are still within the relaxed tolerance level. This degradation is likely due to the approximation incurred by representing the mistuned modes with a truncated set

of tuned modes. Hence, while yielding accurate representations of the relatively smooth blade shapes at lower modes, the effects of this approximation become more pronounced for higher modes in which increasing local waviness is observed. However, in the limit, the mistuning projection method will yield the exact solution in the particular case of mistuning by Young's modulus offsets.

6.4 Forced Response

In this section, engine order excitation is considered in the two veering regions indicated in Fig. 6.3. For Veering #1, this implies an engine order one excitation (1E), which for a 12-bladed assembly has a blade-to-blade forcing phase shift of 30 degrees. Veering #2 requires an engine order three excitation (3E) with a blade-to-blade forcing phase shift of 90 degrees. In both cases, the force is a unit nodal load, $(1,1,1)/\sqrt{3}$, applied to one of the nodes on the blade tip. Hence, this force is able to excite all the fundamental modes of the blade. This applied force was chosen arbitrarily, but it serves to verify the accuracy of the reduced order models.

The amplitude metric employed here, the maximum blade deflection norm, is a scalar value based on the Euclidean norm of the physical displacement vector of each blade. The plotted norms (i.e., the maximum norms) are thus obtained at each driving frequency as

$$A = \max\{A^n\} = \max\left\{\sqrt{\sum_{j=1}^{n_c+n_b} |z_j^n|^2}\right\}, \qquad n = 1,\ldots,N, \tag{6.5}$$

where $|z_j^n|$ is the magnitude of the complex displacement in physical coordinates for the j^{th} DOF of the n^{th} blade, and n_c and n_b are, respectively, the numbers of disk-blade interface and blade interior DOF for one blade. As an alternative, it is realized that from any reduced order model, the physical displacement vector for the n^{th} blade, $\mathbf{z^n}$, is recovered from a modal expansion via some blade modal matrix, $\mathbf{U^n}$, as $\mathbf{z^n} = \mathbf{U^n q}$. Thus, the vector norms

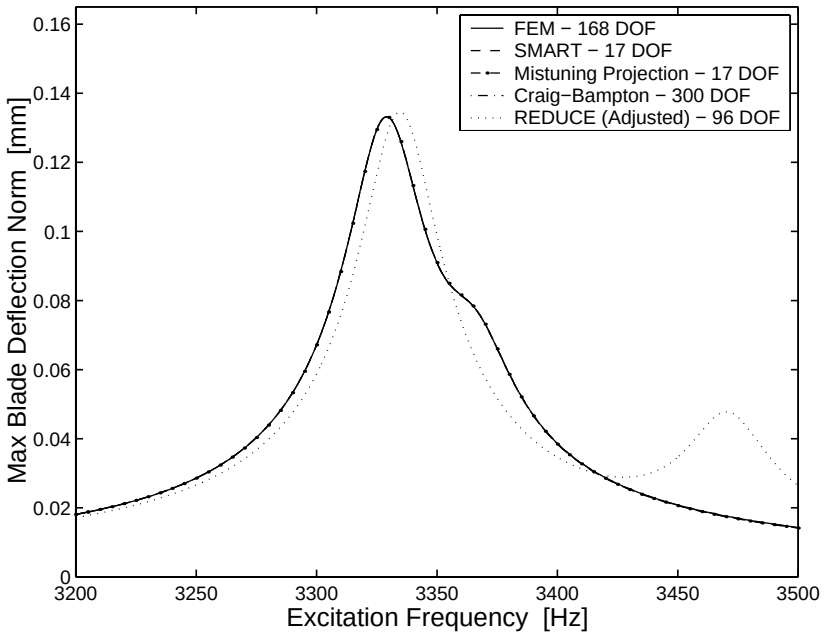

Figure 6.12: Forced response frequency sweep through Veering #1 for engine order one (1E) excitation of the tuned small example model.

may be represented in an equivalent matrix notation as

$$A = \max\{A^n\} = \max\left\{\sqrt{\mathbf{q}^* \mathbf{U}^{\mathbf{n}^*} \mathbf{U}^{\mathbf{n}} \mathbf{q}}\right\}, \qquad n = 1, \ldots, N, \tag{6.6}$$

where $*$ denotes the complex conjugate transpose. Note that the inner matrix products, $\mathbf{U}^{\mathbf{n}^*}\mathbf{U}^{\mathbf{n}}$, may be computed and saved prior to any forced response frequency sweeps or extensive statistical simulations. This allows for fast computations of the blade norms through low-order modal domain matrix projections, instead of tedious computations in physical coordinates.

The resulting tuned and mistuned forced response amplitudes from frequency sweeps over Veering #1 are illustrated in Figs. 6.12 and 6.13, respectively. Clearly, the excellent accuracy displayed by C-B, SMART, and the mistuning projection method in free vibrations translates nicely to the forced response. As demonstrated in Fig. 6.12, the tuned response approximations are practically indistinguishable from the exact solution for these

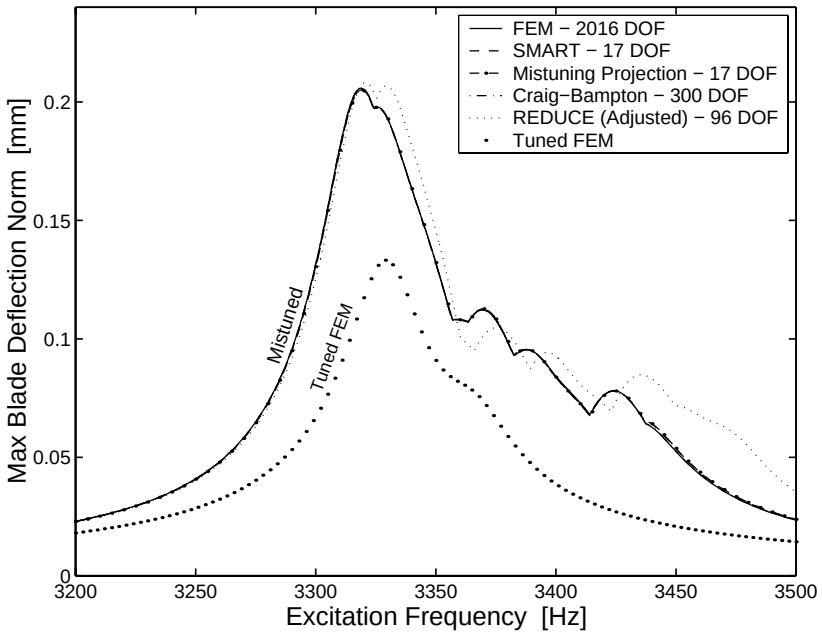

Figure 6.13: Forced response frequency sweep through Veering #1 for engine order one (1E) excitation of the mistuned small example model (tuned FEM solution included for reference).

methods. Also, the capture of the maximum amplitude and the general resonance behavior over the frequency range is outstanding for these three methods. Again, the REDUCE method lacks accuracy in comparison. In particular, in Fig. 6.12 REDUCE predicts a wide separation of the two tuned resonant frequencies, while, in reality, they are very close. Nevertheless, REDUCE gives a fair prediction of the mistuned peak amplitudes in Fig. 6.13, which is the key quantity in studies of forced response statistics.

A second sample of the methods' performances for the mistuned forced response is shown in Fig. 6.14, which illustrates a frequency sweep through Veering #2 for an engine order three (3E) excitation. Qualitatively, the results are similar to those for Veering #1, despite very different circumstances in terms of principal blade motion (different blade mode family) and engine order.

Another point of interest for the turbomachinery industry is blade-to-blade dispersion:

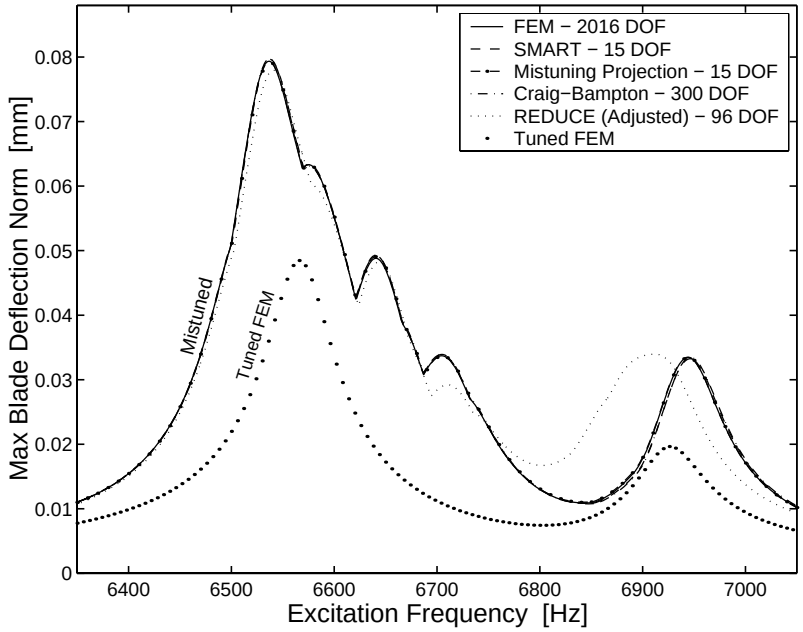

Figure 6.14: Forced response frequency sweep through Veering #2 for engine order three (3E) excitation of the mistuned small example model (tuned FEM solution included for reference).

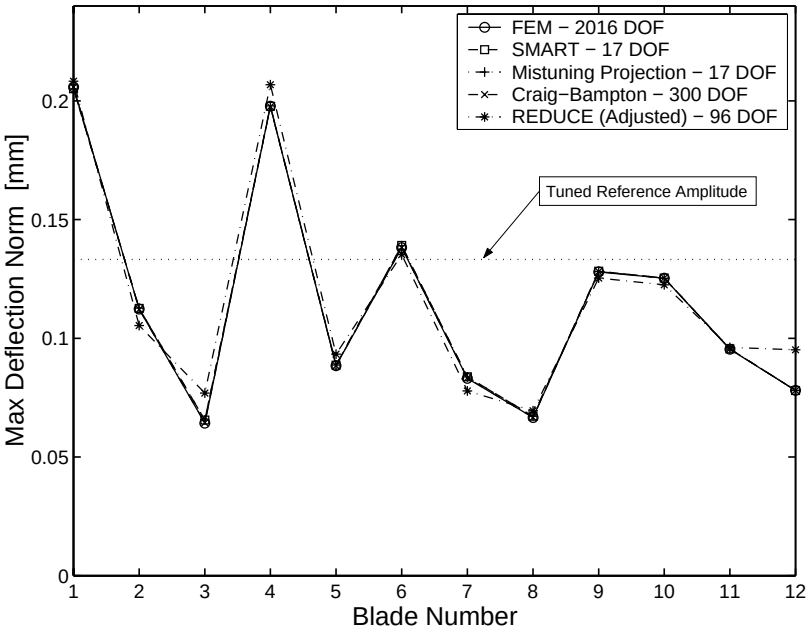

Figure 6.15: Maximum response amplitudes for all blades from forced response frequency sweep through Veering #1 for engine order one (1E) excitation of the mistuned small example model.

blade-to-blade variations in maximum mistuned response amplitudes for a given rotor. This is used to assess mistuning levels from experimental data, and it is also an important aspect when matching computational models with experiments. Figure 6.15 displays the maximum response amplitudes obtained for each blade from the forced response frequency sweep of Fig. 6.13. Again, all methods but REDUCE produce results that are virtually indistinguishable from the finite element values.

Based on the presented results, it is concluded that the C-B, SMART, and the mistuning projection methods are all consistent, high-performance reduced order modeling techniques suitable for mistuned bladed disks. Taking into consideration the differences in efficiency and the final ROM sizes, it is clear that SMART must be considered to be the premier method examined in this study.

6.5 Application of SMART to a Large-Size Model

The feasibility and performance of the SMART approach is further highlighted in this section, where it is applied to the large-size model introduced in Section 6.2.2. The REDUCE method is also included in this comparison to represent the current state of the art.

The tuned natural frequencies of the large model are plotted versus the number of nodal diameters in Fig. 6.16. The character of each family of blade-dominated modes is indicated as flex (F), torsion (T), or axial/edgewise bending (A). Note the excellent global representation of the tuned characteristics displayed by the Craig-Bampton model. For its subsequent use in the SMART approach, it was desirable to get a very accurate C-B model that also spanned a fairly wide frequency band. Therefore, as many as 12 normal disk modes and 16 normal blade modes were employed in its construction.

In contrast, the REDUCE model uses only 5 disk modes and 8 blade modes (312 DOF

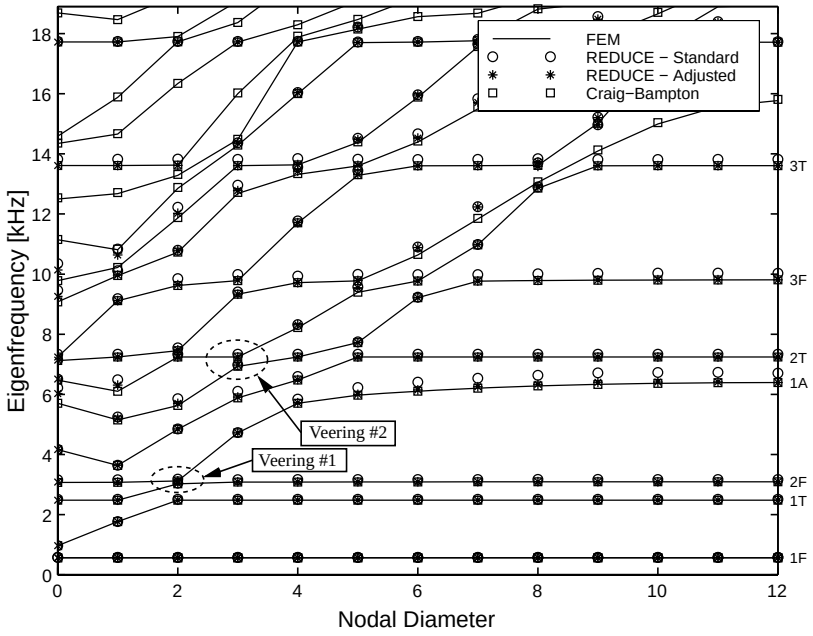

Figure 6.16: Natural frequencies versus nodal diameters for the large example model. The character of each family of blade-dominated modes is indicated on the right, where F=Flex, T=Torsion, and A=Axial (edgewise) bending.

in total), which is why the REDUCE model is missing certain system modes. Considering this inequality in number of retained modes, it may seem unfair to compare the C-B and REDUCE models. However, the improvement gained by including the same number of modes in the REDUCE model as in the C-B model is fairly marginal (recall the poor modal convergence displayed by the REDUCE method in Fig. 6.4).

First, the SMART representation of mistuned mode shapes is investigated. The mode shapes are represented by the vector norms in accordance with Eq. (6.6), although scaled to represent the relative blade deflection. Using the notation of Eq. (6.6), the relative blade displacement norm for each blade is computed as

$$\bar{A}^n = \frac{\sqrt{\mathbf{q}^* \mathbf{U}^{\mathbf{n}^*} \mathbf{U}^{\mathbf{n}} \mathbf{q}}}{\sqrt{\sum_{n=1}^{N} \mathbf{q}^* \mathbf{U}^{\mathbf{n}^*} \mathbf{U}^{\mathbf{n}} \mathbf{q}}}, \qquad n = 1, \ldots, N. \tag{6.7}$$

Figures 6.17 and 6.18 illustrate the 64^{th} and 135^{th} mistuned mode shapes obtained with the

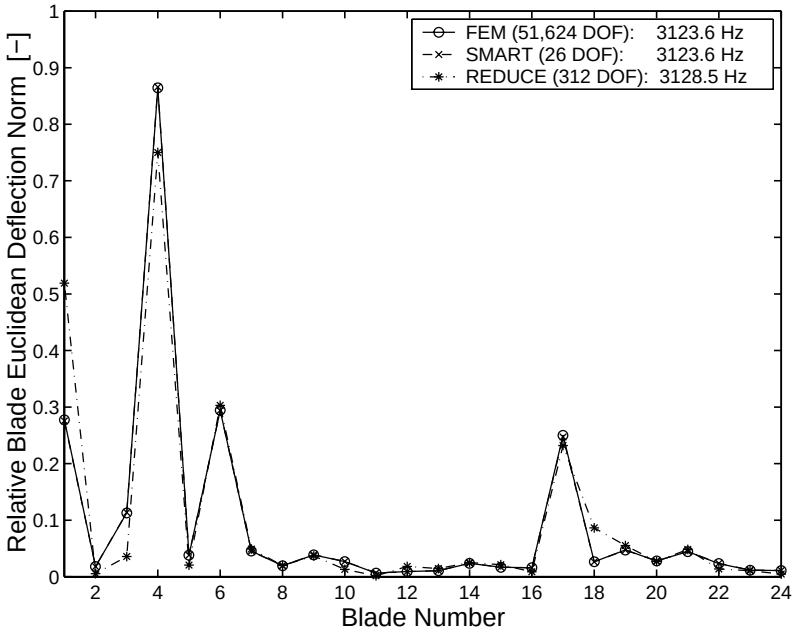

Figure 6.17: Reduced order model representations of mistuned mode shape number 64 for the large example model.

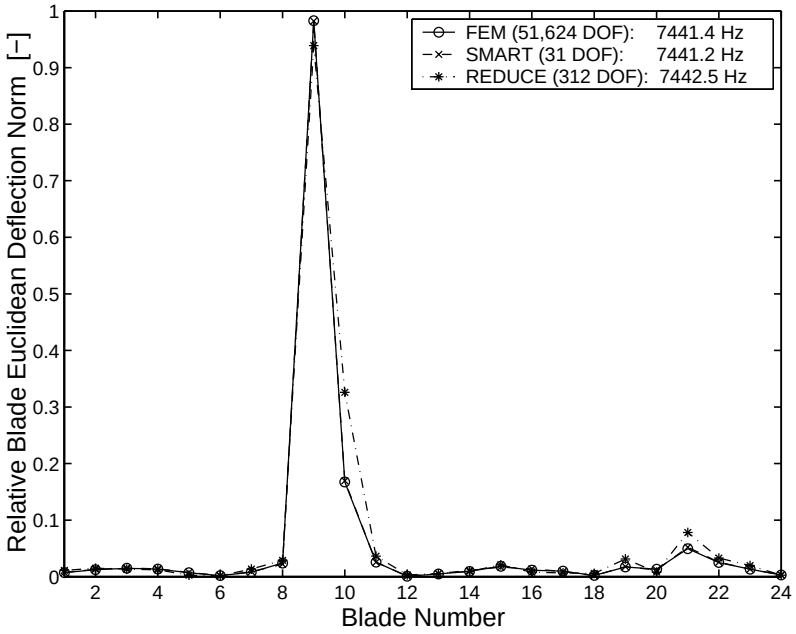

Figure 6.18: Reduced order model representations of mistuned mode shape number 135 for the large example model.

single mistuning pattern listed in Table 6.5. Note from the mistuned natural frequencies that the selected mode shapes are taken from the two families of blade modes that subsequently will be explored in terms of forced response. As indicated, the SMART models in the respective frequency bands contain 26 and 31 modes (DOF), compared to 51,624 DOF for the full mistuned finite element model. Hence, the model size is reduced by more than three orders of magnitude, and yet the SMART models continue to exhibit excellent accuracy in the mistuned case, both in terms of mistuned natural frequencies and mistuned mode shapes. Even though the REDUCE model is approximately one order of magnitude larger than the SMART model, it does not possess the same accuracy.

As shown in Fig. 6.16, the large model exhibits several significant veering regions. This section focuses on the two indicated veering regions, which correspond to a 2E and 3E excitation for the forced response (30 and 45 degrees blade-to-blade forcing phase shift, respectively). The external excitation force used here consists of a unit nodal load applied in the axial direction on the tip of the blade's leading edge. Again, this applied force was chosen arbitrarily for the purpose of verifying the accuracy of the reduced order models.

Figure 6.19 depicts the tuned response in Veering #1, which exhibits well-separated lower and upper resonances. As expected, the SMART model yields a close-to-perfect match with the finite element solution, both in terms of resonant frequencies and peak amplitudes. It is further noted that REDUCE has slight offsets in the resonant frequencies, despite adjustments. What is more disturbing, however, is the fact that the maximum tuned amplitude is overestimated. Using this maximum tuned amplitude as reference in a statistical analysis might result in significantly *underestimated* amplifications due to mistuning, which is not acceptable.

The mistuned response in Veering #1 is depicted in Fig. 6.20. Note the severe amplification of the maximum resonant amplitude due to mistuning — well over 100% in

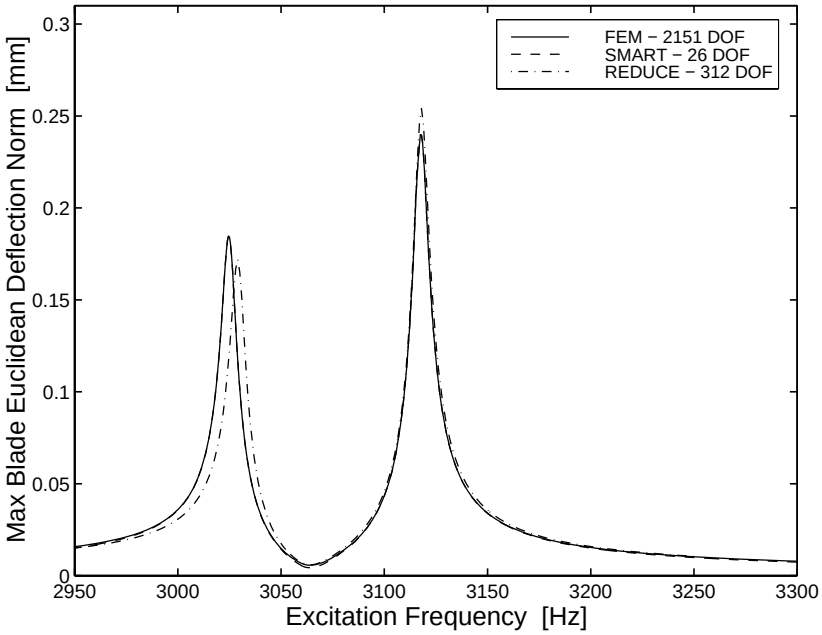

Figure 6.19: Forced response frequency sweep through Veering #1 for engine order two (2E) excitation of the tuned large example model.

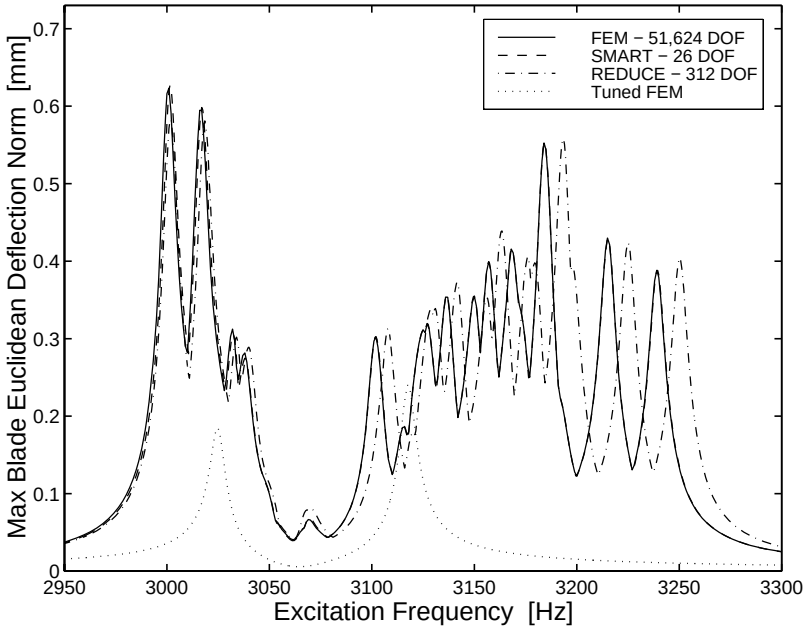

Figure 6.20: Forced response frequency sweep through Veering #1 for engine order two (2E) excitation of the mistuned large example model (tuned FEM solution included for reference).

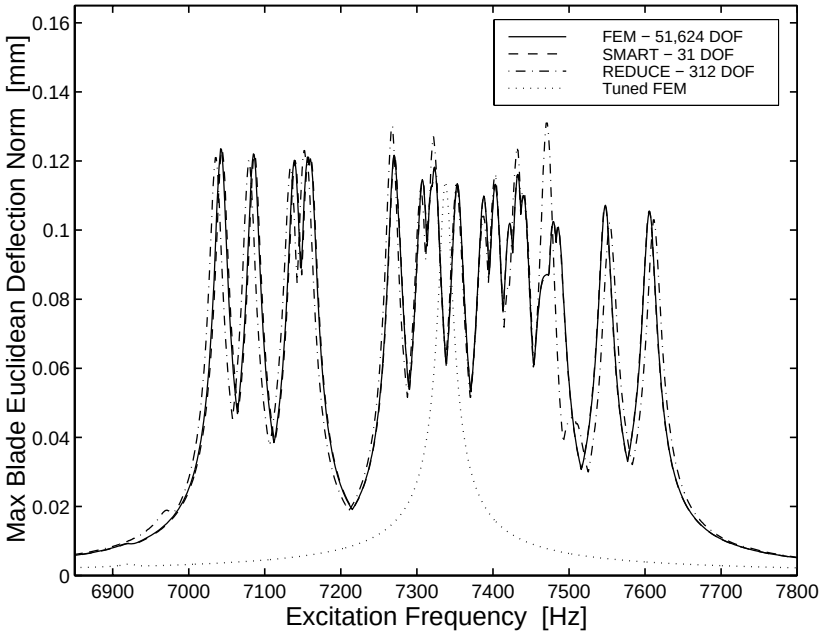

Figure 6.21: Forced response frequency sweep through Veering #2 for engine order three (3E) excitation of the mistuned large example model (tuned FEM solution included for reference).

this case. Again, a slight, insignificant frequency shift is observed for the SMART model, particularly in the group of resonances at the lower frequencies. The conformity is otherwise excellent even for this highly complex resonance pattern. REDUCE yields a fair approximation, although its frequency shift is more pronounced.

To consider another excitation case, the mistuned response in Veering #2 is depicted in Fig. 6.21. Clearly, the disk-blade modal interaction is less critical in this veering, as there is only a very modest amplification of the maximum resonant amplitude. This is explained by the more shallow veering, which suggests strong disk-blade coupling beyond critical levels from a mistuning sensitivity standpoint. As expected, a scenario similar to Fig. 6.20 is seen here in terms of accuracy. Note that even though REDUCE generally matches the natural frequencies better than in the previous case, the predicted resonant amplitudes are significantly worse. From the results presented in this section, it is concluded that the

SMART approach can yield excellent accuracy and efficiency even with a large parent finite element model.

6.6 Conclusions

The primary contribution of this paper is the application of two novel approaches for the reduced order modeling of mistuned bladed disks. These two methods — the mistuning projection method and the secondary modal analysis reduction technique (SMART) — utilize the assumption that tuned and mistuned mode families span the same deformation space. This results in very small reduced order models (ROMs), with matrix dimensions on the order of the number of blades.

In the mistuning projection method, a classical modal analysis is performed on the finite element model of a bladed disk. A coordinate transformation is performed to project the blade mistuning from the finite element domain onto the tuned system modes. In the SMART approach, a primary ROM is generated via component mode synthesis, and then a secondary modal analysis is performed to generate a smaller, secondary ROM. The mistuning data is implemented directly in the blade-component modal coordinates of the primary ROM, and the mistuning is then projected onto the secondary ROM. Using a low-order, modal-domain projection makes the SMART approach highly efficient.

The methods were compared in terms of modal convergence, mistuned mode shape representation, and tuned and mistuned forced response amplitude predictions. It was demonstrated that the mistuning projection and SMART methods outperform current techniques: the new methods exhibit comparable or improved accuracy, while being far superior in computational efficiency. The SMART approach was shown to be exceptionally fast for running simulations of mistuned rotor forced response. Thus, SMART appears to be the most appealing method to date for comprehensive studies of forced response statistics for mistuned bladed disks.

CHAPTER VII

Effects of Multi-Stage Coupling and Disk Flexibility on Mistuned Bladed Disk Dynamics

The effects of disk flexibility and multi-stage coupling on the dynamics of bladed disks with and without blade mistuning are investigated. Both free and forced responses are examined using finite element representations of example single- and two-stage rotor models. The reported work demonstrates the importance of proper treatment of interstage (stage-to-stage) boundaries in order to yield adequate capture of disk-blade modal interaction in eigenfrequency veering regions. The modified disk-blade modal interactions resulting from interstage-coupling-induced changes in disk flexibility are found to have a significant impact on (a) tuned responses due to excitations passing through eigenfrequency veering regions, and (b) a design's sensitivity to blade mistuning. Hence, the findings in this paper suggest that multi-stage analyses may be required when excitations are expected to fall in or near eigenfrequency veering regions or when the sensitivity to blade mistuning is to be accounted for. Conversely, the observed sensitivity to disk flexibility also indicates that the severity of unfavorable structural interblade coupling may be reduced significantly by re-designing the disk(s) and stage-to-stage connectivity. The relatively drastic effects of such modifications illustrated in this work indicate that the design modifications required to alleviate veering-related response problems may be less comprehensive than what might

have been expected.

7.1 Introduction

Dynamic analyses of bladed disks or blisks found in turbomachinery rotors typically involve several idealizations of true conditions. Two such idealizations are of particular interest to the investigation reported in this paper: (a) spatial repetitiveness (cyclic symmetry) of a single rotor stage; and (b) isolated, dynamically independent rotor stages.

The cyclic characteristic (a) enables analysts to reduce both modeling and computational efforts considerably by modeling and analyzing a fundamental disk-blade sector, rather than the entire assembly. However, cyclic symmetry implies that all sectors are identical, i.e., that the system is tuned. Over the past decades, many researchers have conclusively shown that this assumption can be a potentially disastrous idealization of a bladed disk's true behavior — see for instance Wagner [5], Dye and Henry [6], Ewins [7, 46], El-Bayoumy and Srinivasan [9], Irretier [18], and Wei and Pierre [14, 15]. In reality, individual blades exhibit small structural differences — blade mistuning — which may stem from manufacturing and material tolerances or in-service wear. These variations destroy cyclic symmetry and thus require modeling the full bladed disk assembly. More importantly, mistuning may lead to qualitatively different dynamic behavior than that experienced by a perfectly tuned rotor. In particular, mistuning may inhibit the even distribution of vibration energy among blades, and therefore confine most of the energy to only a few blades. This way, mode shapes may become spatially localized, and some blades may experience forced response deflections that are much larger than those predicted by a tuned analysis.

Analyzing each stage independently in accordance with assumption (b) implies that the analyst must choose some boundary conditions that best describe the constraints imposed by adjacent stages. In current practice, this is typically dealt with by imposing

either fully clamped conditions or axial restraints alone, or by modeling adjacent stages as uniformly distributed masses and stiffnesses (to preserve cyclicity). Such approximate constraints may well yield reasonable descriptions of the "global" vibration characteristics of a rotor stage in a multi-stage assembly. However, it may be suspected that the approximate boundary conditions will in general not accurately describe the disk flexibility locally at the interstage (stage-to-stage) boundaries. This will lead to inconsistent representations of the interaction between families of disk- and blade-dominated modes. The disk-blade modal interaction in veering regions is a critically important factor in determining a design's sensitivity to mistuning. Studies by Wei and Pierre [15] and by Óttarsson and Pierre [16] show that the severity of vibration energy localization is to a large extent governed by the level of structural interblade coupling, which results from the disk-blade modal interaction. Thus, when considering a rotor design from a mistuning sensitivity point of view, misrepresentations of the disk flexibility and structural interstage coupling can potentially result in severely misguided conclusions.

The purpose of this paper is to make evident the importance of accurate interstage boundary modeling through inclusion of multi-stage effects. The multi-stage effects are demonstrated using finite element models of simplified example single- and two-stage rotors. The paper describes important general implications of multi-stage coupling on the free and forced vibration characteristics of tuned and mistuned configurations. Its effect on the response in eigenfrequency veering regions is given particular attention, since the level of structural interblade coupling, and thus the mistuning sensitivity, are manifested by the local veering characteristics.

This paper is organized as follows. Section 7.2 introduces the simple finite element single- and two-stage models used in this study. Section 7.3 illustrates and discusses general implications of multi-stage dynamics in the free and forced response, with and without

blade mistuning. Section 7.4 demonstrates more specifically the impact of disk flexibility and structural interstage coupling on the forced response in eigenfrequency veering regions, by using single- and multi-stage models with varying interstage boundary conditions and disk flexibility. Important findings and conclusions from this study are summarized in Section 7.5.

7.2 Description of Example Models

Figure 7.1 depicts the simple example single- and two-stage rotor models employed in this study. A portion of the multi-stage model has been cut out in Fig. 7.1 in order to better illustrate the assembled geometry. The models are constructed entirely from eight-noded brick (linear solid) elements. It should be noted that the stage geometries are very simple, and that the finite element meshes are very coarse, compared to those of typical industrial finite element models. However, the modeled stages still exhibit the essential characteristics of realistic rotors, such as disk- and blade-dominated mode families and their interactions (i.e., eigenfrequency veerings).

The stage 1 model features 12 blades, each with length 60 mm and base width 7.5 degrees ($\sim$13 mm). The blades are slightly tapered along the radial direction, from 5 mm thickness at the base to 2 mm thickness at the tip. The stage 2 model features 16 blades, each with length 48 mm. The stage 2 blades are otherwise identical to those of stage 1. The stage 1 disk has an outer radius of 100 mm, while the outer radius of the stage 2 disk is 104 mm. Both disks have an inner radius of 20 mm, and both disks are clamped at their respective outward rims. The two stages are considered to be welded together at the interstage boundary. Moreover, a uniform structural damping coefficient of 0.5% is used for both stages in the forced response, while any viscous damping is assumed negligible.

For the mistuned results, a single random mistuning pattern is used for each stage with

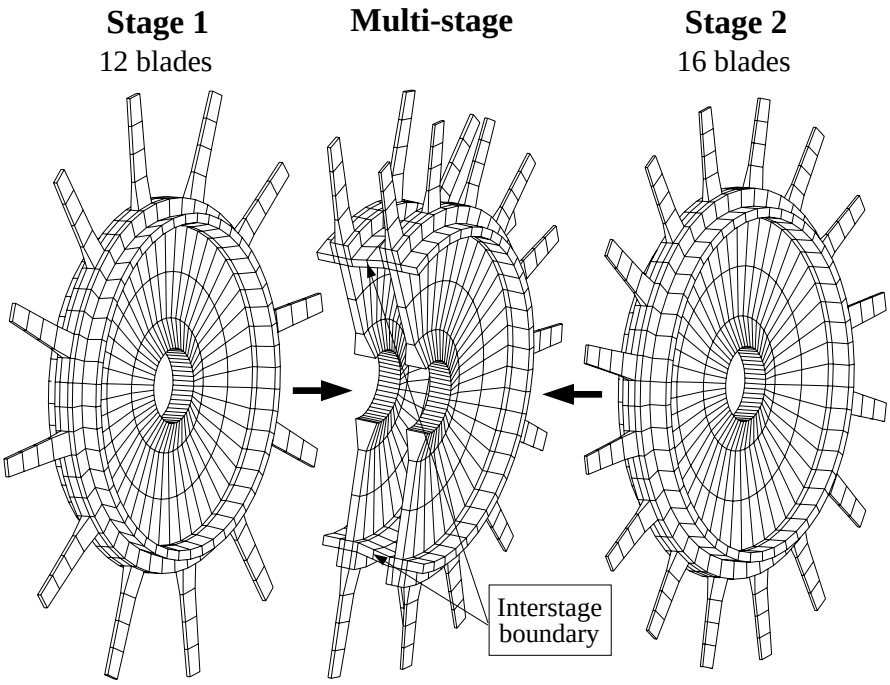

Figure 7.1: Finite element meshes for the single- and two-stage example rotor models.

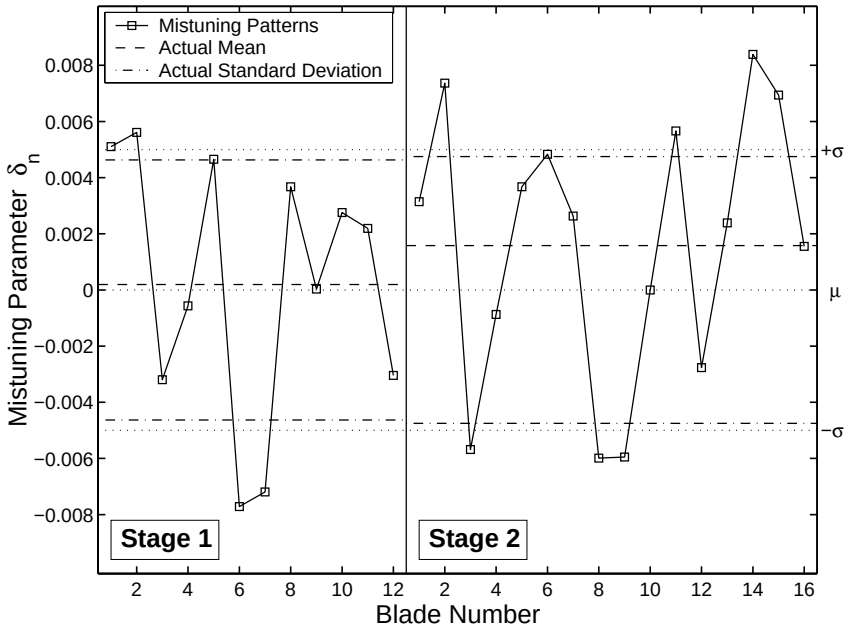

Figure 7.2: Employed blade mistuning patterns sampled from a uniform distribution of mean zero and standard deviation 0.5%.

the mistuning parameter distribution depicted in Fig. 7.2. The two mistuning patterns were sampled from a uniform distribution of mean zero ($\mu = 0$) and standard deviation 0.5% ($\sigma = 0.005$), where one mistuning value, δ_n, is assigned to each blade. Note that a 0.5% standard deviation among the blade modal stiffnesses approximately corresponds to 0.25% standard deviation among blade natural frequencies. Blade mistuning is introduced to the finite element models by varying Young's modulus in the blade elements:

$$E_n = (1 + \delta_n)\, E_o, \qquad n = 1, \ldots, N, \tag{7.1}$$

where n is the blade number and N is the total number of blades in the stage.

7.3 Features of Multi-Stage Response

Before proceeding to explore the free and forced response of multi-stage assemblies, one important feature of any multi-stage model first needs to be clarified. When studying coupled multi-stage models, the concept of "tuned" bladed disks becomes questionable. Typically, adjacent stages will not have the same number of blades (sectors), and the cyclicity and harmonic content of adjacent stages will therefore be incompatible. As a result, coupling of individual stages to form multi-stage rotors will inherently introduce some level of mistuning to the system. Note that the interstage coupling induces disk mistuning, rather than the more commonly considered blade mistuning.

For the particular model used in this work, the level of mistuning induced by the interstage coupling is very small. In fact, although frequency pair splitting is readily observed, the relative frequency split induced by interstage coupling is only on the order of 0.001% for the investigated model. As a result, "tuned" nodal diameter mode shapes are readily identified for both stages, while no circumferential mode localization is observed due to the interstage-coupling-induced mistuning alone. Consequently, the notation "tuned" will therefore still be used in this work to denote cases where blade mistuning has not been

added explicitly. Furthermore, note that the blade number combination of the employed two-stage model (12 and 16 blades) may be somewhat unusual in that the two stages share several nodal-diameter symmetries. As a result, the modal interstage coupling may be stronger and the interstage-coupling-induced mistuning less pronounced for this model compared to models with more "incompatible" blade number combinations (e.g., prime numbers).

7.3.1 Free Vibrations

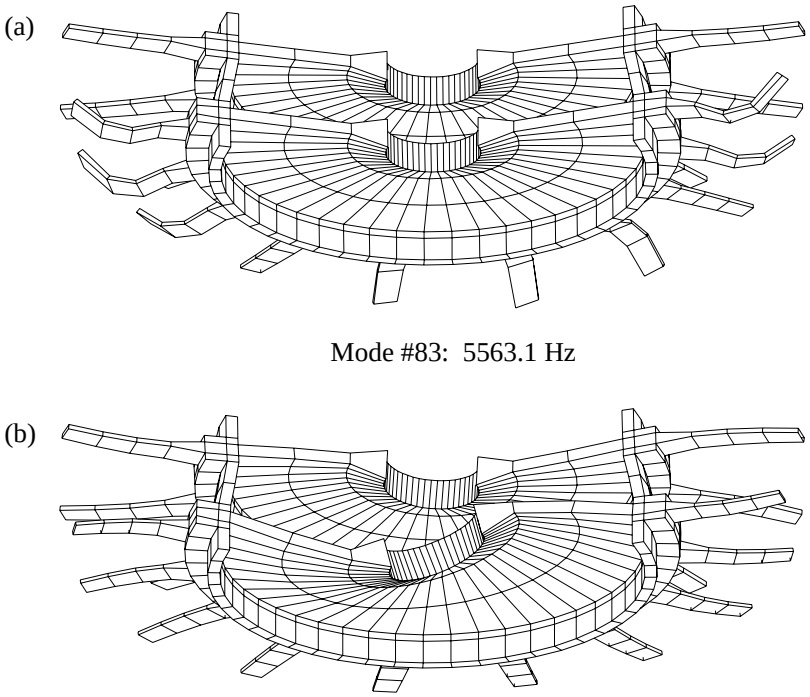

Figure 7.3: Deformed finite element shapes for (a) a blade-dominated mode and (b) a disk-dominated mode, which are both globally localized onto stage 2 (lower stage).

An interesting, but not unexpected, result in the free vibrations of multi-stage assemblies is that most mode shapes exhibit significant (global) localization onto either stage. While this is common for most modes, it is particularly apparent for blade-dominated modes. As illustrative examples, the deformed meshes pertaining to (a) a typical blade-

dominated mode shape and (b) a typical disk-dominated mode shape that feature distinct global localization onto stage 2 are shown in Fig. 7.3. The relative stage participations for the lower modes of the investigated multi-stage model are plotted in Fig. 7.4. The relative participation of stage i for the k^{th} mode, R_k^i, is obtained from a stage-wise comparison of strain energies:

$$R_k^i = \frac{\mathbf{u_k^{i^T} K_i u_k^i}}{\sum_{p=1}^{M} \mathbf{u_k^{p^T} K_p u_k^p}}, \tag{7.2}$$

where $\mathbf{u_k^p}$ is the stage p portion of the k^{th} mode shape; $\mathbf{K_p}$ is the stage p stiffness matrix; and M is the total number of stages. In this representation, it is clear that relatively few modes exhibit significant participation of both stages, which are here denoted system modes. In fact, for this model, system modes only occur when disk-dominated modes of both stages are relatively close in frequency. Note that blade mistuning does not alter the stage participation factors to any significant degree, other than that the mistuning in some instances changes the ordering of the modes, due to slight changes in natural frequencies. Also, note that for other models it is quite possible that significant stage-to-stage interaction could be observed for families of blade-dominated modes, if they are sufficiently close in frequency for two or more stages. To physically illustrate these two fundamental mode types, one system mode and one globally localized mode are depicted in Fig. 7.5. The system mode in Fig. 7.5a exhibits significant participation from both stages, where, interestingly, stage 1 (upper) features more blade-dominated motion and stage 2 (lower) displays a more disk-dominated motion. Moreover, Fig. 7.5b illustrates a mixed disk-blade multi-stage mode shape that exhibits significant localization onto stage 1.

The dynamic characteristics of single-stage tuned bladed disks are conveniently summarized in plots of natural frequencies versus the number of nodal diameters (harmonics), as shown in Figs. 7.6 and 7.7. This data set is essentially a subset of the traditional Campbell diagram [65]. The nearly horizontal connecting lines correspond to assembly modes

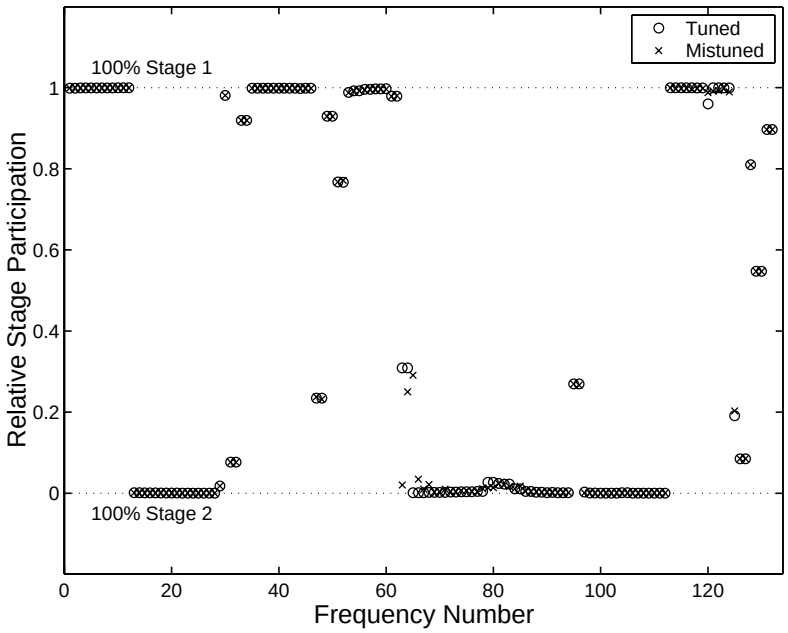

Figure 7.4: Stage 1 strain energies relative to total multi-stage strain energies for “tuned” and blade mistuned multi-stage modes below 8000 Hz.

that are dominated by blade motion. The characteristic blade motion of each family of blade-dominated modes is indicated on the right of Figs. 7.6 and 7.7, where: F=Flexural; A=Axial (edgewise bending); and T=Torsion. Moreover, modes located on the slanted connecting lines are dominated by disk motion. The rapid increase of the eigenfrequencies of the disk-dominated modes is due to stiffening of the disk as the circumferential wavelength decreases with increasing number of nodal diameters.

For sufficiently low levels of interstage-coupling-induced mistuning, the nodal-diameter representation of single-stage free vibration characteristics may also be useful for multi-stage assemblies. Figure 7.8 illustrates two “tuned”, blade-dominated, and globally localized multi-stage mode shapes, as represented by the deflection of a single blade tip DOF. Mode 54 is seen to exhibit significant global localization onto stage 1, whereas mode 83 is globally localized onto stage 1. Together with Figs. 7.3 and 7.5, Fig. 7.8 clearly illustrates the tuned-like, spatially extended characteristic observed for the multi-stage mode

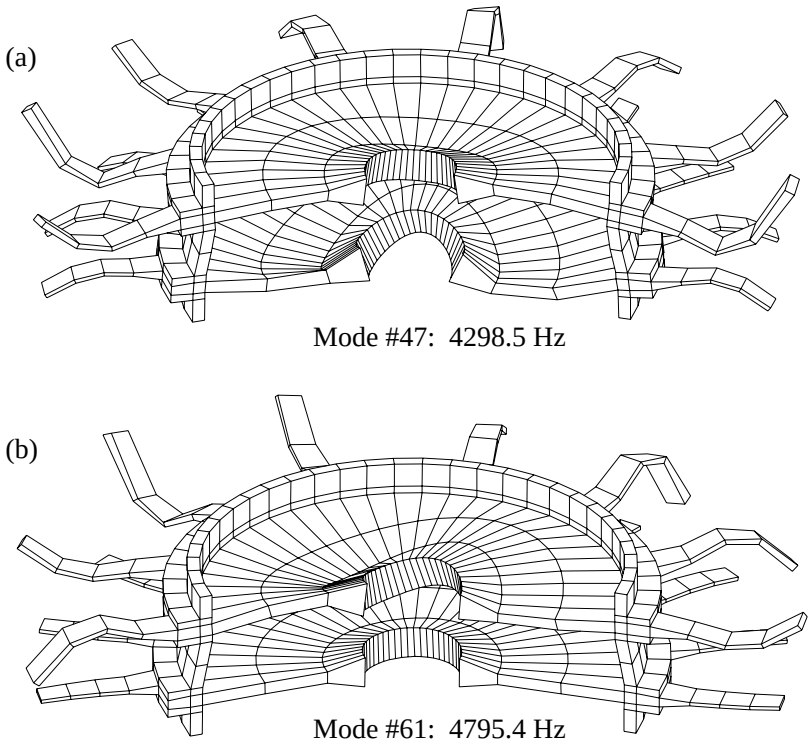

Figure 7.5: Deformed finite element shapes for (a) a multi-stage system mode and (b) a mode globally localized onto stage 1 (upper stage).

shapes, despite the mistuning induced by interstage coupling. Hence, by examining the multi-stage mode shapes with respect to stage participation, zero crossings (for nodal diameter designation), and, for certain particularly non-obvious system modes, single-stage versus multi-stage natural frequency proximity, the multi-stage modes could be divided into stage 1 and stage 2 frequencies as shown in Figs. 7.6 and 7.7. It should be noted that this identification process may be infeasible for more realistic models that may feature both more system modes and much more complex eigenfrequency veering regions. However, the stage identification is carried out here in order to better demonstrate the effect of interstage coupling relative to traditional single-stage analyses.

For the identified stage 1 multi-stage natural frequencies in Fig. 7.6, it is observed that the interstage coupling does not significantly alter the global characteristics from a

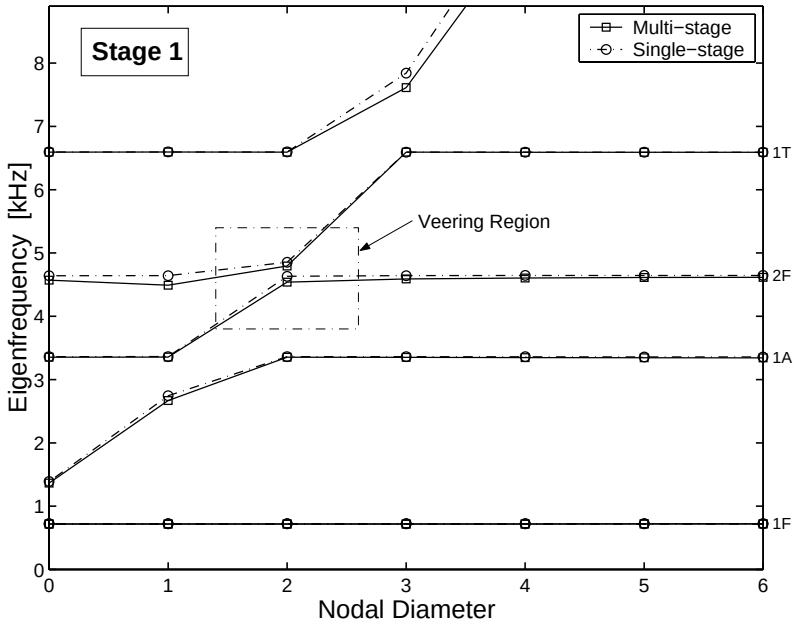

Figure 7.6: Natural frequencies versus number of nodal diameters for the tuned stage 1 model with fixed interstage boundaries, and for the "tuned" multi-stage model for modes localized to stage 1, as obtained with finite element models.

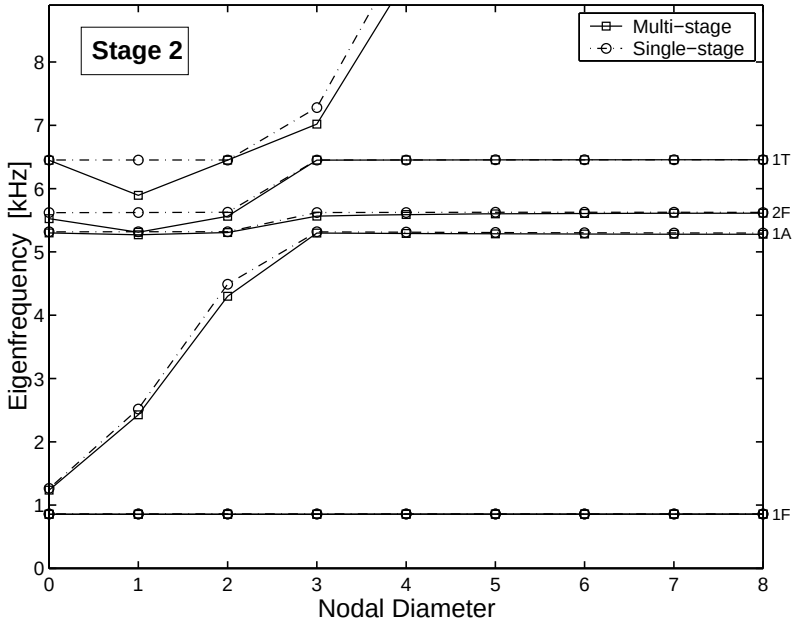

Figure 7.7: Natural frequencies versus number of nodal diameters for the tuned stage 2 model with fixed interstage boundaries, and for the "tuned" multi-stage model for modes localized to stage 2, as obtained with finite element models.

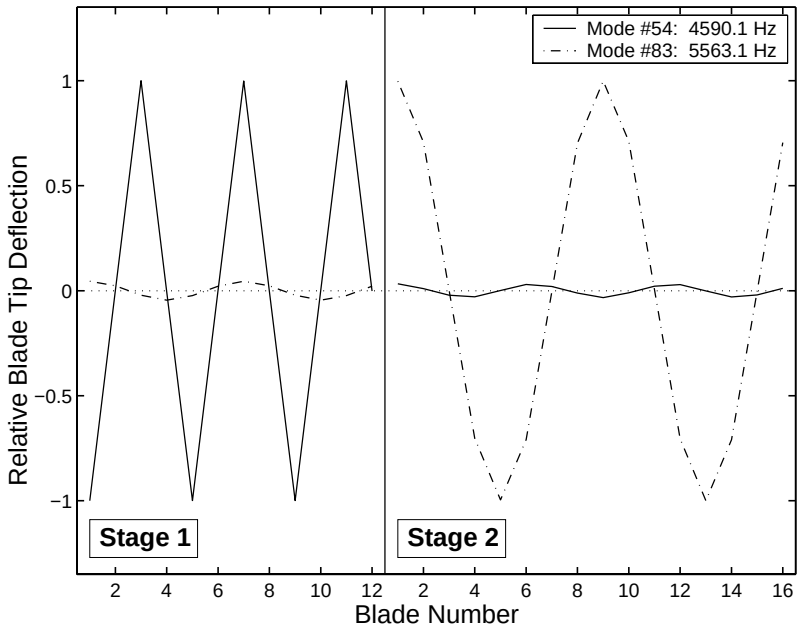

Figure 7.8: Tuned multi-stage mode shapes 54 and 83, as represented by the normalized deflection for one DOF at each blade tip.

clamped interstage single-stage representation. Clearly, however, the disk is more flexible in the multi-stage model, which is manifested by the slight shift downwards of the disk-dominated modes. In contrast, the blade-dominated are practically unchanged. The shift of disk-dominated modes is also observed for stage 2 in Fig. 7.7. For stage 2, however, the inclusion of multi-stage effects clearly has a more dramatic effect on the global characteristics as well. From having a group of three relatively close families of distinctly blade-dominated modes in the single-stage representation, the multi-stage model exhibits the presence of a second family of disk-dominated modes in the lower harmonics of this region, due to the added disk flexibility. This is clearly a drastic change in the free vibration characteristics that is certain to affect the stage 2 forced response for excitations in this region.

An important implication of the modified disk flexibility is that the characteristics of the eigenfrequency veerings are also modified. An example of an affected eigenfrequency

veering region is highlighted in Fig. 7.6. This veering modification means that the mixture of blade and disk dominance, (i.e., the disk-blade modal interaction) among the two mode pairs representing the veering is altered. As mentioned in the introduction, this modification of the disk-blade modal interaction may have a critical impact on mistuning sensitivity. For instance, consider the mistuned single- and multi-stage mode shapes in Fig. 7.9, which correspond in natural frequency order to the tuned multi-stage mode shapes depicted in Fig. 7.8. As illustrated in Fig. 7.9, the stage 1 mistuned mode shapes (mode 54) are very different for single- and multi-stage representations. However, the two representations do exhibit similar levels of "localization", or lack thereof. On the other hand, the levels of localization exhibited by the mistuned stage 2 mode shape (mode 83) in single- and multi-stage representations are vastly different. Here, the single-stage model predicts a strongly localized mode, while the "actual" multi-stage mode shape exhibits a much milder deviation from a tuned, spatially extended behavior. Thus, from a mistuning sensitivity perspective, multi-stage dynamic analyses may be needed in order to yield sufficiently accurate representations of disk flexibility and structural interstage coupling. This will be explored further in the sections to follow.

7.3.2 Forced Response

The forced response examples included in this section are based on stage-wise independent engine order excitations, which are harmonic in time and differ only in phase from blade to blade. The engine order excitations are applied to one stage at a time. This will isolate and better demonstrate the effects of interstage coupling, as it eliminates any subresonances that may be induced by adjacent stage excitations. Specifically, stage 1 is subjected to an engine order 10 (10E) excitation in the frequency range 4–5 kHz, and stage 2 is subjected to an engine order 15 (15E) excitation in the frequency range 5–6 kHz.

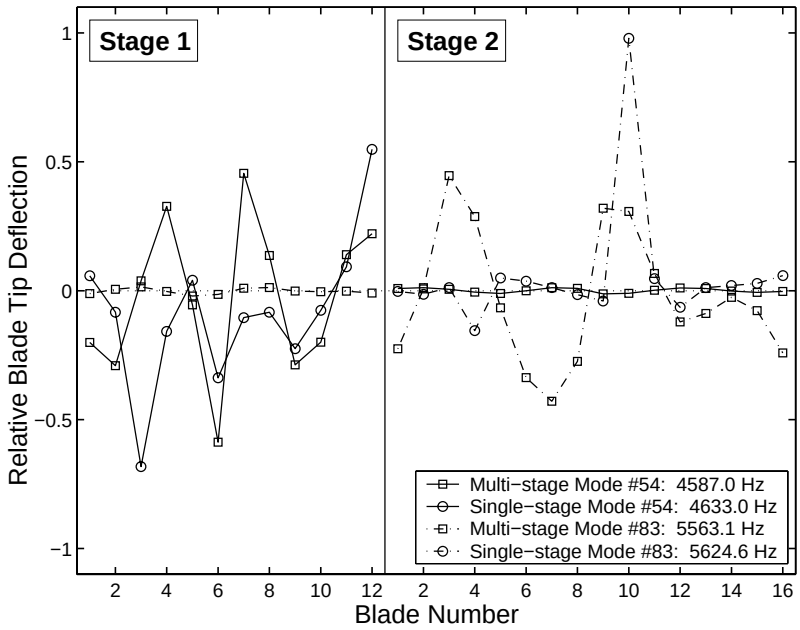

Figure 7.9: Mistuned single- and multi-stage mode shapes 54 and 83, as represented by the normalized deflection for one DOF at each blade tip.

As indicated by the employed engine orders, it is here assumed that the pressure wakes behind the stationary vanes immediately upstream are the dominating sources of excitation. Whereas this excitation may be realistic from an engine order perspective, the blade surface force applied here is highly unrealistic: a single point load on one blade tip node in the axial direction (axis of rotation). However, while unrealistic, it is quite adequate for demonstrative purposes. Furthermore, note that the applied engine order excitations are equivalent to counterrotating engine order 2 (-2E) and 1 (-1E) excitations for stages 1 and 2, respectively. Hence, the applied excitations will pass through the harmonic 2 veering region of stage 1 (see Fig. 7.6), and through the harmonic 1 region of stage 2 that exhibited a drastic change in the free vibration characteristics due to interstage coupling (see Fig. 7.7).

Figures 7.10 and 7.11 depict each stage's response amplitudes resulting from the above excitations. The amplitudes are here represented by the axial displacement magnitude

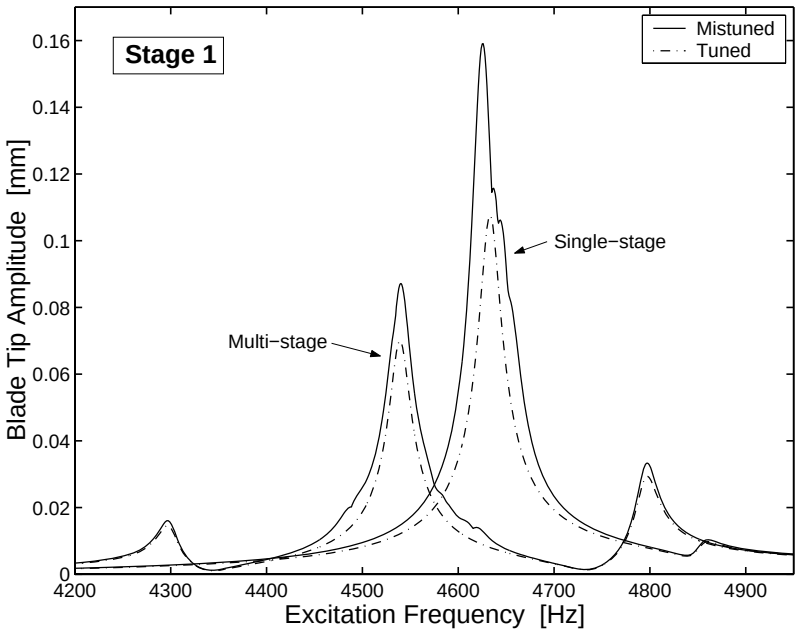

Figure 7.10: Stage 1 forced response from engine order 10 excitation (10E=-2E), using tuned and mistuned finite element single- and multi-stage models.

of one blade tip node for the maximum responding blade in each stage. As shown in Fig. 7.10, the shift in disk flexibility due to interstage coupling observed in Fig. 7.6 results in a significantly changed veering response behavior for stage 1. From the tuned response, it is clear that the added disk flexibility has moved the mode pairs comprising the veering to lower resonant frequencies. Furthermore, the upper mode pair, which was clearly disk-dominated in the single-stage representation, exhibits much more blade participation in the multi-stage response. Conversely, the lower mode pair goes from being distinctly blade-dominated to having significant disk participation. As a consequence, the disk-blade modal interaction has changed to make the sensitivity to mistuning much less pronounced. This is clearly demonstrated by the mistuned results depicted in Fig. 7.10, where the maximum amplitude magnification due to blade mistuning goes from 48% in the clamped interstage case to only 25% in the multi-stage case.

Moreover, note that even when disregarding blade mistuning, the interstage coupling

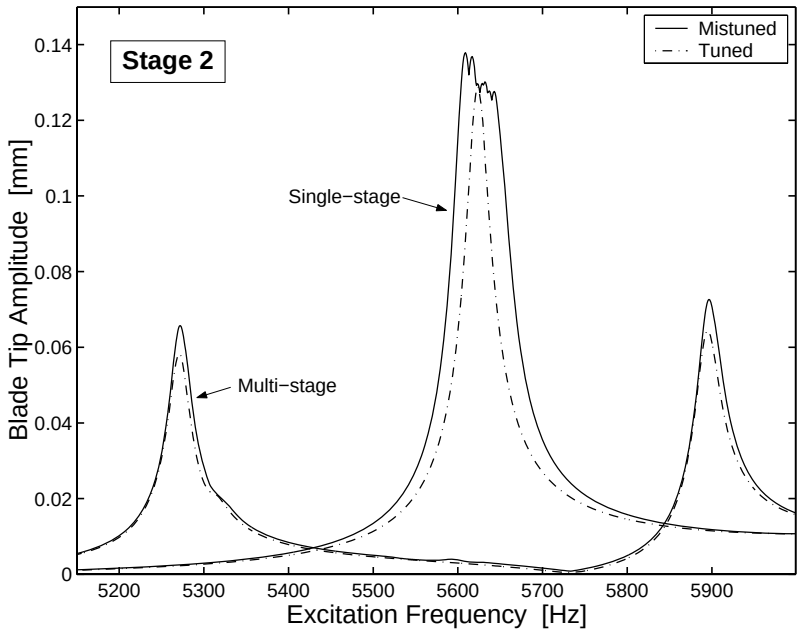

Figure 7.11: Stage 2 forced response from engine order 15 excitation (15E=-1E), using tuned and mistuned finite element single- and multi-stage models.

has a very significant effect on tuned response amplitude levels. The maximum tuned response amplitude for the single-stage model is as much as 54% larger than for the multi-stage model. Hence, a design based on the tuned single-stage response with applicable safety factors, would in reality (i.e., in a multi-stage assembly) enjoy an additional safety factor in this particular case. However, it must be emphasized that the design-endangering opposite scenario might be just as likely to occur for other models.

The stage 2 forced response depicted in Fig. 7.11 demonstrates a similarly dramatic change in response behavior due to interstage coupling. Here, the blade-dominated harmonic 1 mode pair at 5620 Hz has “disappeared” in favor of two more disk-dominated mode pairs at approximately 5270 Hz and 5890 Hz, respectively. The increased disk dominance leads to a maximum tuned response amplitude for the multi-stage model that is 50% lower than that of the single-stage stage 2 model, which features a more blade-dominated response. Note that the stage 2 excitation case exhibits negligible mistuning sensitivity for

both single- and multi-stage representations. Also, note that the blade-dominated family of modes at 5320 Hz does not respond to the applied excitation, since the edgewise blade motion (1A; see Fig. 7.7) of this mode family cannot be excited by the applied force.

An interesting observation is the existence of subresonances for the multi-stage model in both tuned and mistuned configurations. For instance, consider the subresonance appearing for stage 1 in Fig. 7.10 at 4295 Hz. At this resonant frequency, the response is dominated by the motion of a mixed disk-blade two-nodal-diameter mode pair (modes 47 and 48 in Fig. 7.4) with a stage 1 to stage 2 participation ratio of approximately 1:4, and is thus localized to stage 2. Hence, even though the driving excitation is applied to the least responsive part of this pair of system modes, stage 1's mode participation is sufficient to generate resonance. A similar instance of subresonance occurs also for stage 2 near 5310 Hz, as seen in Fig. 7.11. This observation is important, since it demonstrates that the capture of interstage flexibility alone may not be enough — adjacent stage dynamics may also impact significantly the "true" dynamic behavior of a stage in a multi-stage rotor assembly.

7.4 Veering Response Sensitivity

7.4.1 Effects of Disk Flexibility

In this section, the influence of disk flexibility is investigated in more detail. This study is motivated by the significant differences in eigenfrequency veering characteristics and response that resulted from interstage-coupling-induced changes in disk flexibility shown in the previous section. The effective disk flexibility is determined by design (geometry), material, boundary conditions (interstage coupling), and operating conditions (excitation engine orders, centrifugal stiffening). Hence, while interstage coupling has significant impact as shown in the previous section, it is only one contributing factor out of several.

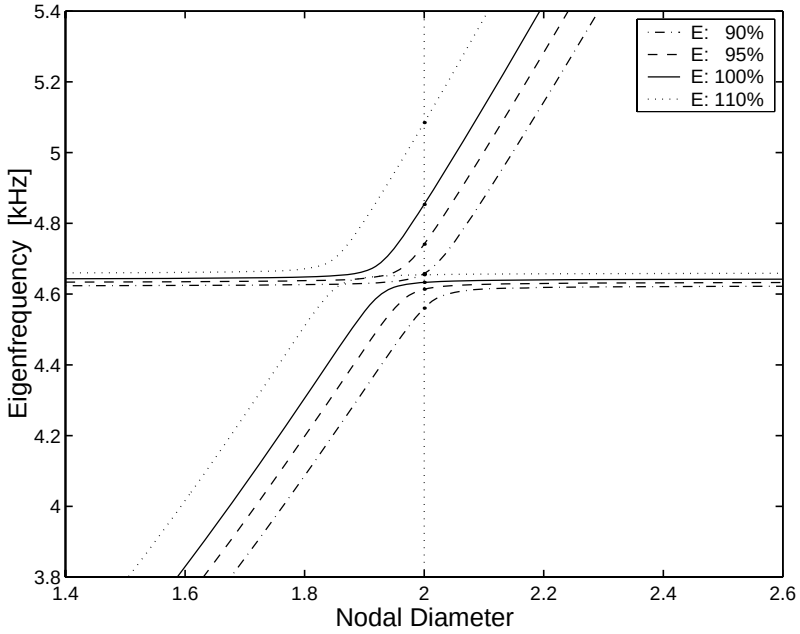

Figure 7.12: Detailed view over the stage 1 eigenfrequency veering region indicated in Fig. 7.6 (single-stage) using a pseudo-continuous interblade phase angle description for varying levels of disk flexibility (E = Young's modulus).

However, a full-scale parametric study involving all factors is far beyond the scope of this paper. Thus, to limit the simulation space, a clamped interstage single-stage representation of stage 1 is considered, where Young's modulus (E) in the disk part is modified to artificially simulate one or more of these factors.

Figure 7.12 shows the detailed behavior of the stage 1 model in the eigenfrequency veering highlighted in Fig. 7.6 for different values of disk Young's modulus. Note that 100% E corresponds to the stage 1 model used in Section 7.3. The results in Fig. 7.12 were obtained using the pseudo-continuous interblade phase angle representation outlined in Bladh *et al*. [66], which enables computation of fictitious non-integer harmonic (nodal-diameter) modes. This approach can be used effectively to obtain approximations of local veering characteristics, such as local veering curvatures and a veering's true distance to an integer engine order excitation. The local lower (negative values) and upper (positive

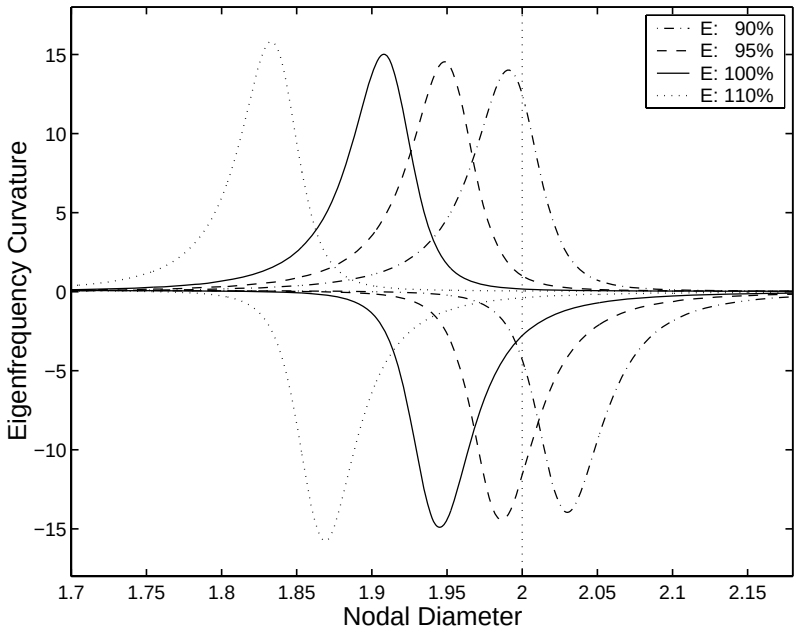

Figure 7.13: Upper and lower eigenfrequency curvatures in the stage 1 veering region indicated in Fig. 7.6 (single-stage) using a pseudo-continuous interblade phase angle description for varying levels of disk flexibility (E = Young's modulus).

values) veering curvatures pertaining to the disk flexibility levels in Fig. 7.12 were computed using a standard fourth order finite difference scheme and are plotted in Fig. 7.13. As demonstrated by Fig. 7.12, the main effect of decreasing the disk flexibility (i.e., increasing E) is to shift the location of the veering to lower interblade phase angles or nodal diameters (i.e., from right to left), while the upward shift in blade-dominated mode frequencies is marginal. This is consistent with the modifying effect of the interstage coupling on disk flexibility observed in the previous section. Furthermore, it is clear from the resulting curvatures in Fig. 7.13 that the disk flexibility variations have a rather mild effect on the local curvatures, as the obtained maximum curvatures do not change significantly.

An important effect of the veering shift observed in Figs. 7.12 and 7.13 is that, as the disk flexibility is decreased (i.e., increasing E), the lower integer harmonic (actual) mode pair will go from disk-dominated (on slanted line) to blade-dominated (on horizontal line)

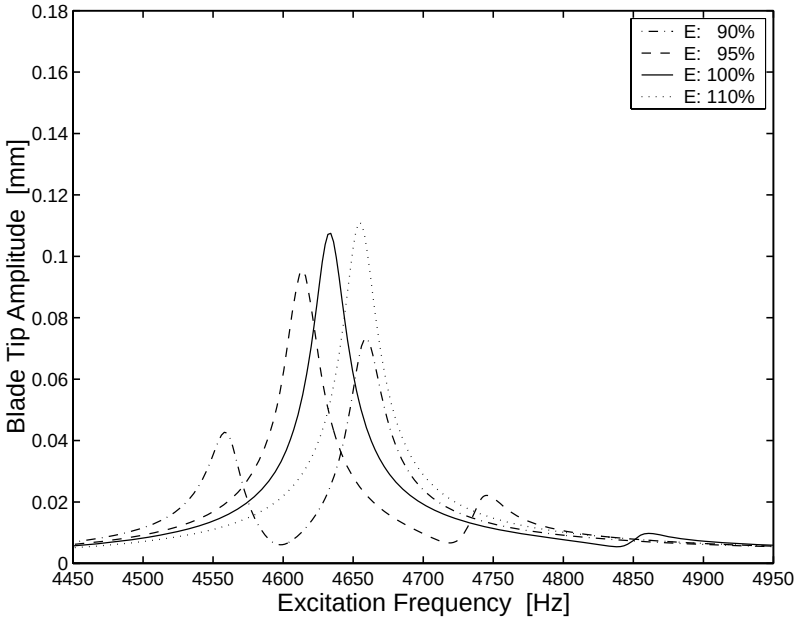

Figure 7.14: Tuned stage 1 forced response from engine order 10 excitation (10E=-2E) using the single-stage finite element model for varying levels of disk flexibility (E = Young's modulus).

via a mixed disk-blade mode type, and vice versa for the upper mode pair. Hence, at some disk flexibility level, when the center of the veering is located at integer harmonic two, both upper and lower mode pairs will be of the mixed disk-blade type. This has a strong impact on the tuned forced response through the veering, as shown in Fig. 7.14. As the lower mode pair goes from being largely disk-dominated to blade-dominated, its resulting maximum blade tip response amplitudes increase monotonically, while, logically, the opposite trend is observed for the upper mode pair response.

Interestingly, the mistuned responses depicted in Fig. 7.15 indicate that the maximum mistuned response amplitude does not exhibit this monotonic behavior. Instead, there exists some intermediate disk flexibility level, or, equivalently, veering-excitation proximity level, for which the amplification due to mistuning (i.e., the ratio of mistuned to tuned response) has a local maximum. To further elucidate the significance of the veering shift, the maximum tuned and mistuned responses were obtained as a function of closely spaced val-

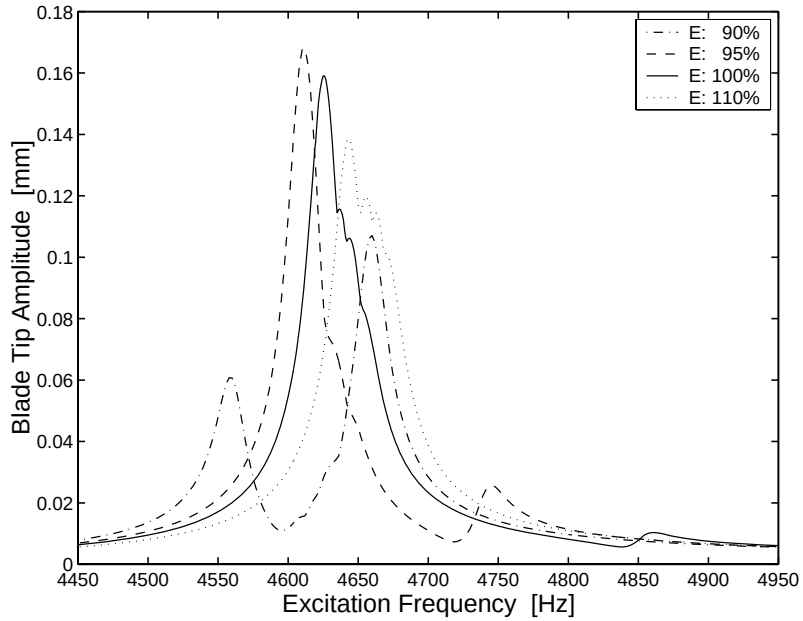

Figure 7.15: Mistuned stage 1 forced response from engine order 10 excitation (10E=-2E) using the single-stage finite element model for varying levels of disk flexibility (E = Young's modulus).

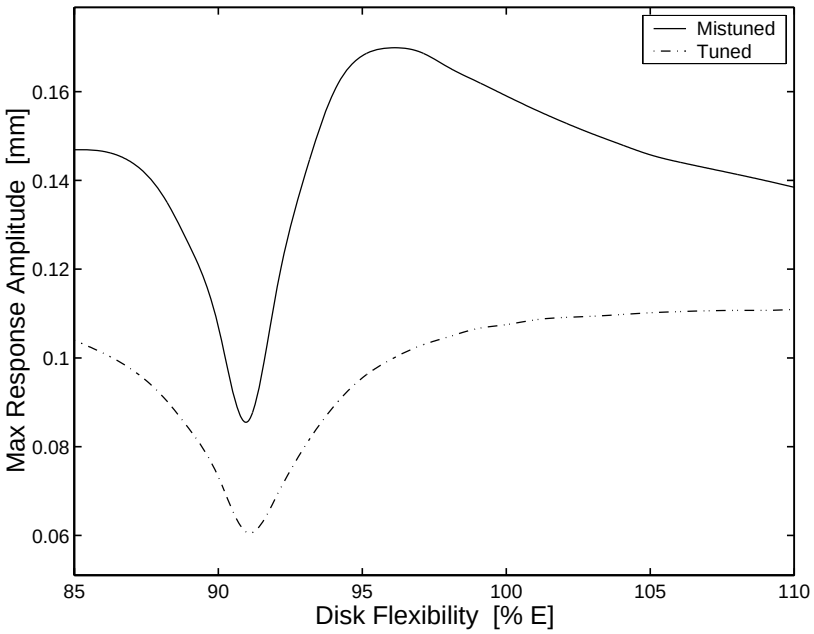

Figure 7.16: Stage 1 maximum tuned and mistuned forced responses from engine order 10 excitation (10E=-2E) as function of disk flexibility (E = Young's modulus) using the single-stage finite element model.

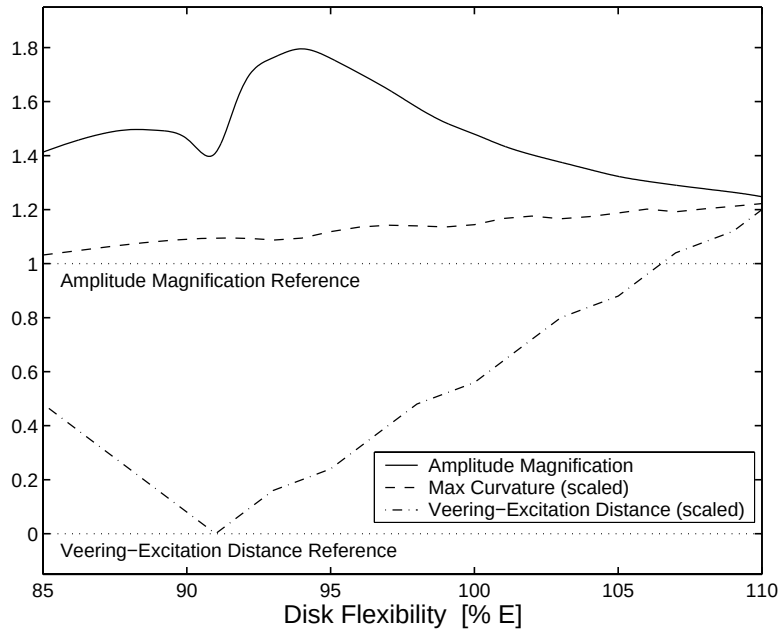

Figure 7.17: Mistuned response amplitude magnification from engine order 10 excitation (10E=-2E) for the stage 1 finite element model (single-stage) as function of disk flexibility (E = Young's modulus), plus the local eigenfrequency veering characteristics (uniformly scaled): maximum veering curvature, and distance between veering and applied excitation.

ues of disk Young's modulus. These results are shown in Fig. 7.16, where both tuned and mistuned responses from veering (-2E) excitation are shown to exhibit a distinct minimum for a specific flexibility level. Looking at the resulting mistuned-to-tuned amplifications in Fig. 7.17, it is observed that the flexibility level of minimum amplification corresponds to the case of a perfectly centered veering. Furthermore, Fig. 7.17 clearly demonstrates the existence of intermediate disk flexibility/veering-excitation proximity levels that yield local amplification maxima on either side of a perfectly centered veering.

While the findings in this section are thoroughly consistent, much work remains to get a clear picture of mistuning sensitivity, and, in particular, to get a firm basis for its quantification. However, the findings in this section support the hypothesis that mistuning sensitivity maxima are obtained for a delicate balance of disk and blade participation in

the highest-responding eigenfrequency veering mode pair. It is hypothesized that significant flexible blade motion is needed to "absorb" the engine order excitation applied to the blades, which will then amplify the elastic differences in the blades (blade mistuning). The disk motion is needed to communicate the vibration energy between sectors, leading to a transfer of energy from low-responding blades to high-responding blades. For a scenario in which the mode pair is too disk-dominated, the elastic discrepancies among the blades will not be sufficiently amplified due to mostly disk-induced rigid-body participation of the blades, hence the relative insensitivity to mistuning. In the other extreme, where the mode pair is too blade-dominated, the relative insensitivity to mistuning is instead due to the fact that sector-to-sector communication is largely disabled by the minimal disk participation, even though the elastic blade differences are amplified. The proposed hypothesis does not necessarily contradict existing ideas concerned with veering characteristics (local curvature, veering-excitation proximity, etc.). However, if true, this consideration may potentially make the issue of defining a quantitative measure of mistuning sensitivity even more delicate. On the other hand, it may allow the analyst to more quickly identify potentially "dangerous" veerings.

7.4.2 Effects of Interstage Coupling

In this section, it will be investigated whether there are some types of "standard" interstage boundary conditions that will result in single-stage dynamic characteristics that could be adequate for practical purposes. Clearly, it would be desirable to avoid multi-stage analyses as far as possible, since they add significant complexity in terms of modeling, and, in addition, make the task of interpreting the results more cumbersome.

As mentioned in the introduction, current practice is to analyze each rotor stage independently, using a set of interstage boundary conditions that the analyst feels will best de-

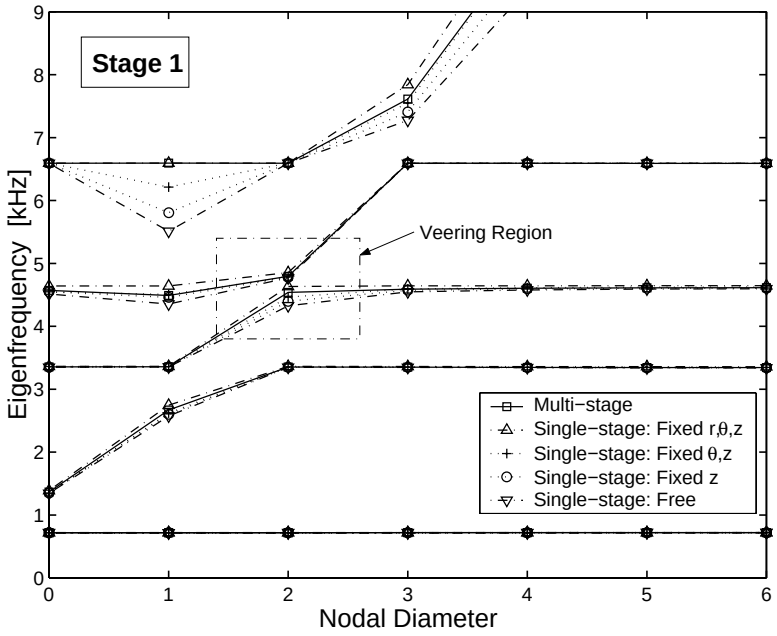

Figure 7.18: Natural frequencies versus number of nodal diameters for the tuned stage 1 rotor model using different interstage boundary conditions, plus identified harmonics of the "tuned" two-stage model.

scribe the constraints imposed by adjacent stages. Typically, this implies imposing either fully clamped conditions or axial restraints alone, or, in more elaborate cases, modeling of adjacent stages as uniformly distributed masses and stiffnesses (to preserve cyclicity). Clearly, the latter modeling approach will benefit from moving local boundary effects well away from the part of interest by virtue of Saint-Venant's principle [67]. However, it will not take into account the incompatible harmonics of adjacent stages, and thus the interstage-coupling-induced mistuning.

Figure 7.18 depicts the tuned natural frequencies versus the number of nodal diameters for various plausible, "standard" interstage boundary conditions — i.e., combinations of fixed radial (r), tangential (θ), and axial (z) directions — using the stage 1 model, plus the corresponding results for the two-stage model. Note that the models used for this case are the same as those in Section 7.3. As shown in Fig. 7.18, the imposed boundary constraints

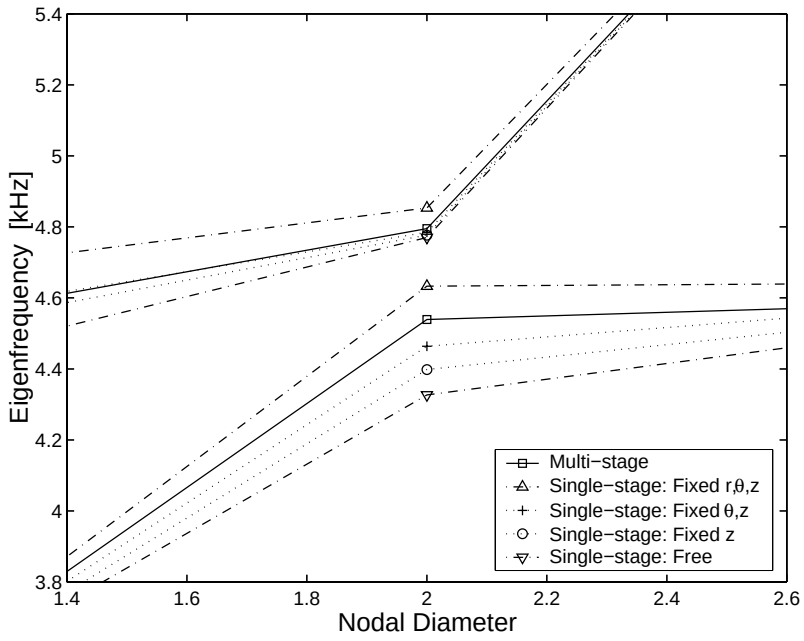

Figure 7.19: Detailed view over the eigenfrequency veering region indicated in Fig. 7.18.

yield a reasonable description of the "global" vibration characteristics of stage 1 compared to the results obtained with the multi-stage model. However, these approximate boundary conditions do not provide consistent representations in the eigenfrequency veerings, and thus fail to accurately describe the interaction between families of disk-dominated modes (slanted lines) and blade-dominated modes (horizontal lines). This unfortunate circumstance is clearly demonstrated in Fig. 7.19, which depicts a detailed view over the frequency veering region indicated in Fig. 7.18. As shown, the upper disk-dominated mode pair is fairly well represented by all boundary approximations, except for fully clamped conditions. In contrast, the approximate representations of the lower mode pair exhibit significant discrepancies from the "true" multi-stage behavior. While the fully clamped approximation predicts an overly blade-dominated mode pair, the others predict too much disk dominance. This is clearly a vital deficiency, since the disk-blade modal interaction in veering regions is a critically important factor in determining a design's sensitivity to

mistuning, as shown in Section 7.4.1.

Figures 7.20 and 7.21 depict the forced response resulting from an excitation through the veering in Fig. 7.19 (-2E). As expected, the upper resonance is approximated reasonably well by all the relaxed boundary conditions, since they also gave reasonable predictions of the free modes of vibration. For the lower resonance, the approximations are well off in terms of the resonant frequencies, which follows from the relatively wide scattering of the predicted eigenfrequencies in Fig. 7.19. Note, however, that the relaxed boundary conditions nevertheless yield reasonably accurate predictions of the maximum tuned response, since these are disk-dominated responses. In the mistuned case, the relaxed approximations tend to exaggerate the amplification due to mistuning, but they still provide reasonable approximations of the maximum mistuned response amplitude. Note that in both the tuned and mistuned cases, the clamped condition does not yield responses that are even reasonably close to the multi-stage responses. It also worth mentioning that, for obvious reasons, the single-stage approximations are unable to display any subresonances induced by adjacent stage dynamics exhibited by the multi-stage model.

It is realized that the model used in this study is highly simplified, and thus, it may not be representative of multi-stage effects for more realistic models. Therefore, in an effort to prove the findings of this study more general, two additional multi-stage cases are presented in this section, in which the stiffness of the disks and interstage rims is significantly different from the original model. For the first case, the stiffness of the disks and interstage rims is increased uniformly by using a Young's modulus (E) that is four times higher than that of the original model. From plate vibration theory (e.g., Meirovitch [45]), it is found that plate modal stiffness follow $\omega^2 \propto Eh^2$, where h is the plate thickness. Hence, in an approximate sense, the four-fold increase in Young's modulus corresponds to a model with a two-fold increase in thickness for the disks and interstage rims. In the second case,

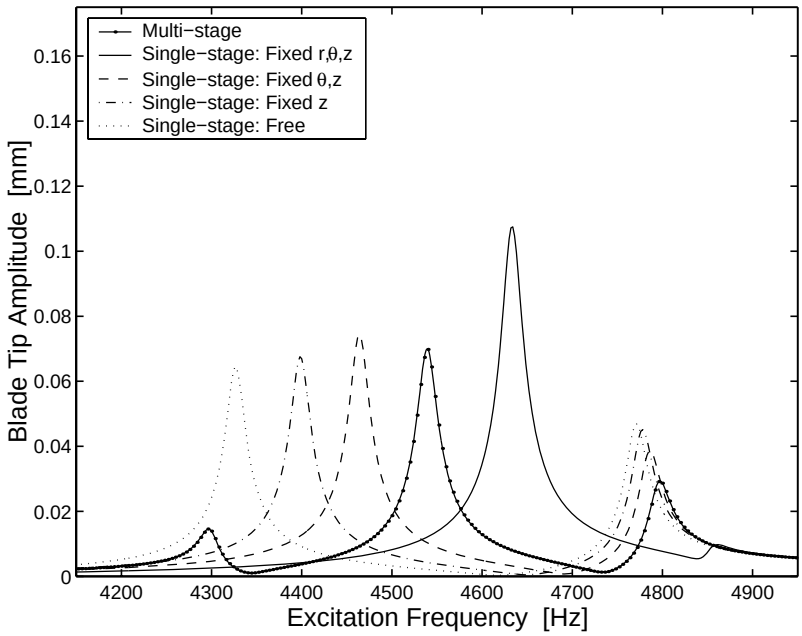

Figure 7.20: Stage 1 tuned finite element forced responses from engine order 10 excitation (10E=-2E) using different interstage boundary conditions, plus the "tuned" multi-stage finite element response.

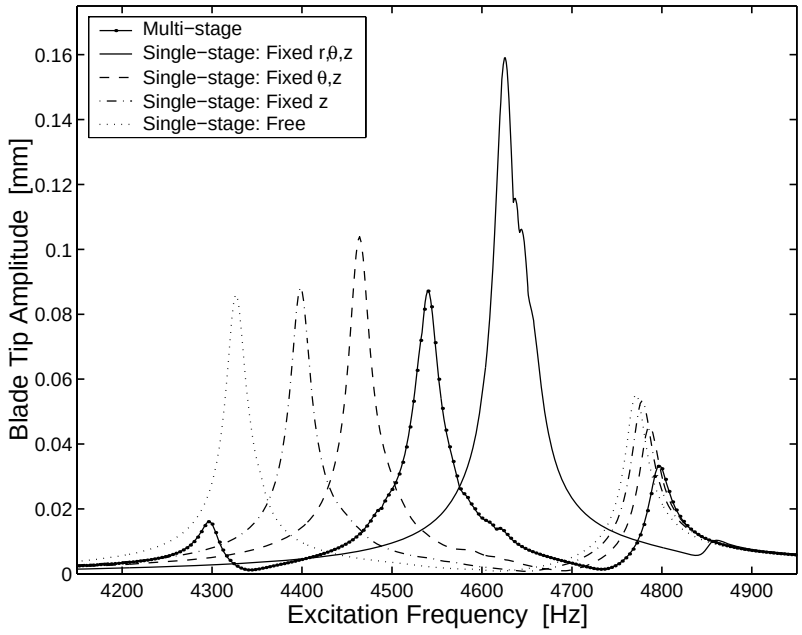

Figure 7.21: Stage 1 mistuned finite element forced responses from engine order 10 excitation (10E=-2E) using different interstage boundary conditions, plus the blade mistuned multi-stage finite element response.

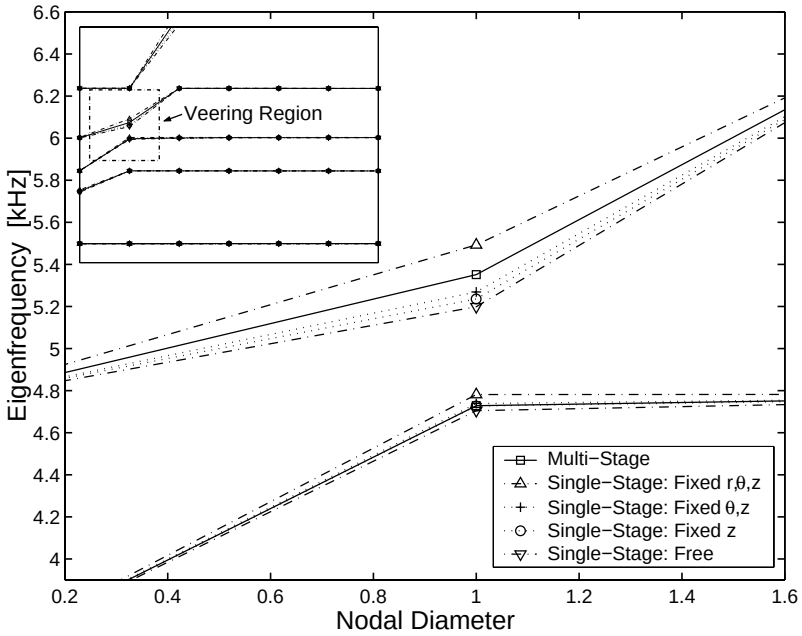

Figure 7.22: Detailed view over the eigenfrequency veering region indicated in the inserted plot of global free vibration characteristics (upper left). Included data is for the tuned stage 1 rotor model using different interstage boundary conditions, plus identified harmonics of the "tuned" two-stage model, with a four-fold increase of Young's modulus in the disk plus interstage rims.

only Young's modulus of the disks are increased by a factor four, while the interstage rims are unchanged. While this is clearly a very artificial way to alter a model, these two additional cases are nevertheless believed to establish that similar interstage coupling effects are likely to occur even though model characteristics may differ significantly.

An important observation made for both these additional cases is that the interstage-coupling-induced mistuning here results in slight deterioration of the spatially extended characteristic for a few blade-dominated modes of higher harmonics. Hence, the stiffer disks increase the mistuning sensitivity of the two-stage model significantly, considering the extremely low level of mistuning that is being induced by the interstage coupling. Furthermore, since the eigenfrequency veering region under investigation in this section is located at lower harmonics, the harmonics of the modes surrounding the veering are readily identified in spite of this deterioration.

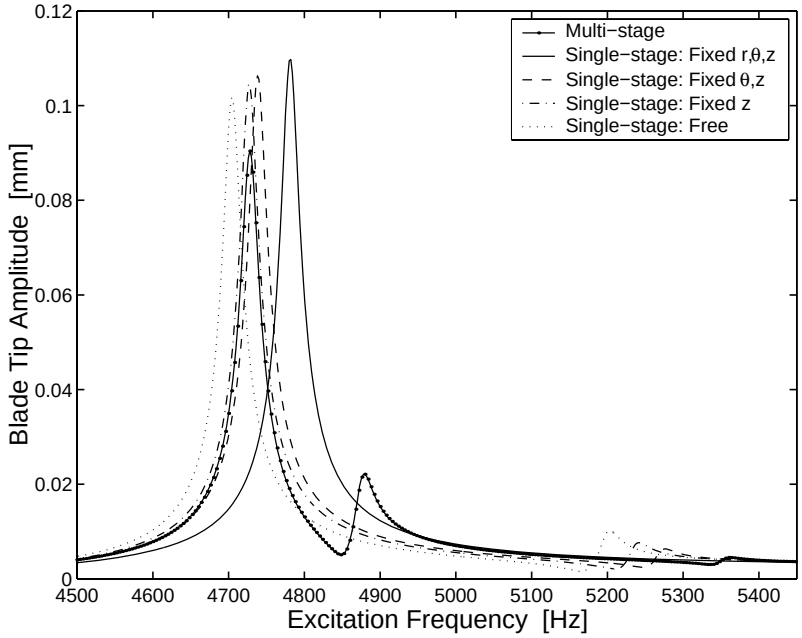

Figure 7.23: Stage 1 tuned finite element forced responses from engine order 11 excitation (11E=-1E) using different interstage boundary conditions, plus the "tuned" multi-stage finite element response, with a four-fold increase of Young's modulus in the disk plus interstage rims.

The uniform stiffening of the entire disks leads to drastically different free vibration characteristics, as shown in Fig. 7.22. The significantly stiffer stage 1 disk has shifted the disk-dominated modes to higher frequencies to form a harmonic 1 veering instead of the original harmonic 2 veering. Moreover, it is observed from Fig. 7.22 that the features of the veering and the boundary approximations are reversed in this case. Here, the boundary approximations exhibit significant discrepancies for the upper (disk-dominated) mode pair, while the lower mode pair has too much blade dominance to be affected by the differing disk flexibilities to any significant extent. Consequently, the approximations of the lower blade-dominated resonance are tightly clustered in frequency, as depicted in Fig. 7.23. Note, however, that all approximate boundary conditions predict similarly exaggerated tuned maximum resonant amplitudes, overshooting the true multi-stage amplitude by 12–21%.

When stiffening only the disks without the interstage rims, the free vibration charac-

teristics are similar to the previous case in that the veering occurs at harmonic 1. However, upon closer examination, the local veering characteristics are found to be drastically different, as depicted in Fig. 7.24. The more flexible interstage rims have shifted the disk-dominated modes to slightly lower frequencies relative to the previous case. Therefore, the veering is now comprised of an upper disk-dominated mode pair and a lower mode pair that is very close to having significant disk participation. In this case, it is particularly notable how well the natural frequency of the more blade-dominated lower mode pair is approximated by the fully clamped condition, while the relaxed boundary conditions are well off target. Recall that the fully clamped condition resulted in the worst approximations in the original disk flexibility case. However, for the upper mode pair, it is again the clamped approximation that is the most off target. Hence, as shown in Fig. 7.25, the clamped condition predicts the true multi-stage resonant frequency very well. However, it is still off considerably in terms of expected maximum amplitude. The relaxed boundary conditions, on the other hand, are well off target in terms of resonant frequency, and, except for the "Fixed θ, z" case, well off in terms of maximum resonant amplitude as well.

The examples presented in this section demonstrate that interstage coupling and adjacent stage dynamics have a significant impact on free and forced response behavior for multi-stage rotor models with widely different characteristics. Furthermore, these examples show that there is no "standard" interstage boundary condition to be used in single-stage analysis that will consistently yield sufficiently good approximations of true multi-stage behavior. Rather, the performance of such boundary conditions is governed by local veering characteristics, including disk-blade mode dominance, and can therefore only be employed with confidence (if at all) on a case-to-case basis.

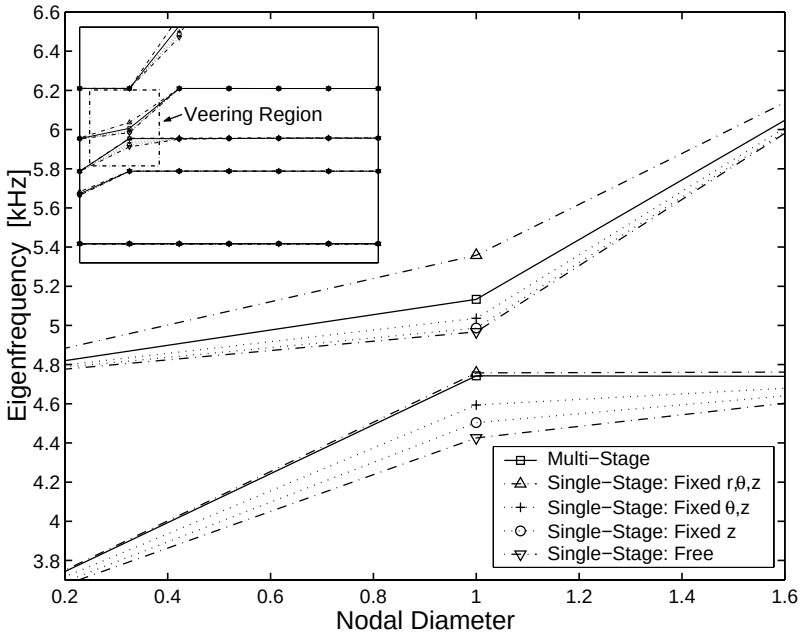

Figure 7.24: Detailed view over the eigenfrequency veering region indicated in the inserted plot of global free vibration characteristics (upper left). Included data is for the tuned stage 1 rotor model using different interstage boundary conditions, plus identified harmonics of the “tuned” two-stage model, with a four-fold increase of Young’s modulus in the disk alone.

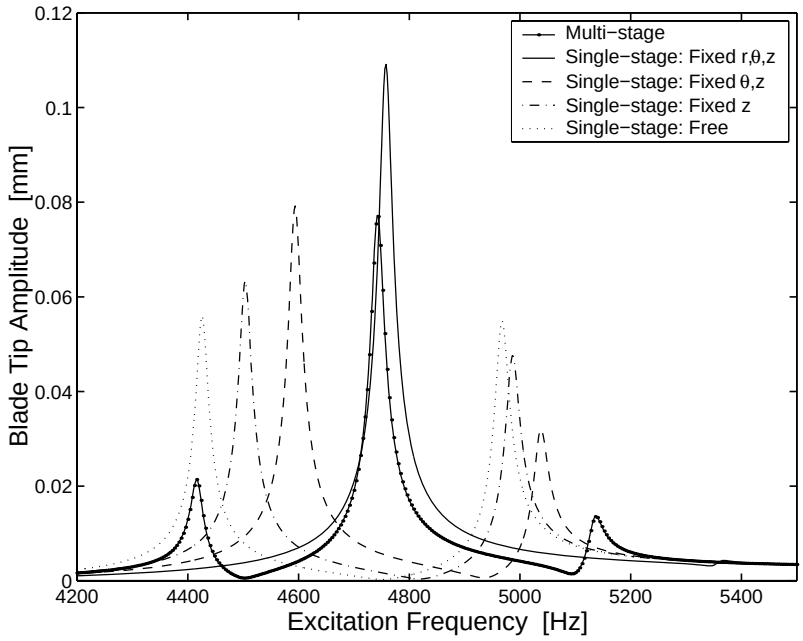

Figure 7.25: Stage 1 tuned finite element forced responses from engine order 11 excitation (11E=-1E) using different interstage boundary conditions, plus the “tuned” multi-stage finite element response, with a four-fold increase of Young’s modulus in the disk alone.

7.5 Conclusions

This paper explored the effects of multi-stage coupling on the dynamics of bladed disks with and without blade mistuning. Both free and forced responses of an example two-stage finite element rotor were examined.

Several important implications of multi-stage coupling were identified in this work. One important observation was that disk mistuning is inherent in the coupled multi-stage system, due to different numbers of sectors for adjacent stages. Furthermore, the reported work demonstrated the importance of proper treatment of interstage (stage-to-stage) boundaries in order to yield adequate capture of a design's disk-blade modal interaction in eigenfrequency regions, also denoted structural interblade coupling. The modifications to the disk-blade modal interactions resulting from structural interstage coupling effects were found to have a significant impact on (a) tuned responses due to excitations passing through eigenfrequency veering regions, and (b) a design's sensitivity to blade mistuning. Hence, the findings in this paper suggest that multi-stage analyses may in fact be required when excitations are expected to fall in or near eigenfrequency veering regions or when the sensitivity to blade mistuning is to be adequately accounted for.

Furthermore, the observations in this paper support the hypothesis that mistuning sensitivity maxima are obtained for a delicate balance of disk and blade participation in the highest-responding eigenfrequency veering mode pair. Significant flexible blade motion is needed to "absorb" the applied engine order excitation, which will then amplify the structural differences in the blades. The disk motion is needed to communicate the vibration energy between sectors, leading to vibration energy localization by partial reflections. This consideration may allow the analyst to more quickly identify potentially "dangerous" eigenfrequency veerings.

The found sensitivity of eigenfrequency veering response complicates significantly the dynamic analysis of multi-stage rotor systems. These findings suggest that multi-stage analyses should be performed when excitations are expected to fall in or near eigenfrequency veering regions. However, the found sensitivity also opens up the possibility of reducing the severity of unfavorable excitation cases by re-designing the disk(s) and interstage connectivity. The relatively drastic effects of such modifications illustrated in this work indicate that the design modifications required to alleviate veering-related response problems may be less comprehensive than what might have been expected.

CHAPTER VIII

Reduced Order Modeling Techniques for Dynamic Analysis of Mistuned Multi-Stage Turbomachinery Rotors

Recent findings indicate that structural interstage (stage-to-stage) coupling in multi-stage rotors can have a critical impact on bladed disk dynamics by altering significantly the flexibility of the disk. This affects local eigenfrequency veering characteristics, and thus a design's sensitivity to mistuning. In response to these findings, two reduced order modeling techniques are presented that accurately capture structural interstage coupling effects, while keeping model sizes at practical levels. Both free and forced responses of an example two-stage rotor are examined using novel component-mode-based reduced order modeling techniques for mistuned multi-stage assemblies. Both techniques employ an intermediate multi-stage model constructed by component mode synthesis (CMS), which is further reduced by either: (a) partial secondary modal analyses on constraint-mode partitions; or (b) a full-scale secondary modal analysis on the entire multi-stage CMS model. The introduced techniques are evaluated using finite element results as a benchmark. The proposed reduced order modeling techniques are shown to facilitate accurate multi-stage modeling and analyses with or without blade mistuning, using only computationally inexpensive modal data from a cyclic disk sector and a single blade per stage. It is concluded that a combination of approaches (a) and (b) is the most promising and practically feasible

approach to the computationally efficient and accurate modeling of the dynamics of mistuned multi-stage rotor assemblies. Furthermore, by alleviating the restriction to single-stage analyses, the multi-stage modeling techniques will enable engineers to analyze the dynamics of mistuned turbomachinery rotor assemblies with greater confidence.

8.1 Introduction

In studies of bladed disk vibration, the analyses are typically based on single-stage models, in which the effects of adjacent stages are approximated by static interstage (stage-to-stage) boundary conditions. Hence, the structural interstage coupling, as well as the dynamics of adjacent rotor stages, are to a large extent ignored in such analyses. Recent findings by Bladh *et al*. [1] indicate that interstage coupling can have a critical impact on bladed disk dynamics by altering significantly the flexibility of the disk. This affects local eigenfrequency veering characteristics, and thus interstage coupling is an important and potentially decisive factor in determining a design's sensitivity to mistuning. However, while the efficient modeling of mistuned single-stage dynamics has received relatively wide attention in the recent literature (Castanier *et al*. [20]; Yang and Griffin [68]; Moyroud *et al*. [69]; Bladh *et al*. [70, 71]), the authors are not aware of any efforts to model the dynamics of mistuned multi-stage rotor assemblies.

To improve upon this situation, the focus of this paper is on the development of two related reduced order modeling approaches for computationally feasible dynamic analyses of mistuned multi-stage rotor systems. The two introduced reduced order modeling techniques facilitate accurate multi-stage modeling and analyses featuring blade mistuning, using inexpensive modal data from a cyclic disk sector and a single blade per stage. The techniques are quite general in that the single-stage models could be derived using any Component Mode Synthesis (CMS) formulation, with only a minimum of modifi-

cations. The single-stage representations employed here are based on the cyclic CMS implementation recently developed by Bladh *et al*. [70], which uses the classical CMS technique formulated by Craig and Bampton [29]. Moreover, both approaches are based on single-stage models with clamped interstage boundaries, which are coupled together through static constraint modes for all interstage degrees of freedom. One of the proposed formulations then utilizes partial secondary modal analyses on the disk-to-blade and the stage-to-stage interface matrix partitions, from which truncated sets of so-called "characteristic constraint modes" (see Tan *et al*. [61]) are retained for significant further model reduction. The second approach uses a full-scale secondary modal analysis on the entire multi-stage CMS model, analogous to the single-stage secondary modal analysis reduction technique (SMART) that was developed by Bladh *et al*. [70]. It is important to note that in both formulations, the resulting reduced order models are exclusively in generalized (modal) coordinates. Thus, the final sizes of the reduced order models are in both cases independent of the size of the parent finite element models, which may be of arbitrary complexity.

This paper is organized as follows. Section 8.2 outlines the proposed reduced order modeling formulations. Section 8.3 presents a test case in which the introduced techniques are applied to the dynamic analysis of a simple two-stage finite element model, including brief modal convergence studies that aid in setting up the reduced order models. The results presented in Section 8.3 serve to validate the reduced order modeling approaches in the free and forced response, with and without blade mistuning. Important conclusions from this study are summarized in Section 8.4.

8.2 Reduced Order Modeling Techniques

The proposed techniques employ as their basis a cyclic implementation of the classical Craig-Bampton (C-B) CMS method [29, 62, 24]. The cyclic C-B implementation for single-stage models was thoroughly outlined in Bladh *et al*. [70], and therefore it will not be repeated in detail. However, the subsequent multi-stage coupling mandates certain modifications to the single-stage theory. Hence, in the following, important differences for the single-stage CMS model are first described, followed by two related extensions to multi-stage reduced order modeling.

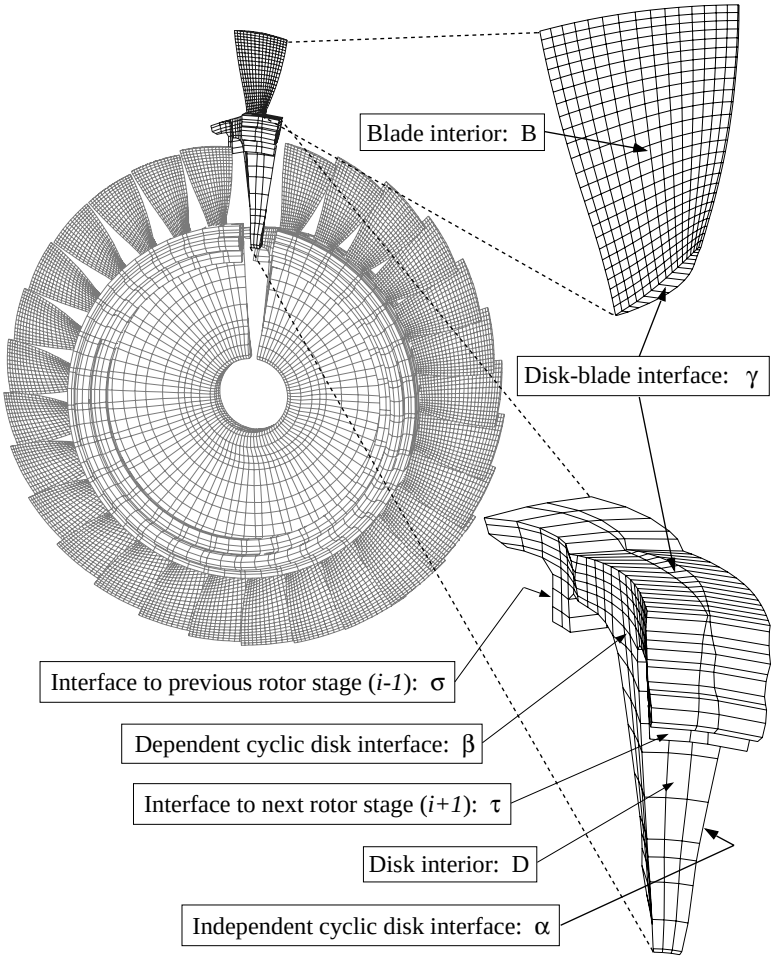

Figure 8.1: Substructuring approach and index notation for the i^{th} rotor stage.

8.2.1 Single-Stage CMS Model

A tuned N-bladed disk assembly can be divided into N identical blades (b) and one disk component (d), where it is assumed that the disk features cyclic symmetry (i.e., N identical sectors). A disk sector and a blade component are depicted in Fig. 8.1, which also outlines the used index notation for the components and the interfaces with neighboring components.

The fundamental difference between the single-stage formulation in Bladh *et al*. [70] and the current work is that the interstage degrees of freedom (DOF) must be retained as active DOF in the multi-stage CMS model. This implies that the total set of interface DOF, which is here denoted Γ, includes the interstage DOF sets (σ,τ), in addition to the disk-blade interface DOF set (γ). Note that cyclic constraints must be applied to those interstage DOF that are located on the fringe of the cyclic disk interfaces (see Bladh *et al*. [70] for details). With this setup, the cyclic C-B component formulation given in Bladh *et al*. [70] may be followed exactly by letting all partitions pertaining to the Γ DOF-set be sub-partitioned as:

$$\mathbf{\Gamma} = \left\{ \begin{array}{c} \gamma \\ \sigma \\ \tau \end{array} \right\}. \tag{8.1}$$

In the cyclic C-B implementation, the disk motion is represented as a linear combination of cyclic normal modes of the disk component with all interstage and disk-blade interface DOF held fixed, $\left(\tilde{\mathbf{\Lambda}}_{\mathbf{d}}, \tilde{\mathbf{\Phi}}^{\mathbf{h}}_{\mathbf{d}}\right)$, and cyclic static constraint modes, $\tilde{\mathbf{\Psi}}^{\mathbf{h}}_{\mathbf{d}}$. The latter mode set is comprised of the static shapes of the disk component due to successive unit displacements of each interface DOF with all other interface DOF held fixed. The two mode sets are obtained for all harmonics $h = 0, \ldots, P$, where P is the highest possible harmonic for an N-bladed disk, defined as $P = \mathbf{int}\,[N/2]$. Note that this implies that the

constraint modes pertaining to the interstage DOF (a subset of $\tilde{\mathbf{\Psi}}^{\mathbf{h}}_{\mathbf{d}}$) will also be in cyclic format. Also, note that the "tilde" notation is used throughout this paper to indicate when a quantity is represented in cyclic coordinates.

The transformation from physical disk coordinates to C-B cyclic disk modal coordinates, $\tilde{\mathbf{p}}^{\mathbf{d}}$, yields the C-B mass and stiffness matrices for the disk component:

$$\tilde{\mu}^{\mathbf{d}} = \begin{bmatrix} \mathbf{I} & \tilde{\mu}_{\mathbf{dc}} \\ \tilde{\mu}^{\mathbf{T}}_{\mathbf{dc}} & \tilde{\mu}_{\mathbf{cc,d}} \end{bmatrix} \qquad \tilde{\kappa}^{\mathbf{d}} = \begin{bmatrix} \tilde{\mathbf{\Lambda}}_{\mathbf{d}} & \mathbf{0} \\ \mathbf{0} & \tilde{\kappa}_{\mathbf{cc,d}} \end{bmatrix}, \tag{8.2}$$

where

$$\begin{aligned} \tilde{\mu}_{\mathbf{dc}} &= \underset{h=0,\ldots,P}{\tilde{\mathbf{B}}\mathbf{diag}}\left[\tilde{\mathbf{\Phi}}^{\mathbf{h}^{\mathbf{T}}}_{\mathbf{d}}\left[\tilde{\mathrm{M}}^{\mathbf{h}}_{\mathbf{d,ss}}\tilde{\mathbf{\Psi}}^{\mathbf{h}}_{\mathbf{d}} + \tilde{\mathrm{M}}^{\mathbf{h}}_{\mathbf{d,s\Gamma}}\right]\right] \\ \tilde{\mu}_{\mathbf{cc,d}} &= \underset{h=0,\ldots,P}{\tilde{\mathbf{B}}\mathbf{diag}}\left[\tilde{\mathbf{\Psi}}^{\mathbf{h}^{\mathbf{T}}}_{\mathbf{d}}\left[\tilde{\mathrm{M}}^{\mathbf{h}}_{\mathbf{d,ss}}\tilde{\mathbf{\Psi}}^{\mathbf{h}}_{\mathbf{d}} + \tilde{\mathrm{M}}^{\mathbf{h}}_{\mathbf{d,s\Gamma}}\right] + \tilde{\mathrm{M}}^{\mathbf{h}^{\mathbf{T}}}_{\mathbf{d,s\Gamma}}\tilde{\mathbf{\Psi}}^{\mathbf{h}}_{\mathbf{d}} + \tilde{\mathrm{M}}^{\mathbf{h}}_{\mathbf{d,\Gamma\Gamma}}\right] \\ \tilde{\kappa}_{\mathbf{cc,d}} &= \underset{h=0,\ldots,P}{\tilde{\mathbf{B}}\mathbf{diag}}\left[\mathrm{K}^{\mathbf{h}}_{\mathbf{d,\Gamma\Gamma}} + \mathrm{K}^{\mathbf{h}^{\mathbf{T}}}_{\mathbf{d,s\Gamma}}\mathbf{\Psi}^{\mathbf{h}}_{\mathbf{d}}\right]. \end{aligned}$$

$\tilde{\mathbf{B}}\mathbf{diag}\left[\bullet\right]$ denotes a pseudo-block-diagonal matrix (see Appendix B), with the argument being the h^{th} "block", and the range of harmonics, h, is shown. Note that there is no coupling between the harmonics due to the orthogonality of the cyclic modes. Moreover, the physical (c) matrix partitions appearing in Eq. (8.2) follow the formulation in Bladh *et al*. [70], with the added sub-partitioning of the Γ-partitions as set forth in Eq. (8.1). The condensed matrices in Eq. (8.2) are thus the C-B representation of a disk with free interstage boundaries.

In a similar fashion, the motion of each blade is represented as a linear combination of normal modes of the blade component clamped at the disk-blade interface, $(\mathbf{\Lambda}_{\mathbf{b}}, \mathbf{\Phi}_{\mathbf{b}})$, and a complete set of static constraint modes, $\mathbf{\Psi}_{\mathbf{b}}$. Recall that the blades are assumed identical (tuned) at this point, and that the blades are not coupled other than through the disk (unshrouded blades). It is therefore sufficient to look at a single blade and then expand to the N blades in the assembly.

The transformation from physical blade coordinates to C-B blade modal coordinates, $\mathbf{p^b}$, yields the C-B mass and stiffness matrices expanded for all N blade components:

$$\bar{\mu}^{\mathbf{b}} = \begin{bmatrix} \mathbf{I} & \mathbf{I} \otimes \mu_{\mathbf{bc}} \\ \mathbf{I} \otimes \mu_{\mathbf{bc}}^{\mathbf{T}} & \mathbf{I} \otimes \mu_{\mathbf{cc,b}} \end{bmatrix} \qquad \bar{\kappa}^{\mathbf{b}} = \begin{bmatrix} \mathbf{I} \otimes \mathbf{\Lambda_b} & \mathbf{0} \\ \mathbf{0} & \mathbf{I} \otimes \kappa_{\mathbf{cc,b}} \end{bmatrix}, \tag{8.3}$$

where

$$\begin{aligned} \mu_{\mathbf{bc}} &= \mathbf{\Phi_b^T} \left[\mathbf{M_{BB}^b \Psi_b} + \mathbf{M_{B\gamma}^b} \right] \\ \mu_{\mathbf{cc,b}} &= \mathbf{\Psi_b^T} \left[\mathbf{M_{BB}^b \Psi_b} + \mathbf{M_{B\gamma}^b} \right] + \mathbf{M_{B\gamma}^{b^T} \Psi_b} + \mathbf{M_{\gamma\gamma}^b} \\ \kappa_{\mathbf{cc,b}} &= \mathbf{K_{\gamma\gamma}^b} + \mathbf{K_{B\gamma}^{b^T} \Psi_b}, \end{aligned}$$

and the symbol $\otimes$ denotes the Kronecker product (see Appendix A).

The single-stage synthesis is achieved by satisfying displacement compatibility over the disk-blade interfaces, which leads to the constraint:

$$\bar{\mathbf{x}}_\gamma^{\mathbf{b}} = \mathbf{p}_\gamma^{\mathbf{b}} = (\mathbf{F} \otimes \mathbf{I})\, \tilde{\mathbf{p}}_\gamma^{\mathbf{d}} = \hat{\mathbf{F}} \tilde{\mathbf{p}}_\gamma^{\mathbf{d}} = \bar{\mathbf{x}}_\gamma^{\mathbf{d}}, \tag{8.4}$$

where $\mathbf{F}$ is the real-valued Fourier matrix defined in Appendix B. Enforcing this constraint, and separating the disk's physical interface (c) partitions into interstage (σ,τ) and disk-blade interface (γ) DOF, the synthesized system matrices for a single stage have the form:

$$\mathcal{S} = \begin{bmatrix} \mathbf{S}_{\sigma\sigma} & \mathbf{S}_{\sigma\mathbf{s}} & \mathbf{S}_{\sigma\tau} \\ \mathbf{S}_{\sigma\mathbf{s}}^{\mathbf{T}} & \mathbf{S}_{\mathbf{ss}} & \mathbf{S}_{\mathbf{s}\tau} \\ \mathbf{S}_{\sigma\tau}^{\mathbf{T}} & \mathbf{S}_{\mathbf{s}\tau}^{\mathbf{T}} & \mathbf{S}_{\tau\tau} \end{bmatrix}, \tag{8.5}$$

where $\mathbf{S}$ is $\mathbf{K}$ or $\mathbf{M}$. The blocks pertaining to the interstage DOF towards the next stage

(τ) are:

$$\begin{aligned}
\mathbf{M}_{\sigma\tau} &= \tilde{\mu}_{\sigma\tau} & \mathbf{K}_{\sigma\tau} &= \tilde{\kappa}_{\sigma\tau} \\
\mathbf{M}_{\mathbf{s}\tau} &= \begin{bmatrix} \tilde{\mu}_{\mathbf{d}\tau} \\ \tilde{\mu}_{\gamma\tau} \\ \mathbf{0} \end{bmatrix} & \mathbf{K}_{\mathbf{s}\tau} &= \begin{bmatrix} \mathbf{0} \\ \tilde{\kappa}_{\gamma\tau} \\ \mathbf{0} \end{bmatrix}, \\
\mathbf{M}_{\tau\tau} &= \tilde{\mu}_{\tau\tau} & \mathbf{K}_{\tau\tau} &= \tilde{\kappa}_{\tau\tau}
\end{aligned} \tag{8.6}$$

and similarly for the σ DOF. The center partition in Eq. (8.5) corresponds to the C-B condensed mass and stiffness matrices for a rotor stage with clamped interstage boundaries:

$$\begin{aligned}
\mathbf{M_{ss}} &= \begin{bmatrix} \mathbf{I} & \tilde{\mu}_{\mathbf{d}\gamma} & \mathbf{0} \\ \tilde{\mu}_{\mathbf{d}\gamma}^{\mathbf{T}} & \tilde{\mu}_{\gamma\gamma,\mathbf{d}} + \mathbf{I} \otimes \mu_{\mathbf{cc,b}} & \hat{\mathbf{F}}^{\mathbf{T}} \left(\mathbf{I} \otimes \mu_{\mathbf{bc}}^{\mathbf{T}} \right) \\ \mathbf{0} & \left(\mathbf{I} \otimes \mu_{\mathbf{bc}} \right) \hat{\mathbf{F}} & \mathbf{I} \end{bmatrix} \\
\mathbf{K_{ss}} &= \begin{bmatrix} \tilde{\mathbf{\Lambda}}_{\mathbf{d}} & \mathbf{0} & \mathbf{0} \\ \mathbf{0} & \tilde{\kappa}_{\gamma\gamma,\mathbf{d}} + \mathbf{I} \otimes \kappa_{\mathbf{cc,b}} & \mathbf{0} \\ \mathbf{0} & \mathbf{0} & \mathbf{K}_{\mathbf{bb}}^{\mathbf{cb}} \end{bmatrix},
\end{aligned} \tag{8.7}$$

where

$$\mathbf{K}_{\mathbf{bb}}^{\mathbf{cb}} = \underset{n=1,\ldots,N}{\mathbf{Bdiag}} \left[\underset{k=1,\ldots,m_b}{\mathbf{diag}} \left[1 + \delta_n^k \right] \mathbf{\Lambda_b} \right]. \tag{8.8}$$

Note that the formulation now includes blade mistuning in the form of Eq. (8.8). Introducing mistuning this way implies that blade mistuning is modeled by offsets in modal stiffnesses Λ — or, equivalently, offsets in natural frequencies ω — of the blades while fixed at the disk-blade interface (cantilevered). Furthermore, the modal stiffnesses of the m_b retained cantilevered blade modes may be mistuned individually in this formulation. When considering variations in Young's modulus as the only source of blade mistuning, the mistuning parameter δ_n^k is replaced by δ_n, which then represents the offset of Young's modulus from its nominal value for the n^{th} blade.

8.2.2 Engine Order Excitation Force

In this work, the external sources of excitation on the rotor stages are assumed to be stage-wise independent engine order excitations, which are harmonic in time and differ only in phase from blade to blade. The phase at the n^{th} blade, φ_n, is then given by:

$$\varphi_n = \frac{2\pi C(n-1)}{N}, \tag{8.9}$$

where C is the engine order of the excitation. The external force vector for one stage can then be expressed as:

$$\mathbf{Q} = \sqrt{N}\mathbf{e}_{\mathbf{C+1}} \otimes \mathbf{f}, \tag{8.10}$$

where $\mathbf{e}_{\mathbf{C+1}}$ is the $(C+1)^{\text{th}}$ column of the complex Fourier matrix defined in Appendix B, and the column vector $\mathbf{f}$ contains the forces on the interior (B) DOF of a fundamental blade. The restriction to interior blade DOF is not an absolute requirement, but it leads to a more compact formulation, and it should be sufficient from a practical perspective.

Projection of the blade component modes ($\mathbf{\Phi_b}$ and $\mathbf{\Psi_b}$) onto the physical blade force vector described in Eq. (8.10) while enforcing the constraints of Eq. (8.4) yields the non-

zero modal force partitions

$$\mathbf{F^{cb}} = \left\{ \begin{array}{c} \mathbf{F_c^{cb}} \\ \cdots \\ \mathbf{F_b^{cb}} \end{array} \right\} = \left\{ \begin{array}{c} \mathbf{0} \\ \vdots \\ \mathbf{0} \\ \sqrt{N}\mathbf{f_{C,c}^T e_{C+1}} \otimes \mathbf{\Psi_b^T f} \\ \sqrt{N}\mathbf{f_{C,s}^T e_{C+1}} \otimes \mathbf{\Psi_b^T f} \\ \mathbf{0} \\ \vdots \\ \mathbf{0} \\ \cdots\cdots\cdots\cdots\cdots \\ \sqrt{N}\mathbf{e_{C+1}} \otimes \mathbf{\Phi_b^T f} \end{array} \right\}. \tag{8.11}$$

Note how orthogonality between columns of $\mathbf{E}$ and $\mathbf{F}$ of different interblade phase angles simplifies the modal force partition pertaining to the constraint modes.

8.2.3 Multi-Stage Synthesis

Multi-stage assembly is achieved by requiring displacement compatibility over interstage boundaries. Since the interstage DOF remain in cyclic coordinates, this is satisfied by:

$$\bar{\mathbf{x}}_\sigma^{\mathbf{i+1}} = \hat{\mathbf{F}}_{\mathbf{i+1}} \tilde{\mathbf{p}}_\sigma^{\mathbf{i+1}} = \mathbf{P_i} \hat{\mathbf{F}}_{\mathbf{i}} \tilde{\mathbf{p}}_\tau^{\mathbf{i}} = \bar{\mathbf{x}}_\tau^{\mathbf{i}}, \tag{8.12}$$

where $\hat{\mathbf{F}}_{\mathbf{i}}$ is the real-valued Fourier matrix based on stage i's number of blades, N_i. $\mathbf{P_i}$ is a matrix containing a set of kinematic constraint equation coefficients (i.e., multi-point constraints in finite element terminology), which may be required to kinematically constrain stage $i+1$'s σ interstage boundary DOF to their counterparts on stage i's τ boundary. Keeping $\bar{\mathbf{x}}_\tau^{\mathbf{i}}$ as active coordinate from Eq. (8.12), the system matrices of a synthesized

chain of rotor stages is obtained schematically as:

$$\mathcal{S}^{\mathbf{m}} = \begin{bmatrix} \ddots & \ddots & \mathbf{0} & & \\ \ddots & \mathbf{S_0^i} & \mathbf{S_1^i} & \mathbf{0} & \\ \mathbf{0} & \mathbf{S_1^{i^T}} & \mathbf{S_0^{i+1}} & \mathbf{S_1^{i+1}} & \mathbf{0} \\ & \mathbf{0} & \mathbf{S_1^{i+1^T}} & \mathbf{S_0^{i+2}} & \ddots \\ & & \mathbf{0} & \ddots & \ddots \end{bmatrix}, \tag{8.13}$$

where

$$\mathbf{S_0^i} = \begin{bmatrix} \mathbf{S_{\tau\tau}^{i-1}} + \mathbf{P_i^{s^T}} \mathbf{S_{\sigma\sigma}^i} \mathbf{P_i^s} & \mathbf{P_i^{s^T}} \mathbf{S_{\sigma s}^i} \\ \mathbf{S_{\sigma s}^{i^T}} \mathbf{P_i^s} & \mathbf{S_{ss}^i} \end{bmatrix} \qquad \mathbf{S_1^i} = \begin{bmatrix} \mathbf{P_i^{s^T}} \mathbf{S_{\sigma\tau}^i} & \mathbf{0} \\ \mathbf{S_{s\tau}^i} & \mathbf{0} \end{bmatrix}.$$

Again, $\mathbf{S}$ is $\mathbf{K}$ or $\mathbf{M}$, and $\mathbf{P_{i+1}^s} = \hat{\mathbf{F}}_{\mathbf{i+1}}^{\mathbf{T}} \mathbf{P_i} \hat{\mathbf{F}}_{\mathbf{i}}$ is the interstage transformation matrix resulting from Eq. (8.12).

Certain important implications of the multi-stage synthesis process should be noted. First, it is realized that adjacent stages will typically not have the same number of blades (i.e., $N_{i+1} \neq N_i$). Hence, in general, the cyclicity of the single-stage representations is therefore destroyed when stages are coupled together via Eq. (8.12). As an important consequence, the coupling of the stages will thus inherently introduce some level of mistuning to the system when $N_{i+1} \neq N_i$. Note that the interstage coupling induces disk mistuning, rather than the more commonly considered blade mistuning. Second, it should be noted that for large, industrial-size models with non-matching sector finite element meshes from one stage to the next, the constraint coefficient matrix $\mathbf{P_i}$ may be somewhat cumbersome to generate. On the other hand, this process should be well suited for code implementation due to stage-wise spatial repetitiveness. Alternatively, the matrix $\mathbf{P_i}$ can be avoided altogether (i.e., $\mathbf{P_i} = \mathbf{I}$) by making sure during modeling that the disk meshes match up perfectly at the interstage boundary. However, it should be noted that this may yield impractically large models in cases where the numbers of blades on adjacent rotor stages are

particularly incompatible (e.g., prime numbers).

8.2.4 Options for Secondary Condensation

The CMS model of the multi-stage rotor in its present form is not practical, since all disk-blade interface and interstage DOF remain in the physical (finite element) domain. For realistic models, the associated matrix partitions may be of considerable size, making the CMS model unsuitable for comprehensive dynamic analyses. To remedy this, a secondary condensation is suggested. To this end, there are several plausible ways in which to proceed, as outlined below.

Option 1: At first glance, it may seem plausible to use the promising full secondary modal analysis with mistuning projection as presented for mistuned single-stage dynamics in Bladh *et al*. [70] (single-stage SMART). This would yield small, manageable models of the individual stages that could be coupled together via interstage constraint modes to form a multi-stage assembly. However, when using fixed interstage single-stage representations, the deformation space spanned by the disk component after the secondary condensation is often severely limited. Typically, only a few disk-dominated modes in eigenfrequency veering region(s) are retained in the single-stage SMART model. As a result, the model cannot adequately represent the added flexibility of the disk in a multi-stage assembly, despite the set of interstage constraint modes. Naturally, retaining secondary modes in a significantly wider range to include more veerings that feature disk-dominated modes would improve the model. Unfortunately, this would also quickly defeat the purpose of the single-stage SMART approach.

Option 2: Perform secondary modal analyses on the partitions that remain in physical coordinates, i.e., the constraint-mode partitions. The idea of secondary modal analyses on the constraint-mode partitions of a traditional C-B model to form truncated sets of

so-called “characteristic constraint modes” was recently formulated by Tan *et al*. [61] for power flow analysis. This has been shown to reduce model sizes significantly, while retaining a high level of accuracy. In this case, there are two types of constraint-mode partitions present in the C-B model: stage-wise cyclic partitions pertaining to disk-blade interfaces; and general structure partitions pertaining to interstage boundaries.

Option 3: Perform secondary modal analyses on the disk-blade constraint-mode plus disk mode partitions, and on the interstage constraint-mode partitions. This way, only the blade modal coordinates are kept intact for direct mistuning input. However, prior experience with this approach has shown no advantages in size or modal convergence compared to secondary modal analyses on the disk-blade interface partitions alone.

Option 4: Perform a full secondary modal analysis on the entire C-B multi-stage model with stage-wise modal domain mistuning projections, analogous to the single-stage SMART approach. The final multi-stage SMART model is likely to be minimal in size and very accurate. However, a drawback of this approach is the size of the eigenvalue problem that needs to be solved in order to obtain the secondary multi-stage modes.

In this study, options 2 and 4 have been selected as the most promising candidates, and their theoretical formulations are presented below. Note that in the following, option 2 is referred to as Characteristic Constraint Modes (CCM), and option 4 as Secondary Modal Analysis Reduction Technique (SMART). The selected reduced order modeling processes are depicted schematically in Fig. 8.2.

8.2.5 Characteristic Constraint Modes (CCM)

The constraint-mode partition for the disk-blade interface of each stage is represented in cyclic coordinates. Therefore, the characteristic modes of the disk-blade interface of

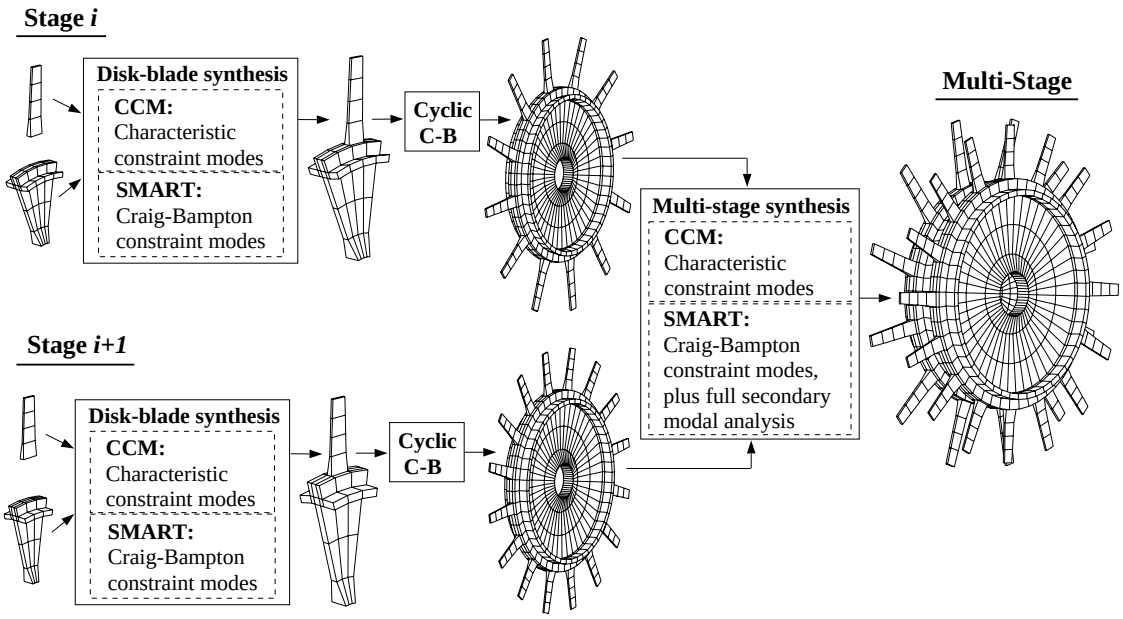

Figure 8.2: Schematic representation of the reduced order modeling processes for the Characteristic Constraint Modes (CCM) and the full Secondary Modal Analysis Reduction Technique (SMART) approaches.

each stage i, $\tilde{\psi}^{\mathbf{h,i}}_{\mathbf{cc}}$, are obtained successively for each harmonic h as:

$$\left[\tilde{\mathbf{K}}^{\mathbf{cb,h,i}}_{\mathbf{cc,d}} + \tilde{\mathbf{K}}^{\mathbf{cb,h,i}}_{\mathbf{cc,b}} - \omega^2 \left[\tilde{\mathbf{M}}^{\mathbf{cb,h,i}}_{\mathbf{cc,d}} + \tilde{\mathbf{M}}^{\mathbf{cb,h,i}}_{\mathbf{cc,b}}\right]\right] \tilde{\psi}^{\mathbf{h,i}}_{\mathbf{cc}} = \mathbf{0}, \qquad h = 0, \ldots, P_i, \tag{8.14}$$

where

$$\begin{aligned}
\tilde{\mathbf{K}}^{\mathbf{cb,h,i}}_{\mathbf{cc,d}} &= \mathbf{K}^{\mathbf{h,i}}_{\mathbf{d},\gamma\gamma} + \mathbf{K}^{\mathbf{h,i^T}}_{\mathbf{d,S}\gamma} \mathbf{\Psi}^{\mathbf{h,i}}_{\mathbf{d},\gamma} \\
\tilde{\mathbf{M}}^{\mathbf{cb,h,i}}_{\mathbf{cc,d}} &= \tilde{\mathbf{\Psi}}^{\mathbf{h,i^T}}_{\mathbf{d},\gamma} \left[\tilde{\mathbf{M}}^{\mathbf{h,i}}_{\mathbf{d,SS}} \tilde{\mathbf{\Psi}}^{\mathbf{h,i}}_{\mathbf{d},\gamma} + \tilde{\mathbf{M}}^{\mathbf{h,i}}_{\mathbf{d,S}\gamma}\right] + \tilde{\mathbf{M}}^{\mathbf{h,i^T}}_{\mathbf{d,S}\gamma} \tilde{\mathbf{\Psi}}^{\mathbf{h,i}}_{\mathbf{d},\gamma} + \tilde{\mathbf{M}}^{\mathbf{h,i}}_{\mathbf{d},\gamma\gamma} \\
\tilde{\mathbf{K}}^{\mathbf{cb,h,i}}_{\mathbf{cc,b}} &= \kappa^{\mathbf{i}}_{\mathbf{cc,b}} \quad \text{or} \quad \begin{bmatrix} \kappa^{\mathbf{i}}_{\mathbf{cc,b}} & \mathbf{0} \\ \mathbf{0} & \kappa^{\mathbf{i}}_{\mathbf{cc,b}} \end{bmatrix},
\end{aligned}$$

and correspondingly for $\tilde{\mathbf{M}}^{\mathbf{cb,h,i}}_{\mathbf{cc,b}}$.

To study the response of a limited set of blade mode families, only a relatively small number of interface modes is usually required for adequate accuracy. Typically, it is sufficient to keep interface modes that represent interface motion due to blade torsion and

flexural motion. This mode selection may be done manually, either by inspection of visualized shapes, or by the order of the interface generalized stiffnesses (usually, lower generalized stiffness implies more "fundamental" interface motion). As a third option, the modes may be selected in a more automated fashion via the commonly used Modal Assurance Criterion (MAC) [63]. This implies selecting the modes based on how well they conform with the global C-B eigenvectors of interest. The selected interface modes are collected into a cyclic modal matrix $\tilde{\mathbf{\Psi}}^{\mathbf{s,i}}_{\mathbf{cc}}$, and the corresponding eigenvalues are collected into a diagonal generalized stiffness matrix $\tilde{\mathbf{\Lambda}}^{\mathbf{s,i}}_{\mathbf{cc}}$.

In a similar fashion, truncated sets of characteristic constraint modes are obtained for all the stage-to-stage interfaces in the multi-stage C-B model. From the definitions in Eqs. (8.2), (8.6), and (8.13), the eigenvalue problems take on the form:

$$\left[\mathbf{K}^{\mathbf{i-1}}_{\tau\tau} + \mathbf{P}^{\mathbf{s}^{\mathrm{T}}}_{\mathbf{i}}\mathbf{K}^{\mathbf{i}}_{\sigma\sigma}\mathbf{P}^{\mathbf{s}}_{\mathbf{i}} - \omega^2\left[\mathbf{M}^{\mathbf{i-1}}_{\tau\tau} + \mathbf{P}^{\mathbf{s}^{\mathrm{T}}}_{\mathbf{i}}\mathbf{M}^{\mathbf{i}}_{\sigma\sigma}\mathbf{P}^{\mathbf{s}}_{\mathbf{i}}\right]\right]\psi^{\mathbf{i}}_{\sigma} = \mathbf{0}. \tag{8.15}$$

Note that these partitions have no cyclic properties, except in the special case $N_i = N_{i-1}$. The selected characteristic interstage constraint modes are collected into a modal matrix $\mathbf{\Psi}^{\mathbf{s,i}}_{\sigma}$, and the corresponding eigenvalues are collected into a diagonal generalized stiffness matrix $\mathbf{\Lambda}^{\mathbf{s,i}}_{\sigma}$.

The columns of $\tilde{\mathbf{\Psi}}^{\mathbf{s,i}}_{\mathbf{cc}}$ and $\mathbf{\Psi}^{\mathbf{s,i}}_{\sigma}$ represent, respectively, reduced bases for the motion of the disk-blade and stage-to-stage interfaces pertaining to the i^{th} stage. This gives secondary modal expansions of the $\tilde{\mathbf{p}}^{\mathbf{i}}_{\mathbf{c}}$ and $\mathbf{p}^{\mathbf{i}}_{\sigma}$ portions of the C-B generalized coordinates as $\tilde{\mathbf{p}}^{\mathbf{i}}_{\mathbf{c}} = \tilde{\mathbf{\Psi}}^{\mathbf{s,i}}_{\mathbf{cc}}\tilde{\mathbf{q}}^{\mathbf{i}}_{\mathbf{c}}$ and $\mathbf{p}^{\mathbf{i}}_{\sigma} = \mathbf{\Psi}^{\mathbf{s,i}}_{\sigma}\mathbf{q}^{\mathbf{i}}_{\sigma}$, respectively, which yield the reduced CCM multi-stage representation:

$$\bar{\mathcal{M}}\ddot{\bar{\mathbf{p}}}_{\varsigma} + \bar{\mathcal{C}}\dot{\bar{\mathbf{p}}}_{\varsigma} + (1+Gj)\,\bar{\mathcal{K}}\bar{\mathbf{p}}_{\varsigma} = \bar{\mathbf{F}}_{\varsigma}, \tag{8.16}$$

with DOF ordering leading to the following matrix (S) and vector (U) structures:

$$\bar{\mathcal{S}} = \begin{bmatrix} \ddots & \ddots & \mathbf{0} & & \\ \ddots & \bar{\mathbf{S}}_{\mathbf{0}}^{\mathbf{i}} & \bar{\mathbf{S}}_{\mathbf{1}}^{\mathbf{i}} & \mathbf{0} & \\ \mathbf{0} & \bar{\mathbf{S}}_{\mathbf{1}}^{\mathbf{i}^{\mathbf{T}}} & \bar{\mathbf{S}}_{\mathbf{0}}^{\mathbf{i+1}} & \bar{\mathbf{S}}_{\mathbf{1}}^{\mathbf{i+1}} & \mathbf{0} \\ & \mathbf{0} & \bar{\mathbf{S}}_{\mathbf{1}}^{\mathbf{i+1}^{\mathbf{T}}} & \bar{\mathbf{S}}_{\mathbf{0}}^{\mathbf{i+2}} & \ddots \\ & & \mathbf{0} & \ddots & \ddots \end{bmatrix} \qquad \bar{\mathcal{U}} = \begin{Bmatrix} \vdots \\ \bar{\mathbf{U}}^{\mathbf{i}} \\ \bar{\mathbf{U}}^{\mathbf{i+1}} \\ \bar{\mathbf{U}}^{\mathbf{i+2}} \\ \vdots \end{Bmatrix}, \tag{8.17}$$

where S denotes either mass (M), viscous damping (C), or stiffness (K); and U is either force (F) or displacement (p). The details of the vector partitions above that pertain to stage i are expressed as:

$$\bar{\mathbf{F}}_{\varsigma}^{\mathbf{i}} = \begin{Bmatrix} \mathbf{0} \\ \mathbf{0} \\ \tilde{\mathbf{\Psi}}_{\mathbf{cc},\varsigma}^{\mathbf{s,i}^{\mathbf{T}}} \mathbf{F}_{\mathbf{c}}^{\mathbf{cb,i}} \\ \mathbf{F}_{\mathbf{b}}^{\mathbf{cb,i}} \end{Bmatrix} \qquad \bar{\mathbf{p}}_{\varsigma}^{\mathbf{i}} = \begin{Bmatrix} \mathbf{q}_{\sigma}^{\mathbf{i}} \\ \tilde{\mathbf{p}}_{\mathbf{d}}^{\mathbf{i}} \\ \tilde{\mathbf{q}}_{\mathbf{c}}^{\mathbf{i}} \\ \bar{\mathbf{p}}_{\mathbf{b}}^{\mathbf{i}} \end{Bmatrix}. \tag{8.18}$$

Note that only characteristic disk-blade interface constraint modes of harmonic ς get involved in the secondary modal force projection, where ς denotes the considered excitation engine order. Correspondingly, the matrix partitions pertaining to stage i may be written as:

$$\bar{\mathbf{M}}_{\mathbf{0}}^{\mathbf{i}} = \begin{bmatrix} \mathbf{I} & \mathbf{\Psi}_{\sigma}^{\mathbf{s,i}^{\mathbf{T}}} \mathbf{P}_{\mathbf{i}}^{\mathbf{s}^{\mathbf{T}}} \tilde{\mu}_{\sigma\mathbf{d}}^{\mathbf{i}} & \mathbf{\Psi}_{\sigma}^{\mathbf{s,i}^{\mathbf{T}}} \mathbf{P}_{\mathbf{i}}^{\mathbf{s}^{\mathbf{T}}} \tilde{\mu}_{\sigma\gamma}^{\mathbf{i}} \tilde{\mathbf{\Psi}}_{\mathbf{cc}}^{\mathbf{s,i}} & \mathbf{0} \\ & \mathbf{I} & \tilde{\mu}_{\mathbf{dc}}^{\mathbf{i}} \tilde{\mathbf{\Psi}}_{\mathbf{cc}}^{\mathbf{s,i}} & \mathbf{0} \\ & & \mathbf{I} & \tilde{\mathbf{\Psi}}_{\mathbf{cc}}^{\mathbf{s,i}^{\mathbf{T}}} \hat{\mathbf{F}}_{\mathbf{i}}^{\mathbf{T}} \hat{\mu}_{\mathbf{bc}}^{\mathbf{i}^{\mathbf{T}}} \\ \mathbf{Sym} & & & \mathbf{I} \end{bmatrix}$$

$$\bar{\mathbf{M}}_{\mathbf{1}}^{\mathbf{i}} = \begin{bmatrix} \mathbf{P}_{\mathbf{i}}^{\mathbf{s}^{\mathbf{T}}} \tilde{\mu}_{\sigma\tau}^{\mathbf{i}} & \mathbf{0} & \mathbf{0} & \mathbf{0} \\ \tilde{\mu}_{\mathbf{d}\tau}^{\mathbf{i}} \mathbf{\Psi}_{\sigma}^{\mathbf{s,i}} & \mathbf{0} & \mathbf{0} & \mathbf{0} \\ \tilde{\mathbf{\Psi}}_{\mathbf{cc}}^{\mathbf{s,i}^{\mathbf{T}}} \tilde{\mu}_{\gamma\tau}^{\mathbf{i}} \mathbf{\Psi}_{\sigma}^{\mathbf{s,i}} & \mathbf{0} & \mathbf{0} & \mathbf{0} \\ \mathbf{0} & \mathbf{0} & \mathbf{0} & \mathbf{0} \end{bmatrix}$$

$$
\begin{aligned}
\bar{\mathbf{C}}_{\mathbf{0}}^{\mathbf{i}} &= \begin{bmatrix} \mathbf{0} & \mathbf{0} & \mathbf{0} & \mathbf{0} & \\ & \mathbf{0} & \mathbf{0} & \mathbf{0} & \\ & & \mathbf{0} & \mathbf{0} & \\ \mathbf{Sym} & & & \mathbf{I} \otimes \underset{k=1,\ldots,m_{b,i}}{\mathbf{diag}} \left[2\zeta^{k,i}\right] \sqrt{\mathbf{\Lambda}_{\mathbf{b}}^{\mathbf{i}}} \end{bmatrix} \\
\bar{\mathbf{C}}_{\mathbf{1}}^{\mathbf{i}} &= \mathbf{0} \\
\bar{\mathbf{K}}_{\mathbf{0}}^{\mathbf{i}} &= \begin{bmatrix} \mathbf{\Lambda}_{\sigma}^{\mathbf{s,i}} & \mathbf{0} & \mathbf{\Psi}_{\sigma}^{\mathbf{s,i^T}} \mathbf{P}_{\mathbf{i}}^{\mathbf{s^T}} \tilde{\kappa}_{\sigma\gamma}^{\mathbf{i}} \tilde{\mathbf{\Psi}}_{\mathbf{cc}}^{\mathbf{s,i}} & \mathbf{0} \\ & \tilde{\mathbf{\Lambda}}_{\mathbf{d}}^{\mathbf{i}} & \mathbf{0} & \mathbf{0} \\ & & \tilde{\mathbf{\Lambda}}_{\mathbf{cc}}^{\mathbf{s,i}} & \mathbf{0} \\ \mathbf{Sym} & & & \mathbf{K}_{\mathbf{bb}}^{\mathbf{cb,i}} \end{bmatrix} \\
\bar{\mathbf{K}}_{\mathbf{1}}^{\mathbf{i}} &= \begin{bmatrix} \mathbf{P}_{\mathbf{i}}^{\mathbf{s^T}} \tilde{\kappa}_{\sigma\tau}^{\mathbf{i}} & \mathbf{0} & \mathbf{0} & \mathbf{0} \\ \mathbf{0} & \mathbf{0} & \mathbf{0} & \mathbf{0} \\ \tilde{\mathbf{\Psi}}_{\mathbf{cc}}^{\mathbf{s,i^T}} \tilde{\kappa}_{\gamma\tau}^{\mathbf{i}} \mathbf{\Psi}_{\sigma}^{\mathbf{s,i}} & \mathbf{0} & \mathbf{0} & \mathbf{0} \\ \mathbf{0} & \mathbf{0} & \mathbf{0} & \mathbf{0} \end{bmatrix},
\end{aligned}
\tag{8.19}
$$

where

$$
\mathbf{K}_{\mathbf{bb}}^{\mathbf{cb,i}} = \underset{n=1,\ldots,N_i}{\mathbf{Bdiag}} \left[\underset{k=1,\ldots,m_{b,i}}{\mathbf{diag}} \left[1 + \delta_n^{k,i}\right] \mathbf{\Lambda}_{\mathbf{b}}^{\mathbf{i}} \right];
$$

$\hat{\mu}_{\mathbf{bc}}^{\mathbf{i}} = \mathbf{I} \otimes \mu_{\mathbf{bc}}^{\mathbf{i}}$; and $\zeta^{k,i}$ is the viscous damping coefficient associated with the k^{th} blade component mode for stage i.

Note that the above equations of motion are written for frequency-domain solutions for a single excitation engine order component at a time. By virtue of the orthogonality of integer Fourier time-harmonic components [72], frequency domain solutions for different engine orders ς may be linearly superposed in the time domain as

$$
\bar{\mathbf{p}}(t) = \sum_{\varsigma \in \mathcal{E}} \bar{\mathbf{p}}_{\varsigma} e^{j\varsigma\omega_r t},
\tag{8.20}
$$

where $\mathcal{E}$ is a set of excitation engine orders under consideration, and ω_r is the angular rotor speed. $\bar{\mathbf{p}}(t)$ represents the combined forced response in generalized coordinates of a multi-stage rotor assembly subjected to multiple engine orders of excitation, from which maximum response amplitudes may be determined.

8.2.6 Full Secondary Modal Analysis (SMART)

The multi-stage SMART model is obtained by performing a full-scale secondary modal analysis on the entire multi-stage C-B model. The secondary modal analysis is then based on those modes that fall within a frequency range of interest for the dynamic analyses. Since the blade modal coordinates will not be retained explicitly, this approach requires projection of blade mistuning data. However, since the intermediate C-B representation provides direct access to blade modal stiffnesses, this projection is carried out inexpensively in the low-order modal domain.

The first step is to obtain the secondary modes from which to form the new reduced basis. This is done using the entire C-B multi-stage model from Eq. (8.13) as:

$$\left[\mathcal{K}^{\mathbf{m}} - \omega^2 \mathcal{M}^{\mathbf{m}}\right] \mathbf{u}_{\mathbf{m}} = \mathbf{0}, \tag{8.21}$$

The next step is to select a small subset of the obtained multi-stage modes. This subset is then used to form a further reduced order model by classical modal analysis. In the typical case, the analyst is likely to focus on a particular family of blade modes and/or specific eigenfrequency veerings that are deemed critical due to engine operating conditions for one stage at the time. The mode selection is then based on a frequency range that encompasses the blade mode family (or families) of interest. Hence, the number of modes needed, and thus the size of the multi-stage SMART model, can be taken to be as low as on the order of the number of blades in the stage under investigation. However, it is important to note that all harmonics $h = 0, \ldots, P$ must be present for the investigated

stage in the secondary mode set, in order to form an adequate basis for mistuned mode shapes. The constraint-mode portions of the selected mode shapes, $\mathbf{u}_{\mathbf{m}}^{\mathbf{c}}$, are collected into a modal matrix $\mathbf{U}_{\mathbf{m}}^{\mathbf{s,c}}$, while the normal-blade-mode portions, $\mathbf{u}_{\mathbf{m}}^{\mathbf{b}}$, are collected into $\mathbf{U}_{\mathbf{m}}^{\mathbf{s,b}}$. The associated eigenvalues are collected into a generalized stiffness matrix $\mathbf{\Lambda}_{\mathbf{m}}^{\mathbf{s}}$.

As shown in Eq. (8.8), mistuning is represented in the C-B model by perturbing the diagonal elements of the normal-blade-mode (*bb*) partition for each stage. These diagonal elements represent the individual modal stiffnesses for each cantilevered blade mode of each blade in a rotor stage. Using the selected modes as the basis for the secondary modal expansion, mistuning enters into the SMART model by projecting these modal stiffness perturbations onto the selected modes of the multi-stage assembly. Hence, the mistuning projection for stage i takes the form:

$$\mathbf{\Delta K}_{\mathbf{m}}^{\mathbf{s,i}} = \mathbf{U}_{\mathbf{m}}^{\mathbf{s,b,i^T}} \mathbf{B} \underset{n=1,\ldots,N_i}{\mathbf{diag}} \left[\underset{k=1,\ldots,m_{b,i}}{\mathbf{diag}} \left[\delta_n^{k,i} \right] \mathbf{\Lambda}_{\mathbf{b}}^{\mathbf{i}} \right] \mathbf{U}_{\mathbf{m}}^{\mathbf{s,b,i}}. \tag{8.22}$$

Note that only the mode shape portions pertaining to the blade normal modes for stage i are involved in the projection.

With the mistuning projection in place, the SMART multi-stage model may be formulated as

$$\ddot{\mathbf{q}} + \mathcal{C}_{\mathbf{m}}^{\mathbf{s}} \dot{\mathbf{q}} + (1 + Gj) \left[\mathbf{\Lambda}_{\mathbf{m}}^{\mathbf{s}} + \sum_{i=1}^{M} \mathbf{\Delta K}_{\mathbf{m}}^{\mathbf{s,i}} \right] \mathbf{q} = \mathbf{F}_{\mathbf{m}}^{\mathbf{s}}, \tag{8.23}$$

where

$$\mathcal{C}_{\mathbf{m}}^{\mathbf{s}} = \sum_{i=1}^{M} \mathbf{U}_{\mathbf{m}}^{\mathbf{s,b,i^T}} \left[\mathbf{I} \otimes \underset{k=1,\ldots,m_{b,i}}{\mathbf{diag}} \left[2\zeta^{k,i} \right] \sqrt{\mathbf{\Lambda}_{\mathbf{b}}^{\mathbf{i}}} \right] \mathbf{U}_{\mathbf{m}}^{\mathbf{s,b,i}}$$

$$\mathbf{F}_{\mathbf{m}}^{\mathbf{s}} = \sum_{i=1}^{M} \mathbf{U}_{\mathbf{m}}^{\mathbf{s,c,i^T}} \mathbf{F}_{\mathbf{c}}^{\mathbf{cb,i}} + \mathbf{U}_{\mathbf{m}}^{\mathbf{s,b,i^T}} \mathbf{F}_{\mathbf{b}}^{\mathbf{cb,i}},$$

and M is the total number of stages included in the model. Note that the stiffness deviation projection matrices, $\mathbf{\Delta K}_{\mathbf{m}}^{\mathbf{s,i}}$, do not possess any particular matrix structure other than symmetry. Thus, in general, the multi-stage SMART stiffness matrix becomes fully populated

when mistuning is introduced. As for the CCM model, the stated SMART multi-stage equations of motion are intended for frequency-domain solutions for a single excitation engine order component at a time. The linear time domain superposition for multiple engine order response is analogous to Eq. (8.20).

8.3 Test Case: Simple Two-Stage Rotor Model

In this section, the derived reduced order modeling techniques are validated in the free and forced response, both with and without blade mistuning. The technique validation is carried out using full finite element solutions as benchmarks to assess the performances of the CCM and SMART approaches. Figure 8.3 depicts the example single- and two-stage rotor models, where a portion of the multi-stage model has been cut out in order to better illustrate the assembled geometry. These finite element models, as well as the free and forced response samples used in validating the techniques, are the same as those used in Bladh *et al*. [1]. The reader is therefore referred to Bladh *et al*. [1] for details on the finite element models, as well as on the employed mistuning implementation and blade mistuning patterns. It should be noted that the stage geometries are very simple, and that the finite element meshes are very coarse, compared to those of typical industrial finite element models. However, the modeled stages still exhibit the essential characteristics of real rotors, such as disk- and blade-dominated mode families and their interaction (eigen-frequency veerings). Also, since the reduced order models are derived from these same parent finite element models, the unrealistic appearance of the models is not an issue for technique validation.

8.3.1 Setup of CCM and SMART Reduced Order Models

To construct the reduced order models in a more rigorous manner, brief modal convergence studies were conducted. The modal convergence studies also aid in exposing

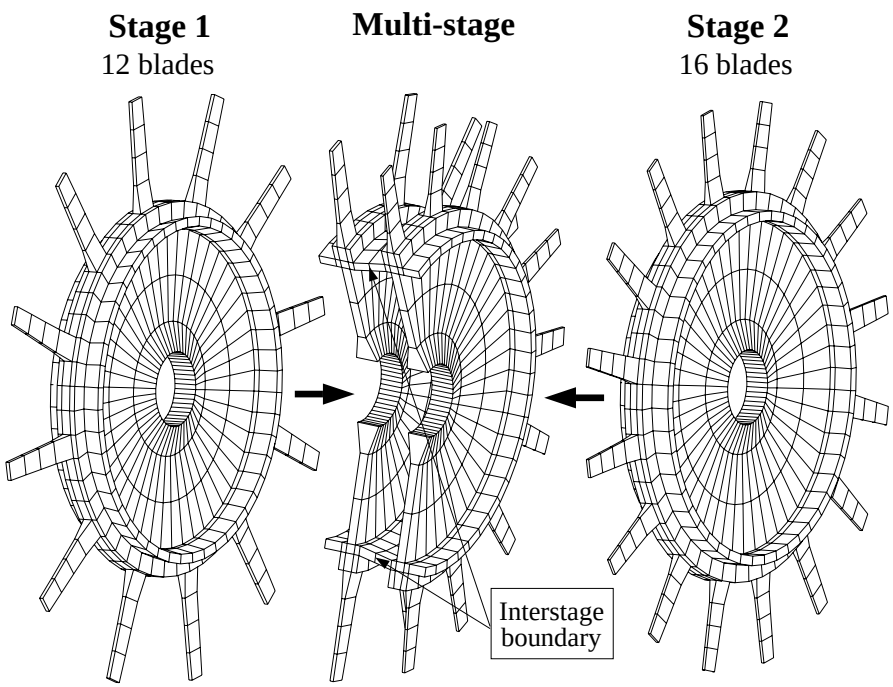

Figure 8.3: Finite element meshes for the single- and two-stage example rotor models (from Bladh *et al*. [1]).

important properties of the proposed reduced order modeling techniques. The adopted convergence measures are the mean and maximum of the frequency errors relative to the tuned single- or multi-stage finite element models (as appropriate) for all obtained natural frequencies below 8000 Hz.

Figure 8.4 depicts the single- and multi-stage modal convergence trends for proportionally increasing number of retained disk and blade component normal modes in the primary single-stage CMS models. Note that the results for the multi-stage model are here obtained with the full sets of interface DOF in physical coordinates. Clearly, the single-stage representations quickly converges to very low error levels by using only a few of the lower component normal modes. However, while adequate for most engineering applications, the error level of the multi-stage model is disproportionately higher. This is likely a result of using fixed interstage disk components. While retaining only a few of the lower disk

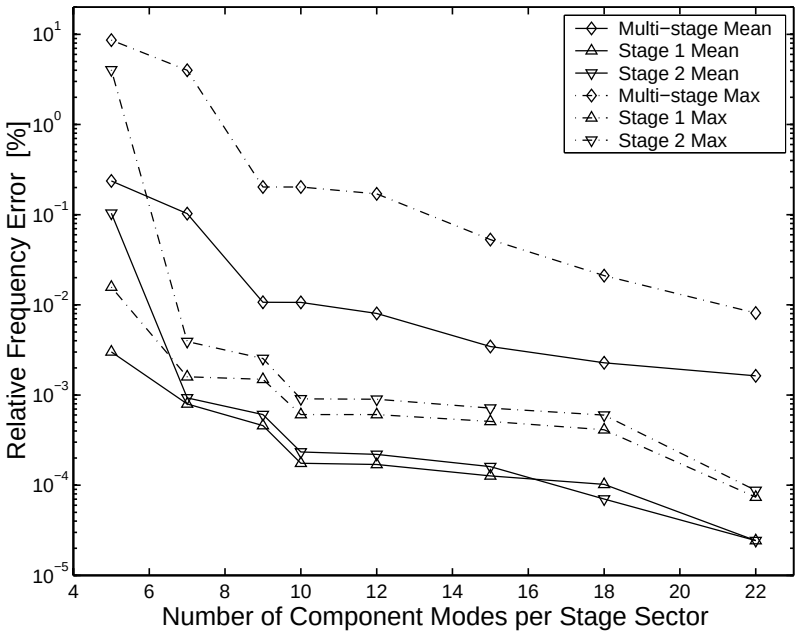

Figure 8.4: Single- and multi-stage modal convergence: mean and max relative frequency error below 8000 Hz as a function of retained component normal modes in the primary CMS model.

modes as is done here, the motion of the disk near the interstage boundaries is essentially described through the interstage constraint modes alone. Clearly, this is not sufficient to make the multi-stage accuracy comparable to that of single-stage representations. Hence, in order to properly span the expanded deformation space required by the now flexible interstage region, the multi-stage model would likely benefit significantly from higher-order disk modes. Unfortunately, this would also increase model sizes beyond practical limits. A possible remedy could be to use a formulation that employs free interstage disk component modes. However, free interstage disk component modes may prove to give adverse effects by instead exhibiting too much motion in interstage regions relative to the motion in remaining portions of the disk component. The free interstage option is not considered in this work, but this is clearly a topic for future investigations.

Based on the multi-stage modal convergence in Fig. 8.4, a total of 9 component modes

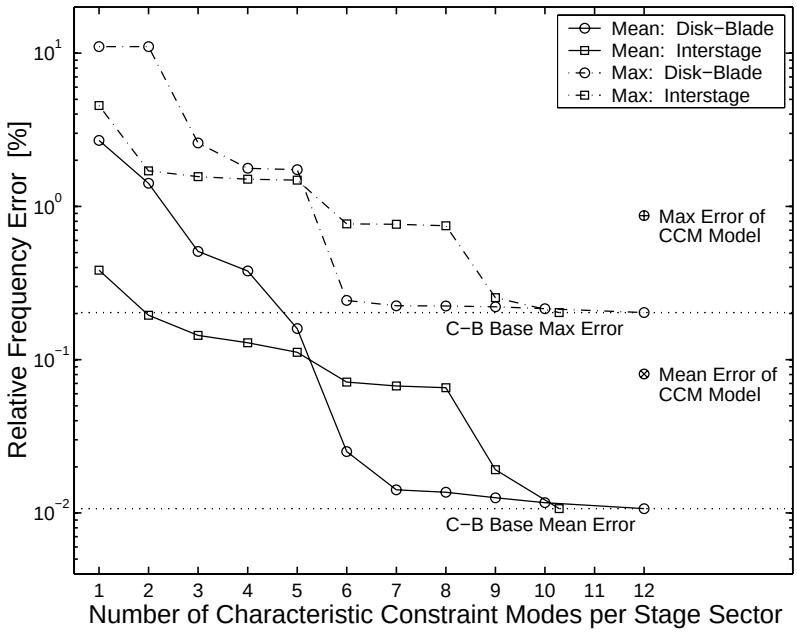

Figure 8.5: Modal convergence of multi-stage CCM model: mean and max relative frequency error below 8000 Hz as a function of retained disk-blade interface and interstage characteristic constraint modes.

(3 disk plus 6 blade modes) per stage sector are chosen for the CCM model, while 22 component modes (10 disk plus 12 blade modes) per stage sector are chosen for the SMART model. It is realized that this discrepancy may result in unfair comparisons between the two models, but these choices are based on practical considerations: the number of retained component modes has a direct impact on the size of the final CCM model, whereas the size of the SMART model is determined by the number of retained secondary system modes. Hence, for the SMART model, only the size of the secondary eigenvalue problem is affected by the number of retained component modes, and solving this eigenvalue problem is a one-time effort.

Figure 8.5 shows the obtained modal convergence for the multi-stage CCM model for an increasing number of retained characteristic constraint modes. The error levels obtained without any truncation of characteristic constraint modes (i.e., with full, physical-domain

interface partitions) are indicated in the plot as “C-B Base” errors, which correspond to the multi-stage errors in Fig. 8.4, using 9 component modes. The convergence trends are studied separately for disk-blade interface and interstage secondary condensations. Hence, one partition type is kept intact (full) while condensing the other. It is observed from Fig. 8.5 that there is a notable difference in modal convergence rates between the two types of partial secondary condensation. The rapid convergence exhibited by the characteristic disk-blade interface constraint modes is explained by the fact that a vast majority of the compared modes (i.e., all modes below 8000 Hz) are blade-dominated. The accuracy of these modes is heavily dependent on how well the motion over the disk-blade interface is captured. Hence, any improvement in the disk-blade interface representation resulting from an increased number of retained characteristic disk-blade interface constraint modes leads to a dramatic reduction of the total error level. Moreover, it is clear from Fig. 8.5 that the higher-order characteristic constraint modes provide only very marginal contributions to the disk-blade interface representation in the considered frequency region. As shown, the rate of modal convergence slows down considerably beyond the first six modes, which is a positive indication of the suitability of this type of partial secondary condensation.

It is further noted that the errors induced by truncating interstage characteristic constraint modes appear to be relatively small. This is due to the relatively mild effect overall on the natural frequencies from the interstage coupling, relative to the clamped interstage single-stage representation (see Bladh *et al*. [1]). In particular, blade-dominated modes experience almost no shift in frequency at all. Hence, when looking at the error levels alone, it may seem acceptable from a practical perspective to use only one or two interstage characteristic constraint modes per stage sector. However, this would yield extremely poor representations of what occurs in the frequency veering regions when introducing interstage coupling. Closer examination of mode participation reveals that it may be critically

important to have the retained fixed interstage disk component modes and *all* interstage constraint modes available when reconstructing the motion of the multi-stage assembly. As will be shown later on, rather subtle changes in the veering regions may lead to qualitatively altered responses. It is therefore concluded that a secondary condensation of the interstage partitions may not be a recommended approach.

Based on the convergence trends in Fig. 8.5, a total of 6 characteristic constraint modes per stage sector were retained in the CCM model for both disk-blade interface and interstage partitions. The resulting mean and max errors for this configuration are included in the right-hand portion of Fig. 8.5. Assuming that the modal convergence trends observed for this particular model hold true also for more elaborate industrial models, the final size of a CCM model can be expected to be a minimum of $\mathcal{O}\left(10\sum_{i=1}^{M} N_i\right)$, where N_i is the number of blades on stage i, and M is the number of included stages. In contrast, the final size of the SMART model may be selected to be as low as $\mathcal{O}\left(N_i\right)$, depending on the scope of the dynamic analyses to be performed. The sizes of the various finite element and reduced order models used in this study are listed in Table 8.1. It is observed from Table 8.1 that the model reductions achieved for the highly simplified multi-stage model in Fig. 8.3 are relatively modest. However, it should be noted that the developed reduced order models are entirely in modal coordinates. An important implication of this is that the reduced model sizes are completely independent of the size of the parent finite element model. It must therefore be emphasized that the reduced order models will remain practically unchanged in size regardless of the levels of parent finite element model mesh refinement and geometry sophistication. Hence, far greater and more impressive model size reductions would result for more realistic, industrial-size models.

Finally, note that the partial secondary condensation is not used in the multi-stage SMART model in the form it is presented in this paper. However, the modal convergence

Model	FEM	CCM	SMART
Stage 1	3168	180	14 (4–5 kHz)
Stage 2	3360	240	32 (5–6 kHz)
Multi-stage	6816	588	50 (4–6 kHz)

Table 8.1: Finite element and reduced order model sizes (DOF).

trends presented in Fig. 8.5 indicate that it may be advantageous to perform a secondary condensation of the disk-blade interface partitions before performing a full, now *tertiary*, modal analysis on the entire multi-stage model. In fact, such an approach may even be required for models that include many stages and/or contain sector finite element models with highly detailed interface portions.

8.3.2 Free Vibrations

The tuned characteristics of the single-stage models are first considered, since they will serve as references when examining the results obtained for the multi-stage model. The dynamic characteristics of single-stage tuned bladed disks are conveniently summarized in plots of natural frequencies versus the number of nodal diameters (harmonics), as shown in Figs. 8.6 and 8.7. This data set is essentially a fixed rotor speed subset of the traditional Campbell diagram [65]. In this representation, the modes on nearly horizontal connecting lines correspond to assembly modes that are dominated by blade motion. The characteristic blade motion of each family of blade-dominated modes is indicated on the right of Figs. 8.6 and 8.7, where F=Flexural; A=Axial (edgewise bending); and T=Torsion. The modes on slanted connecting lines correspond to disk-dominated modes. The rapid increase of the eigenfrequencies of the disk-dominated modes is due to stiffening of the disk as the circumferential wavelength decreases with increasing number of nodal diameters. Figures 8.6 and 8.7 further demonstrates the excellent agreement between the “bench-

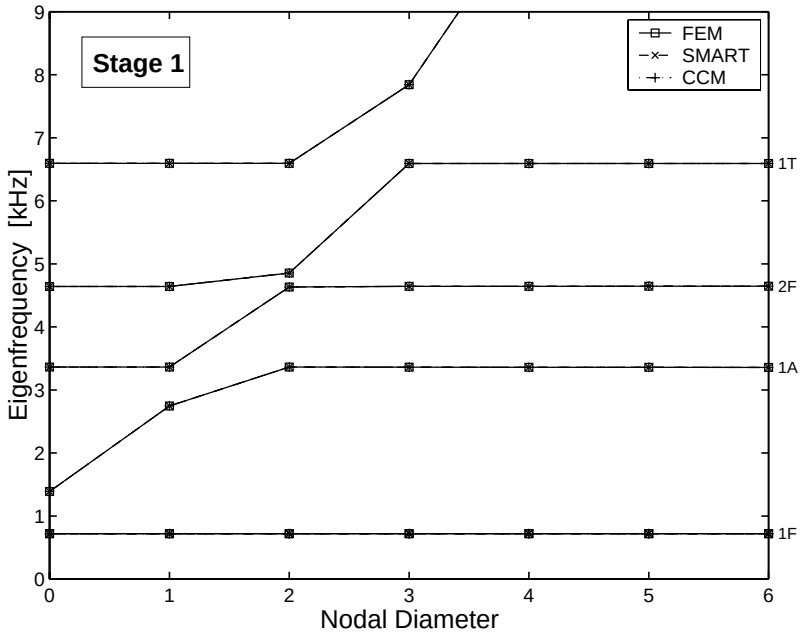

Figure 8.6: Natural frequencies versus number of nodal diameters for the tuned stage 1 model with fixed interstage boundaries, as obtained with finite element and reduced order models.

mark" finite element results and the results of both single-stage reduced order models. In fact, the results are indistinguishable in these plots. Recall from Section 8.3.1 that the two single-stage reduced order models use different sets of retained component modes, and, in addition, the CCM model use only a truncated set of characteristic constraint modes for the disk-blade interface. Clearly, the more severe mode truncation of the CCM model does not degrade visibly its single-stage representation in the depicted frequency range.

Turning the attention to the multi-stage model, there are certain features of multi-stage assemblies that first need to be addressed. As mentioned previously, the concept of "tuned" bladed disks generally becomes questionable when individual stages are coupled together, due to incompatible cyclicity properties of adjacent stages. However, the level of mistuning induced by the interstage coupling is very small for this model, and, as a result, "tuned" nodal diameter mode shapes are readily identified for both stages. Hence, the

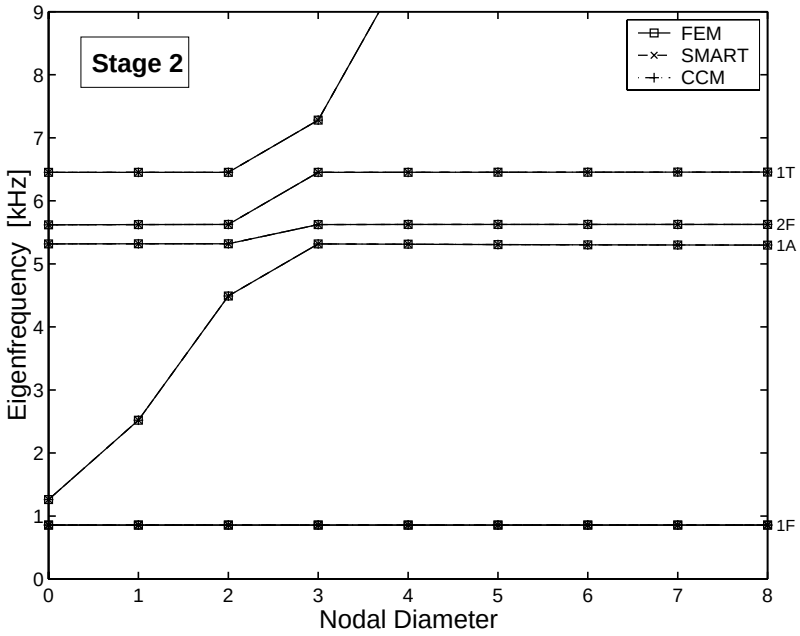

Figure 8.7: Natural frequencies versus number of nodal diameters for the tuned stage 2 model with fixed interstage boundaries, as obtained with finite element and reduced order models.

"tuned" designation will still be used in this work to denote cases where blade mistuning has not been added explicitly.

The retained tuned-like, spatially extended characteristic of the "tuned" multi-stage mode shapes is clearly demonstrated in Fig. 8.8, which depicts two "tuned" blade-dominated multi-stage mode shapes, as represented by the deflection of a single blade tip DOF. While no stage-wise, or local, mode localization occurs, an interesting observation from Fig. 8.8 is that the depicted mode shapes exhibit significant (global) localization onto either stage. In this particular case, mode 54 is seen to exhibit significant global localization onto stage 1, whereas mode 83 is globally localized onto stage 2. This global localization is common for most modes of the employed multi-stage model. For this model, modes that exhibit significant participation of both stages, which are here denoted system modes, only occur when disk-dominated modes of both stages are relatively close in frequency.

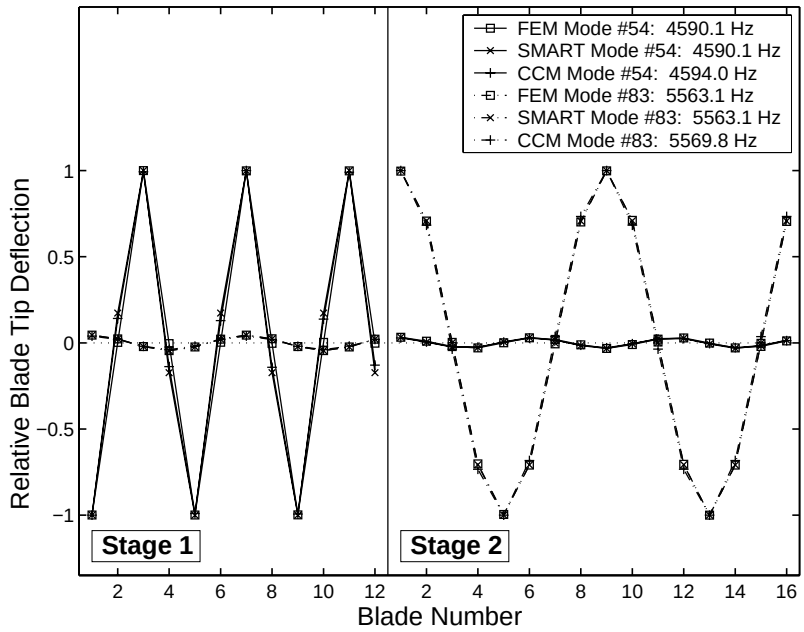

Figure 8.8: "Tuned" multi-stage mode shapes 54 and 83, as represented by normalized single blade tip DOF deflections for both stages.

Moreover, note the accurate "tuned" multi-stage mode shape representations of both CCM and SMART reduced order models. The relative blade deflections, as well as the degrees of global localization, are well captured by both techniques. Note that even though the depicted mode shapes have the appearance of being spatially extended, they differ from perfectly tuned, cyclic single-stage mode shapes in one important aspect. Namely, while the circumferential position of a perfectly tuned, cyclic mode shape is arbitrary, all multi-stage mode shapes, no matter how tuned-like, are fixed circumferentially due to the interstage coupling-induced mistuning. Hence, the slight discrepancies seen for mode 54 that may appear to be a simple circumferential shift are in fact shape errors. This circumstance is also evidenced by the nearly perfect matches for the blades experiencing the peak deflections.

As indicated by Fig. 8.8, the nodal-diameter representation of single-stage free vibration characteristics can be used also for multi-stage assemblies, provided that the levels

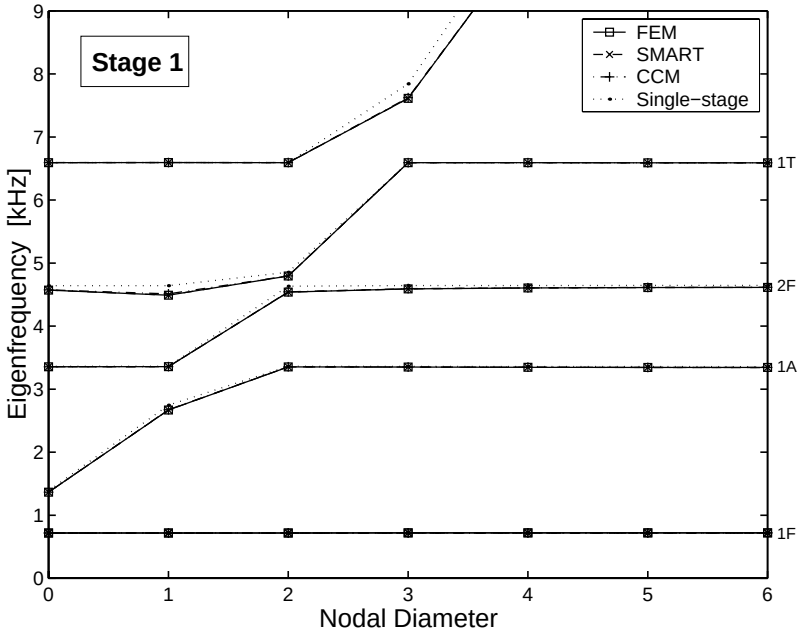

Figure 8.9: Natural frequencies versus number of nodal diameters for the "tuned" multi-stage model for modes localized to stage 1, as obtained with finite element and reduced order models. The finite element single-stage natural frequencies are included for reference.

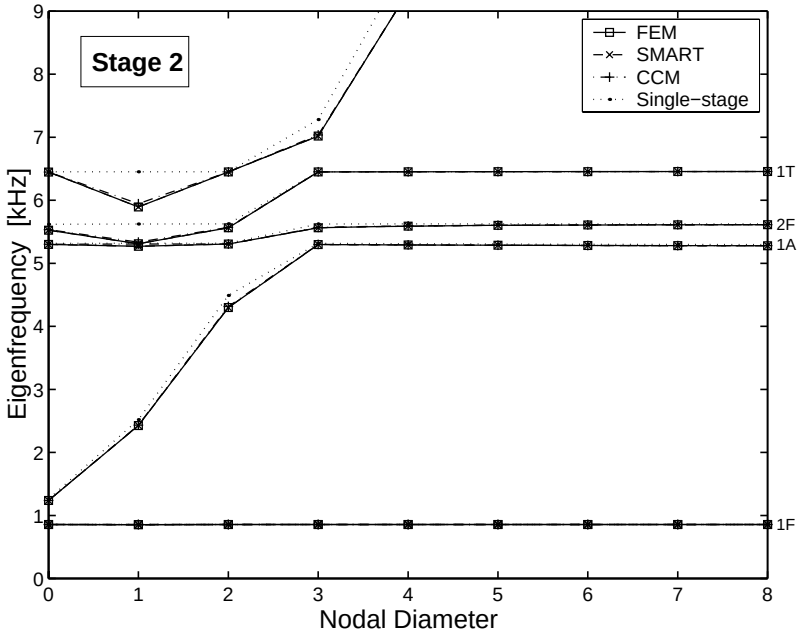

Figure 8.10: Natural frequencies versus number of nodal diameters for the "tuned" multi-stage model for modes localized to stage 2, as obtained with finite element and reduced order models. The finite element single-stage natural frequencies are included for reference.

of interstage coupling-induced mistuning are sufficiently low. Hence, by examining the multi-stage mode shapes with respect to global stage localization and zero crossings for nodal diameter designation, the multi-stage modes can be divided into stage 1 and stage 2 modes. This mode identification process was carried out for FEM, CCM, and SMART multi-stage models, and the results are shown in Figs. 8.9 and 8.10. It is clear from Figs. 8.9 and 8.10 that both CCM and SMART reduced order models do an excellent job in capturing the important effects of the increased flexibility in the interstage region, when compared to clamped interstage single-stage representations. Both approaches yield multi-stage natural frequencies that are virtually indistinguishable from the benchmark finite element solution. Only very slight offsets can be seen for the CCM model for the disk-dominated harmonic 1 modes in the 4–6 kHz region for both stages. These discrepancies will also manifest themselves in the forced response samples later on. Since this paper focuses on the reduced order models and their performance, the reader is referred to Bladh *et al*. [1] for further discussions on the important effects of structural interstage coupling displayed in Figs. 8.9 and 8.10.

Finally, two examples of mistuned multi-stage mode shapes are depicted in Fig. 8.11. These two modes correspond in natural frequency order to the “tuned” multi-stage mode shapes depicted in Fig. 8.8. The blade mistuning has clearly destroyed the spatially extended characteristic exhibited by the corresponding “tuned” mode shapes. However, the response of each stage does not exhibit significant localization. Note that the global localization onto either stage remains largely unchanged from Fig. 8.8 for both modes. The performances of the CCM and SMART reduced order models are consistent with earlier results. The CCM mode shapes conform well with finite element mode shapes, but they do not match the exceptional accuracy of the SMART mode shapes. Note from Table 8.1 that the SMART model achieves this accuracy while being less than 10% the size of the

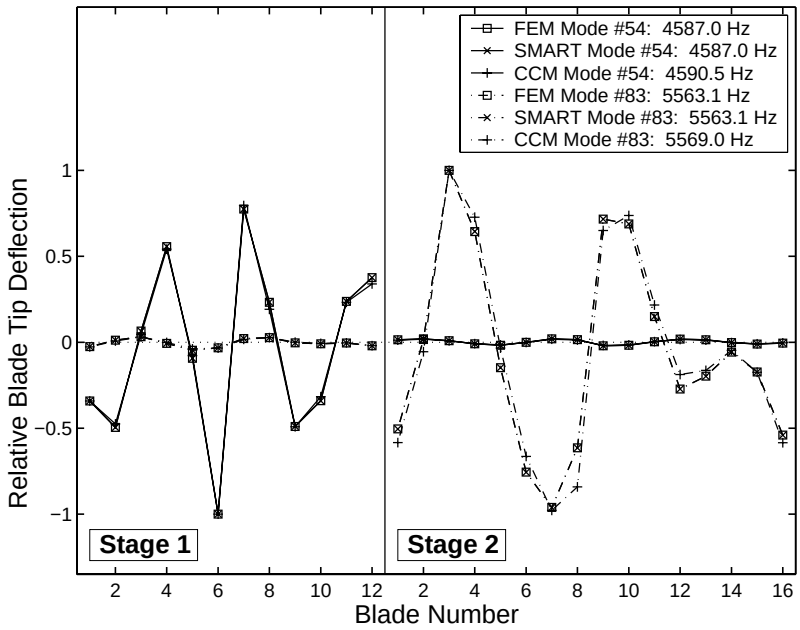

Figure 8.11: Mistuned multi-stage mode shapes 54 and 83, as represented by normalized single blade tip DOF deflections for both stages.

CCM model.

8.3.3 Forced Response

The forced response samples are based on stage-wise independent engine order excitations. In one simulation, stage 1 is subjected to an engine order 10 (10E) excitation in the frequency range 4–5 kHz. In a separate simulation, stage 2 is subjected to an engine order 15 (15E) excitation in the frequency range 5–6.2 kHz. The applied blade force is a single point load on one blade tip node in the axial direction (axis of rotation). This blade force is clearly unrealistic, but it is adequate for demonstrative purposes. Furthermore, note that the applied discrete blade-to-blade engine order excitations are equivalent to counterrotating engine order 2 (-2E) and 1 (-1E) excitations for stages 1 and 2, respectively. Hence, the applied excitations will pass through the harmonic 2 veering region of stage 1 and the harmonic 1 region of stage 2 (see Figs. 8.9 and 8.10). For bounded re-

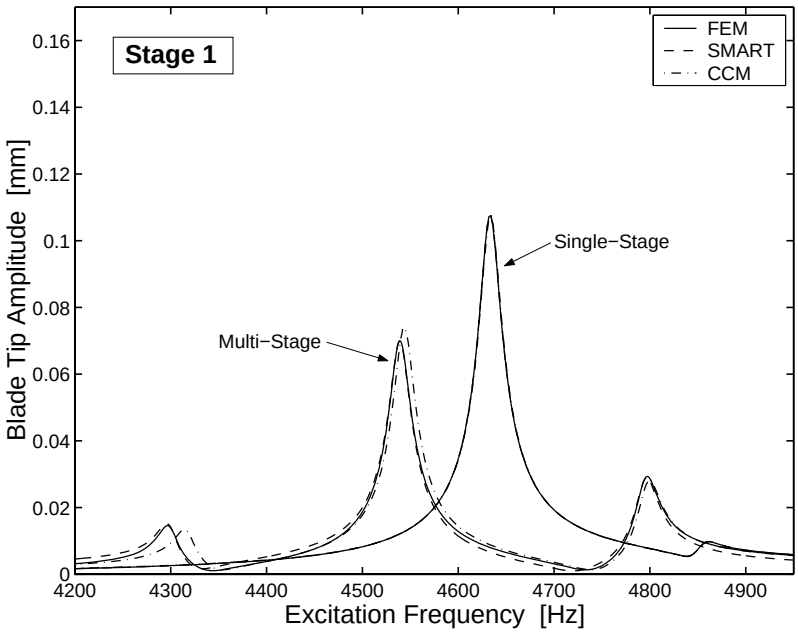

Figure 8.12: Tuned stage 1 forced response from engine order 10 excitation (10E=-2E) using finite element and reduced order single- and multi-stage models.

sponses, the structural damping coefficient is arbitrarily taken to be $G = 0.005$ (0.5%), while viscous damping is assumed negligible.

Figure 8.12 depicts the tuned response amplitudes experienced by the stage 1 blades. The amplitudes are here represented by the axial displacement magnitude of one blade tip node for the maximum responding blade in the stage. As shown in Fig. 8.12, the increased disk flexibility due to interstage coupling results in a significantly changed veering response behavior for stage 1 by moving the mode pairs comprising the veering to lower resonant frequencies. The upper mode pair, which was clearly disk-dominated in the single-stage representation, exhibits much more blade participation in the multi-stage response. Conversely, the lower mode pair goes from being distinctly blade-dominated to having significant disk participation. As a consequence, the sensitivity to mistuning is much less pronounced for the multi-stage model (25% versus 48% amplitude magnification), which is evident from the mistuned response in Fig. 8.13.

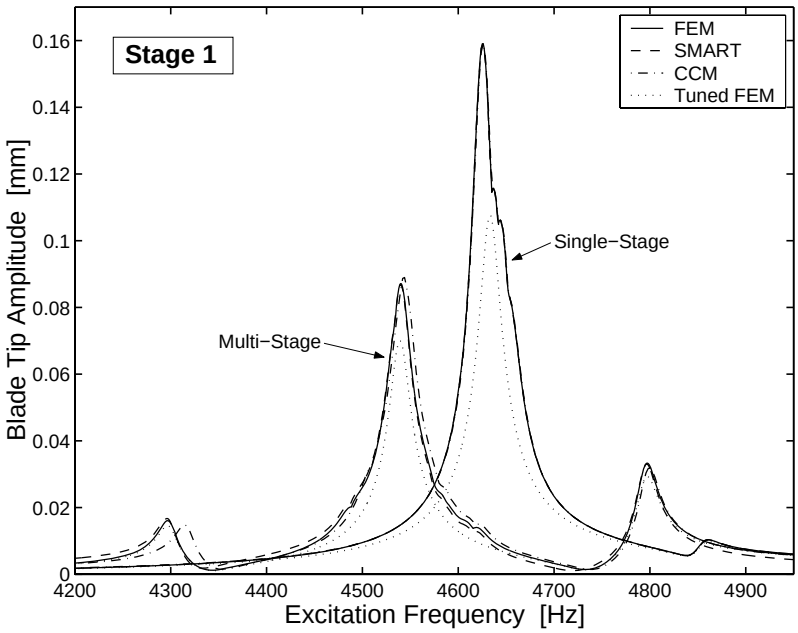

Figure 8.13: Mistuned stage 1 forced response from engine order 10 excitation (10E=-2E) using finite element and reduced order single- and multi-stage models. The tuned stage 1 finite element single- and multi-stage responses are included for reference.

There is a notable difference in accuracy between both tuned and mistuned CCM and SMART reduced order models. The overly stiff CCM model provides a more blade-dominated response at maximum resonance, which leads to an overestimated maximum resonant amplitude. The predicted maximum tuned and mistuned multi-stage resonant amplitudes are within 0.4% for the SMART model, but only within 6% for the CCM model. Note that the corresponding accuracy levels for the single-stage SMART and CCM representations are 0.04% and 0.2%, respectively. Furthermore, an interesting observation in Figs. 8.12 and 8.13 is that, while resonant frequencies and amplitudes are extraordinarily well captured by the SMART model, well superior to the CCM model, the SMART model's off-resonance behavior is less accurate than that of the CCM model. Clearly, the minimal SMART model does not contain the necessary information to yield adequate capture of the quasi-static off-resonance response. However, this information appears to

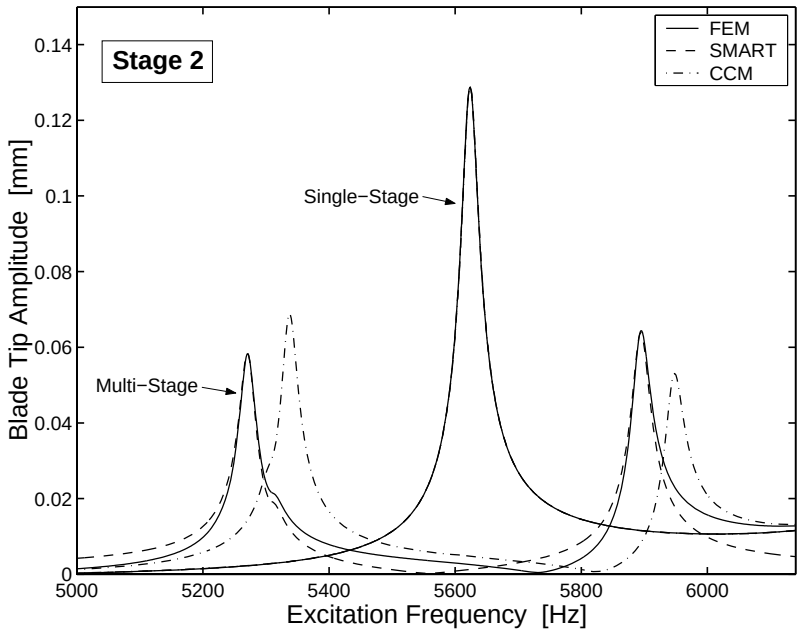

Figure 8.14: Tuned stage 2 forced response from engine order 15 excitation (15E=-1E) using finite element and reduced order single- and multi-stage models.

be carried by the larger CCM model. This cannot be viewed as a serious deficit of the SMART model, however, since the primary target is typically to obtain the best possible estimate of maximum resonant amplitude, and the SMART approach is clearly unmatched in this regard. Also, note that this behavior is distinctly different from the single-stage response, where both reduced order model responses closely follow the finite element solution both at and off resonance. Furthermore, note that both reduced order models provide indications of the subresonance occurring at 4295 Hz, which is a phenomenon specific to multi-stage response (see Bladh *et al*. [1]).

The tuned and mistuned stage 2 forced responses depicted in Figs. 8.14 and 8.15 demonstrate an even more dramatic change in response behavior due to interstage coupling. Here, the blade-dominated harmonic 1 mode pair in the clamped interstage single-stage representation has been replaced by two more disk-dominated mode pairs. Consequently, the maximum resonant amplitudes for the multi-stage model are much lower than

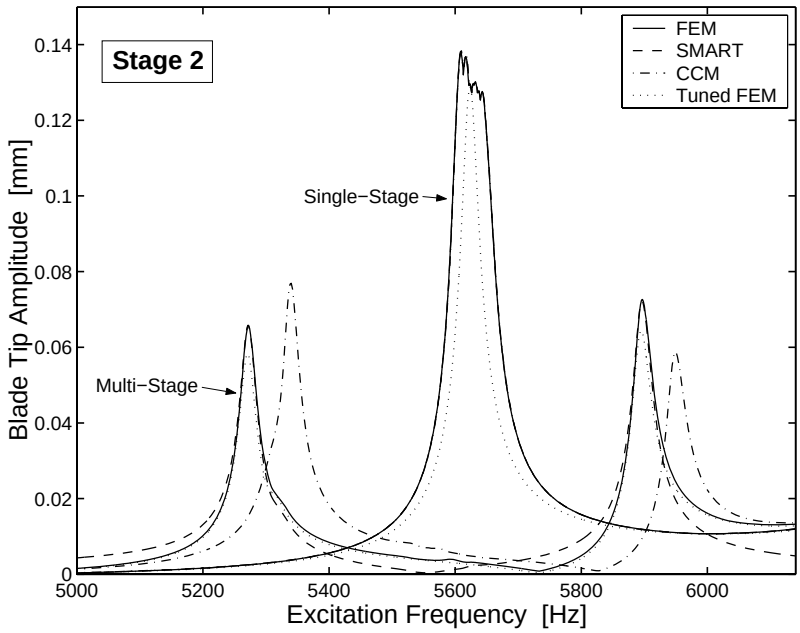

Figure 8.15: Mistuned stage 2 forced response from engine order 15 excitation (15E=-1E) using finite element and reduced order single- and multi-stage models. The tuned stage 2 finite element single- and multi-stage responses are included for reference.

those of the single-stage model. Note that stage 2 exhibits negligible mistuning sensitivity for both single- and multi-stage representations. The performances of the CCM and SMART models follow the trends seen in the stage 1 responses, although the differences in accuracy and off-resonance behavior are even more pronounced in the stage 2 responses. As mentioned in Section 8.3.2, the harmonic 1 multi-stage CCM modes in the considered frequency region are slightly off target. This inaccuracy becomes quite obvious in the depicted responses, where the multi-stage CCM model is significantly stiffer than the parent finite element model. Meanwhile, the SMART model yields excellent predictions of both tuned and mistuned multi-stage maximum resonant amplitudes (within 1%), while, again, providing a less accurate prediction of the off-resonance behavior.

It is obvious from the included forced response samples in Figs. 8.12–8.15 that the quality of the CCM model is inferior to that of the SMART model. This is largely due to

the restrictions on the interstage deformation space imposed by the truncated set of characteristic interstage constraint modes. Unfortunately, the only viable remedy is to keep all interstage DOF in the CCM model, and this will render the CCM model completely unsuitable for any comprehensive dynamic response analyses. In contrast, the use of truncated sets of characteristic disk-blade interface constraint modes does not have nearly as adverse effects on the model quality. It is therefore concluded that using a SMART approach, in combination with characteristic disk-blade interface constraint modes in the intermediate CMS model, is the most promising and pragmatic approach to the computationally efficient and accurate modeling of the dynamics of mistuned multi-stage rotor assemblies.

8.4 Conclusions

This paper explored the feasibility of reduced order modeling of multi-stage bladed disk dynamics, with and without blade mistuning. Both free and forced responses of an example two-stage rotor were examined using novel component-mode-based reduced order modeling techniques for mistuned multi-stage assemblies. Two approaches were investigated: (a) partial secondary modal analyses on constraint-mode partitions; and (b) a full-scale secondary modal analysis on the intermediate multi-stage model constructed by component mode synthesis. Finite element results were used as a benchmark to validate the introduced techniques.

The two introduced reduced order modeling approaches were shown to facilitate multi-stage modeling and analyses featuring blade mistuning, using only computationally inexpensive modal data from a cyclic disk sector and a single blade per stage. Approach (a) resulted in good approximations of multi-stage free and forced responses. However, the relatively large size of the reduced order model using this approach may be impractical

for comprehensive dynamic analyses when the number of included stages increases. In contrast, approach (b) was shown to yield exceptionally small reduced order models that produced extremely accurate results in the free and forced response. The drawback of this approach is that the secondary eigenvalue problem may be of considerable size for more expansive models. Thus, it was concluded that a combination of the two approaches (a) and (b) is the most promising and practical approach to the computationally efficient and accurate modeling of the dynamics of mistuned multi-stage rotor assemblies. For this combined approach, it is proposed that a secondary condensation of the disk-blade interface partitions be performed by means of characteristic constraint modes, followed by a tertiary modal analysis on the entire multi-stage model.

The computational tools developed in this work will enable engineers to analyze the dynamics of mistuned multi-stage rotor assemblies with greater confidence by properly accounting for the interstage boundary conditions.

CHAPTER IX

Current Topics in Bladed Disk Modeling

This chapter presents two topics that have been the subjects of preliminary investigations pertaining to the modeling of mistuned bladed disk vibrations using component mode synthesis (CMS). Finite-element-based CMS techniques are popular tools used in structural dynamics analyses of complex structures for a wide array of applications. In CMS, the original structure is subdivided into smaller substructures, or components, for which normal modes are computed independently, and more inexpensively. The assembled system is then represented by a truncated set of component modes through necessary compatibility constraints applied in a systematic fashion. The result is highly-reduced order models based on parent finite element models of arbitrary complexity. CMS techniques are usually characterized by the manner in which the component normal modes are computed: (a) with fixed interfaces; or (b) with free interfaces. This order also happens to coincide with the CMS development timeline (see Chapter I: Introduction). For surveys on the development of CMS techniques, the interested reader is referred to the survey papers by Craig [24] and by Seshu [25].

9.1 Numerical Instability of Classical Free-Interface Component Mode Synthesis Techniques

In general, the classical CMS methods perform very well, yielding reliable results with highly-reduced order models. However, in this section it is shown that while the fixed-interface CMS technique of Craig and Bampton [29] is highly robust and stable in every aspect, the classical free-interface CMS methods incorporating residual effects as formulated by Rubin [32] and by Craig and Chang [33] do have "built-in" numerical instability. As far as the author is aware, this important and unfortunate circumstance has not been documented in the open literature. The numerical instability occurs when there are only very small residual contributions (i.e., for large numbers of retained component modes), due to matrix ill-conditioning. This matrix ill-conditioning appears abruptly and can have a devastating effect on the accuracy of these methods, as any likeness to the behavior of the parent finite element model vanishes entirely. Moreover, there are no means of determining the onset of these numerical problems *a priori*.

The numerical instability is not a concern for most engineering applications, where only a very small fraction of the total number of component modes is retained. However, it may be critically important to keep this in mind in certain special cases. Specifically, in the context of mistuned bladed disk modeling employing the secondary modal analysis reduction technique (SMART) developed by Bladh *et al*. [70, 71], the primary purpose of using CMS is to cast the model in a form that is better suited for input of blade mistuning, rather than to achieve model reduction. Hence, for simpler "academic" models used in parameter studies, where high model accuracy is desired, the number of retained modes may well approach or even go beyond this unknown stability limit.

The numerical instability is demonstrated using a simple three-dimensional, two-component finite element model with two different boundary conditions. The two different boundary

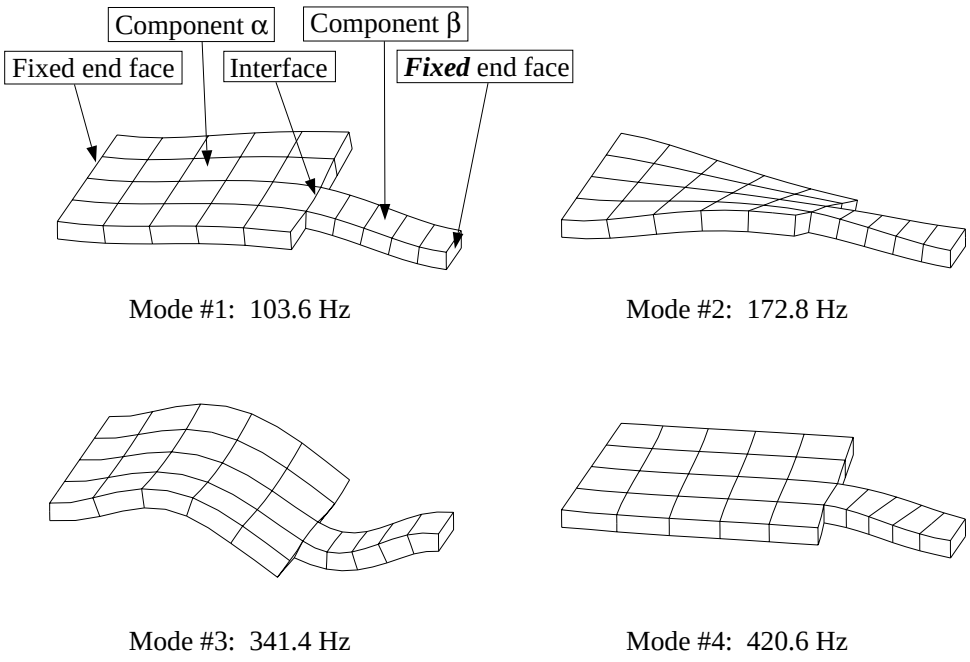

Figure 9.1: Deformed finite element meshes for the four lowest modes of the fixed-tip two-component test model.

conditions serve the additional purpose of demonstrating the unavoidable approximation in the case of an unconstrained component (i.e., a component featuring rigid-body modes). Furthermore, a rather modest modification to the Craig-Chang formulation is presented that alleviates the numerical instability suffered by the classical free-interface CMS techniques.

9.1.1 Test Model Description

The used test model is depicted in Figs. 9.1 and 9.2, which show the deformed meshes for the four lowest modes when the non-interfacing end face of the smaller component (β; right) is free and fixed, respectively. The model is constructed from second-order brick elements (20-noded solids), and the two-component substructuring is shown in the figures. The total number of unconstrained degrees of freedom (DOF) is 651 for the fixed-tip model, and 675 for the free-tip model.

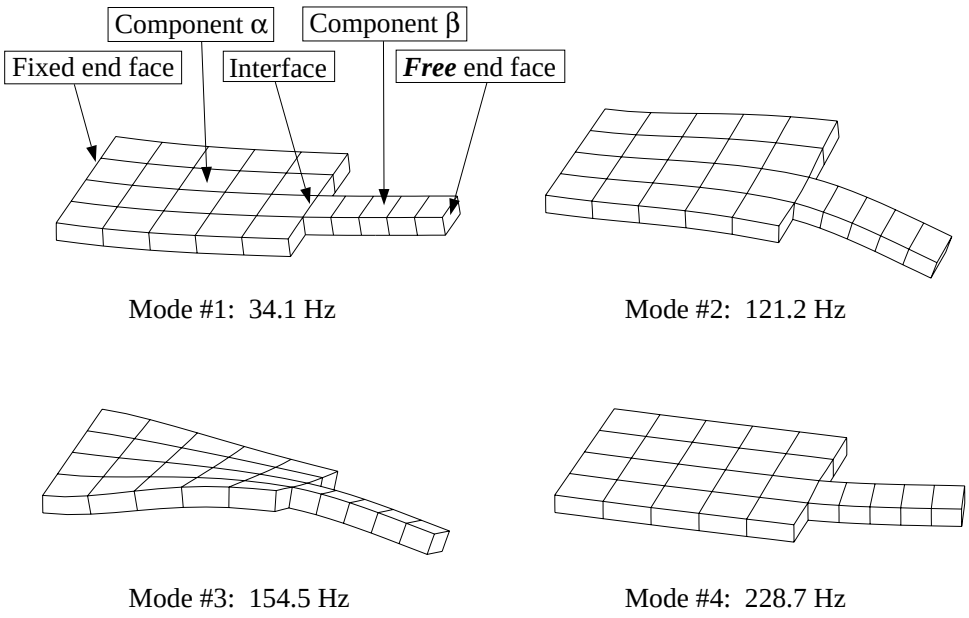

Figure 9.2: Deformed finite element meshes for the four lowest modes of the free-tip two-component test model.

It is assumed throughout the following that the unconstrained DOF of each component are partitioned into interior (Δ) DOF and interface (Γ) DOF. Hence, the physical (i.e., finite element) mass and stiffness matrices and the displacement vector of the α-component are represented as:

$$\mathbf{M}^{\alpha} = \begin{bmatrix} \mathbf{M}^{\alpha}_{\Delta\Delta} & \mathbf{M}^{\alpha}_{\Delta\Gamma} \\ \mathbf{M}^{\alpha^{\mathbf{T}}}_{\Delta\Gamma} & \mathbf{M}^{\alpha}_{\Gamma\Gamma} \end{bmatrix} \quad \mathbf{K}^{\alpha} = \begin{bmatrix} \mathbf{K}^{\alpha}_{\Delta\Delta} & \mathbf{K}^{\alpha}_{\Delta\Gamma} \\ \mathbf{K}^{\alpha^{\mathbf{T}}}_{\Delta\Gamma} & \mathbf{K}^{\alpha}_{\Gamma\Gamma} \end{bmatrix} \quad \mathbf{x}^{\alpha} = \begin{Bmatrix} \mathbf{x}^{\alpha}_{\Delta} \\ \mathbf{x}^{\alpha}_{\Gamma} \end{Bmatrix}, \qquad (9.1)$$

and similarly for the β-component.

9.1.2 Classical CMS Formulations in Brief

• ***Fixed-Interface Method: Craig-Bampton.*** The Craig-Bampton (C-B) method has been used extensively in previous chapters, but the main results are restated here for convenience. The C-B method uses as component modal basis a truncated set (k) of component normal modes of vibration ($\mathbf{\Lambda}$,$\mathbf{\Phi}$), where the interface DOF are held fixed, and a complete set (c) of static constraint modes ($\mathbf{\Psi}$) induced by successive unit deflections of each inter-

face DOF, while all other interface DOF are held fixed. This results in a transformation to C-B generalized (modal) coordinates ($\mathbf{p}$) as:

$$\mathbf{x} = \left\{ \begin{array}{c} \mathbf{x_\Delta} \\ \\ \mathbf{x_\Gamma} \end{array} \right\} = \left[\begin{array}{cc} \mathbf{\Phi} & \mathbf{\Psi} \\ \\ \mathbf{0} & \mathbf{I} \end{array} \right] \left\{ \begin{array}{c} \mathbf{p_k} \\ \\ \mathbf{p_c} \end{array} \right\} = \mathbf{U}\mathbf{p}. \tag{9.2}$$

Using this modal basis, the condensed C-B mass (μ) and stiffness (κ) matrices for each component become:

$$\mu = \left[\begin{array}{cc} \mathbf{I} & \mu_{\mathbf{kc}} \\ \\ \mu_{\mathbf{kc}}^{\mathbf{T}} & \mu_{\mathbf{cc}} \end{array} \right] \qquad \kappa = \left[\begin{array}{cc} \mathbf{\Lambda} & \mathbf{0} \\ \\ \mathbf{0} & \kappa_{\mathbf{cc}} \end{array} \right] \qquad \mathbf{p} = \left\{ \begin{array}{c} \mathbf{p_k} \\ \\ \mathbf{p_c} \end{array} \right\}, \tag{9.3}$$

where

$$\begin{aligned} \mu_{\mathbf{kc}} &= \mathbf{\Phi}^{\mathbf{T}} \left[\mathbf{M}_{\mathbf{\Delta\Delta}} \mathbf{\Psi} + \mathbf{M}_{\mathbf{\Delta\Gamma}} \right] \\ \mu_{\mathbf{cc}} &= \mathbf{\Psi}^{\mathbf{T}} \left[\mathbf{M}_{\mathbf{\Delta\Delta}} \mathbf{\Psi} + \mathbf{M}_{\mathbf{\Delta\Gamma}} \right] + \mathbf{M}_{\mathbf{\Delta\Gamma}}^{\mathbf{T}} \mathbf{\Psi} + \mathbf{M}_{\mathbf{\Gamma\Gamma}} \\ \kappa_{\mathbf{cc}} &= \mathbf{K}_{\mathbf{\Gamma\Gamma}} + \mathbf{K}_{\mathbf{\Delta\Gamma}}^{\mathbf{T}} \mathbf{\Psi}. \end{aligned}$$

The component assembly, or synthesis, is achieved by satisfying displacement compatibility over the component interfaces (i.e., $\mathbf{x}_{\mathbf{\Gamma}}^{\alpha} = \mathbf{x}_{\mathbf{\Gamma}}^{\beta}$), which becomes from Eq. (9.2):

$$\mathbf{x}_{\mathbf{\Gamma}}^{\alpha} = \mathbf{p}_{\mathbf{c}}^{\alpha} = \mathbf{p}_{\mathbf{c}} = \mathbf{p}_{\mathbf{c}}^{\beta} = \mathbf{x}_{\mathbf{\Gamma}}^{\beta}. \tag{9.4}$$

This constraint equation leads to the synthesized C-B representation of a two-component structure:

$$\mathbf{M}^{\mathbf{CB}} = \left[\begin{array}{ccc} \mathbf{I} & \mu_{\mathbf{kc}}^{\alpha} & \mathbf{0} \\ \mu_{\mathbf{kc}}^{\alpha^{\mathbf{T}}} & \mu_{\mathbf{cc}}^{\alpha} + \mu_{\mathbf{cc}}^{\beta} & \mu_{\mathbf{kc}}^{\beta^{\mathbf{T}}} \\ \mathbf{0} & \mu_{\mathbf{kc}}^{\beta} & \mathbf{I} \end{array} \right] \quad \mathbf{K}^{\mathbf{CB}} = \left[\begin{array}{ccc} \mathbf{\Lambda}^{\alpha} & \mathbf{0} & \mathbf{0} \\ \mathbf{0} & \kappa_{\mathbf{cc}}^{\alpha} + \kappa_{\mathbf{cc}}^{\beta} & \mathbf{0} \\ \mathbf{0} & \mathbf{0} & \mathbf{\Lambda}^{\beta} \end{array} \right] \quad \mathbf{p}^{\mathbf{CB}} = \left\{ \begin{array}{c} \mathbf{p}_{\mathbf{k}}^{\alpha} \\ \\ \mathbf{p_c} \\ \\ \mathbf{p}_{\mathbf{k}}^{\beta} \end{array} \right\}. \tag{9.5}$$

• ***Free-Interface Method with Residual Flexibility: Craig-Chang.*** The Craig-Chang (C^2) method uses as component modal basis a truncated set (k) of component normal

modes of vibration ($\mathbf{\Lambda}$,$\mathbf{\Phi}$), where all the interface DOF are free. A complete set (d) of residual attachment modes ($\mathbf{\Psi}$) are then used to supplement the normal modes. The residual attachment modes represent purely computational shapes induced in the residual structure (i.e., after removing the flexibility represented by the retained normal modes) by successively applied unit loads on each interface DOF with all other interface DOF free and unloaded. This results in a transformation to C^2 generalized coordinates as:

$$\mathbf{x} = \left\{ \begin{array}{c} \mathbf{x_\Delta} \\ \mathbf{x_\Gamma} \end{array} \right\} = \left[\begin{array}{cc} \mathbf{\Phi_\Delta} & \mathbf{\Psi_\Delta} \\ \mathbf{\Phi_\Gamma} & \mathbf{\Psi_\Gamma} \end{array} \right] \left\{ \begin{array}{c} \mathbf{p_k} \\ \mathbf{p_d} \end{array} \right\} = \mathbf{Up}. \tag{9.6}$$

In computing the residual attachment modes, one must distinguish between the case of constrained components and the case of unconstrained components (i.e., "free-free" structures such as blades), since the latter exhibit rigid-body modes $\phi_\mathbf{r}$. Recall that the β-component is unconstrained in the free-tip case. For a constrained component, the flexibility matrix is simply the inverse of its stiffness matrix: $\mathbf{G} = \mathbf{K}^{-1}$. For an unconstrained component, however, the stiffness matrix is singular, and its inverse therefore does not exist. To circumvent this problem, a sufficient number of arbitrarily chosen DOF (r) are constrained "artificially", in order to eliminate all rigid-body translations and rotations. Hence, a minimum of six non-colinear DOF must be held fixed in a three-dimensional problem. Moreover, the r DOF-set cannot contain any component interface (Γ) DOF, and r is thus a subset of the interior (Δ) DOF-set. Specifically for the free-tip test model in Fig. 9.2, three of the four corner nodes on the tip of the β-component were held fixed to serve as artificial constraints (i.e., nine DOF). With this additional DOF subdivision $\Delta \rightarrow [r\ \Delta']$, the component stiffness matrix may be re-partitioned as:

$$\mathbf{K} = \left[\begin{array}{ccc} \mathbf{K_{rr}} & \mathbf{K_{r\Delta'}} & \mathbf{K_{r\Gamma}} \\ \mathbf{K^T_{r\Delta'}} & \mathbf{K_{\Delta'\Delta'}} & \mathbf{K_{\Delta'\Gamma}} \\ \mathbf{K^T_{r\Gamma}} & \mathbf{K^T_{\Delta'\Gamma}} & \mathbf{K_{\Gamma\Gamma}} \end{array} \right] = \left[\begin{array}{cc} \mathbf{K_{rr}} & \mathbf{K_{rc}} \\ \mathbf{K^T_{rc}} & \mathbf{K_{cc}} \end{array} \right], \tag{9.7}$$

where $\mathbf{K_{cc}}$ is the non-singular stiffness matrix of the artificially constrained component. $\mathbf{K_{cc}}$ is used to form a "special" flexibility matrix:

$$\mathbf{G_c} = \begin{bmatrix} \mathbf{0} & \mathbf{0} \\ \mathbf{0} & \mathbf{K_{cc}^{-1}} \end{bmatrix}, \tag{9.8}$$

where it is noted that the entries pertaining to the artificially constrained DOF are identically zero. Then, by applying to the component an equilibrated load set that consists of any applied external loads equilibrated by the d'Alembert force due to rigid-body acceleration, the unconstrained component's flexibility matrix is obtained as:

$$\mathbf{G} = \mathbf{A^T G_c A} \quad ; \quad \mathbf{A} = \mathbf{I} - \mathbf{M}\phi_\mathbf{r}\phi_\mathbf{r}^\mathbf{T}. \tag{9.9}$$

With the flexibility matrix in place for both constrained and unconstrained components, the residual flexibility matrix is in both cases formed as:

$$\mathbf{G^r} = \begin{bmatrix} \mathbf{G^r_{\Delta\Delta}} & \mathbf{G^r_{\Delta\Gamma}} \\ \mathbf{G^{r^T}_{\Delta\Gamma}} & \mathbf{G^r_{\Gamma\Gamma}} \end{bmatrix} = \mathbf{G} - \mathbf{G^k} = \mathbf{G} - \mathbf{\Phi_f \Lambda^{-1} \Phi_f^T}, \tag{9.10}$$

where $\mathbf{\Phi_f}$ contains the retained *flexible* normal modes, i.e., exclusive of any rigid-body modes (if applicable). Hence, $\mathbf{\Phi_f} = \mathbf{\Phi}$ for constrained components, whereas $\mathbf{\Phi_f}$ is a subset of $\mathbf{\Phi}$ for unconstrained components. In other words, the residual flexibility represents the remaining flexibility of the system after the *elastic* contributions of the retained normal modes have been removed. Note that in the limiting case where *all* normal modes are retained, $\mathbf{G^r}$ will be a null matrix. However, as will be shown later on, the diminishing nature of $\mathbf{G^r}$ as the number of retained modes increases gives rise to numerical problems far earlier than the limiting case.

Since the C^2 method uses successive unit loads on the interface DOF to form the residual attachment modes, these mode shapes are simply the columns of $\mathbf{G^r}$ that pertain to the

interface DOF:

$$\Psi = \begin{bmatrix} \Psi_\Delta \\ \Psi_\Gamma \end{bmatrix} = \begin{bmatrix} G^r_{\Delta\Gamma} \\ G^r_{\Gamma\Gamma} \end{bmatrix}. \tag{9.11}$$

Using this modal basis, the condensed C^2 mass and stiffness matrices for each component become:

$$\mu = \begin{bmatrix} I & 0 \\ 0 & \Psi^T M \Psi \end{bmatrix} \qquad \kappa = \begin{bmatrix} \Lambda & 0 \\ 0 & \Psi_\Gamma \end{bmatrix} \qquad p = \begin{Bmatrix} p_k \\ p_d \end{Bmatrix}. \tag{9.12}$$

The component assembly is achieved by satisfying interface displacement compatibility and interface force equilibrium (i.e., $f^\alpha_\Gamma + f^\beta_\Gamma = 0$), which after simplification (see Craig [62]) result in the constraints:

$$x^\alpha_\Gamma = \Phi^\alpha_\Gamma p^\alpha_k + \Psi^\alpha_\Gamma p^\alpha_d = \Phi^\beta_\Gamma p^\beta_k + \Psi^\beta_\Gamma p^\beta_d = x^\beta_\Gamma \tag{9.13}$$

$$f^\alpha_\Gamma + f^\beta_\Gamma = p^\alpha_d + p^\beta_d = 0. \tag{9.14}$$

These two sets of constraint equations lead to the synthesized C^2 representation of a two-component structure:

$$\begin{aligned} M^{C^2} &= \begin{bmatrix} I + \Phi^{\alpha T}_\Gamma M_1 \Phi^\alpha_\Gamma & -\Phi^{\alpha T}_\Gamma M_1 \Phi^\beta_\Gamma \\ -\Phi^{\beta T}_\Gamma M_1^T \Phi^\alpha_\Gamma & I + \Phi^{\beta T}_\Gamma M_1 \Phi^\beta_\Gamma \end{bmatrix} \\ K^{C^2} &= \begin{bmatrix} \Lambda^\alpha + \Phi^{\alpha T}_\Gamma K_1 \Phi^\alpha_\Gamma & -\Phi^{\alpha T}_\Gamma K_1 \Phi^\beta_\Gamma \\ -\Phi^{\beta T}_\Gamma K_1^T \Phi^\alpha_\Gamma & \Lambda^\beta + \Phi^{\beta T}_\Gamma K_1 \Phi^\beta_\Gamma \end{bmatrix} \qquad p^{C^2} = \begin{Bmatrix} p^\alpha_k \\ p^\beta_k \end{Bmatrix}, \end{aligned} \tag{9.15}$$

where

$$\begin{aligned} K_1 &= \left[\Psi^\alpha_\Gamma + \Psi^\beta_\Gamma\right]^{-1} \\ M_1 &= K_1 \left[\Psi^{\alpha T} M^\alpha \Psi^\alpha + \Psi^{\beta T} M^\beta \Psi^\beta\right] K_1. \end{aligned} \tag{9.16}$$

Note that only the generalized coordinates pertaining to the component normal modes of vibration remain in the final C^2 representation. This makes the C^2 model particularly compact, and therefore exceptionally efficient.

• ***Free-Interface Method with Residual Flexibility and Inertia: Rubin.*** As in the C^2 method, the Rubin (R) method uses as component modal basis a truncated set (k) of component normal modes of vibration ($\mathbf{\Lambda}$,$\mathbf{\Phi}$), where all the interface DOF are free. However, there is a distinct difference in the way the two methods capture residual flexibility effects. Namely, the R technique retains the physical interface DOF ($\mathbf{x_\Gamma}$) in order to solve for an arbitrary force on the component interface ($\mathbf{f_\Gamma}$), while C^2 uses residual attachment modes induced by a pre-defined, complete set of successive unit loads on the interface DOF. In addition, the R technique allows for inclusion of residual inertia by using a second-order Maclaurin series expansion when solving for the interface force.

The procedures for obtaining the residual flexibility matrix $\mathbf{G^r}$ for both constrained and unconstrained components follow the C^2 approach exactly. With forces acting on the component interface DOF only, the first-order (static) residual deflections of the interface DOF are obtained as:

$$\mathbf{\Psi_\Gamma^{r,1}} = \mathbf{G_{\Gamma\Gamma}^r f_\Gamma}. \tag{9.17}$$

Using Eq. (9.17) and assuming harmonic motion, the second-order residual deflections of the interface DOF are obtained as:

$$\mathbf{\Psi_\Gamma^{r,2}} = \mathbf{G_{\Gamma\Gamma}^r}\left(\mathbf{f_\Gamma} - \mathbf{M\ddot{\Psi}_\Gamma^{r,1}}\right) = \left(\mathbf{G_{\Gamma\Gamma}^r} + \omega^2\mathbf{H_{\Gamma\Gamma}^r}\right)\mathbf{f_\Gamma}, \tag{9.18}$$

where $\mathbf{H_{\Gamma\Gamma}^r}$ is the interface partition of the residual inertia matrix, which is computed as:

$$\mathbf{H^r} = \begin{bmatrix} \mathbf{H_{\Delta\Delta}^r} & \mathbf{H_{\Delta\Gamma}^r} \\ \mathbf{H_{\Delta\Gamma}^{r^T}} & \mathbf{H_{\Gamma\Gamma}^r} \end{bmatrix} = \mathbf{G^r M G^r}, \tag{9.19}$$

by virtue of orthogonality between retained and residual flexibility with respect to the mass matrix, i.e., $\mathbf{G^k M G^r} \equiv \mathbf{0}$ (see Rubin [32]).

The physical displacements of the interface DOF can now be represented as a superposition of the truncated set of normal modes of vibration (including rigid-body modes, if

applicable) and the second-order residual deflections from Eq. (9.18):

$$\mathbf{x_\Gamma} = \mathbf{\Phi_\Gamma p_k} + \mathbf{\Psi_\Gamma^{r,2}} = \mathbf{\Phi_\Gamma p_k} + \left[\mathbf{G^r_{\Gamma\Gamma}} + \omega^2 \mathbf{H^r_{\Gamma\Gamma}}\right] \mathbf{f_\Gamma}. \tag{9.20}$$

Using a second-order Maclaurin series expansion in ω, the interface force may be solved from Eq. (9.20) as:

$$\mathbf{f_\Gamma} \approx \left[\mathbf{K^r_{\Gamma\Gamma}} - \omega^2 \mathbf{M^r_{\Gamma\Gamma}}\right] \left[\mathbf{x_\Gamma} - \mathbf{\Phi_\Gamma p_k}\right], \tag{9.21}$$

where

$$\mathbf{K^r_{\Gamma\Gamma}} = \mathbf{G^{r^{-1}}_{\Gamma\Gamma}} \qquad \mathbf{M^r_{\Gamma\Gamma}} = \mathbf{G^{r^{-1}}_{\Gamma\Gamma}} \mathbf{H^r_{\Gamma\Gamma}} \mathbf{G^{r^{-1}}_{\Gamma\Gamma}}. \tag{9.22}$$

In addition, the retained modes must satisfy dynamic equilibrium:

$$\left[\mathbf{\Lambda} - \omega^2 \mathbf{I}\right] \mathbf{p_k} = \mathbf{\Phi_\Gamma^T f_\Gamma}. \tag{9.23}$$

Identification of mass and stiffness terms in Eqs. (9.21) and (9.23) yields the condensed R mass and stiffness matrices for each component as:

$$\mu = \begin{bmatrix} \mu_{\mathbf{kk}} & \mu_{\mathbf{k\Gamma}} \\ \mu_{\mathbf{k\Gamma}}^{\mathbf{T}} & \mu_{\mathbf{\Gamma\Gamma}} \end{bmatrix} \qquad \kappa = \begin{bmatrix} \kappa_{\mathbf{kk}} & \kappa_{\mathbf{k\Gamma}} \\ \kappa_{\mathbf{k\Gamma}}^{\mathbf{T}} & \kappa_{\mathbf{\Gamma\Gamma}} \end{bmatrix} \qquad \mathbf{p} = \begin{Bmatrix} \mathbf{p_k} \\ \mathbf{x_\Gamma} \end{Bmatrix}, \tag{9.24}$$

where

$$\begin{aligned} \mu_{\mathbf{kk}} &= \mathbf{I} + \mathbf{\Phi_\Gamma^T M^r_{\Gamma\Gamma}} \mathbf{\Phi_\Gamma} & \kappa_{\mathbf{kk}} &= \mathbf{\Lambda} + \mathbf{\Phi_\Gamma^T K^r_{\Gamma\Gamma}} \mathbf{\Phi_\Gamma} \\ \mu_{\mathbf{k\Gamma}} &= -\mathbf{\Phi_\Gamma^T M^r_{\Gamma\Gamma}} & \kappa_{\mathbf{k\Gamma}} &= -\mathbf{\Phi_\Gamma^T K^r_{\Gamma\Gamma}} \\ \mu_{\mathbf{\Gamma\Gamma}} &= \mathbf{M^r_{\Gamma\Gamma}} & \kappa_{\mathbf{\Gamma\Gamma}} &= \mathbf{K^r_{\Gamma\Gamma}}. \end{aligned}$$

The component assembly is achieved by satisfying displacement compatibility and force equilibrium over the interface, resulting in the constraints:

$$\mathbf{x_\Gamma^\alpha} = \mathbf{x_\Gamma^\beta} \tag{9.25}$$

$$\begin{aligned} \mathbf{f_\Gamma^\alpha} + \mathbf{f_\Gamma^\beta} = &\left[\kappa_{\mathbf{k\Gamma}}^{\alpha^{\mathbf{T}}} - \omega^2 \mu_{\mathbf{k\Gamma}}^{\alpha^{\mathbf{T}}}\right] \mathbf{p_k^\alpha} + \left[\kappa_{\mathbf{\Gamma\Gamma}}^{\alpha} - \omega^2 \mu_{\mathbf{\Gamma\Gamma}}^{\alpha}\right] \mathbf{x_\Gamma^\alpha} + \\ &+ \left[\kappa_{\mathbf{k\Gamma}}^{\beta^{\mathbf{T}}} - \omega^2 \mu_{\mathbf{k\Gamma}}^{\beta^{\mathbf{T}}}\right] \mathbf{p_k^\beta} + \left[\kappa_{\mathbf{\Gamma\Gamma}}^{\beta} - \omega^2 \mu_{\mathbf{\Gamma\Gamma}}^{\beta}\right] \mathbf{x_\Gamma^\beta} = \mathbf{0}. \end{aligned} \tag{9.26}$$

These two sets of constraint equations lead to the synthesized R representation of a two-component structure:

$$\mathbf{M^R} = \begin{bmatrix} \mu^{\alpha}_{\mathbf{kk}} & \mu^{\alpha}_{\mathbf{k\Gamma}} & \mathbf{0} \\ \mu^{\alpha^{\mathbf{T}}}_{\mathbf{k\Gamma}} & \mu^{\alpha}_{\mathbf{\Gamma\Gamma}} + \mu^{\beta}_{\mathbf{\Gamma\Gamma}} & \mu^{\beta^{\mathbf{T}}}_{\mathbf{k\Gamma}} \\ \mathbf{0} & \mu^{\beta}_{\mathbf{k\Gamma}} & \mu^{\beta}_{\mathbf{kk}} \end{bmatrix} \quad \mathbf{K^R} = \begin{bmatrix} \kappa^{\alpha}_{\mathbf{kk}} & \kappa^{\alpha}_{\mathbf{k\Gamma}} & \mathbf{0} \\ \kappa^{\alpha^{\mathbf{T}}}_{\mathbf{k\Gamma}} & \kappa^{\alpha}_{\mathbf{\Gamma\Gamma}} + \mu^{\beta}_{\mathbf{\Gamma\Gamma}} & \kappa^{\beta^{\mathbf{T}}}_{\mathbf{k\Gamma}} \\ \mathbf{0} & \kappa^{\beta}_{\mathbf{k\Gamma}} & \kappa^{\beta}_{\mathbf{kk}} \end{bmatrix} \quad \mathbf{p^R} = \begin{Bmatrix} \mathbf{p}^{\alpha}_{\mathbf{k}} \\ \mathbf{x}_{\mathbf{\Gamma}} \\ \mathbf{p}^{\beta}_{\mathbf{k}} \end{Bmatrix}. \tag{9.27}$$

Hence, comparing this model with the C^2 model, the effects of residual inertia is included in the R model (in an approximate sense) at the expense of retained physical interface DOF.

9.1.3 A Stabilized Free-Interface CMS Method

The proposed stabilized free-interface CMS method is a simple modification of the previously derived C^2 method, and it will therefore be referred to as Stabilized Craig-Chang (SC^2). In fact, it may even be appropriate to describe this approach as a less refined C^2 method in that it takes one less step in using the constraints of Eqs. (9.13) and (9.14). Using $\mathbf{p}^{\beta}_{\mathbf{d}} = -\mathbf{p}^{\alpha}_{\mathbf{d}} = \mathbf{p_d}$ from Eq. (9.14) in Eq. (9.13) yields:

$$\mathbf{\Phi}^{\alpha}_{\mathbf{\Gamma}}\mathbf{p}^{\alpha}_{\mathbf{k}} - \mathbf{\Phi}^{\beta}_{\mathbf{\Gamma}}\mathbf{p}^{\beta}_{\mathbf{k}} + \left[\mathbf{\Psi}^{\alpha}_{\mathbf{\Gamma}} + \mathbf{\Psi}^{\beta}_{\mathbf{\Gamma}}\right]\mathbf{p_d} = \mathbf{0}. \tag{9.28}$$

In the C^2 method, the generalized coordinates $\mathbf{p_d}$, which pertain to the complete set of residual attachment modes and thus are equal in number to the physical interface DOF, are solved from Eq. (9.28) to yield a particularly compact model. However, solving for $\mathbf{p_d}$ in Eq. (9.28) assumes that the inverse of $\left[\mathbf{\Psi}^{\alpha}_{\mathbf{\Gamma}} + \mathbf{\Psi}^{\beta}_{\mathbf{\Gamma}}\right]$ exists (see $\mathbf{K_1}$ in Eq. (9.16)), and thus that the conditioning of the summed interface residual flexibilities (see Eq. (9.11)) is sufficient. While this assumption is likely to be adequate for most engineering applications, it will not be true when the numbers of retained component normal modes become sufficiently large, since the residual flexibility partitions involved will approach null matrices.

Hence, in order to yield a numerically stable formulation, the key is to avoid the inverse of the summed residual flexibilities. The key difference between the classical C^2 method and the proposed SC^2 approach is therefore that the $\mathbf{p_d}$ coordinates are being retained in the SC^2 model, governed by Eq. (9.28). This leads to the synthesized SC^2 representation of a two-component structure as follows:

$$\mathbf{M^{SC^2}} = \begin{bmatrix} \mathbf{I} & \mathbf{0} & \mathbf{0} \\ \mathbf{0} & \mathbf{0} & \mathbf{0} \\ \mathbf{0} & \mathbf{0} & \mathbf{I} \end{bmatrix} \quad \mathbf{K^{SC^2}} = \begin{bmatrix} \mathbf{\Lambda}^{\alpha} & \mathbf{\Phi}_{\mathbf{\Gamma}}^{\alpha^{\mathbf{T}}} & \mathbf{0} \\ \mathbf{\Phi}_{\mathbf{\Gamma}}^{\alpha} & \mathbf{\Psi}_{\mathbf{\Gamma}}^{\alpha} + \mathbf{\Psi}_{\mathbf{\Gamma}}^{\beta} & -\mathbf{\Phi}_{\mathbf{\Gamma}}^{\beta} \\ \mathbf{0} & -\mathbf{\Phi}_{\mathbf{\Gamma}}^{\beta^{\mathbf{T}}} & \mathbf{\Lambda}^{\beta} \end{bmatrix} \quad \mathbf{p^{SC^2}} = \begin{Bmatrix} \mathbf{p}_{\mathbf{k}}^{\alpha} \\ \mathbf{p_d} \\ \mathbf{p}_{\mathbf{k}}^{\beta} \end{Bmatrix}. \tag{9.29}$$

Note that while the SC^2 formulation leads to a numerically stable model, it is achieved at the expense of a substantial increase in model size. This increased model size is clearly undesirable, and it is therefore proposed that the SC^2 approach may serve as a C^2 model quality assessment tool. The unstable C^2 model may be checked against the stable SC^2 model for consistency during the CMS model construction, before proceeding to comprehensive dynamic analyses using the more computationally efficient C^2 model. Since the SC^2 model is based on exactly the same component modal quantities as the C^2 model, such consistency checks can be made relatively inexpensively.

As a final remark, note that the R method cannot be stabilized, since the inversion of residual flexibilities is inherent in solving for the interface force by the second-order Maclaurin series expansion in Eq. (9.21).

9.1.4 Modal Convergence and Numerical Stability Issues

In this section, the modal convergence trends are investigated for the four derived techniques, using the simple two-component test model with fixed- or free-tip β-component. The convergence measure is the relative errors of the CMS model representations for the four lowest natural frequencies versus reference finite element values.

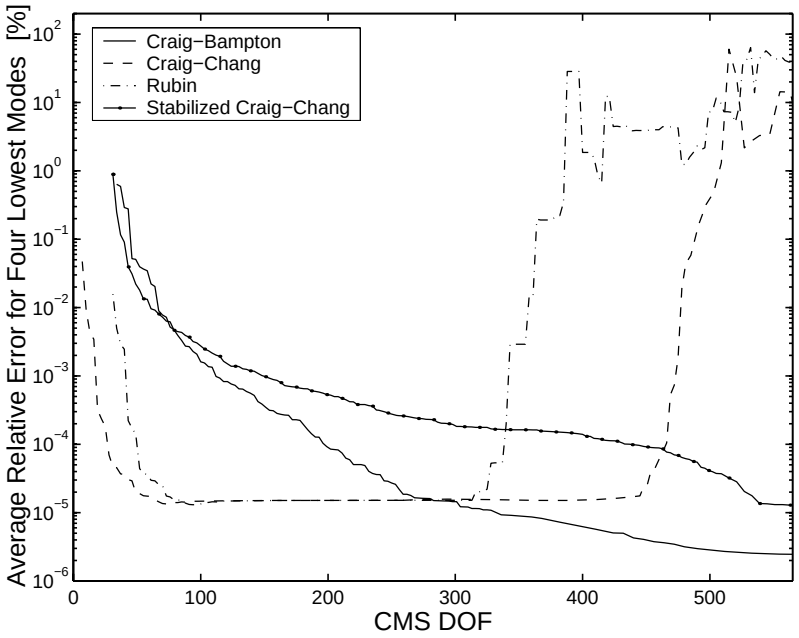

Figure 9.3: Convergence of the four lowest natural frequencies of the fixed-tip model relative to finite element results for the considered CMS methods.

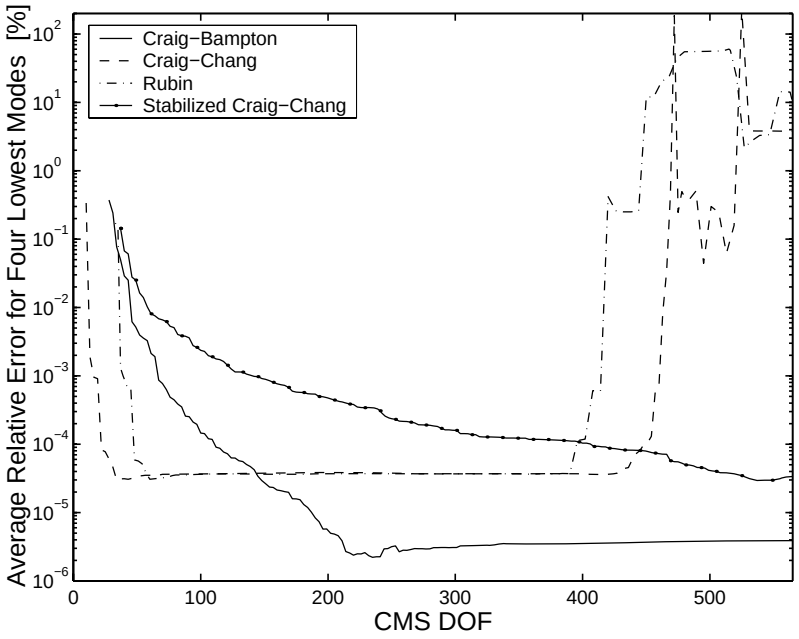

Figure 9.4: Convergence of the four lowest natural frequencies of the free-tip model relative to finite element results for the considered CMS methods.

Figures 9.3 and 9.4 depict the convergence trends using the fixed- and free-tip β-components, respectively. In both cases, it is notable how quickly the two classical free-interface CMS techniques — C^2 and R — converge to yield highly accurate reduced order models. The C^2 model is particularly impressive, reaching excellent accuracy levels with only very few DOF in the model due to the eliminated interface DOF. Moreover, beyond certain numbers of retained normal modes, both these techniques exhibit sudden onsets of dramatic deterioration in model quality. Beyond these points, natural frequencies and mode shapes bear little or no resemblance with the reference solutions. In contrast, while clearly sufficiently accurate for most applications, the C-B and SC^2 models display slower modal convergence than the classical free-interface CMS techniques for both test models. On the other hand, both these methods are unconditionally stable, as would be predicted from their respective formulations. Note that the steady improvement in accuracy as the number of retained component normal modes increases continues for these two methods until all component normal modes are included.

As mentioned in the earlier discussion, the onset of this apparent numerical instability for the classical free-interface CMS methods is prompted by the inversion of residual flexibility matrix partitions, either separate (R) or summed (C^2). These matrices become progressively more ill-conditioned as the number of retained normal modes (i.e., the retained flexibility) increases, and they will, in theory, eventually become null matrices. The direct coupling between the condition of the residual flexibility matrix (i.e., $\mathrm{cond}\,[\mathbf{G^r}]$) and the numerical instability is clearly illustrated in Fig. 9.5, which depicts the behavior of the fixed-tip R model as a demonstrative example. As shown, the onset of numerical instability at just over 300 CMS DOF is clearly marked by a nearly two orders of magnitude degrading shift in residual flexibility matrix conditioning. Moreover, the later onset of instability exhibited by the C^2 model is explained by the inversion of the summed resid-

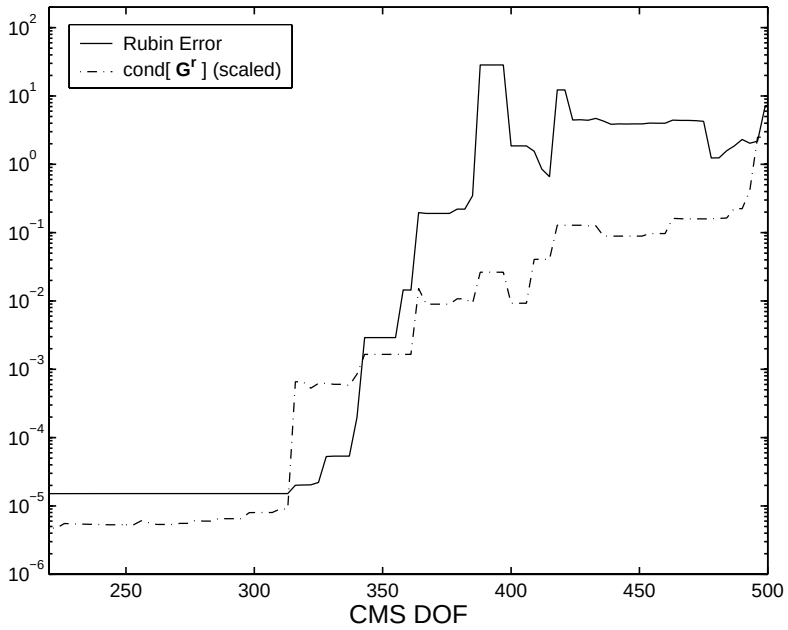

Figure 9.5: Relationship between the condition of the residual flexibility matrix and Rubin natural frequency errors for the fixed-tip test model.

ual flexibility matrices, as opposed to the separate inversions of component-wise matrices of the R model, since this means that both matrices involved must be sufficiently close to null matrices to make the sum ill-conditioned.

Furthermore, an interesting common property of the C^2 and R models is the lack of further improvement beyond the initial rapid convergence. The error levels stay practically stationary, even if large numbers of component modes are added into the models. It is hypothesized that the improvement from the additional retained modes may be balanced by degrading residual matrix conditioning in this stationary region. Moreover, note that these stationary error levels differ by approximately a factor two between the fixed- and free-tip cases. One reason for this difference may be the application of artificial constraints to the free-tip β-component in order to eliminate rigid-body motion during the construction of the C^2 and R models. This implies that the flexibility associated with the artificially constrained DOF is not properly captured, and these DOF must therefore be chosen with

care.

Clearly, the found numerical instability of the classical free-interface CMS methods is of little practical importance for “normal” engineering applications. Unless a very large fraction of the total number of component normal modes is retained, this is not likely to present a problem. However, as mentioned previously, there may be special cases, particularly in studies of highly simplified “academic” models, where this numerical instability can become a factor, and where the awareness of this limitation of classical free-interface CMS methods may become critical.

9.2 “Optimal” Component Mode Basis for Dynamic Analyses of Mistuned Bladed Disks

In Chapter V, a highly accurate and computationally efficient secondary modal analysis reduction technique (SMART) was developed for dynamic analyses of mistuned bladed disks. This technique employs a two-step approach: first, component mode synthesis (CMS) is used to isolate the blade properties and to provide a primary reduced order model; second, a modal analysis is performed on the CMS model to generate a very small reduced order model based on the global modes in a frequency range of interest. The SMART formulation in Chapter V employed a cyclic Craig-Bampton method with fixed-interface component normal modes to form the intermediate CMS model. However, it is realized that there may be other CMS approaches that provide better intermediate CMS representations of bladed disks. To this end, there are primarily three CMS model properties that are of particular interest: (a) fast modal convergence; (b) “natural” normal mode selection; and (c) suitability to blade mistuning input. The “optimal” method should exhibit all three of these properties. As a result, equally or more accurate CMS models would then be obtained using fewer and more easily-identified retained modes, compared

to the present cyclic Craig-Bampton models.

The two classical free-interface CMS methods by Craig and Chang [33] and by Rubin [32], which were reviewed and discussed in the previous section, may be considered as alternative CMS bases for the SMART approach. These methods include the contributions of residual flexibility and inertia for accelerated modal convergence. Furthermore, when considering the physical behavior of a realistic bladed disk assembly, it is realized that the disk-blade interfaces and thus the blades are likely to follow the motion of the much stiffer disk. Conversely, motion of the much more flexible blades will likely have a minimal impact on the disk, except for local deformations at the disk-blade interfaces. This implies that using fixed-interface normal modes for the disk component may not be ideal from a modal convergence perspective, and a free-interface CMS approach should therefore provide a better component mode basis for the disk component. However, from the same physical consideration, the flexible blade motion is likely to be much closer to a fixed-interface (i.e., cantilevered) representation than a free-interface (i.e., "free-free") representation, which would thus favor a fixed-interface (Craig-Bampton) CMS approach. Therefore, in an attempt to optimize the representations of both components, a new hybrid-interface CMS method is developed that uses a free-interface disk component and a fixed-interface blade component.

9.2.1 A Hybrid-Interface CMS Approach

The proposed hybrid-interface CMS implementation (H) is based on a free-interface disk component following the Craig-Chang (C^2) approach and a fixed-interface (Craig-Bampton; C-B) blade component. The key difference between using a hybrid-interface representation and using the same representation for both components is a slightly more complicated and less straightforward set of constraint equations to ensure displacement

compatibility and force equilibrium over the component interface. Using a C^2 formulation for the α-component and a C-B formulation for the β-component from Section 9.1, the constraint equations take the form:

$$\mathbf{x}_{\mathbf{\Gamma}}^{\alpha} = \mathbf{\Phi}_{\mathbf{\Gamma}}^{\alpha}\mathbf{p}_{\mathbf{k}}^{\alpha} + \mathbf{\Psi}_{\mathbf{\Gamma}}^{\alpha}\mathbf{p}_{\mathbf{d}}^{\alpha} = \mathbf{p}_{\mathbf{c}}^{\beta} = \mathbf{x}_{\mathbf{\Gamma}}^{\beta} \tag{9.30}$$

$$\mathbf{f}_{\mathbf{\Gamma}}^{\alpha} + \mathbf{f}_{\mathbf{\Gamma}}^{\beta} = \mathbf{p}_{\mathbf{d}}^{\alpha} - \omega^2 \mu_{\mathbf{kc}}^{\beta^{\mathbf{T}}}\mathbf{p}_{\mathbf{k}}^{\beta} + \left[\kappa_{\mathbf{cc}}^{\beta} - \omega^2\mu_{\mathbf{cc}}^{\beta}\right]\mathbf{p}_{\mathbf{c}}^{\beta} = \mathbf{0}. \tag{9.31}$$

These two sets of constraint equations lead to the synthesized H representation of a two-component structure:

$$\mathbf{M}^{\mathbf{H}} = \begin{bmatrix} \mathbf{I} + \mathbf{\Phi}_{\mathbf{\Gamma}}^{\alpha^{\mathbf{T}}}\mu_{\mathbf{cc}}^{\beta}\mathbf{\Phi}_{\mathbf{\Gamma}}^{\alpha} & \mathbf{\Phi}_{\mathbf{\Gamma}}^{\alpha^{\mathbf{T}}}\mu_{\mathbf{cc}}^{\beta}\mathbf{\Psi}_{\mathbf{\Gamma}}^{\alpha} & \mathbf{\Phi}_{\mathbf{\Gamma}}^{\alpha^{\mathbf{T}}}\mu_{\mathbf{kc}}^{\beta^{\mathbf{T}}} \\ \mathbf{\Psi}_{\mathbf{\Gamma}}^{\alpha^{\mathbf{T}}}\mu_{\mathbf{cc}}^{\beta}\mathbf{\Phi}_{\mathbf{\Gamma}}^{\alpha} & \mathbf{\Psi}^{\alpha^{\mathbf{T}}}\mathbf{M}^{\alpha}\mathbf{\Psi}^{\alpha} + \mathbf{\Psi}_{\mathbf{\Gamma}}^{\alpha^{\mathbf{T}}}\mu_{\mathbf{cc}}^{\beta}\mathbf{\Psi}_{\mathbf{\Gamma}}^{\alpha} & \mathbf{\Psi}_{\mathbf{\Gamma}}^{\alpha^{\mathbf{T}}}\mu_{\mathbf{kc}}^{\beta^{\mathbf{T}}} \\ \mu_{\mathbf{kc}}^{\beta}\mathbf{\Phi}_{\mathbf{\Gamma}}^{\alpha} & \mu_{\mathbf{kc}}^{\beta}\mathbf{\Psi}_{\mathbf{\Gamma}}^{\alpha} & \mu_{\mathbf{kk}}^{\beta} \end{bmatrix} \tag{9.32}$$

$$\mathbf{K}^{\mathbf{H}} = \begin{bmatrix} \mathbf{\Lambda}^{\alpha} + \mathbf{\Phi}_{\mathbf{\Gamma}}^{\alpha^{\mathbf{T}}}\kappa_{\mathbf{cc}}^{\beta}\mathbf{\Phi}_{\mathbf{\Gamma}}^{\alpha} & \mathbf{\Phi}_{\mathbf{\Gamma}}^{\alpha^{\mathbf{T}}}\kappa_{\mathbf{cc}}^{\beta}\mathbf{\Psi}_{\mathbf{\Gamma}}^{\alpha} & \mathbf{0} \\ \mathbf{\Psi}_{\mathbf{\Gamma}}^{\alpha^{\mathbf{T}}}\kappa_{\mathbf{cc}}^{\beta}\mathbf{\Phi}_{\mathbf{\Gamma}}^{\alpha} & \left[\mathbf{I} + \mathbf{\Psi}_{\mathbf{\Gamma}}^{\alpha^{\mathbf{T}}}\kappa_{\mathbf{cc}}^{\beta}\right]\mathbf{\Psi}_{\mathbf{\Gamma}}^{\alpha} & \mathbf{0} \\ \mathbf{0} & \mathbf{0} & \kappa_{\mathbf{kk}}^{\beta} \end{bmatrix} \qquad \mathbf{p}^{\mathbf{H}} = \begin{Bmatrix} \mathbf{p}_{\mathbf{k}}^{\alpha} \\ \mathbf{p}_{\mathbf{d}}^{\alpha} \\ \mathbf{p}_{\mathbf{k}}^{\beta} \end{Bmatrix}.$$

The definitions of the various modal component quantities appearing in Eq. (9.32) are found in Section 9.1 for the respective methods (α = Craig-Chang; β = Craig-Bampton).

9.2.2 Modal Convergence Trends

In this section, the modal convergence trends are investigated for the various derived methods — C-B, C^2, R, SC^2, and H — using a simple two-component model in the shape of a highly simplified disk-blade sector as shown in Fig. 9.6. The test model is constructed from linear brick elements (8-noded solids). Moreover, as Fig. 9.6 indicates, only the inner hub of the "disk" component is fully constrained while all other boundaries are free, resulting in a total of 198 unconstrained finite element DOF. The simple test model in Fig. 9.6 may not be ideal, since it is not coupled by cyclic symmetry constraints to form

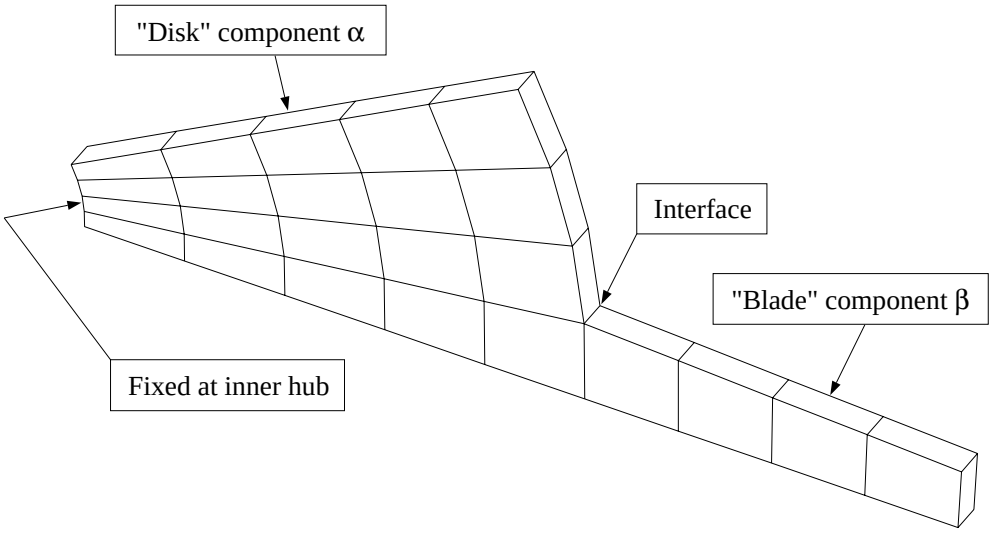

Figure 9.6: Finite element mesh for simple two-component disk-blade sector model.

a multi-sector assembly, nor is the normally very large difference in stiffness between the disk and the blade components properly accounted for. However, the model is nevertheless believed to be adequate for a preliminary validation and performance evaluation of the H approach.

The obtained modal convergence trends are depicted in Fig. 9.7. The modal convergence for each method is measured as the average relative error for the five lowest natural frequencies compared to reference finite element values. Note that, based on the numerical precision of input data, the resulting numerical precision limit can in this case be expected to be approximately $\mathcal{O}\left(10^{-5}\right)$–$\mathcal{O}\left(10^{-4}\right)$. As expected, the classical free-interface CMS techniques (C^2 and R) exhibit numerical instability for this model, too. An important observation from Fig. 9.7 is that the onsets of instability occur at significantly lower fractions of the total number of component normal modes for this test model ($< 40\%$) compared to the results in Section 9.1 ($> 50\%$). It is further noted that the SC^2 method is a robust performer. However, the SC^2 approach does not possess the convergence rates and accuracy levels of the other techniques considered.

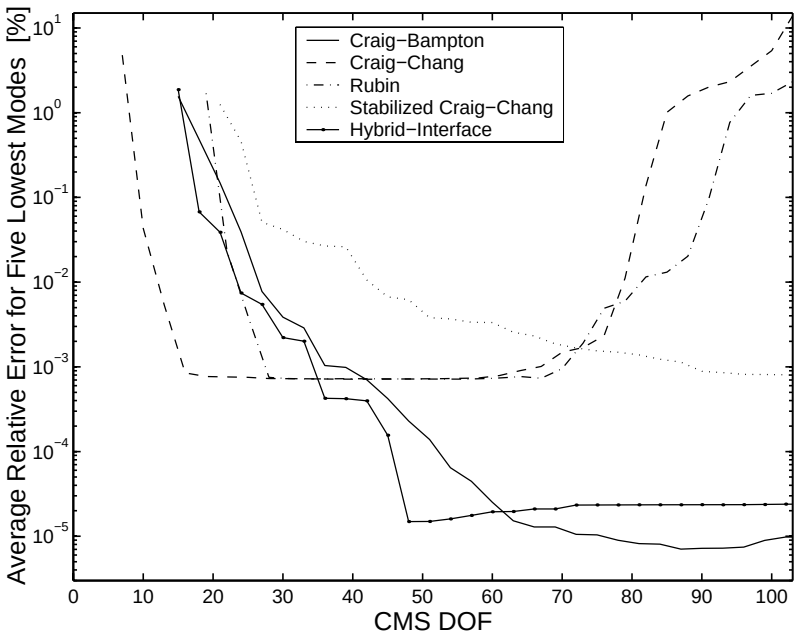

Figure 9.7: Convergence of the five lowest natural frequencies of the simple two-component disk-blade sector model in Fig. 9.6 relative to finite element results for the considered CMS methods.

The performance of the C^2 model is once again (see Section 9.1) extremely impressive for "normal", practical numbers of retained component modes, since this model is the only one that does not retain any DOF pertaining to the interface. Hence, from a modal convergence perspective, the C^2 method is clearly the most appealing approach. However, the C^2 method fails in that it does not provide a "natural" mode selection in bladed disk applications, since it is constructed from the normal modes of a "free-free" blade, including a set of rigid-body modes. This mode set is not ideal in that the normal modes will not conform with the characteristic motion of blade-dominated assembly modes (e.g., first flex (1F), second torsion (2T), etc.), which instead closely follow the normal modes of a fixed-interface (i.e., cantilevered) blade. Furthermore, in the context of blade mistuning, it is reasonable to assume that experimental measurements of blade natural frequencies are obtained for a cantilevered configuration, rather than for "free-free" blades. Hence,

in cases where differing mistuning levels for individual blade mode types (i.e., individual mode mistuning) are to be considered, a C^2 blade representation requires computationally expensive projections of extracted stiffness deviations in the finite element domain, similar to the mistuning implementation for shrouded blades presented in Chapter IV.

Figure 9.7 further shows that the C-B and H techniques exhibit very similar overall performances, displaying fast modal convergence. Both these techniques satisfy the "natural" mode selection criterion in terms of blade normal modes, and the H approach satisfies this criterion also with respect to disk normal modes. Furthermore, blade mistuning input is particularly straightforward in both C-B and H models, since the modal stiffnesses of the cantilevered blades are readily accessible. It is important to note that the novel H approach consistently yields more accurate reduced order models than C-B. In addition, the H technique is likely to perform even better (versus C-B) when applied to models that feature more realistic differences in stiffness between disks and blades. The improved performance exhibited by the H approach may become a critical advantage in certain applications, where it may be imperative to minimize the CMS model while retaining straightforward blade mistuning input (e.g., multi-stage analysis, mistuning identification). Thus, the preliminary results presented in this section indicate that a hybrid-interface CMS method may provide an optimal basis for dynamic analyses of mistuned bladed disks when using a component mode approach.

CHAPTER X

Conclusions

The effects of mistuning (i.e., small, unavoidable variations in blade properties) on bladed disk dynamics continue to be of concern to the turbomachinery community. The potential for vibration energy localization and therefore dramatic increases in forced response amplitudes and stresses is likely to place significant constraints on blade design optimization. The complicating effect of mistuning on bladed disk response predictions is twofold: (a) mistuning destroys the traditionally assumed cyclic symmetry of a rotor, and thus requires full assembly modeling; and (b) mistuning is a random quantity, requiring blade fatigue life assessments based on reliable forced response statistics. These two considerations imply that using traditional analysis techniques such as finite element analysis is not practical, since full assembly models are often prohibitively large and therefore unsuitable for comprehensive statistical analyses. It is thus essential to be able to predict accurately the dynamics of mistuned bladed disks using highly reduced order models. Only when such reduced order models meet very demanding standards in terms of accuracy and computational efficiency can mistuning considerations enter as an integral part of the turbomachinery rotor design process.

The doctoral research documented in this dissertation has addressed this industry-wide need through the development of several high-performance reduced order modeling tech-

niques that enable highly accurate and computationally efficient dynamic analyses of mistuned bladed disks. The presented work has resulted in significant advances on each of the two critical fronts — reduced order model *accuracy* and computational *efficiency*.

10.1 Dissertation Contributions

Significant contributions of this dissertation include:

- Successful extension of the technique by Castanier *et al*. [20] to bladed disk assemblies featuring shrouded blades. The extended formulation uses projection of individual blade mode mistuning onto the cyclic modes of the blade-shroud-ring assembly. This included the formulation of a novel technique for extracting stiffness deviations from experimentally obtained blade frequency data.

- Successful formulation, implementation, and validation of a state-of-the-art reduced order modeling technique for the dynamic analysis of mistuned bladed disks — a secondary modal analysis reduction technique (SMART). The SMART approach uses a cyclic implementation of a fixed-interface component mode synthesis technique as an intermediate reduced order model basis. A secondary modal analysis is performed on the intermediate model, from which only a small number of system modes of interest are retained. Blade mistuning is input in the intermediate generalized coordinates and projected onto the secondary generalized coordinates in the low-order modal domain. This results in highly accurate and computationally efficient minimized models that are exceptionally well suited for comprehensive analyses of response statistics.

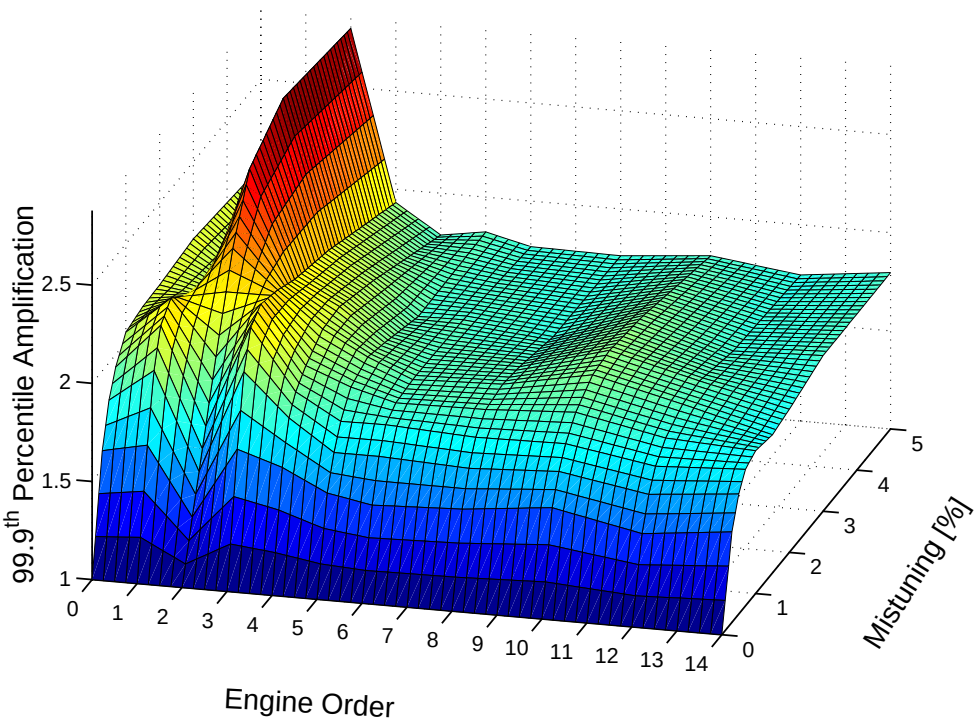

Figure 10.1: Example results from a mistuning sensitivity analysis based on comprehensive response statistics for the industrial compressor stage model depicted in Fig. 3.1.

Method	**DOF**	**Estimated CPU**	**Amplitude Error**
FEM	126,846	6,000,000 min. (11 years)	(reference)
REDUCE	435	10,000 min. (7 days)	1–10%
SMART	31	5 min.	0.01–0.1%

Table 10.1: Computational efficiency and accuracy trends of developed techniques, with reference to the mistuning sensitivity analysis results in Fig. 10.1.

An example application of the SMART approach is shown in Fig. 10.1, with method performance data listed in Table 10.1. This table also includes estimates for the reference finite element model (FEM) and the reduced order model by Castanier *et al*. [20] (REDUCE) for comparison.

- Thorough investigation and documentation of important effects of disk flexibility and interstage coupling on the response behavior and mistuning sensitivity of bladed disks.

- Formulation and validation of a SMART approach for accurate and efficient reduced order modeling of mistuned multi-stage rotor assemblies, capable of accurately capturing potentially critical interstage coupling effects.

10.2 Future Research

Based on the work presented in this dissertation, some ideas for future research are summarized as follows.

- Further efforts are required to establish the "optimal" component mode basis for the SMART approach. Preliminary results in Chapter IX indicate that a hybrid-interface component mode synthesis approach with a cyclic free-interface disk component and a fixed-interface blade component may be the most appropriate and practical representation for mistuned bladed disks.

- To make the SMART approach useful as a design tool in industrial applications, it is imperative that aerodynamic coupling is incorporated into the formulation and validated thoroughly. In the current format, where blades are represented in real-valued cyclic fixed-interface form, this may be achieved relatively easily. Assuming that aerodynamic analyses use fixed-interface blade modes employing complex-form cyclic symmetry, the resulting aerodynamic coefficients (any combination of mass, viscous damping, structural damping, and stiffness entries) may be transformed into an equivalent real-valued cyclic representation that can be introduced directly to the intermediate model in the SMART approach.

- The significant impact of interstage coupling revealed in this work implies that single-stage analysis may not always be appropriate. However, in order to model the system efficiently and interpret the results clearly, it is certainly desirable to analyze one rotor stage at a time. Hence, it is suggested that single-stage representations that incorporate interstage coupling effects in some condensed form may be the most feasible and appropriate manner to realistically model and analyze the dynamics of mistuned bladed disks. One such "suspended single-stage" representation can be obtained from the multi-stage formulation in Chapter VIII by including the adjacent stages but neglecting their dynamic content (i.e., by assuming zero retained normal modes for the adjacent stages). The interstage flexibility and inertia are then condensed onto the interstage degrees of freedom via projections of adjacent stage mass and stiffness matrices onto the static interstage constraint modes.

- To obtain more complete and realistic models of bladed disks, it is further suggested that present linear techniques formulated primarily for the accurate capture of mistuning effects (e.g., SMART) be merged with concurrently developed non-linear techniques for accurate modeling of blade friction dampers and intershroud friction. Shrouds and dry friction dampers are frequently used to reduce the vibratory response of blades, and the inclusion of such model features in reduced order model representations is likely to be of significant value to the turbomachinery community.

APPENDICES

APPENDIX A

The Kronecker Product

The Kronecker product of two matrices is defined as:

$$\mathbf{A} \otimes \mathbf{B} = \begin{bmatrix} a_{11}\mathbf{B} & a_{12}\mathbf{B} & \dots & a_{1N}\mathbf{B} \\ a_{21}\mathbf{B} & a_{22}\mathbf{B} & \dots & a_{2N}\mathbf{B} \\ \vdots & \vdots & \ddots & \vdots \\ a_{N1}\mathbf{B} & a_{N2}\mathbf{B} & \dots & a_{NN}\mathbf{B} \end{bmatrix}. \tag{A.1}$$

Selected useful properties of the Kronecker product:

$$(\mathbf{A} \otimes \mathbf{B})(\mathbf{C} \otimes \mathbf{D}) = (\mathbf{AC}) \otimes (\mathbf{BD}) \tag{A.2}$$

$$(\mathbf{A} \otimes \mathbf{B})^{-1} = \mathbf{A}^{-1} \otimes \mathbf{B}^{-1} \tag{A.3}$$

$$(\mathbf{A} \otimes \mathbf{B})^{\mathbf{T}} = \mathbf{A}^{\mathbf{T}} \otimes \mathbf{B}^{\mathbf{T}}. \tag{A.4}$$

APPENDIX B

Circulant Matrices

The mass and stiffness matrices of any linear cyclic system may be cast in circulant or block-circulant form. Hence, the application of cyclic symmetry in this paper makes frequent use of the properties of circulant matrices and their eigenvectors. The properties of circulant matrices are thoroughly examined in Davis [73]. The general form of a square circulant matrix is:

$$\mathbf{C} = \mathbf{circ}\left(c_1, c_2, \ldots, c_N\right) = \begin{bmatrix} c_1 & c_2 & \ldots & c_N \\ c_N & c_1 & \ldots & c_{N-1} \\ \vdots & \vdots & \ddots & \vdots \\ c_2 & c_3 & \ldots & c_1 \end{bmatrix}. \tag{B.1}$$

All circulant matrices of order N possess N independent eigenvectors. In particular, they share the same set of eigenvectors that make up the complex Fourier matrix, $\mathbf{E}$:

$$\mathbf{E} = [e_{ki}] \;;\quad e_{ki} = \tfrac{1}{\sqrt{N}} e^{j\alpha(i-1)(k-1)}, \quad k, i = 1, \ldots, N, \tag{B.2}$$

where $j = \sqrt{-1}$ and $\alpha = 2\pi/N$. In addition, there exists an "almost-equivalent" real-valued form of Eq. (B.2):

$$\mathbf{F} = \begin{bmatrix} \mathbf{f_0} & \mathbf{f_{1,c}} & \mathbf{f_{1,s}} & \cdots & \mathbf{f_{n,c}} & \mathbf{f_{n,s}} & \cdots & \mathbf{f_{N/2}} \end{bmatrix} = \ldots \tag{B.3}$$

$$\ldots = \begin{bmatrix} \frac{1}{\sqrt{N}} & \sqrt{\frac{2}{N}} & 0 & \cdots & \frac{1}{\sqrt{N}} \\ \frac{1}{\sqrt{N}} & \sqrt{\frac{2}{N}}\cos\alpha & \sqrt{\frac{2}{N}}\sin\alpha & \cdots & -\frac{1}{\sqrt{N}} \\ \frac{1}{\sqrt{N}} & \sqrt{\frac{2}{N}}\cos 2\alpha & \sqrt{\frac{2}{N}}\sin 2\alpha & \cdots & \frac{1}{\sqrt{N}} \\ \vdots & \vdots & \vdots & & \vdots \\ \frac{1}{\sqrt{N}} & \sqrt{\frac{2}{N}}\cos(N-1)\alpha & \sqrt{\frac{2}{N}}\sin(N-1)\alpha & \cdots & \frac{(-1)^{N-1}}{\sqrt{N}} \end{bmatrix},$$

where the last column only exists if N is even.

Note that both $\mathbf{E}$ and $\mathbf{F}$ are orthonormal, or unitary, such that $\mathbf{E}^*\mathbf{E} = \mathbf{F}^\mathbf{T}\mathbf{F} = \mathbf{I}$, where $\mathbf{I}$ is an identity matrix of size N, and $*$ denotes the Hermitian adjoint (complex conjugate transpose). In addition, this implies that $\mathbf{E}^{-1} = \mathbf{E}^*$ and $\mathbf{F}^{-1} = \mathbf{F}^\mathbf{T}$, such that the transformation products $\mathbf{E}^*\mathbf{C}\mathbf{E}$ and $\mathbf{F}^\mathbf{T}\mathbf{C}\mathbf{F}$ are similarity transformations [64].

The reason behind calling $\mathbf{F}$ "almost-equivalent" to $\mathbf{E}$ is that the columns of $\mathbf{F}$ are not true eigenvectors of $\mathbf{C}$, and hence, the similarity transformation $\mathbf{F}^\mathbf{T}\mathbf{C}\mathbf{F}$ will not yield a diagonalized matrix. However, it will result in a matrix where all non-zero elements will be grouped into 2×2 blocks ("double" harmonics) on the diagonal, except for the $(1,1)$ and, for N even, the (N,N) elements ("single" harmonics). This matrix type is referred to as pseudo-block-diagonal.

These properties are readily extended to the case of block-circulant matrices by expanding $\mathbf{E}$ and $\mathbf{F}$ as $\mathbf{E} \otimes \mathbf{I}$ and $\mathbf{F} \otimes \mathbf{I}$, respectively. The scalar c_i then represents a matrix block $\mathbf{C_i}$, where $\mathbf{C_i}$ and $\mathbf{I}$ are of the same size.

BIBLIOGRAPHY

BIBLIOGRAPHY

[1] R. Bladh, M. P. Castanier, and C. Pierre. Effects of Multi-Stage Coupling and Disk Flexibility on Mistuned Bladed Disk Dynamics. In Tentatively accepted for *The 46th ASME Gas Turbine and Aeroengine Technical Congress, Exposition and Users Symposium,* New Orleans, Louisiana, 2001.

[2] J. Zenneck. Ueber die freien Schwingungen nur annähernd vollkommener kreisförmiger Platten. *Annalen der Physik*, 67:165–184, 1899.

[3] S. A. Tobias and R. N. Arnold. The Influence of Dynamical Imperfection on the Vibration of Rotating Disks. *Proceedings of the Institution of Mechanical Engineers*, 171:669–690, 1957.

[4] P. W. Anderson. Absence of Diffusion in Certain Random Lattices. *Physical Review,* 109(5):1492–1505, 1958.

[5] J. T. Wagner. Coupling of Turbomachine Blade Vibrations Through the Rotor. *ASME Journal of Engineering for Power,* 89(4):502–512, 1967.

[6] R. C. F. Dye and T. A. Henry. Vibration Amplitudes of Compressor Blades Resulting From Scatter in Blade Natural Frequencies. *ASME Journal of Engineering for Power*, 91(3):182–188, 1969.

[7] D. J. Ewins. The Effects of Detuning Upon the Forced Vibrations of Bladed Disks. *Journal of Sound and Vibration*, 9(1):65–79, 1969.

[8] D. J. Ewins. A Study of Resonance Coincidence in Bladed Discs. *Journal Mechanical Engineering Science*, 12(5):305–312, 1970.

[9] L. E. El-Bayoumy and A. V. Srinivasan. Influence of Mistuning on Rotor-Blade Vibrations. *AIAA Journal*, 13(4):460–464, 1975.

[10] L. K. H. Lu and P. C. Warner. A Statistical Assessment of the Effect of Variable Root Flexibility on the Vibration Response of Shrouded Blades. In *Vibrations of Bladed Disk Assemblies, Proceedings of the ASME 9th Biennial Conference on Mechanical Vibration and Noise,* Dearborn, Michigan, pages 147–151, 1983.

[11] J. H. Griffin and T. M. Hoosac. Model Development and Statistical Investigation of Turbine Blade Mistuning. *ASME Journal of Vibration, Acoustics, Stress, and Reliability in Design*, 106(2):204–210, 1984.

[12] B. A. H. Abbas and K. M. Kamal. Vibration of Turbomachinery Blades with Root Flexibility Effects. In *Bladed Disk Assemblies, Proceedings of the ASME 11th Biennial Conference on Mechanical Vibration and Noise*, Boston, Massachusetts, pages 31–41, 1987.

[13] C.-C. Lin and M. P. Mignolet. An Adaptive Perturbation Scheme for the Analysis of Mistuned Bladed Disks. *ASME Journal of Engineering for Gas Turbines and Power*, 119(1):153–160, 1997.

[14] S. T. Wei and C. Pierre. Localization Phenomena in Mistuned Assemblies with Cyclic Symmetry, Part I: Free Vibrations. *ASME Journal of Vibration, Acoustics, Stress, and Reliability in Design*, 110(4):429–438, 1988.

[15] S. T. Wei and C. Pierre. Localization Phenomena in Mistuned Assemblies with Cyclic Symmetry, Part II: Forced Vibrations. *ASME Journal of Vibration, Acoustics, Stress, and Reliability in Design*, 110(4):439–449, 1988.

[16] G. S. Óttarsson and C. Pierre. On the Effects of Interblade Coupling on the Statistics of Maximum Forced Response Amplitudes in Mistuned Bladed Disks. In *Proceedings of the 36th AIAA/ASME/ASCE/AHS Structures, Structural Dynamics, and Materials Conference*, New Orleans, Louisiana, volume 5, pages 3070–3078, 1995. Also, *Journal of Sound and Vibration*, in press.

[17] A. V. Srinivasan. Flutter and Resonant Vibration Characteristics of Engine Blades. *ASME Journal of Engineering for Gas Turbines and Power*, 119(4):742–775, 1997.

[18] H. Irretier. Spectral Analysis of Mistuned Bladed Disk Assemblies by Component Mode Synthesis. In *Vibrations of Bladed Disk Assemblies, Proceedings of the ASME 9th Biennial Conference on Mechanical Vibration and Noise*, Dearborn, Michigan, pages 115–125, 1983.

[19] Z.-C. Zheng and F.-R. Wang. Dynamic Analysis of Blade Groups Using Component Mode Synthesis. In *Vibrations of Blades and Bladed Disk Assemblies, Proceedings of the ASME 10th Biennial Conference on Mechanical Vibration and Noise*, Cincinnati, Ohio, pages 97–103, 1985.

[20] M. P. Castanier, G. Óttarsson, and C. Pierre. A Reduced-Order Modeling Technique for Mistuned Bladed Disks. *ASME Journal of Vibration and Acoustics*, 119(3):439–447, 1997.

[21] M. J. Kruse and C. Pierre. Forced Response of Mistuned Bladed Disks Using Reduced-Order Modeling. In *Proceedings of the 37th AIAA/ASME/ASCE/AHS Structures, Structural Dynamics, and Materials Conference*, Salt Lake City, Utah, volume 4, pages 1938–1950, 1996.

[22] M. J. Kruse and C. Pierre. Dynamic Response of an Industrial Turbomachinery Rotor. In *Proceedings of the 32nd AIAA/ASME/SAE/ASEE Joint Propulsion Conference and Exhibit*, Lake Buena Vista, Florida, 1996.

[23] R. Bladh, M. P. Castanier, and C. Pierre. Reduced Order Modeling and Vibration Analysis of Mistuned Bladed Disk Assemblies with Shrouds. *ASME Journal of Engineering for Gas Turbines and Power*, 121(3):515–522, 1999.

[24] R. R. Craig. Substructure Methods in Vibration. *ASME Journal of Mechanical Design*, 117:207–213, 1995.

[25] P. Seshu. Substructuring and Component Mode Synthesis. *Shock and Vibration*, 4(3):199–210, 1997.

[26] M.-T. Yang and J. H. Griffin. A Reduced Order Approach for the Vibration of Mistuned Bladed Disk Assemblies. *ASME Journal of Engineering for Gas Turbines and Power*, 119(1):161–167, 1997.

[27] M.-T. Yang and J. H. Griffin. A Normalized Modal Eigenvalue Approach for Resolving Modal Interaction. *ASME Journal of Engineering for Gas Turbines and Power*, 119(3):647–650, 1997.

[28] W. C. Hurty. Dynamic Analysis of Structural Systems Using Component Modes. *AIAA Journal*, 3(4):678–685, 1965.

[29] R. R. Craig and M. C. C. Bampton. Coupling of Substructures for Dynamics Analyses. *AIAA Journal*, 6(7):1313–1319, 1968.

[30] R. L. Goldman. Vibration Analysis by Dynamic Partitioning. *AIAA Journal*, 7(6):1152–1154, 1969.

[31] R. H. MacNeal. A Hybrid Method of Component Mode Synthesis. *Computers and Structures*, 1:581–601, 1971.

[32] S. Rubin. Improved Component-Mode Representation for Structural Dynamic Analysis. *AIAA Journal*, 13(8):995–1006, 1975.

[33] R. R. Craig and C.-J. Chang. Free-Interface Methods of Substructure Coupling for Dynamic Analysis. *AIAA Journal*, 14(11):1633–1635, 1976.

[34] A. L. Hale and L. Meirovitch. A General Substructures Synthesis Method for Dynamic Simulation of Complex Structures. *Journal of Sound and Vibration*, 69(2):309–326, 1980.

[35] E. L. Wilson, M. Yuan, and J. M. Dickens. Dynamic Analysis by Direct Superposition of Ritz Vectors. *Earthquake Engineering and Structural Dynamics*, 10:813–821, 1982.

[36] E. L. Wilson and E. P. Bayo. Use of Special Ritz Vectors in Dynamic Substructure Analysis. *ASCE Journal of Structural Engineering*, 112:1944–1954, 1986.

[37] R. R. Arnold, R. L. Citerley, M. Chargin, and D. Gallant. Application of Ritz Vectors for Dynamic Analysis of Large Structures. *Computers and Structures*, 21:461–467, 1985.

[38] A. A. Abdallah and A. A. Huckelbridge. Boundary Flexible Method of Component Mode Synthesis Using Static Ritz Vectors. *Computers and Structures*, 35:51–61, 1990.

[39] R. R. Craig and A. L. Hale. Block-Krylov Component Synthesis Method for Structural Model Reduction. *AIAA Journal of Guidance, Control, and Dynamics*, 11:562–570, 1988.

[40] J. A. Morgan, C. Pierre, and G. M. Hulbert. Calculation of Component Mode Synthesis Matrices From Measured Frequency Response Functions, Part 1: Theory. *ASME Journal of Vibration and Acoustics*, 120(2):503–508, 1998.

[41] W.-H. Shyu, Z.-D. Ma, and G. M. Hulbert. A New Component Mode Synthesis Method: Quasi-Static Mode Compensation. *Finite Elements in Analysis and Design*, 24:271–281, 1997.

[42] D. L. Thomas. Dynamics of Rotationally Periodic Structures. *International Journal for Numerical Methods in Engineering*, 14:81–102, 1979.

[43] J. A. Joseph. Cyclic Symmetry in MSC/NASTRAN. In *MSC/NASTRAN Application Manual*, chapter 3.2, pages 10–24. The MacNeal-Schwendler Corporation, 1981.

[44] C. L. Fortescue. Method of Symmetrical Co-ordinates Applied to the Solution of Polyphase Networks. In *Transactions of the American Institute of Electrical Engineers*, volume 37, pages 1027–1115, 1918.

[45] L. Meirovitch. *Analytical Methods in Vibrations*. Macmillan, New York, New York, 1967.

[46] D. J. Ewins. Vibration Characteristics of Bladed Disc Assemblies. *Journal Mechanical Engineering Science*, 15(3):165–186, 1973.

[47] C. Pierre. Mode Localization and Eigenvalue Loci Veering Phenomena in Disordered Structures. *Journal of Sound and Vibration*, 126(3):485–502, 1988.

[48] M. P. Mignolet and C.-C. Lin. Identification of Structural Parameters in Mistuned Bladed Disks. *ASME Journal of Vibration and Acoustics*, 119(3):428–438, 1997.

[49] M. P. Castanier and C. Pierre. Consideration on the Benefits of Intentional Blade Mistuning for the Forced Response of Turbomachinery Rotors. In *Proceedings of the 1997 ASME International Mechanical Engineering Congress and Exposition,* Dallas, Texas, volume 55, pages 419–425, 1997.

[50] R. Ramakumar. *Engineering Reliability: Fundamentals and Applications*. Prentice Hall, Englewood Cliffs, New Jersey, 1993.

[51] E. J. Gumbel. *Statistics of Extremes*. Columbia University Press, New York, New York, 1958.

[52] D. S. Whitehead. Effect of Mistuning on the Vibration of Turbomachine Blades Induced by Wakes. *Journal Mechanical Engineering Science*, 8(1):15–21, 1966.

[53] D. S. Whitehead. The Maximum Factor by Which Forced Vibration of Blades Can Increase Due to Mistuning. *ASME Journal of Engineering for Gas Turbines and Power*, 120(1):115–119, 1998.

[54] R. Bladh, M. P. Castanier, and C. Pierre. Reduced Order Modeling and Efficient Forced Response Statistics Prediction for Mistuned Bladed Disks. In *Proceedings of The 3rd National Turbine Engine High Cycle Fatigue Conference*, San Antonio, Texas, 1998.

[55] D. J. Mead. Wave Propagation and Natural Modes in Periodic Systems, I: Mono-Coupled Systems. *Journal of Sound and Vibration*, 40(1):1–18, 1975.

[56] V. Elchuri, G. C. C. Smith, and A. M. Gallo. NASTRAN Forced Vibration Analysis of Rotating Cyclic Structures. *ASME Journal of Vibration, Acoustics, Stress, and Reliability in Design*, 106(2):224–234, 1984.

[57] D. Hitchings and M. Singh. Cyclic Symmetry Through Constraint Equations with Application to the Analysis of Steam Turbines. In *Bladed Disk Assemblies, Proceedings of the ASME 11th Biennial Conference on Mechanical Vibration and Noise*, Boston, Massachusetts, volume 6, pages 113–119, 1987.

[58] A. V. Srinivasan, S. R. Lionberger, and K. W. Brown. Dynamic Analysis of an Assembly of Shrouded Blades Using Component Modes. *ASME Journal of Mechanical Design*, 100(3):520–527, 1978.

[59] C-H. Menq, J. H. Griffin, and J. Bielak. The Forced Response of Shrouded Fan Stages. *ASME Journal of Vibration, Acoustics, Stress, and Reliability in Design*, 108(1):50–55, 1986.

[60] N. A. Valero and O. O. Bendiksen. Vibration Characteristics of Mistuned Shrouded Blade Assemblies. *ASME Journal of Engineering for Gas Turbines and Power*, 108(2):293–299, 1986.

[61] Y.-C. Tan, M. P. Castanier, and C. Pierre. Modal Approximations of Power Flow Between Coupled Component Structures. *Shock and Vibration Digest*, 32(1):65, 2000.

[62] R. R. Craig. *Structural Dynamics, An Introduction to Computer Methods.* Wiley, New York, New York, 1981.

[63] R. J. Allemang and D. L. Brown. A Correlation Coefficient for Modal Vector Analysis. In *Proceedings of the First International Modal Analysis Conference*, Orlando, Florida, pages 110–116, 1982.

[64] G. Strang. *Linear Algebra and Its Applications*. Saunders HBJ, Orlando, Florida, third edition, 1988.

[65] W. Campbell. The Protection of Steam-Turbine Disk Wheels from Axial Vibration. *Transactions of the ASME*, 46:31–160, 1924.

[66] R. Bladh, M. P. Castanier, and C. Pierre. Models of Rotor Mistuning and the Prediction of Mistuned Blade Forced Response. In *Proceedings of The 4th National Turbine Engine High Cycle Fatigue Conference,* Monterey, California, 1999.

[67] S. P. Timoshenko and J. N. Goodier. *Theory of Elasticity*. McGraw-Hill, New York, New York, third edition, 1970.

[68] M.-T. Yang and J. H. Griffin. A Reduced Order Model of Mistuning Using A Subset of Nominal System Modes. In *Proceedings of the 44th ASME Gas Turbine and Aeroengine Technical Congress, Exposition and Users Symposium,* Indianapolis, Indiana, 1999.

[69] F. Moyroud, G. Jacquet-Richardet, and T. Fransson. A Comparison of Two Finite Element Reduction Techniques for Mistuned Bladed-Disks. In *Proceedings of the 45th ASME Gas Turbine and Aeroengine Technical Congress, Exposition and Users Symposium,* Munich, Germany, 2000.

[70] R. Bladh, M. P. Castanier, and C. Pierre. Component-Mode-Based Reduced Order Modeling Techniques for Mistuned Bladed Disks, Part I: Theoretical Models. In *ASME Paper 2000-GT-0360,* in *Proceedings of The 45th ASME Gas Turbine and Aeroengine Technical Congress, Exposition and Users Symposium,* Munich, Germany, 2000. Also, *ASME Journal of Engineering for Gas Turbines and Power*, in press.

[71] R. Bladh, M. P. Castanier, and C. Pierre. Component-Mode-Based Reduced Order Modeling Techniques for Mistuned Bladed Disks, Part II: Application. In *ASME Paper 2000-GT-0361*, in *Proceedings of The 45th ASME Gas Turbine and Aeroengine Technical Congress, Exposition and Users Symposium*, Munich, Germany, 2000. Also, *ASME Journal of Engineering for Gas Turbines and Power*, in press.

[72] R. Courant and D. Hilbert. *Methods of Mathematical Physics, Volume I*. Wiley-Interscience, New York, New York, 1953.

[73] P. J. Davis. *Circulant Matrices*. Chelsea Publishing, New York, New York, second edition, 1994.